Investigation of the Defect Structure and Energetics of Nickel Doped Alkaline Earth Perovskite-type Titanates using Computational Chemistry Modelling

by

Michael Paul

Davy Faraday Research Laboratory

Kathleen Lonsdale Building

University College London

Gower Street

London

WC1E 6BT

2008

ProQuest LLC
789 East Eisenhower Parkway
P.O. Box 1346
Ann Arbor, MI 48106-1346

To my fantastic wife, Ruth, and wonderful children, Richard and Angharad

Abstract

Atomistic computational modelling has been used to enhance the understanding of experimental studies into nickel doped alkaline earth titanate materials for use as catalysts for the partial oxidation of methane to synthesis gas. In particular, computational studies have allowed a model to be formulated of the structure of the metastable pre catalytical materials and the release of the dopant cations onto the surface at elevated temperatures prior to reduction to form the catalytically active phases. A rationale is proposed to explain the higher catalytic activity of nickel doped strontium titanate over the other nickel doped alkaline earth titanate systems.

Two computational modelling techniques have been employed: interatomic potential based simulations and density functional theory. In the former, the long range and short range potentials that exist between the ions of the lattice are used to model the crystal properties. Density functional theory is an *ab initio* electronic structure technique which calculates the electron density associated with the lowest energy for a given arrangement of atomic nuclei.

The substitution of Ni^{2+} and Ni^{3+} cations has been considered at both cation sites of the host perovskite lattices in the bulk and at the surface. The substitution of Ni^{3+} is shown to be highly unfavourable. A clear correlation between the instability of the doping process at the perovskite lattice A site and the size mismatch of the host and dopant cations has been identified. The dopant cation is also shown to be more stable at the surface than in the bulk and so the materials are expected to be enriched with dopant cations at the surface. For all systems, the dissolution of NiO into the lattice is found to be endothermic and therefore all nickel doped alkaline earth titanate systems would be expected to phase separate on heating.

We conclude that the growth of clusters of NiO at the surface of the doped lattices is likely to be seeded from Ni^{2+} cations at the perovskite lattice A site in $CaTiO_3$ and $SrTiO_3$ and the perovskite B site in $BaTiO_3$. We suggest that the positioning of the proposed seed cation for the growth of NiO clusters suggests that the $SrTiO_3$ host will be unique in anchoring the NiO clusters to the surface which will stop them merging to form larger clusters. Therefore, the $Ni/SrTiO_3$ system will be unique in forming small, highly dispersed NiO particles on the surface thus enhancing its catalytic activity on reduction.

Table of Contents

List of Tables

List of Figures

1. Introduction

The ability to control metal particle size and morphology on oxide supports is one of the most sought after design aspects in heterogeneous catalysis. Metal particle size and morphology impact on catalytic activity and selectivity across a wide range of industrially significant catalytic processes such as combustion, steam reforming, dry reforming and direct partial oxidation of methane (including solid oxide fuel cell and membrane applications), hydrogenation, methanol synthesis, Fischer Tropsch synthesis, methanation and auto-exhaust depollution. In addition, control of metal particle size is a key to moderating sintering and the reduction in useful catalytic lifetime resulting from loss of activity and selectivity.

In outline, the principal manufacturing routes for oxide supported metal catalysts involve preparation of precursors, where one or more metal salts are impregnated onto the oxide surface or the metal cation or cations are incorporated into a host lattice during preparation involving precipitation from a solution phase. In both cases, the final catalyst is prepared by a sequence of calcination and reduction steps. While the former route is often easier and provides an immediate surface layer, for example chloroplatinic acid on alumina, the latter method is of importance since solution phase preparation leads to precipitation of more homogeneous precursor materials, for example Cu/Zn in hydroxyl carbonates for methanol synthesis [1].

Regarding this second method, there is a growing body of evidence that, amongst complex oxide host lattices, the unique stability of the perovskite lattice provides a robust 'platform' for generating stable metal dispersions with high surface area.. An interesting example is the reported behaviour for Pd supported on $La(FeCo)O_3$ perovskite in three way exhaust depollution catalysts, where the catalyst responds reversibly in terms of its chemistry and structure to changes in the macro reaction environment, re-oxidising or reducing [2]. Other important examples include Ni supported on titanate perovskites, such as $SrTiO_3$ for partial oxidation of methane, $Pd/BaTiO_3$ for CH_4 combustion and Ni supported on $La(FeCo)O_3$ for Fischer Tropsch synthesis [3].

In the work presented here the results of a computational study of the three $Ni/ATiO_3$ systems are discussed, where $A=Ca^{2+}$, Sr^{2+} or Ba^{2+}, i.e the alkaline earth perovskite-type titanates. These materials have been extensively investigated by

Hayakawa and Takehira in relation to direct partial oxidation and CO_2 reforming of methane [4]. Superior performance in terms of conversion (93%) and selectivity (98%) was observed for $SrTiO_3$, where Ni had been doped into the lattice by a sol-gel route prior to in situ reduction in the test reactor, compared to the other titanates and also surface impregnated material. In addition, carbon formation was low and substantially less than for Ni supported on γ-Al_2O_3 prepared by an impregnation route.

The work in this thesis focuses on understanding the differences, and similarities, of both the bulk and surface interactions between nickel dopant cations and the host perovskite lattices to answer the question: "Why does nickel doped strontium titanate produce a superior catalytic material?". Of particular interest is the use of computational modelling to predict the energy associated with dissolution of NiO into the titanates with nickel substituted at both perovskite cationic sites in the bulk (as Ni^{2+} and Ni^{3+}) and at the surface of the lattice. In addition, the relaxations of the crystal around the dopant cations are considered in detail, which together with local conformational detail around the defect site from EXAFS analysis, allows a model of the catalytic materials to be built up.

Two computational chemistry tools were used to model the systems under investigation: interatomic potentials (or atomistic modelling); and density functional theory. Interatomic potential calculations model periodic ionic crystal lattices by considering the forces (both long range electrostatic and short range dispersive and repulsive), on an atomistic level. Electrons are not explicitly considered in these simulations. Density functional theory is an *ab initio* electronic structure technique where the system is modelled by finding the electron density for a given arrangement of atoms which gives the lowest energy.

2. Background

2.1. The Structure and Uses of Perovskite-type Oxides

2.1.1. The Structure of Perovskites

Perovskites have the general formula ABX_3 where X can be one of a number of anions, e.g. F^- or O^{2-} [5]. However, in relation to catalysis, it is the mixed metal oxide formulations which are of prime interest. In this case, in order to balance the 6- charge on the three oxide ions the combined charge of the A and B cations must equal 6+, which can be a combination of 2+/4+; 3+/3+; or 1+/5+ for the A and B ions respectively, for example: for 2+/4+ the alkaline earth titanates ($MTiO_3$, where M=Ca, Ba or Sr); and for 3+/3+ lanthanum metalates ($LaMO_3$, where M is a first row transition metal in the 3+ oxidation state). The A site cations occupy sites surrounded by 12 oxide ions, while the B sites are surrounded by 6 oxide ions to form a tight octahedral arrangement around the cation. A unit cell for the perovskite structure is illustrated in Figure 1

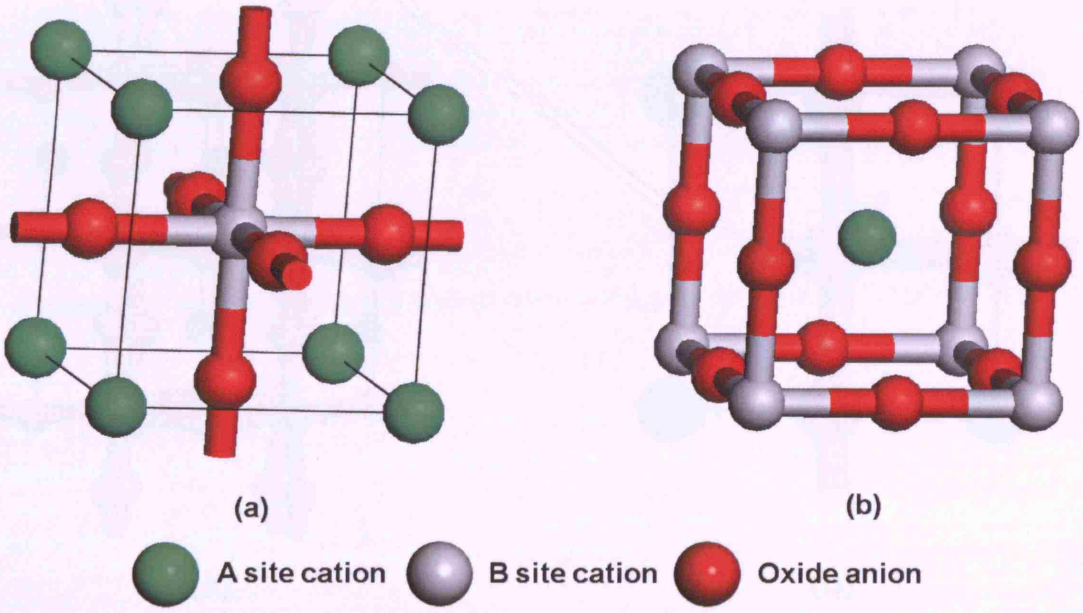

Figure 1 Two projections illustrating the unit cell of the cubic perovskite lattice showing (a) the octahedrally coordinated B site cation and (b) the 12 fold coordinated A site cation

In the unit cell shown in Figure 1(a) there are 8 "A" sites each located at each of the corners, one "B" site in the centre and 6 "X" sites at the centre of each face. The cell shown has a cubic symmetry.

One of the important features of the perovskite lattice is its tendency to distort unless the ratio of the sizes of the A and B cations is such to favour the cubic structure. The degree of distortion is controlled by the Goldschmidt tolerance factor, t, which is derived from a hard sphere model [6]:

$$t = \frac{r_A + r_O}{\sqrt{r_B + r_O}} \quad (1)$$

where r_A, r_B and r_O are the atomic radii of the A, B and O ions respectively. The normal range for t is $0.78<t<1.05$, with the lower cationic radii limits being $r_A > 0.09$nm and $r_B > 0.051$nm. For a cubic lattice t = 1, and the further away from unity the value of t is, the more distorted the structure. As the value of t decreases, due to reduced the size of the A site cation relative to the B site cation, systems commonly display rhombohedral symmetry above t = 0.9, and orthorhombic structures below t = 0.9. Other distortions are known including tetragonal, hexagonal, monoclinic or triclinic. Two common distortions of the perovskite lattice are shown in Figure 2.

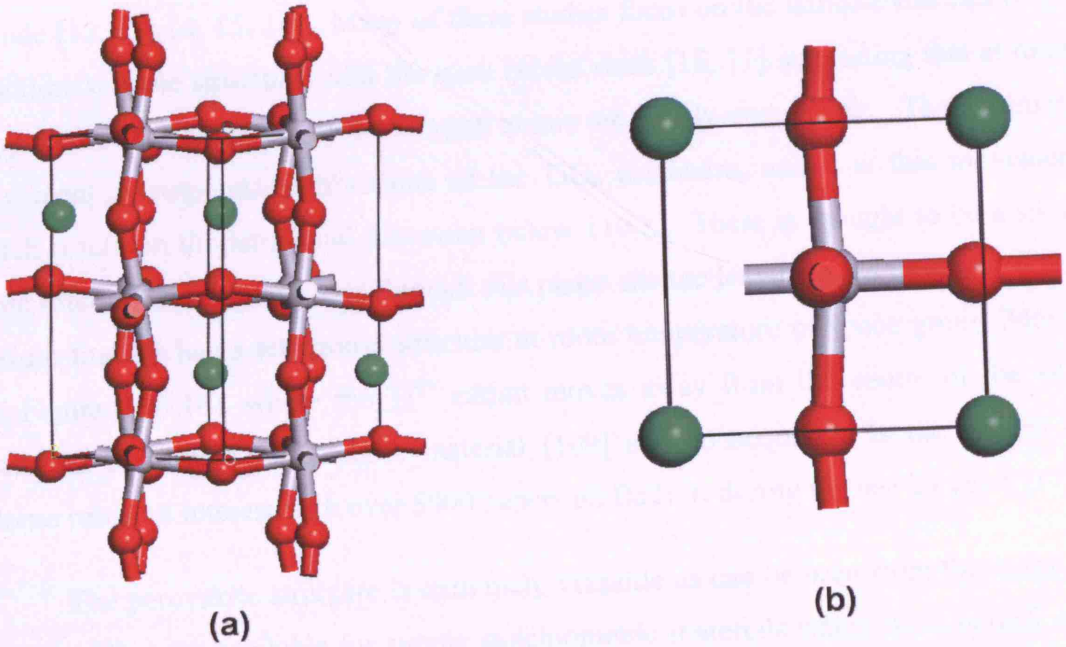

Figure 2 – Two common distortions of the cubic perovskite structure where (a) $t<1$ leading to an orthorhombic structure where the BO_6 octahedra tilt and (b) $t>1$ leading to the B site cation moving off centre forming a ferroelectric distortion.

In Figure 2(a) $t<1$ and so the A site cations are relatively small compared to the B site cations causing the BO_6 octahedra to tilt around the A site cations, the structure

shown is for $CaTiO_3$ [7]. In Figure 2(b) t>1 and the A site cations are relatively larger compared with the B site cations causing the B site cations to move off centre and form a tetragonal phase displaying ferroelectric properties, the structure shown is for $BaTiO_3$ [8].

The tolerance factor should only be used as a guide and is most reliable at predicting structure at room temperature. Solid/solid phase transitions are common for perovskites as the temperature is varied, as will be examined in more detail below.

The primary focus of this work are the alkaline earth titanates $MTiO_3$ (M=Ca, Sr, Ba). Calcium titanate has an orthorhombic structure at room temperature with space group Pbnm, see Figure 2(a), and exhibits two phase transitions on heating, changing to tetragonal I4/mcm at 1498 K and cubic Pm-3m at 1634 K [7]. Strontium titanate has a cubic structure at room temperature of space group Pm-3m, see Figure 1 [5, 9, 10, 11]. A phase transition occurs on cooling to around 110 K where the lattice changes from cubic to tetragonal symmetry, space group I4/mcm. This phase change has been the subject of many experimental and theoretical studies over the years; some examples include [12, 13, 14, 15, 16]. Many of these studies focus on the lattice-dynamics of the strontium titanate structure, with the most recent work [16, 11] suggesting that at room temperature the vibrations of the oxygen atoms are highly anisotropic. Their primary movement corresponds to librations of the TiO_6 octahedra, and it is this movement which results in the tetragonal distortion below 110 K. There is thought to be a small static rotation around the c axis through this phase change leaving a c/a ratio of 1.0005. Barium titanate has a tetragonal structure at room temperature of space group P4mm, see Figure 2(b) [8], where the Ti^{4+} cation moves away from the centre of the BO_6 octahedra to form a ferroelectric material [109] and consequently is the subject of intense research interest with over 5000 papers on $BaTiO_3$ during the last 25 years [17].

The perovskite structure is extremely versatile as can be seen from the range of structures that are available for simple stoichiometric materials where there is only one type of cation on the A site and one type of cation on the B site. A whole range of structures with interesting properties can be synthesized by considering non-stoichiometric systems which are derived from the basic perovskite structure with mixtures of cations on the A and B sites giving a rich variety of defect related chemistry. Furthermore, layered structures containing layers of perovskite combined with non-perovskite layers extend the chemical possibilities still further [18]. Some

examples of these perovskite related phases include: Dion-Jacobson phases [19], Ruddlesden-Popper phases [20, 21], Aurivillius phases [22], pyrochlores [23] and brownmillerite [24].

2.1.2. Defect Properties

Of central importance to this study, as well as to a range of uses of perovskite-type materials, as discussed below, are the properties of defect structures. In this section the effect of defects within the perovskite lattice are considered.

In common with other solid state materials, real perovskite lattices will contain a number of intrinsic imperfections such as oxygen vacancies. However the number of defects within the system can be readily enhanced by the addition of dopant ions either at the 'A' or 'B' cationic sites of the lattice.

There are two types of non-stoichiometry within the perovskite lattice: reductive, where there is an oxide ion deficiency; and oxidative, where there is a cation deficiency, examples of which are $LaCoO_{2.955}$ and $LaMnO_{3.110}$ for reductive and oxidative non-stoichiometry respectively [25]. However, it must be noted that the exact composition of a sample is strongly dependent on the reaction conditions during its formation, particularly the oxygen partial pressure. The driving force behind the formation of vacancies in these type of perovskites, i.e. $LaMO_3$, is the oxidation/reduction potential of the B site cation, which can be illustrated using the examples given above. For $LaCoO_{3-\delta}$, there is a tendency for Co^{3+} to reduce to Co^{2+} and so there is a need for the lattice to lose negative charge, in the form of O^{2-} vacancies, to maintain neutrality. Similarly, for $LaMnO_{3+\delta}$ there is a tendency of Mn^{3+} to oxidise to Mn^{4+} which necessitates the crystal to lose excess positive charge in the form of cation vacancies.

In addition to lattice vacancies there are two other types of defects possible within the perovskite lattice, namely electron rich and electron poor regions, where ions are still in the lattice, but there has been a change in electron charge. The creation of any of these three types of defect can be understood in the form of a balanced chemical equation using the Kroger-Vink notation [26], which provides a useful way of understanding the options for defect formation in terms of charge balance and the conditions to achieve appropriate effects.

The notation provides a set of symbols to describe the location and type of defect. Each site represented within the equation has the following form:

2] $$P_Q^R$$

where P either represents the symbol of the element occupying the site or is V if there is a vacancy; Q represents either the site or is I if it is an interstitial defect; R represents the change in charge of that site compared with the non-defect lattice and is given one of three symbols: $^{\times}$ denotes no change; $'$ denotes a unit of one less positive charge; and $^{\bullet}$ denotes a unit of one more positive charge. For example, $La_{La}^{\times}$ represents a lanthanum on a lanthanum site, $V_O^{\bullet\bullet}$ represents an oxide ion vacancy with the site having two more positive charges (having lost a 2- ion), and $Co_{Co}^{'}$ represents the reduction of a Co^{3+} to Co^{2+} ion with the site having one less positive charge. Further explanation and examples of this notation are given in Table 1.

When the defect formation process is written in the form of an equation it must be balanced in the same way as any other chemical equation. For example, to represent the processes involved in the creation of reductive and oxidative non-stoichiometry for $LaCoO_{3-\delta}$ and $LaMnO_{3+\delta}$, respectively, the following equations can be written:

3] $$2Co_{Co}^{\times} + O_O^{\times} \rightarrow Co_{Co}^{'} + V_O^{\bullet\bullet} + \frac{1}{2}O_2 \quad \text{(reductive)}$$

4] $$3Mn_{Mn}^{\times} + La_{La}^{\times} + \frac{3}{2}O_2 \rightarrow 3Mn_{Mn}^{\bullet} + V_{La}^{'''} + \frac{1}{2}La_2O_3 \quad \text{(oxidative)}$$

Note, a common terminology in use is to call $P^{\bullet}$ an electron hole where an electron has been lost from a site (e.g. $Mn^{3+} \rightarrow Mn^{4+}$), and P' an electron trap where an electron has been "gained" by a site (e.g. $Co^{3+} \rightarrow Co^{2+}$). Using this notation it is possible to consider the different defect processes that may occur when different dopants are introduced into the lattice.

Table 1 Defect structure - notation and definition of terms.

Type of Site	Symbol	Description	Examples
Unperturbed lattice site	A, B, O/Atomic symbol	Ions in unperturbed lattice sites. A is 12-fold and B 6-fold coodinated. Subscript - the atomic symbol identifies the site. Superscript - (×) - indicates unperturbed valency state.	$Sr_{Sr}^{\times}(A_A^{\times}), Ti_{Ti}^{\times}(B_B^{\times})$ and $O_O^{\times}$ are the unperturbed Sr^{2+}, Ti^{4+} and O^{2-} sites in $SrTiO_3$ (ABO_3).
Dopant cation	M/Atomic symbol	Substituted site, i.e. cations doped into the lattice to replace cations from the unperturbed lattice. Typically M is divalent or tetravalent and substitutes in the A site (e.g. Ni). Subscript - the atomic symbol identifies the original host lattice site. Superscript ($'$ or $^{\bullet}$) - indicates the charge perturbation at this site. ($'$) - less positive/more negative than the unsubstituted site. ($^{\bullet}$) - less negative/more positive.	$Ni_{Sr}^{\times}(M_{Sr}^{\times})$ and $Ni_{Ti}^{//}(M_{Ti}^{//})$ represent replacement of Sr^{2+} and $Ti^{4+}$by Ni^{2+} respectively in $SrTiO_3$
Vacancy	V	Ion missing from any lattice site. Subscript - atomic symbol identifies original filled lattice site. Superscript ($'$ or $^{\bullet}$) - indicates charge perturbation at the vacant site. ($^{n'}$) - n units less positive/more negative than the filled site. ($^{n\bullet}$) - n units less negative/more positive	$V_{Ti}^{////}$ - vacancy at the Ti^{4+} site. $V_O^{\bullet\bullet}$ - vacancy at the O^{2-} site.

Table 1/cont

Hole/Trap	A, B, O/Atomic Symbol	Filled lattice site with a perturbation in electronic charge, i.e. an electron hole/trap (positive or negative resulting from the subtraction or addition of an electron). Subscript -atomic symbol identifies the ion site. Superscript ($^{/}$ or $^{\bullet}$) - indicates charge perturbation at the site. ($^{n/}$) - n units less positive/more negative than the unperturbed site - trap. ($^{n\bullet}$) - n units more positive/less negative - hole.	Ti'_{Ti} indicates Ti^{3+} at the Ti^{4+} site in $SrTiO_3$ - trap. $Co^{\bullet}_{Co}$ indicates Co^{4+} at the Co^{3+} site in $LaCoO_3$ – hole. $O^{\bullet}_{O}$ would represent O^{-} occupying the O^{2-} site - hole.
Electron	$h^{\bullet}_{e}$ / $e^{/}$	Used to describe electron processes, e.g. ion/electron pair behaviour.	e'_{e} - represents a free electron introduced into the lattice e.g. $Co^{3+} / e'_{e} \leftrightarrow Co^{2+}$ $h^{\bullet}_{e}$ represents an electron deficient site e.g $Mn^{3+} / h^{\bullet}_{e} \leftrightarrow Mn^{4+}$
Interstitial species	Atomic symbol with subscript *i*	Species located between lattice sites. Superscript ($^{/}$ or $^{\bullet}$) - indicates charge perturbation within the lattice space ($^{n/}$) - n units less positive/more negative than the unperturbed site. ($^{n\bullet}$) - n units more positive/less negative.	O''_{i} - would represent interstitial O^{2-} (e.g. following creation of a vacancy $O^{x}_{O} \leftrightarrow V^{\bullet\bullet}_{O} + O''_{i}$) $Sr^{\bullet\bullet}_{i}$ - would represent interstitial Sr^{2+}.

Table 2 Possible defect processes when divalent and tetravalent cations are doped into the A site of perovskites of the form $LaBO_3$.

Dopant	Equation	Notes
Divalent Cation M^{2+}	$MO + La_{La}^{\times} + \frac{1}{2}O_O^{\times} \rightarrow M_{La}^{'} + \frac{1}{2}V_O^{\bullet\bullet} + \frac{1}{2}La_2O_3$	Creates an oxide vacancy
Divalent Cation M^{2+}	$MO + B_B^{\times} + La_{La}^{\times} + \frac{1}{4}O_2 \rightarrow M_{La}^{'} + h_B^{\bullet} + \frac{1}{2}La_2O_3$	Creates an electron hole
Tetravalent Cation M^{4+}	$MO_2 + \frac{4}{3}La_{La}^{\times} \rightarrow M_{La}^{\bullet} + \frac{1}{3}V_{La}^{'''} + \frac{2}{3}La_2O_3$	Creates a cation vacancy
Tetravalent Cation M^{4+}	$MO_2 + La_{La}^{\times} + B_B^{\times} \rightarrow M_{La}^{\bullet} + h_B^{'} + \frac{1}{2}La_2O_3 + \frac{1}{4}O_2$	Creates an electron trap

Table 2 gives a summary of the defects that may occur when a perovskite of the form $LaBO_3$ is doped at the A site. As can be seen, for a given doping process there is more than one possible defect that may be formed. The actual defect created will depend on the host perovskite lattice, e.g. Co^{3+} at the B site can be readily reduced to Co^{2+} so may favour the formation of an electron trap for tetravalent doping at the A site, but Co^{3+} will less easily oxidise to Co^{4+} and so the system would have to create oxide ion vacancies for divalent doping at the A site. Also, the conditions under which doping occurs will affect the favoured defect, for example, for divalent A site doping with the creation of oxide ion vacancies may be favoured under low oxygen partial pressures, whereas hole formation may be favoured under high oxygen partial pressures.

2.1.3. Phase Changes in Perovskites

As mentioned above, perovskite crystals have a variety of different symmetries which have a strong correlation to the ratio of the sizes of the "A" site to the "B" site cations. A number of solid state phase changes are known for perovskite-type materials as the conditions of temperature and pressure are changed. In this section the causes of these phase changes are considered with particular emphasis on the case of strontium titanate.

Three types of atomic displacements have been identified which lead to the 23 different crystal symmetries known for the perovskite structure [27]:

- tilting of the anion octahedra
- displacement of the cations
- distortions of the octahedra

As mentioned above, $SrTiO_3$ has the perfect undistorted cubic structure at room temperature and pressure, $CaTiO_3$ has tilted octahedra and $BaTiO_3$ has displaced cations. At high temperature all three alkaline earth perovskites have the undistorted cubic structure [28] which is brought about by small displacements in the positions of the atomic centres. When the crystal symmetry is altered by small displacements the two crystal structures are simply distorted versions of each other and the phase change is known as displacive phase transition [29]. It is important to note that the vast majority of displacive phase transitions involve a change in symmetry, for example the cubic to ferroelectric phase transition on cooling found in $BaTiO_3$ involves elongation of the crystal c axis associated with the displacement of the Ti^{4+} cations leading to the tetragonal symmetry. In the case of the ferroelectric distortion there is also a loss of the 3 fold rotation axis found for the cubic system and a change in space group from Pm-3m to I4mm.

The phase that exists under given thermodynamic conditions will be the one with the lowest free energy and this can be used to explain why the lower symmetry phase is usually stable at low temperatures. The free energy is dominated by the enthalpy at low temperature, which in turn is dominated by the energy contributions of the bonds in the system. A more compact, lower symmetry structure will have a lower enthalpy than the higher symmetry phase. In contrast, at higher temperature the entropy will dominate and since the higher symmetry phase is likely to have slightly lower phonon frequency modes than the lower symmetry phase, the entropy of the higher symmetry phase will be higher leading to a more favourable free energy.

Displacive phase transitions are usually described by a variable called the order parameter (η) which is a measure of the atomic displacement/s associated with the phase change. For example the tetragonal to cubic transition found for $SrTiO_3$ is associated with rotation of the TiO_6 octahedra around the x axis of the crystal (R_x) and so the order

parameter is simply the size of R_x and which of course drops to zero at the transition temperature T_c. A plot of order parameter η versus temperature shows two distinct system dependant behaviours which are associated with so called first order and second order phase transitions. In first order transitions there is a discontinuity in the value of η at T_c whereas in the second order case the value of η drops continuously to zero as the temperature reaches T_c. First order phase changes display a discontinuity in the entropy of the system at T_c, which is the first derivative of the free energy, whereas second order changes display a discontinuity in the heat capacity of the system at T_c, which is the second derivative of free energy.

The atomic displacements which lead to the phase change can be identified through a lattice dynamics calculation of the system, see Section 3.1.6, where one particular phonon frequency of the high symmetry, high temperature form will fall to zero at the transition temperature. The phonon frequency is said to have gone soft. In the case of $SrTiO_3$ the phonon frequency associated with the librations of the TiO_6 octahedra about the x-axis is the mode that goes soft at T_c.

2.1.4. Uses of Perovskites

The range of interesting uses of perovskite and perovskite related structures is considerable and includes: superconductivity [30], colossal magnetoresistance [31], ferroelectricity [32], catalytic activity [33], gas absorption and storage [34, 35], and uses related to ionic mobility such as in solid oxide fuel cells (SOFCs) [36]. In this section the non-catalytic uses of perovskites are considered briefly along with a more detailed review of the catalytic behaviours.

2.1.4.1. Non-Catalytic Uses

One of the more dramatic episodes in the history of the uses of perovskites is its association with high temperature superconductivity. It was realised in the 1970s that a combination of 4f ions at the 'A' site and 3d ions at the 'B' site gave rise to reasonably conducting phases at room temperature such as $LaCrO_3$ [37, 38], although it was not the development of these materials which led to the high temperature superconductors. In 1975 the highest temperature superconductor was $BaBiPbO_x$ developed by Sleight et al [39]. The first material with a T_c over 30 K was $BaLaCuO_x$ [40], although the most significant was the discovery of $YBa_2Cu_3O_{7-\delta}$ with a T_c of 93 K, above the boiling point of nitrogen [41]. Since this breakthrough extensive research has only increased T_c by

around 30 K. The commercialisation of superconductors has been hindered by a set of practical issues such as matching of thermal properties (expansion and conductivity) to other substrates that they are adhered to as thin films, and electrical characteristics (low dielectric loss, dielectric constants and dielectric coefficient).

Colossal magnetoresistance (CMR) materials, such as $Re_{1-x}A_xMnO_3$ (where Re is a rare earth and A is an alkaline earth cation) [42] and pyrochlores [43], exhibit large changes in electrical conductivity in the presence of an external magnetic field which is attributed to the aligning of electron spins in the presence of a magnetic field making electronic conductivity easier in these materials [44]. There are several potential applications of CMR materials including in read/write heads, magnetic storage and spintronics.

Ferroelectric materials exhibit an electric dipole even in the absence of an applied electric field since the centre of the negative charge of the crystal does not coincide with the centre of positive charge [109]. The unusual electrical response characteristics of perovskites, in particular $BaTiO_3$, have been known since the 1940s [37] when the search for materials with high dielectric constants for capacitors was very important [45, 46, 47]. Soon afterwards the reason for the high dielectric constant of $BaTiO_3$ was confirmed [48, 49]. In $BaTiO_3$ the ferroelectric nature arises from a shift in the position of the central Ti^{4+} cation away from the centre of the TiO_6 octahedra leading to one short and one long Ti-O bond around the cation. However, as with other aspects of perovskite phenomena, the variety of distortions available to the lattice leads to other so called ferroic effects such as antiferroelectric and ferromagnetic effects. There are well over 100 simple ferroelectric compounds known and many more compounds where the ferroelectric properties are derived from the tilting of the BO_6 octahedra [37]. The uses of ferroic materials is widespread and some examples are given in Table 3.

Table 3 Some of the practical uses of simple ferroic perovskites and their solid solutions [37].

Ferroic Perovskite	Comments/Applications
$BaTiO_3$	Capacitors, PTC (for hair dryers etc.)
$PbTiO_3$	Pyroelectric detectors, hydrophone
$Pb(Zr_{1-x}Ti_x)O_3$	Piezoelectric applications of all kind. Simple modifications of compositions or dopants are hydrophones, actuators, x-y translator, e.g. AFM
$PbLa(ZrTi)O_3$	Transparent ceramics, electrooptic shutters, EO goggles etc. for high altitude flying pilots.
$LiNbO_3$	Variant of perovskite; Optical modulators
$LiTaO_3$	Variant of perovskite; pyroelectric sensors
$KNbO_3$	Best second harmonic generator
Doped Rh: $BaTiO_3$, $KNbO_3$, Fe: $LiNbO_3$	Photorefractive materials
$SrTiO_3$, $(KTaO_3)$	Tunable microwave devices

As shown in Section 2.1.2, the defect chemistry of perovskites is extremely rich. With appropriate cation doping a large number of oxygen anion vacancies can be expected within the lattice so greatly enhancing ionic conductivity through the lattice. There is considerable interest in the area of ionic mobility due to the possible applications in the area of environmentally friendly technologies such as hydrogen storage [50], lithium ion conductors [51] and solid oxide fuel cells (SOFCs) [52] amongst others. Application in SOFCs is a good example of the use of the defect chemistry in perovskites, as well as making use of the other properties of perovskites such as their high thermal stability and electrical conductivity[53]. SOFCs consist of 3 main components – the anode, the electrolyte and the cathode. The material demands on these three components are quite different and perovskites have been used as both the anodes and cathodes [52, 53].

At the cathode the reduction of oxygen is catalysed:

5] $$\frac{1}{2}O_{2(g)} + 2e^- \rightarrow O^{2-}$$

The ions are then transported over the electrolyte and the oxide ions combined with H_2 at the anode:

6] $$H_{2(g)} + O^{2-} \rightarrow H_2O + 2e^-$$

At the anode the material must operate under extremely harsh conditions, at temperatures exceeding 500°C and oxygen partial pressures of around 10^{-15} atm. In addition, it is desirable to carry out a steam reforming reaction here of natural gas to supply the hydrogen for the cell, however traditional materials suffer from carbonaceous build up during the reforming reaction and it is hoped that perovskites will offer a solution to this issue. Perovskites are the traditional choice of material for the cathode due to their thermal stability, high ionic and electronic conductivities, however the drive to operate SOFCs at lower temperatures leads to several issues that need to be resolved including the reduced activity of the cathode to reduce $O_{2(g)}$, the reduced transport of the oxide ion and the reduced gas transport properties.

2.1.4.2. Catalysis

In this section the role of perovskites as catalytic materials is considered, with the exception of partial oxidation of methane which will be covered in Section 2.2.2.1.

Perovskites are used in a wide variety of catalytic processes, for example: oxidation reactions, pollution abatement, hydrogenations, photocatalysis, chemical sensors and electrocatalysis [33]. The versatility of perovskites as catalysts is once again down to the ability of the structure to display a variety of properties such as: ionic mobility; adsorption; porosity; acid/base behaviour; and redox behaviour. However, despite the advantages of perovskite materials they have yet to be used as commercial catalysts.

An important use of perovskites as oxidation catalysts is for the complete combustion of methane and other low molecular weight alkanes [54]. The activity of the catalysts is primarily affected by two factors: the surface area; and the availability of surface/lattice oxygen. High surface areas lead to higher catalytic activities. The surface area is determined by the synthetic route of the perovskite, for example the ceramic method [55] with its high calcination temperature leads to a low surface area material, whereas the much lower temperatures employed for methods such as the citrate synthesis [56] can yield perovskites with surface areas exceeding $20m^2g^{-1}$. Two types of oxygen, adsorbed surface (suprafacial) and lattice (intrafacial), have been identified, with the former being the primary source at low temperatures (<500°C) and the latter at high temperatures (>600°C) [57]. Substitution at the A site in perovskites of the type $LaBO_3$, where B is a transition metal, leads to increased oxygen vacancies which enhance anionic mobility and so increases the catalytic activity.

The oxidation of ammonia to NO for the production of nitric acid is an industrially important process [58]. The ability of perovskites to act as selective catalysts for this oxidation process is thought to be due to the presence of transition metal ions in the octahedral coordination which leads to optimum bonding strength to the terminal oxygens on the (1 0 0) face. The mechanism is thought to involve activation of the ammonia molecule on M^{3+} surface cations followed by reaction with ion-radical oxygen species adsorbed on vacancies [59].

The oxidation of CO over perovskites has been used as a probe reaction to correlate the observed activity with the electronic state of the transition metal species in perovskites of the form $LnBO_3$, where Ln is a lanthanide and B is a transition metal [60]. In these systems the Ln^{3+} ion is essentially inert whereas M^{3+} is active in the catalytic pathway. The reaction mechanism is thought to involve the steps described as follows [61]:

7] $$O_{2(g)} \rightarrow O^-_{2(ad)} \rightarrow 2O^-_{(ad)}$$

8] $$CO_{(g)} \rightarrow CO_{(ad)}$$

9] $$CO_{(ad)} + 2O^-_{(ad)} \rightarrow CO^{2-}_{3(ad)} \quad \text{(slow)}$$

10] $$CO^{2-}_{3(ad)} \rightarrow CO_{2(ad)} + O^{2-}_{(ad)} \rightarrow CO_{2(g)} + O^{2-}_{(ad)}$$

In step 7 oxygen is reductively adsorbed onto M^{2+} sites at the surface, whilst CO is adsorbed onto oxide sites at the surface in step 8. The slow step in the reaction is the formation of the carbonate species, which is followed by decomposition and desorption in step 9 and 10. The electronic band structure near the Fermi level is thought to play a key role in the mechanism with $LaCoO_3$ being the most active species [62] of the $LaBO_3$ series and $LaCrO_3$ the least active member of the series. Oxygen vacancies also play an important role as illustrated using the reaction over $LaCuO_{3-\delta}$ which can be prepared as orthorhombic $LaCuO_{2.55}$, monoclinic $LaCuO_{2.73}$ or tetragonal $LaCuO_{2.95}$ depending on the oxygen partial pressure during preparation [63]. During the oxidation of CO the most active phase is the orthorhombic one with the largest oxygen deficiency, followed by the monoclinic and then the tetragonal compounds.

An important possible application for perovskite materials is in the area of pollution abatement where they have potential to be used as so called three way catalysts for the simultaneous conversion of hydrocarbons, NO_x and CO to less harmful species in exhaust gas emissions [64]. Traditionally such catalysts are composed of small particles of Pt, Pd or Rh dispersed on a ceria-alumina ceramic substrate. However with the increasing cost of these precious metals, perovskites offer an attractive alternative. Incorporation of the precious metals into a perovskite host lattice is also a possibility as this protects against sintering, volatilisation and solid state reaction with the substrate [33]. As an example, small amounts of Rh have been added to the oxidatively non-stoichiometric perovskite $LaMnO_{3.15}$ and used as a three way catalyst for the model mixture of $CO+NO+C_3H_6$ [65]. Here the Rh is essentially for the reduction of NO, while the presence of Mn^{4+} cations allow for the total oxidation of CO and C_3H_6. The catalyst performance was measured over various conditions from very reducing to very oxidising by varying the stoichiometric factor of the reactants ($s=(2O_2+NO)/(CO+9C_3H_6)$). The catalytic activity was found to be similar over all

conditions measured and this is attributed to the ready capture of oxygen to regenerate the over stoichiometric $LaMnO_{3.15}$ substrate in either excess O_2 or NO conditions. A drawback of the $Rh/LaMnO_{3.15}$ system is that NO reduction is strongly inhibited by the presence of water which was attributed to (i) absorption of water at the surface poisoning the active sites and (ii) the presence of the water gas shift and reforming reactions.

Perovskites have been used to study the reaction mechanisms involved in the hydrogenation of carbon oxides to yield a variety of products including paraffins, olefins, alcohols, ethers and esters [33]. One such reaction is the hydrogenation of carbon monoxide from syngas ($CO+H_2$) to give methanol and a mixture of hydrocarbons. In a study of the effect of reduction pretreatments on the activity of $LaRhO_3$ [66] it was found that the CH_3OH/HCs ratio is highly temperature dependent implying that there are two reaction mechanisms involved: CH_3OH is formed through a non-dissociative adsorption of CO route; whereas HCs are formed via a dissociative mechanism. The differing ratios of products is then due to competing H- vs. CO-insertion reactions and the availability of dissociatively and non-dissociatively adsorbed CO species. At temperatures below 500 K methanol is the major product, whereas above 620 K the hydrocarbons predominate. Surface analysis revealed that the activated catalysts contained Rh^+ species and a small amount of Rh^0.

Strontium titanate ($SrTiO_3$) has been used as a photocatalyst for the decomposition of H_2O to H_2 and O_2 since the conduction band edges are more negative than the H^+/H_2 energy level [67]. Observable production of hydrogen from irradiated $SrTiO_3$ powders only occurs in the presence of a metal coating [68]. A metal coated semiconductor effectively forms a short circuited photochemical cell where the oxidation and reduction reactions occur simultaneously at different sites. The metal also decreases the recombination rate of photoproduced electrons and holes by increasing the electron conduction rate. A system which has been tested for photocatalysis is $NiO/SrTiO_3$ where the evolution of H_2 was ascribed to the formation of some Ni/NiO domains, whereas the O_2 is evolved from sites located on the $SrTiO_3$ phase [69]. The role of the nickel phase was thought to be to enhance the electron transfer between the NiO and $SrTiO_3$ phases. Photocatalytic activity has been found for other reactions using $SrTiO_3$ as well as $BaTiO_3$ such as the synthesis of NH_3 from N_2 and H_2O [70].

Semi-conducting perovskites have potential as gas sensor materials since their electrical conductivity is sensitive to gas adsorption [33]. $LnMO_3$ (where Ln is a lanthanide and M = Mn, Cr, Co), for example, are p-type semiconductors which show a decrease in electrical conductivity on the adsorption of reducing gases such as CO or CH_3OH [71]. The adsorption process can be the represented as follows:

11] $$CO_{(g)} + O^{2-}_{(ad)} \rightarrow CO_{2(ad)} + 2e^-$$

12] $$CH_3OH_{(g)} + 3O^{2-}_{(ad)} \rightarrow CO_2 + 2H_2O_{(ad)} + 6e^-$$

When reducing species are adsorbed onto these materials electrons are released which reduces the number of holes and so decreases the p-type conductivity of the system.

2.2. Synthesis Gas and the Partial Oxidation of Methane

2.2.1. Composition and Uses of Synthesis Gas

Synthesis gas (syngas), a mixture of hydrogen and carbon monoxide, is a key precursor during many chemical processes, for example, in the production of methanol and higher alcohols [72]. Furthermore, the amount of hydrogen formed can be enhanced using the water gas shift reaction [73]:

13] $$CO + H_2O \rightarrow H_2 + CO_2$$

The hydrogen can be put to many uses including the manufacture of ammonia, hydrogenation of unsaturated compounds, and direct reduction of iron ore.

2.2.2. Manufacture of Synthesis Gas

There are three major routes for the synthesis of syngas: steam reforming; dry reforming; and partial oxidation of methane. The reactions and enthalpy changes for these processes are given in Table 4. As can be seen both the steam and dry reforming routes are highly endothermic, whereas the partial oxidation of methane is exothermic. Also of note is that the H_2/CO ratio varies from 3:1, to 1:1, to 2:1 for steam reforming, dry reforming and partial oxidation of methane respectively. The desired ratio varies from process to process. In this work, the focus will be on the direct partial oxidation process.

Table 4 Chemical equations and reaction enthalpies for the three major process used for the production of syngas [72].

Process	Equation	$\Delta H_{298}°$
Steam Reforming	$CH_4 + H_2O \rightarrow CO + 3H_2$	206
Dry Reforming	$CH_4 + CO_2 \rightarrow 2CO + 2H_2$	247
Partial Oxidation	$2CH_4 + O2 \rightarrow 2CO + 4H_2$	-38

Each of these reactions are carried out in the presence of a solid state catalyst. Most commonly supported Ni catalysts are used [72, 74, 75], but many other metals have been shown to be catalytically active including Co, Fe, Pd, Rh, Ru, Ir and Pt [74].

There are many considerations to take into account during the manufacturing process including:

- The desired H_2/CO ratio.
- Catalyst poisoning by carbon lay down or sulphur.
- Subsequent reactions within the reaction mixture such as the shift reaction.
- The economic viability within the particular context in question.

In order to address these issues, every aspect of the process conditions must be considered including the temperature, pressure, purity of feedstock, and catalyst. In this study it is the role of the latter that is of primary importance during the partial oxidation of methane. Therefore, it is the issues relating to the catalyst which are considered in most detail here. For a more detailed review of the other aspects of the reforming process see [72] and [75].

2.2.2.1. Partial Oxidation of Methane

There are two proposed mechanisms for the partial oxidation of methane: (i) a combustion reforming pathway, in which CO_2 and H_2O are the primary products and CO and H_2 are formed by their reactions with CH_4 (the dry- and steam- reforming reactions from Table 4); and (ii) a pyrolysis pathway, in which CO is the primary product formed by the pyrolysis of methane, $CH_4 \rightarrow CH_x + (2\text{-}½x)H_2$, followed by the oxidation of carbon- containing species to give CO without preformation of CO_2. The former is currently the more accepted mechanism [74, 76]. In this pathway a highly exothermic step, the complete combustion of methane ($\Delta H_{298}° = -801.7$ kJmol^{-1}), is

followed by two possible, endothermic steps which are the reforming processes, see Table 4.

There are four major issues associated with the catalytic partial oxidation of methane: build up of hot spots within the catalyst bed; formation of carbonaceous deposits on the catalyst; sintering of the active catalytic particles; and the requirement for a pure oxygen feed. The latter of these is a significant constraint in making this process economically viable and is another active area of research into perovskites as dense, oxygen permeating, solid oxide membranes, but is not considered here. In order to address the other three issues a good catalyst for the partial oxidation of methane should be:

- Highly thermally stable.
- Highly mechanically stable.
- Resistant to carbon formation reactions.
- Resistant to sintering.

As mentioned above, many catalysts have been used for this reaction, the most popular of which have been supported Ni –catalysts on alumina, but also other binary oxide supports such as Yb_2O_3, CaO, TiO_2, ZrO_2, ThO_2, UO_2 and rare earth oxide-modified alumina supports [74, 75, 76]. These catalysts are prepared by impregnating the oxide support with nickel in solution followed by calcination and finally pre-reduction of surface NiO. All of these systems have been shown to be highly active and selective catalysts at very low contact time. However, catalyst deactivation inevitably occurs due to Ni particle sintering and carbon deposition. Some progress was made with the Ni/MgO system, which was shown to be resistant to sintering due to the formation of a solid solution with Ni occupying sites within the MgO lattice [77]. However, the problem of carbon deposition remains in this system.

There are two possible routes for the formation of carbon, namely the methane decomposition and the Boudouard reaction [74]:

14] $CH_4 \rightarrow C_{(s)} + 2H_2$ (methane decomposition)

15] $2CO \rightarrow C_{(s)} + CO_2$ (Boudouard reaction)

To resist carbon deposition catalysts must either suppress these reactions or oxidise any carbon formed. The use of nickel supported on ceria (CeO_2) catalysts has been shown to resist carbon lay down, and the effect can be enhanced by the addition rare earth species such as lanthanum [78], which is thought to be due to the ability of ceria to "store" oxygen, which can oxidise carbon formed on the nickel particles. Oxygen availability is achieved by the ready reduction of Ce(IV) to Ce(III) and the creation of oxygen vacancies together with the high mobility of oxygen through the lattice. The addition of lanthanum increases the number of lattice defects and enhances oxygen mobility. Indeed, a similar mechanism has been proposed recently for Ni supported on perovskites as discussed below in relation to steam reforming [79]. Other supports such as $CaAl_2O_4$ and $AlPO_4$ also produce catalysts, which are active, selective, resistant to sintering and carbon deposition [74]. However, with time on stream $AlPO_4$ is transformed into tridymites, and the surface area of the support decreases dramatically.

2.2.2.2. Studies of Perovskites as Catalysts for the Partial Oxidation of Methane

As alternatives to alumina, perovskites are very promising materials for use as supports. Studies have shown that they can be doped with nickel to produce catalysts which are highly active, highly selective, suffer from minimal carbon formation and do not appear to sinter [80, 81, 82, 79]. In particular studies have been carried out on alkaline earth titanates – $CaTiO_3$, $SrTiO_3$ and $BaTiO_3$, and lanthanum metal oxides – $LaMO_3$ where M is a variety of trivalent ions such as Al^{3+} and first row transition metals. The samples were prepared either by the citrate method [80], where dopant ions are incorporated into the lattice, or impregnation [79] where dopant ions are absorbed onto the lattice.

Firstly, consider catalysts (*c*-Ni/$CaTiO_3$, *c*-Ni/$BaTiO_3$ and *c*-Ni/$SrTiO_3$) prepared by the citrate method and (*imp*-Ni/$SrTiO_3$) prepared by the impregnation method [80]. The citrate procedure involves formation of a sol of organic metal complex formed by the addition of citric acid and ethylene glycol to an aqueous mixture of nickel nitrate, alkaline earth carbonates and titanium isopropoxide. The sol is decomposed in a two stage process by heating at 200°C for 5 hours, then 500°C for 5 hours, and finally calcination at 850°C in air for 10 hours. The impregnation involves contact between the perovskite, which had been previously prepared by the citrate method, and a solution

containing the dopant cations. All samples were prepared having an atomic ratio of Ni:Ti of 0.2:1.0, corresponding to a Ni loading of 5.9 wt%. The prepared catalysts were characterised using a variety of methods namely: x-ray diffraction (XRD); transmission electron microscopy (TEM); the BET surface area and temperature programmed reduction (TPR). Catalytic testing was carried out using temperature-programmed analysis in a mixture of $CH_4/O_2/N_2$ = 10/5/20 ml min^{-1}. These samples were not pre-reduced prior to catalyst testing and therefore were reduced *in situ*. However, the *spc*-$Ni_{0.2}/CaTiO_3$ was not active until it was pre-reduced, see below.

Two distinct stages seen during the reaction were attributed to the complete combustion of methane to carbon dioxide and steam followed by the reforming reactions from the mechanism discussed above. The percentage conversions and selectivities for these three catalysts are shown in Table 5 from [82]. As can be seen all three systems show high conversion rates and high selectivities. However it was necessary to hold the $Ni_{0.2}/CaTiO_3$ under a reducing atmosphere at 1073 K for 30 min. The most active of the catalysts is $Ni_{0.2}/SrTiO_3$ as evidenced by the light-off temperatures.

Table 5 CH_4 oxidation over the Ni/Perovskite Catalysts [82].

	Conversion (%)		Selectivity (%)			
Catalyst	CH_4	O_2	CO	H_2	CO_2	Light off Temperature (K)
spc-$Ni_{0.2}/CaTiO_3$	24.8	100	0	1.4	100	1070
spc-$Ni_{0.2}/CaTiO_3$*	93.8	100	98.3	98.2	1.7	-
spc-$Ni_{0.2}/SrTiO_3$	94.4	100	97.9	97.9	2.1	980
spc-$Ni_{0.2}/BaTiO_3$	93.9	100	96.5	95.9	3.5	1020
imp-Ni0.2/$SrTiO_3$	94.7	100	97.8	97.8	2.3	1070

* After reaction under a reducing atmosphere at 1073 K for 30 min.

The catalysts were characterised by XRD before and after the oxidation. All four showed evidence for NiO before reaction, which had been reduced to Ni metal after reaction, in addition to the perovskite phase. The diffraction peaks were strong and sharp for the impregnated sample and much weaker and broad for the citrate method prepared samples due to the differing sizes of the NiO and Ni particles.

The size of the metal particles were examined using TEM following reaction and found to be about 40-50 nm for *imp*-$Ni_{0.2}/SrTiO_3$, 20-30 nm in diameter for

spc-$Ni_{0.2}/CaTiO_3$ and <20 nm for *spc*-$Ni_{0.2}/BaTiO_3$. No direct evidence for Ni metal particles could be found on the *spc*-$Ni_{0.2}/SrTiO_3$ catalysts, but a large number of "dark" spots were observed by TEM which were attributed to very small, well dispersed Ni metal particles with diameters of <1 nm. It would normally be expected that such small particles would sinter. However, this does not seem to happen in this case and a "strong interaction" between the particles and the support is suggested for this.

Following the 6 hour reaction the weight percent of carbon for the calcium, strontium and barium titanates were 4.7, 0.22 and 0.32 wt% respectively. Again the $Ni_{0.2}/SrTiO_3$ shows the most desirable behaviour and is attributed partly to the very finely dispersed nature of the Ni metal particle promoting reforming reactions and partly to "mobile oxygen species" reacting with the coke.

The TPR studies suggested two Ni sites on the citrate method as prepared materials: firstly there is NiO present on the surface of the catalyst as a separate phase which is reduced under H_2 in the range 800-850K; and secondly some "oxidised" nickel is incorporated into the lattice during the formation of the catalyst which is harder to reduce at temperatures of around 960 K. The ratio of the "surface" to the "lattice" species is roughly 1:2. The impregnated prepared sample showed a single peak confirming the absence of nickel incorporation into the lattice.

Recently, the extended X-ray absorption fine structure or EXAFS technique has been used to study the local structure around nickel dopants in strontium titanate at key stages in the preparation of the catalyst [83]. The samples were prepared using a hydrothermal synthesis route whereby a mixture of aqueous nickel, strontium and titanium salts, together with ethylene glycol and potassium hydroxide, were heated at 150°C for 20 hours and then washed. The resulting material was calcined by heating at 5°C/minute up to 950°C. Finally the affect of reducing the catalyst was examined by heating them up to 900°C and 950°C in a 5% H_2/He atmosphere. EXAFS analysis was carried out after the low temperature hydrothermal synthesis, calcination and both reduction phases.

Table 6 shows bond distances and coordination numbers for the nearest oxygen, strontium and titanium shells around the nickel cations in the lattice. For comparison the bond distances and coordination numbers around the titanium cations in the undoped lattice are also shown. These results clearly show that nickel cations occupy

the Ti^{4+} site within the strontium titanate lattice at all stages in the preparation of the catalytic materials. The main difference between the undoped and doped samples is the distance from the B site cation to the nearest oxygen anions as there is a ~3.5% increase in the length of these bonds, which is readily explained by the larger size of the Ni^{2+} cation compared to the Ti^{4+} cation. Upon calcination and reductive heating the coordination number around the nickel cation reduces implying an increased number of vacancies in this shell. The change in the environment for the nickel upon reduction is shown by the reduction in the Ni-Ni bond distances from 2.95 Å to 2.50 Å, which is thought to be due to the reduction of the nickel in the lattice.

Table 6 Results of EXAFS analysis, Beale et al [83].

Sample	Shell	R(Å)	CN	Debye-Waller ($2\sigma^2$)	R-factor
Ni/$SrTiO_3$ (5%)	Ni-O	2.03	5.6 (6)	0.010	40.23
	Ni-Sr	3.35	8.0	0.023	
	Ni-Ti	3.95	6.0	0.006	
Calcined 850°C	Ni-O	2.02	4.5	0.014	42.34
	Ni-Sr	3.37	8.0	0.026	
	Ni-Ti	3.98	6.0	0.012	
	Ni-Ni	2.95	2.96	0.022	
Reduced 900°C	Ni-O	2.01	3.4	0.012	40.14
	Ni-Sr	3.35	8.0	0.024	
	Ni-Ti	3.98	6.0	0.011	
	Ni-Ni	2.50	3.1	0.022	
Reduced 950°C	Ni-O	2.01	2.4	0.010	47.83
	Ni-Sr	3.35	8.0	0.029	
	Ni-Ti	3.97	6.0	0.012	
	Ni-Ni	2.49	4.1	0.017	
Undoped $SrTiO_3$*	Ti-O	1.95	6.0	-	-
	Ti-Ni	3.38	8.0	-	-
	Ti-Ti	3.90	6.0	-	-

*For comparison Yamanaka et al[10]

Another recent study focussing on Ni impregnated materials has considered the steam reforming of methane over a series of Ni supported perovskite catalysts – $LaAlO_3$, $LaFeO_3$, $SrTiO_3$, $BaTiO_3$ and $La_{0.4}Ba_{0.6}Co_{0.2}Fe_{0.8}O_{3-\delta}$ [79]. The synthesis involved preparation of the perovskite support followed by a nickel impregnation step using an aqueous solution of $Ni(NO_3)_2.6H_2O$ to produce a Ni loading of 10 wt%. The resulting compounds were dried overnight at 393 K, and calcined at 773 K for 1 hr.

Analysis of the catalysis was carried out in a continuous flow system with a fixed bed of catalyst at atmospheric pressure. The catalyst was first reduced in a

hydrogen stream at 1073 K for 1 hr., before exposure to a mixture of steam and methane in a ratio of 1 or 2 at 1073 K and 0.1 MPa. Characterisation was carried out using temperature programmed reduction (TPR), temperature programmed oxidation (TPO), X-ray diffraction (XRD), BET analysis, and the active surface area of Ni was found by CO chemisorption.

Results showed consistency with the work of Takehira et al [82] despite the different preparative methods. XRD showed that $Ni/SrTiO_3$ and $Ni/BaTiO_3$, along with $Ni/LaAlO_3$, have nickel oxide and perovskite phase in the as prepared samples, with the nickel oxide being reduced to the metal following reduction and activity runs. The most active catalysts were $Ni/SrTiO_3$, again in agreement with above, as well as $Ni/LaAlO_3$ and $Ni/\alpha\text{-}Al_2O_3$. The conversion of CH_4 for the $Ni/SrTiO_3$ catalyst was 88.4%, which is slightly less than for the partial oxidation of methane study, see Table 5. A significant contrast to the previous work was that the $Ni/BaTiO_3$ showed very low activity. This difference in activity is attributed to the difference in dispersion and size of Ni particles on the surface of the catalyst derived from XRD peak-width, as can be seen in Table 7 [79].

Table 7 Dispersion, particle size and specific surface area of Ni/perovskites [79].

Catalyst	Dispersion (%)	Particle size (nm)	Surface Area m^2/g-cat
$Ni/LaAlO_3$	1.6	64	15.9
$Ni/SrTiO_3$	1.2	82	13.4
$Ni/BaTiO_3$	0.36	280	15.0

Although the Ni particle sizes are an order of magnitude larger than those for those catalysts formed by the citrate method, it is clear that the most active catalysts have the smallest particle size and highest dispersions. How the perovskite support controls this dispersion is not tackled in this paper, but is no clear correlation between activity and overall support surface area.

Unfortunately no analysis of carbonaceous lay down was presented for the $Ni/SrTiO_3$ catalyst. However, analysis for $Ni/LaAlO_3$ showed that it was resistant to this effect. This is attributed to the availability of lattice oxygen to suppress the formation of some forms of carbon on the catalyst.

Further evidence for the "non-passive" role of the perovskite support was provided by TPR analysis. In other words, the perovskite not only controls the dispersion of the Ni particles, but is also involved in some of the reaction pathways that are occurring within the system. There are three important findings from this analysis. Firstly, it was shown that lattice oxygen is lost from unsupported catalysts under reducing conditions. Secondly, the presence of nickel promotes the reduction of the perovskite support as more oxygen is lost than for the unsupported samples. Thirdly, some of the lattice oxygen is replenished during the steam reforming conditions. It is inferred that the efficiency of this interplay between nickel and support is strongly correlated to the nickel particle size and dispersion. Although the nature of the "reduced perovskite lattice" is not considered in this work, it is interesting to note that electrons remaining in the structure following the removal of oxygen could reduce Ti^{4+} to Ti^{3+} in the $Ni/SrTiO_3$ system. However for the $Ni/LaAlO_3$ system neither perovskite cation can be reduced, which may result in electrons being left in the oxygen vacancy forming an "F centre".

Similar reaction mechanisms involving the support oxide lattice and the interplay between the Ni particles and the support have been proposed for dry reforming over Ni on Sm and Gd doped CeO_2 [84].

It is the incorporation of Ni into, and interaction with, $SrTiO_3$ which is of central importance to the presented study in this thesis. Evidence for the control of metal particle dispersion by perovskites is also present for other systems. Two examples are:

Pd supported on $LaMO_3$ perovskites (M = transition metal (Co, Fe)) to produce "intelligent" catalysts for automotive emission control [85]. It is claimed that the Pd is reversibly reduced from the lattice and re-oxidised to re-enter the lattice as a function of reduction/oxidation potential of the exhaust gas.

Pd supported on $BaZrO_3$ for the complete combustion of methane [86]. Again $BaZrO_3$ controls the dispersion of Pd and allows reversibility of the reduction/oxidation of metal through support-metal interaction.

In summary, it can be seen that supported metal catalyst systems are of central importance in the production of syngas. The lifetime of these catalysts is primarily limited by sintering of the metal particles and poisoning by carbon lay down. The use of perovskites, particularly $SrTiO_3$, as host lattices gives catalysts which resist both of

these effects. The enhancement of lifetime is thought to be due to a strong interaction between the metal and the host which promotes the formation of well dispersed metal particles and prevents them from sintering. Of importance here, too, is the ability of the perovskite to both lose and gain lattice oxygen (depending on the conditions) which can oxidise any carbonaceous material and subsequently be replenished. Furthermore, the ability of the perovskite lattice to accommodate a variety of defects such as oxygen vacancies and redox processes may allow the host to play an active role within the catalytic reaction pathways.

The above discussion raises a number of important issues such as the solubility of nickel in the host lattice, differences between surfaces and the bulk and the effect of preparation. It is the intention of this thesis to use computational modelling to gain a greater understand of the interaction between nickel and the alkaline earth titanate lattices both in the bulk and at the surface.

2.3. Computational Modelling of Alkaline Earth Perovskite-type Titanates

2.3.1. Development of Pair Potential Parameters

In this section the development of the parameters used in the Buckingham potential and for the core-shell contributions (see Sections 3.1.2 and 3.1.3) is explained.

The first of these to be developed was for the O^{2-}-O^{2-} short range interaction during a study of point defects and electronic properties of uranium dioxide [111]. These parameters were developed in a two stage process firstly using the results of a Hartree-Fock molecular orbital calculation on the O_2^{2-} species followed by empirical fitting to experimental data. Note, it was necessary to consider the interaction of two O^- ions as the O^{2-} ion is an unbound species, with the second electron only held within the lattice site by the Madelung potential of the crystal. It was also necessary to assume that the screening of the short range anion-anion potential by the unbound electrons may be neglected. The results of the Hartree-Fock calculation were used to fit the A, ρ and C variables in the Buckingham potential, then the values of A and ρ were fixed (the repulsive component) and C (the dispersive component) was refitted to the following empirical experimental data: elastic constants; and lattice parameter.

This O^{2-}-O^{2-} short range potential was used as one of the foundations for the development of a comprehensive set of parameters for ionic oxides and semi-ionic

oxides [106]. This study primarily focused on fitting a set of parameters for cations in a series of binary oxides, although the transferability of these parameters between binary and tertiary oxides were also considered. Three methods were used to formulate the parameters depending on the availability of extensive the experimental data for a given oxide. These methods are outlined below:

1. In this method, as for the second method below, only short range potentials are derived. In other words these methods assume a rigid ion model where no polarisability of the ions is allowed. The method is used for oxides with minimal experimental data. Here, oxides which are structurally and chemically similar to each other, for example divalent first row transition metals, can be assumed to have the same hardness parameter, ρ, as an oxide for which more experimental data is known. For first row transition metals, this comparison was assumed to be with CaO. With a fixed value for ρ, the A parameter could be fitted to lattice parameter data.

2. For lower symmetry oxides, such as trivalent first row transition metal oxides, the structural data holds more information than for simple cubic lattices, and so both A and ρ can be fitted to this data.

3. For those oxides with considerable experimental data such as elastic constants, dielectric constants, cohesive energy and structure both short range and polarisability parameters can be derived. In this method shell parameters were obtained in one of two ways. Firstly, it was assumed that in MgO the cation is rigid and the oxygen parameters fitted to crystal properties. The oxygen polarisability was then adjusted for other crystals based on the assumption that it is strongly dependent on the Madelung potential and can be found knowing the polarisability and Madelung potential in one crystal (in this case MgO) and only knowing the Madelung potential in the second crystal. The cation polarisabilities were assumed to be transferable from the corresponding halides. Secondly, the polarisability of Mg^{2+} is given the Pauling value of 0.1 $Å^3$ and the anion polarisability then fitted from experimental data. Other anion polarisabilities are then calculated as above.

Lewis and Catlow produced a set of parameters which were derived in a consistent matter, and have been used as the basis for many future atomistic

investigations of oxides. The values for Ni^{2+} used in this thesis are taken from Lewis and Catlow work [106]. Furthermore, it was shown that by re-parameterising the A parameter by taking into account the changes in coordination number for a cation between a binary and a tertiary oxide, that these parameters could be used to successfully model tertiary oxide systems such as perovskites.

A set of parameters was derived for $BaTiO_3$ based on the Lewis and Catlow work described above, and refined by fitting to known crystal properties [112]. Subsequently, the Ti^{4+} and O^{2-} parameters were used unmodified in an analysis of $SrTiO_3$ based on the assumption that the Ti^{4+}-O^{2-} and O^{2-}-O^{2-} environments, and therefore, interactions were essentially the same in the two perovskites [113]. A new set of parameters for the Sr^{2+}-O^{2-} interaction were fitted since there is a large change in coordination number of the cation between the rock salt structure of SrO and the A site of the perovskite structure, i.e. from 6 to 12. To obtain a suitable parameter set a fitting procedure was performed to elastic and dielectric constants. It is these parameters that have been used for Sr^{2+}, Ti^{4+} and O^{2-} in the research presented here. The earlier study was primarily concerned with doping a wide variety of cations into the perovskite lattice at both the A and B sites to consider a range of defect options, including doping $SrTiO_3$ with Ni^{2+} and so provides a direct comparison with the present work.

At the time of the original calculations for calcium titanate only one set of Ca^{2+}-O^{2-} parameters could be found [87]. However the O^{2-}-O^{2-} and Ti^{4+}-O^{2-} used in Zacate et al work paper where inconsistant with those used in this present work. Therefore, a set of parameters were fitted to the orthorhombic structure of $CaTiO_3$ based on the parameters developed by Lewis and Catlow [112] which agree well with a recent work by Mather et al [88].

2.3.2. Modelling the Defect Structure

The study of the defect structure and energetics of $SrTiO_3$ and $BaTiO_3$ using both atomistic [113, 112, 89, 90] and *ab initio* [91, 92, 93, 94, 95] simulations remains an active area of research, however the body of work for CaTiO3 is considerably less [88].

Atomistic simulations of the defect structure of the alkaline earth titanates have concentrated on understanding the effect of single defects and defect clusters on the structure and energetics of the system. In general it is found that there is a correlation

between the energy cost of placing the defect into the lattice and the size mismatch between the defect and non-defect ions. In addition clustering of defects reduces the energy cost of disrupting the lattice. In the recent study on the defect structure of $CaTiO_3$ [88], a range of trivalent (Al^{3+}, Mn^{3+}, Fe^{3+}, Co^{3+}, Ga^{3+}, Sc^{3+}) and divalent (Fe^{2+}, Ni^{2+}) cations were substituted into the Ti^{4+} site. The most favourable single defect dopant was found to be Mn^{3+} and the most favourable cluster configuration was a defect centre with two adjacent nearest neighbour oxygen ion vacancies. In the extensive study of the defect structure of $SrTiO_3$ by Akhtar et al [113] a series of monvalent, divalent, trivalent and tetravalent cations were substituted at both the Sr^{2+} and Ti^{4+} sites different charge compensation mechanisms including oxygen ion vacancies and electron hole formation. The authors found that [113]:

- Monovalent, divalent and larger trivalent cations readily replace Sr^{2+} ions.
- Small, highly charged ions show a marked preference for substitution at the titanium sites.
- Large tetravalent cations substitute at the Sr^{2+} site in the presence of charge compensating defects.
- Trivalent cations of intermediate size tend to distribute evenly on both the Sr^{2+} and the Ti^{4+} sites leading to self charge compensation.
- These conclusions can be compared to the results of similar simulations using the $BaTiO_3$ host lattice [112] in particular:
- In BaTiO3, Mg^{2+} and Ni^{2+} are predicted to partially substitute at Ti^{4+} sites, whereas in $SrTiO_3$ all divalent cations substitute at Sr^{2+} sites.
- Mn^{3+} and Fe^{3+} substitute at Ti^{4+} sites in $BaTiO_3$, whereas self compensation is predicted in $SrTiO_3$.
- In $BaTiO_3$, all tetravalent cations substitute at Ti^{4+} sites, whereas in $SrTiO_3$, M^{4+} ions with larger size substitute at Sr^{2+} sites with electron compensation.

In contrast to the atomistic simulations, *ab initio* calculations have concentrated on the modifications to the band structure and electronic conductivity introduced by the addition of defects to the lattice. In studies of oxygen vacancies in $SrTiO_3$ [91, 94] using the LDSA formulism of DFT, a strong correlation was found between electronic properties and the oxygen vacancy concentration and charge. The most stable configuration was for an oxygen vacancy with a +2 charge where excess electrons were donated into the Ti d-states of the crystal conduction band. For vacancies with a +1 or neutral charge spin polarisation states were predicted. No new band gap states were found for the +2 charged vacancy system, but a defect state was found for the +1 and neutral charged vacancy simulations. The substititution of Fe^{4+} at the titanium site of $SrTiO_3$ [92] using a periodic HF based approach predicts that the high spin state is much lower in energy than the low spin state and the energy level positions are strongly dependent on the asymmetric displacement mode of the six nearest O ions which is a combination of the Jahn-Teller and breathing modes. A considerable amount of covalent bonding between the Fe ion and the four nearest O ions is also predicted. For substitution of V and Sc into titanium sites, as studied by periodic DFT methods [93], it is predicted that the distortions of the lattice are very small around the defects and that hole doping yields a larger density of states at the Fermi level electron doping.

2.3.3. Modelling the Surface

The knowledge of the surface structure of perovskites is key to understanding many of the applications of these materials, from heterogeneous catalysis to ferroelectronics, and consequently the modelling of the surfaces of perovskites is a very active area of research [96., 97, 98, 99, 100, 101, 102, 103]. In this section some of the work relating to the simulation of the surfaces the alkaline earth titanate is reviewed.

The most commonly modelled surfaces of the perovskite structure are different cuts parallel to the (1 0 0) crystal plane since these surfaces predominate experimentally. For the perovskite structure, the surfaces parallel to the (1 0 0) crystal plane are non-polar which is convenient for computational modelling purposes, see Section 3.1.8 and Figure 4. There are two terminations possible, one contains A site cations ($Ca^{2+}/Sr^{2+}/Ba^{2+}$) and oxide anions labelled as the O(Ca/Sr/Ba) surface, the other only contains B (Ti^{4+}) site cations and oxide anions, labelled OTiO.

Atomistic modelling of the alkaline earth titanates [96] revealed that the surface energy of the unrelaxed surface, i.e. atoms occupy their bulk atomic positions, is the same for both of the possible terminations with values of 1.335 Jm^{-2}, 1.310 Jm^{-2} and 1.418 Jm^{-2} for $BaTiO_3$, $SrTiO_3$ and $CaTiO_3$ respectively. The higher surface energy of $CaTiO_3$ is due to the small size of the Ca^{2+} cation [104]. Upon relaxation the OTiO terminations of $BaTiO_3$ and $SrTiO_3$ become the preferred surfaces, whereas the OCa termination is found to be the preferred surface of $CaTiO_3$. During relaxation all surfaces rumple such that the anions and cations which are in the same plane in the bulk are no longer in the same plane. The rumpling of the surface forms a dipole perpendicular to the surface which leads to long range Coulomb interactions which may attract or repel charged species above the surface. The surface dipole is negative for $BaTiO_3$ and $SrTiO_3$, but positive for $CaTiO_3$ since the OTiO terminations give negative surface dipoles, but the OA termination give positive surface dipoles.

No work on the *ab initio* modelling of the surface of the orthorhombic phase of $CaTiO_3$ have been found, but studies of the cubic phase of this material have been carried out using periodic DFT using plane waves [97]. The *ab initio* simulations confirm that the OCaO termination has a lower surface energy than the OTiO termination as predicted by atomistic calculations. Rumpling of the surface upon relaxation is predicted, however the magnitude of the shift in the positions of the atomic centres for the OTiO terminated surface is calculated to be greater in the first layer down into the surface, rather than at the surface itself. Analysis of the band structures of the unrelaxed versus relaxed structures for the OCaO and OTiO terminated surfaces reveals that there is very little change in the band gap upon relaxation of the OCaO terminated surface, but a reduction in the band gap upon relaxation of the OTiO terminated surface which is attributed to the large displacement of the second layer of atoms for the latter.

Several studies have investigated the surface structure and electronic features of $BaTiO_3$ and $SrTiO_3$ [98, 99, 100, 101, 102, 103]. In the work by Piskunov et al [101] a comparison of these two materials, along with $PbTiO_3$, is carried out using DFT with re-optimised Gaussian type basis sets. In common with other studies this work focuses on the surface relaxations and electronic band structure of the cubic phases of $BaTiO_3$, $SrTiO_3$ and $PbTiO_3$. The atoms at the surface were allowed to move along the z-axis only since there are no forces by symmetry along the x and y axes. In common with

both the atomistic modelling of these titanates and the *ab initio* work on $CaTiO_3$, the movement of surface cations is much larger than that of surface oxide ions leading to a rumpling of the surface. In general all atoms moved towards the bulk lattice with the only exception being the oxygen ions of the OSrO terminated surface of $SrTiO_3$. On the other hand all the atoms in the second layer relaxed outwards towards the surface. A difference in the rumpling behaviour between $BaTiO_3$ and $SrTiO_3$ was predicted with the OSrO terminated surface of $SrTiO_3$ rumpling more than the OTiO terminated surface, whereas for $BaTiO_3$ the OTiO terminated surface rumpled more than the OBaO terminated surface. The surface energies for both terminations in the perovskites were calculated to be similar, however the surface energy for the OSrO termination in $SrTiO_3$ is slightly lower than the surface energy for the OTiO terminated surface (1.15 eV vs 1.23 eV respectively), whereas the situation is reserved for $BaTiO_3$ (1.19 eV vs 1.07 eV respectively).

Analysis of the electronic charge redistribution upon relaxation of the surfaces predicted that there is no significant change in the nature of the Sr-O or Ba-O bonds and that they remain essentially ionic, whereas the covalent nature of the Ti-O bonds for both perovskites on the OTiO terminated surfaces becomes more pronounced as the Ti-O bonds lengths are reduced due to surface relaxations. The band structures for $BaTiO_3$ and $SrTiO_3$ are similar and indicate that the top of the valence band mainly consists of O 2p orbitals and the bottom of the conduction band is mainly Ti 3d in character. On the OSrO and OBaO terminated surfaces it is the O 2p orbitals from the central layer of the simulation slab which form the top of the valence band and Ti 3d orbitals from the subsurface layer which form the bottom of the conduction band. On the OTiO terminated surfaces the top of the valence band consists of O 2p orbitals from the surface atoms, and the bottom of the conduction band is formed by Ti 3d orbitals from the 3^{rd} layer of the slab. In all case the band gap is reduced upon surface relaxation.

3. Computational Techniques

3.1. Atomistic Modelling of Periodic Crystals Using Interatomic Potentials

Periodic solids including ionic materials can be modelled at an atomistic level using interatomic potentials which represent the energy of the system as a functional of atomic coordinates. The energy can be calculated by separating these interactions into long range electrostatic, or Coulombic, forces, where the energy is calculated using the Ewald summation [105], and short range dispersive forces where the energy is calculated using a range of forms for the potential energy. Most commonly, only forces between pairs of ions are considered and the two most widely used forms for the potential energy are the Buckingham[106] and Lennard-Jones [107] potentials discussed below. An important extension to this model is to consider the polarisability of ions within the system which is achieved using the shell model [108]. In the following sections, the concepts outlined above are explained, along with the methods used to optimise the geometry of the lattice, model crystal properties, simulate point defects. We also describe how these techniques are extended to consider the surface properties of a periodic lattice.

3.1.1. Long Range Electrostatic Interactions and the Ewald Sum

The potential energy in Joules due to the Coulombic interaction between ions is given by:

16] $$U_{ij}^{Coulomb} = \frac{q_i q_j}{r_{ij}}$$

where q_i and q_j are the charges on the ions in Coulombs, ε_0 is the permittivity of free space and r_{ij} is the distance in metres between the ions. As can be seen, the potential energy between ions drops off with respect to 1/r. However, the number of interacting ions increases with the surface area of a sphere given by $4\pi r^2$. Hence the number of interactions for a given ion within the system increases faster than the interactions decay with increasing distance and an attempt to calculate the energy with a sum of terms may not be convergent.

To overcome this an Ewald summation is employed where the real space sum is split into two rapidly convergent summations, one in real and one in reciprocal

space[105, 109], and a cut off radius is chosen such that the number of terms used in each summation is minimised. The reciprocal space summation in effect calculates the energy due to a system with a Gaussian distribution of charge placed at the lattice point with signs the same as the charges at those points. The effect of the Gaussian charge distributions is then removed by calculating the energy of a system where Gaussian charge distributions are superimposed on each of the lattice points, with opposite sign to the charge at those points which are summed in real space. How rapidly these two sums converge is controlled by a factor η, which effectively defines the width of the Gaussian distributions. The real (U^{real}) and imaginary (U^{im}) summations have the following forms:

17] $$U^{real} = \frac{1}{2}\sum_{i=1}^{N}\sum_{j=1}^{N}\frac{q_i q_j}{r_{ij}} erfc\left(\eta^{\frac{1}{2}} r_{ij}\right),$$

18] $$U^{im} = \sum_{i=1}^{N}\sum_{j=1}^{N}\sum_{G}\frac{4\pi}{V}\exp(iG.r_{ij})\frac{\exp\left(-\frac{G^2}{4\eta}\right)}{G^2},$$

where q is the charge on an ion, G is a reciprocal lattice vector (where the special case G=0 is excluded) and V is the volume of the unit cell.

3.1.2. Short Range Interactions and the Buckingham Potential

As noted above, short range pair potentials are normally modelled by the Lennard-Jones [107] or Buckingham [106] potentials:

19] $$U_{ij}^{Lennard-Jones} = \frac{C_m}{r_{ij}^m} - \frac{C_6}{r_{ij}^6},$$

20] $$U_{ij}^{Buckingham} = A\exp\left(\frac{r_{ij}}{\rho}\right) - \frac{C_6}{r_{ij}^6}$$

Essentially, these describe the potential between two ions by separating the energy into a repulsive part (the first term in the equations above), and an attractive part (the second term), with the latter dominating at larger and the former at smaller distances. Throughout this work the Buckingham potential form has been used. The Buckingham potential form is very reliable at normal interionic distances. However, if

the ions approach each other too closely the exponential in the repulsive term approaches zero and the r^{-6} term dominates causing the ions to strongly attract leading to very large energies which is known as the Buckingham catastrophe. However, with appropriate parameters, the problem is only encountered at unphysically short distances.

In order to use the Buckingham potential, three parameters must be defined for each ion-ion pairing considered in the calculation. It is customary to assume that there is no short range cation-cation interactions as these will be small compared to the anion-anion and anion-cation interactions [106]. In this thesis interatomic pair potential parameters were needed for the following pairs of ions: O^{2-}-O^{2-}; O^{2-}-Ca^{2+}; O^{2-}-Sr^{2+}; O^{2-}-O^{2-};O^{2-}-Ti^{4+}; O^{2-}-Ni^{2+}; O^{2-}-Ni^{3+}. Parameter sets are found by:

empirical fitting to experimental data whereby parameters are adjusted, usually by a least squares fitting routine, so as to achieve the best possible agreement between calculated and experimental crystal properties.

fitting to data obtained from high quality *ab initio* simulations where the values of A, C and ρ can be found from the depth of the potential energy well, the equilibrium interatomic distance, and the form of the potential energy surface [110].

It is then assumed that the values are valid in predicting structures and properties in unknown situations.

The three parameters that must be found are A, ρ and C. A is closely related to the size of the ion and ρ to the "hardness". In some cases the attractive part of the short range interaction is neglected and C is set to zero. The parameter sets used, with the exception of the O^{2-}-Ni^{3+} set, were derived by Catlow and co workers [106, 111, 112, 113] and are shown in Table 8, see Section 2.3.1 for an explanation of how they were developed. The development of the O^{2-}-Ni^{3+} pair potentials are described in Section 5.4.

Table 8 Interatomic pair potentials

Interaction	A / eV	ρ / Å^{-1}	C / eVÅ^6
O^{2-}-O^{2-}	22764.3	0.14900	43.000
O^{2-}-Ca^{2+}	1340.2	0.3214	0.000
O^{2-}-Sr^{2+}	776.84	0.35867	0.000
O^{2-}-Ba^{2+}	1214.400	0.35220	8.000
O^{2-}-Ti^{4+}	877.20	0.38096	9.000
O^{2-}-Ni^{2+}	1582.50	0.28820	0.000

3.1.3. Polarisabiliity

As noted, lattice polarisation is described using the shell model of Dick and Overhauser [108] whereby the charge on an ion is split between two point charges (core and shell) attached by an harmonic spring of constant k. The charges are Coulombically screened from each another. By convention the short range forces only act on the shells, whereas the Coulombic potential acts on both the core and the shell. Hence, the short range forces damp the polarisability of the ions. As for the short range potential, the variable parameter charges on the core and shell and for the spring constant must be found by fitting simulations to known crystal properties especially dielectric constants. In the present thesis work, formal ionic charges are used and the shell charges and spring constants are given in Table 9

Table 9 Parameters used for the Charges on the Core and the Shell of the Ions and the Spring Constants of the Springs Contecting the Core and the Shell [106, 111, 112, 113]

Ion	Charge on Shell (q_{shell}) / e	Spring Constant (k) / eVÅ^{-2}
O^{2-}	-2.389	1.410
Ca^{2+}	3.135	110.2
Sr^{2+}	1.526	11.406
Ba^{2+}	1.848	29.100
Ti^{4+}	-35.863	65974
Ni^{2+}	3.344	93.700

3.1.4. Optimisation of the Crystal Structure

The next stage is normally to determine the energy minimum on the potential energy surface. Ideally this would be the lowest possible minimum , i.e. global minimum, but there is no guarantee that this will be achieved as generally for a complex system there are multiple minima. In this section the three common minimisation methods for finding stationary points on the potential energy surface are described.

The simplest proceedure is called the Steepest Descent method [114] whereby the first derivative or gradient of the energy function is used to find the direction in which the function increases most rapidly. The energy surface is searched at points along the direction which is opposite to the direction of the steepest gradient until the energy starts to increase and a new search direction is found starting from the new lowest energy point. The process continues until the gradient becomes smaller (flatter) than a predefined cut off value. Although this method is rapid and always guaranteed to find an energy minimum it has two main disadvantages: it tends to oscillate around the true energy minimum; and the rate at which it converges on the energy minimum decreases as it approaches the minimum.

A more complex variant on the steepest descent method is the Conjugate Gradient [115] whereby the previous search direction(s) is/are considered when finding the new search direction:

21] $$\mathrm{d}_i = -\mathrm{g}_i + \beta_i \mathrm{d}_{i-1}$$

where d is the search direction, g is the gradient, i is the step number and β is a mixing factor. The form of β is different for each conjugate gradient method. The use of previous search directions stops the minimiser from returning to parts of the energy surface previously explored which happens in the simple Steepest Descent method. The main advantage of the conjugate gradient method is that is tends to find energy minima in fewer steps than steepest descent. However information about the previous search directions must also be stored, so memory requirements are greater.

The most sophisticated methods for finding the stationary points are called Newton-Raphson methods [116] which expand the energy function around the current point using the first and the second derivatives:

22] $$f(x) \simeq f(x_0) + \mathrm{g}^t(x - x_0) + \frac{1}{2}(x - x_0)^t \mathrm{H}(x - x_0)$$

where g is the gradient vector and H is the second derivative matrix known as the Hessian. The requirement that the gradient of this second order approximation is zero leads an expression for the step that needs to be taken to get to the point of zero gradient:

23] $$(x - x_0) = -\mathrm{H}^{-1}\mathrm{g}$$

Equation 23 is exact for a harmonic energy surface whereby given the exact form of the gradient vector and the Hessian matrix the minimum point on the energy surface would be found in one step. In reality the energy surface is anharmonic and an iterative procedure is necessary except when very close to the minimum. Unlike the methods described above, the optimisation is equally likely to find a minimum, maximum or saddle point on the potential energy surface, and therefore, a slightly modified version of Equation 23 is used:

24) $$(x - x_0) = -\alpha\mathrm{H}^{-1}\mathrm{g}$$

where the factor α is a scalar quantity and is determined by performing a line search along the search direction to find a one dimensional minimum and the whole process becomes iterative again.

This method has the potential to find the stationary points extremely efficiently. However, it is by far the most computationally demanding in that the Hessian matrix must be determined and, most demanding, inverted, a process which would be counterproductive if carried out at each optimisation step. Various algorithms have been proposed which approximate the new Hessian matrix such as those by Davis-Fletcher-Powell (DFP) [117] and Broyden-Fletcher-Goldfarb-Shanno (BFGS) [118]. The optimiser employed in this work used the BFGS method for which the form of the update algorithm is:

25] $$\mathrm{H}_{i+1}^{\mathrm{BFGS}} = \mathrm{H}_i^{\mathrm{BFGS}} + \frac{\Delta x \otimes \Delta x}{\Delta x.\Delta \mathrm{g}} - \frac{\left(\mathrm{H}_i^{\mathrm{BFGS}}.\Delta \mathrm{g}\right) \otimes \left(\mathrm{H}_i^{\mathrm{BFGS}}.\Delta \mathrm{g}\right)}{\Delta \mathrm{g}.\mathrm{H}_i^{\mathrm{BFGS}}.\Delta \mathrm{g}} + \left[\Delta \mathrm{g}.\mathrm{H}_i^{\mathrm{BFGS}}.\Delta \mathrm{g}\right] v \otimes v$$

$$v = \frac{\Delta x}{\Delta x.\Delta \mathrm{g}} - \frac{\mathrm{H}_i^{\mathrm{BFGS}}.\Delta \mathrm{g}}{\Delta \mathrm{g}.\mathrm{H}_i^{\mathrm{BFGS}}.\Delta \mathrm{g}}$$

In practice the initial Hessian is calculated and inverted at the start of the optimisation. A new Hessian is only calculated when one of a series of tests fails meaning that the new Hessian is unlikely to be a good enough representation of the true Hessian at this point. The tests are:

- The maximum number of cycles for updating is exceeded

- The angle between the gradient vector and the search vector exceeds a given threshold
- The energy has dropped by more than a certain threshold in one cycle, so the curvature is likely to have altered
- The energy cannot be lowered by line minimisation along the current search vector

Complete optimisation of the system is unnecessary as the results are limited by the accuracy of the forcefields used. Optimisation is said to have been achieved when a series of adjustable convergence tests have been met which are based on the following:

- the gradient norm (root mean square gradient per variable)
- the maximum individual gradient component
- the norm of the estimated displacement vector
- the change in the function (energy, enthalpy or free energy) between successive cycles
- the change in the variables between successive cycles.

3.1.5. Modelling Point Defects

There are two contrasting approaches to the modelling of point defects within a crystal lattice i.e. the use of supercells or the Mott Littleton approach which models isolated points. In the former approach a defect is introduced into the centre of a supercell which is then repeated using 3D periodic boundary conditions. The energy of the supercell is calculated in the usual way. Clearly the larger the supercell the more dilute the defect concentration.

The supercell approach is normally used in electronic structure based techniques and surface calculations, as discussed below. However, interatomic potential based studies have commonly employed the Mott Littleton method [119], in which an isolated defect or defect cluster is modelled which represents an infinitely dilute system. The ions within the lattice are split into three spherical regions surrounding the defect (regions 1, 2a and 2b), with region 1 being the ions closest to the defect as shown in Figure 3. The spheres are centred on the defect itself if there is a single defect, or in the centre of the defect region in the case of a defect cluster. The radii for regions 1 and 2a are user defined and then region 2b extends out to infinity.

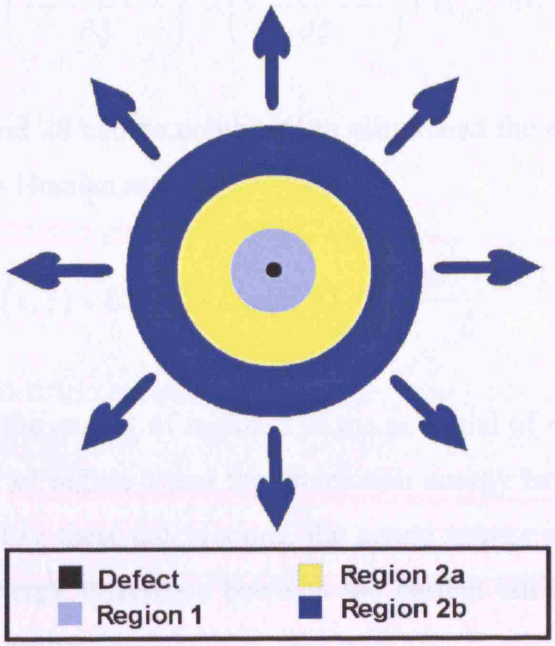

Figure 3 Illustration of the regions surrounding the defect in the Mott Littleton approach.

The effect of the defect will be most important in region 1 and so the ions are allowed to relax freely here, whereas in region 2 the movement of the ions and the energy associated with this region are approximated. During a calculation it is important to ensure that the size of regions 1 and 2 are sufficiently large to make the energy of the system independent of the number of ions included in each region.

The total energy of the system can be expressed by Equation 26

26] $$U_{tot}(x,\xi) = U_{11}(x) + U_{12}(x,\xi) + U_{22}(\xi)$$

where $U_{11}(x)$ is the energy of region 1 in terms of the Cartesian coordinate, $U_{22}(\xi)$ is the energy of region 2 in terms of the Cartesian displacements and $U_{12}(x,\xi)$ is the energy of interaction between the two regions. There is no distinction between regions 2a and 2b at this stage. Since the forces on the ions in region 2 are small, their movement will be purely harmonic and can be written as in Equation 27

27] $$U_{22}(x,\xi) = \frac{1}{2}\xi^{T}\mathrm{H}_{22}\xi$$

where H_{22} is the Hessian matrix for this region. By assuming that the positions of the ions in region 2 are equilibrium positions, Equation 28 can be defined:

28] $$\left(\frac{\partial U_{tot}(x,\xi)}{\partial \xi}\right)_x = \left(\frac{\partial U_{12}(x,\xi)}{\partial \xi}\right) + \mathrm{H}_{22}\xi = 0$$

Equations 27 and 28 can be combined to eliminated the energy of region 2 and the need to calculate its Hessian matrix:

29] $$U_{tot}(x,\xi) = U_{11}(x) + U_{12}(x,\xi) - \frac{1}{2}\left(\frac{\partial U_{12}(x,\xi)}{\partial \xi}\right)_x \xi$$

So to calculate the energy of region 1 in the potential of region 2 it is necessary to calculate the energy of region 1 and the interaction energy between regions 1 and 2 only. To further simplify these calculations, the actual energy computed is the defect energy which is the energy difference between the perfect lattice of regions 1 and 2, U_{tot}^{p}, and the defective lattice, U_{tot}^{d}:

30] $$U_{defect}(x,\xi) = U_{tot}^{d}(x,\xi) - U_{tot}^{p}(x,\xi)$$

An important point during defect calculations is that the perfect bulk structure must be at an energy minimum otherwise displacements of ions may cause the structure to become unstable leading to unphysical results.

Now the differences between regions 2a and 2b are considered. In region 2a the forces on the atoms, and consequently their displacements, are calculated using both the short range interactions and the Coulombic forces. However, the region 2b the short range interactions are ignored and only the forces from the long range Coulombic forces are considered. In fact, to simplify the calculations further, only the net charge on the defect is considered in the perturbation of region 2b.

3.1.6. Phonons

The calculation of energy based on long range Coulombic and short range Buckingham potentials gives the internal energy of the system (U) at absolute zero and zero pressure which can be easily be extended to include the external pressure of a system and so find the enthalpy using Equation 31:

31] $$H = U + PV$$

To obtain information about the stability of the system, its free energy and several other properties it is necessary to consider the ionic motions. In this section the treatment of phonons is considered, with the calculation and minimisation of free energy detailed in Section 3.1.7.

In the absence of an external force, the motions of the ions that make a contribution to the energy of the system for a solid crystal are the vibrations about the minimum energy position. At low temperature, the vibrations will be harmonic, but as the temperature increases they become increasingly anharmonic. Clearly for an infinite 3D system, the number of phonon modes will be infinite.

The results of the calculations of phonon properties are displayed in the first Brillouin zone of reciprocal space [109]. There will be 3N, where N is the number of ionic centres, modes per wavevector (k point), and the lowest three of these modes, known as acoustic modes, tend to zero in the centre of the Brillouin zone (k=0,0,0) or Γ point. These modes represent purely translational modes of the crystal at this point, so clearly should be zero here. Dispersion curves, i.e. plots of phonons versus k points, yield important information about the stability of the system. In particular, "negative" phonon frequencies show that the structure is inheritantly unstable since these modes lead a reduction in the energy of the system and show that ions cannot be at a minimum energy positions.

Phonon calculations require the force constant matrix, i.e. the second derivatives of the energy of the atoms in Cartesian space, see Equation 32:

32] $$F_{i\alpha j\beta}(k) = \sum_R \left(\frac{\partial^2 U}{\partial\alpha\partial\beta} \right) \exp\left(ik\left(r_{ij} + R \right) \right),$$

which gives the force constant matrix for two atoms i and j and involves the summation over all lattice vectors R within the cut-off radius which is then converted to the dynamical matrix by multiplying by the inverse square root masses of the ions:

33] $$D_{i\alpha j\beta}(k) = \frac{1}{\left(m_i m_j \right)^{1/2}} F_{i\alpha j\beta}(k)$$

3.1.7. Free Energy and its Minimisation

The calculation of free energy is based on the theories of statistical mechanics where microsopic properties of individual atoms or ions are related to macroscopic thermodynamic and other properties of the material [120]. Of central importance to the calculation of macroscopic properties is the evaluation of the partition function Z^{tot} as defined in Equation 34:

34] $$Z^{tot}(T,V,N_1,N_2,...) = \sum_i e^{-E_i/k_B T}$$

Z^{tot} is dependent on the temperature, volume and constitution of the system. Note, k_B is the Boltzmann constant (1.38×10^{-23} JK^{-1}). The partition function is directly related to the Helmholtz free energy A via Equation 35:

35] $$A = -kT \ln Z$$

Once a value for A has been obtained all other thermodynamic properties of the system can be calculated, for example, the entropy $S = -(\partial A / \partial T)_{V,N_1,N_2,...}$.

In order to calculate the partition function it is necessary to assume that the rotational, translational, vibrational and electronic components of the energy are independent and so the total partition function can be separated into these different parts. In simulations of 3D ionic lattices the rotational and translational energy of the system are not relevant; the electronic partition function is not calculated in the force field methods discussed here, leaving only the vibrational partition function Z^{vib} to be evaluated.

The m^{th} vibrational energy level for simple harmonic oscillators is given in Equation 36:

36] $$U_m^{vib}(n,k) = \left(n + \frac{1}{2}\right) h\omega(n,k)$$

From this, the vibrational partition function can be shown to be as in Equation 37:

37] $$Z^{vib} = \sum_m \sum_k \frac{\exp\left(-\frac{h\omega}{2k_BT}\right)}{\left(1-\exp\left(-\frac{h\omega}{k_BT}\right)\right)}$$

From Equation 37 the contribution to the internal energy and the free energy from the vibrational modes can be found using Equation 38 and 39:

38] $$U^{vib} = \sum_m \sum_k w_k \left(\frac{1}{2} h\omega + \frac{h\omega}{\left(\exp\left(-\frac{h\omega}{k_BT}\right)-1\right)} \right)$$

39] $$A^{vib} = \sum_m \sum_k w_k \left(\frac{1}{2} h\omega + k_BT \ln\left(1-\exp\left(-\frac{h\omega}{k_BT}\right)\right) \right)$$

Note U^{vib} in Equation 38 represents the zero point vibrational energy. The factor w_k is the weighting factor given at each k point that is included in the sum. Strictly speaking the sums should be integrals over the phonon density of states, however, in practice a sum over a mesh of discrete k points is used. There are different methods for choosing the k point mesh. The GULP program uses the Monkhorst and Pack [121] scheme in which three so-called shrinking factors are given by the user which define the number of evenly spaced k points along each of the vertices in reciprocal space. Since a larger unit cell leads to a smaller Brillouin zone, the larger the unit cell the less fine the k point needs to be (i.e. the smaller the shrinking factors). It is important to ensure that the calculated properties, in this case free energy, are well converged with respect to the shrinking factors used.

An alternative, complementary approach is molecular dynamics (MD) [122], which includes anharmonic vibrations, and is better suited to high temperatures, whereas conventional lattice dynamics is based on the harmonic approximation and is more effective at low temperatures. As a general rule, lattice dynamics is appropriate up to around half the melting point temperature and it is this technique, as implemented in the GULP code [123, 124], which is used here. In lattice dynamics, a quasi harmonic approach is commonly implemented whereby conventional harmonic lattice dynamics is

used with the cell parameters subsequently adjusted to minimise the free energy of the system.

As with energy minimisation, free energy minimisation requires at least the first derivatives of the energy, but preferably the second to access the most efficient methods, see Section 3.1.4. Analytical expressions for the first derivatives of the energy have been derived [125], for example the derivative of free energy with respect to strain is shown in Equation 40:

40] $$\left(\frac{\partial A}{\partial \varepsilon}\right)=\left(\frac{\partial U_{static}}{\partial \varepsilon}\right)+\sum_{k}\sum_{m}\left\{\frac{h}{2\omega}\left(\frac{1}{2}+\frac{1}{\exp\left(\frac{h\omega}{k_B T}\right)-1}\right)\left(\frac{\partial \omega^2}{\partial \varepsilon}\right)\right\}$$

The expression is written in terms of the squares of the frequencies since these are the eigenvalues of the dynamical matrix, see Equation 33. The derivatives of the dynamical matrix eigenvalues can be obtained by perturbation theory and expressed as derivatives of the dynamical matrix projected onto the corresponding eigenvectors as in Equation 41:

41] $$\left(\frac{\partial \omega(k,m)^2}{\partial \varepsilon}\right)=e_m^*(k)\left(\frac{\partial D(k)}{\partial \varepsilon}\right)e_m(k)$$

Consequently the minimisation of free energy using a simple steepest descent optimisation requires the third derivative of energy with respect to three Cartesian coordinates. Newton-Raphson methods, strictly speaking, require the fourth derivatives of the energy. However, this is computationally expensive and the Hessian matrix is usually approximated here by assuming that the free energy contribution to the curvature of the potential energy surface is small.

3.1.8. Modelling the Surface of a Periodic Lattice

The ability to model the surface of a material is of utmost importance in many fields of materials science, for example predicting morphologies [126] and reactivities [127]. There are two stages to the modelling of surface which are the creation of the surface and optimisation of its structure and properties.

A surface is usually created by cleaving it from a section of the bulk by defining both a crystal plane using a set of Miller indices (*h k l*) and a distance away from this plane, known as the shift, at which to cleave the surface. For example, in the rock salt structure the (001) plane will define one of the sides of the unit cell and will contain equal numbers of positive and negative ions for a cut on the plane. In fact, for the rock salt structure all cuts parallel to the (001) plane will form the same surface. In the perovskite structure, see Section 2.1.4, there are two possible cuts of the (001) plane, one containing A site cations and oxygens and one containing B site cations and oxygens, see Figure 4.

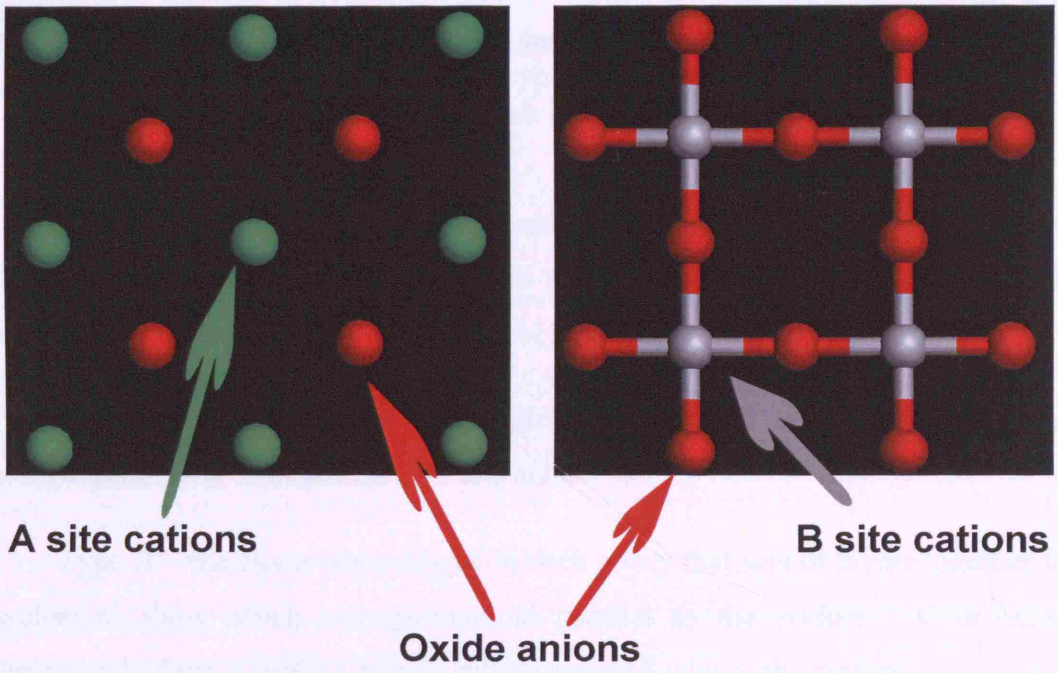

Figure 4 The two possible terminations possible for surfaces parallel to the (001) crystal planes for the cubic perovskite surface. One of the surfaces contains A site cations and oxide ions, the other contains B site cations and oxide ions.

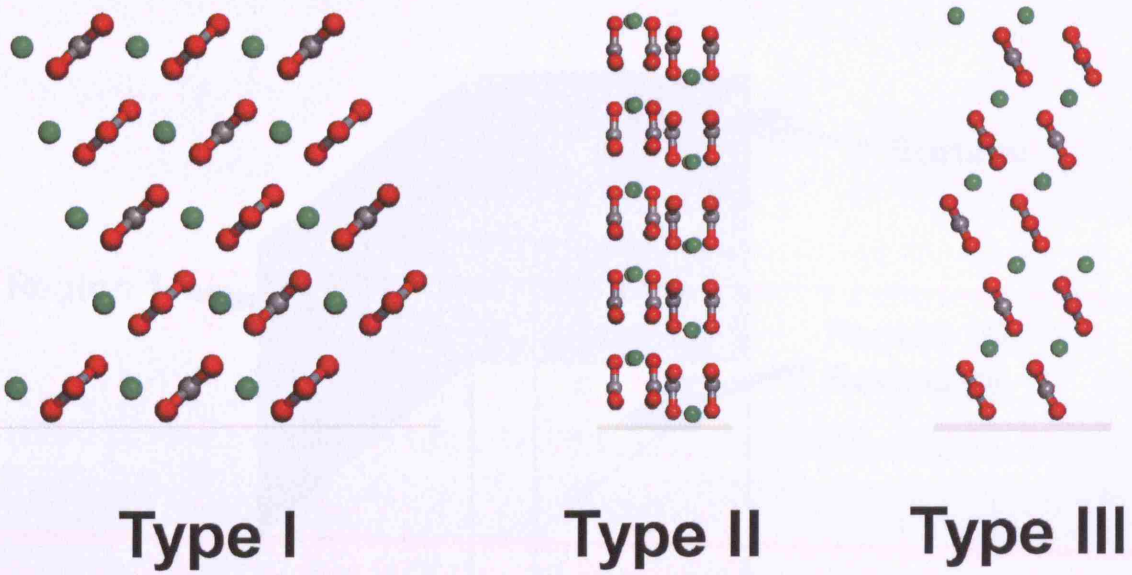

Figure 5 Illustration of the 3 types of surfaces using two polymorphs of calcium carbonate as an example. The type I and type III surfaces are cuts parallel to the (104) and (110) planes of calcite, and the type II surface is parallel to the $(10\bar{2})$ plane of aragonite.

An important consideration is that only surfaces without a dipole perpendicular to the surface can be modelled, as surfaces with a such a dipole have infinite energy. Three types of surfaces have been identified [128, 129] as illustrated in Figure 5

Type I – each layer of atoms parallel to the plane is charge neutral giving no dipole perpendicular to the surface for any cuts.

Type II – the atoms are arranged in such a way that sets of layers together form non-charged slabs which are symmetrical parallel to the surface. Cuts between complete slabs form a surface with no dipole perpendicular to the surface.

Type III – there are alternating layers of positive and negative charge and all cuts give a dipole perpendicular to the surface.

Once the surface cut has been identified, the number of layers to be included in the simulation from the sub surface layers is defined by two parameters which give the number of layers in two regions, I and II, as in Figure 6 [128].

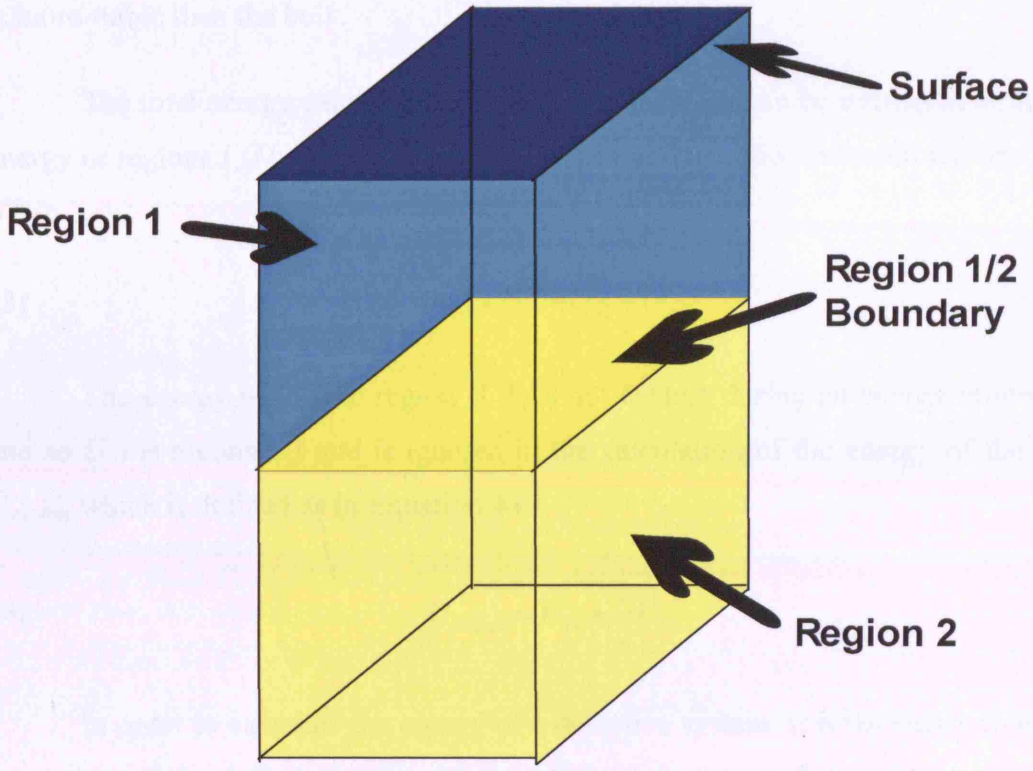

Figure 6 Two layer model for simulation of surfaces

The surface is generated by periodically repeating regions I and II in two dimensions. In region I, the ions are allowed to move freely to minimise the forces on the atoms, just as in the three dimensional bulk calculations. In region II, the atoms are fixed and are used to simulate the effective constraining potential of the real bulk lattice. An important step in the calculation of surface structures and properties is to ensure that they are converged with respect to the number of layers included in the two regions.

Of particular significance in this work is the calculation of the surface energy (ΔU_{SE}) which is the thermodynamic penalty for cleaving a surface from the bulk and is defined as in Equation 42:

42] $$\Delta U_{SE} = \frac{\left(U_{surface} - U_{bulk}\right)}{A}$$

where $U_{surface}$ is the energy of the surface, U_{bulk} is the energy of the bulk and A is the surface area. Note, the number of ions in the bulk and the surface must be the same to ensure a valid comparison between the surface and the bulk energies. Clearly, the

surface energy must be positive as a negative value energy would imply that the surface is more stable than the bulk.

The total energy calculated in a surface simulation can be written in terms of the energy of regions I (U_{11}) and II (U_{22}) as well as the interaction between regions I and II (U_{12}):

43] $$U_{tot} = U_{11} + U_{12} + U_{22}$$

The energy of ions in region II does not change during an energy minimisation and so U_{22} is a constant and is ignored in the calculation of the energy of the surface $U_{surface}$ which is defined as in Equation 44:

44] $$U_{surface} = U_{11} + \frac{1}{2}U_{12}$$

In order to calculate the energy of a defective system, it is necessary to compare the energy of the defective bulk with that of the defective surface to obtain the surface energy in Equation 42. As the energy of the defective surface ($U_{surface}^{def}$) is not readily available from the GULP output, it is calculated using Equation 45:

45] $$U_{surface}^{def} = U_{tot}^{def} - \frac{1}{2}U_{12}^{def} - U_{22}^{def}$$

The energy of the impure bulk material is obtained from the three dimensional simulation of the doped material.

3.2. Electronic Structure Techniques

The forcefield method described in Section 3.1 is a powerful technique for describing the structure, properties and energetics of crystals, however they do not implicitly model electrons and electronic states. In this section two important approaches to modelling electronic structure are described: Hartree-Fock (HF) and Density Functional Theory (DFT).

3.2.1. Hartree-Fock Theory

Hartree-Fock theory attempts to solve the Schrödinger equation [130, 131, 132] for which an exact solution is possible only for a one particle system such as a particle in a box and one atom systems, e.g. H and He^+.

3.2.1.1. Schrödinger Equation

The full time dependent Schrödinger equation which represents the movement of a particle, mass *m*, under the influence of an external potential *V* is given in Equation 46 [133]:

46] $$\left\{-\frac{\hbar}{2m}\left(\frac{\partial^2}{\partial x^2}+\frac{\partial^2}{\partial y^2}+\frac{\partial^2}{\partial z^2}\right)+V\right\}\Psi(r,t)=i\hbar\frac{\partial\Psi(r,t)}{\partial t}$$

where Ψ is the wavefunction which describes the motion of the particle and is used to find various properties of the particle including its energy. In the majority of calculations the external potential is considered to be independent of time and so equation 46 can be simplified to equation 47 which only depends on the spatial coordinates of the particle, r.

47] $$\left\{-\frac{\hbar^2}{2m}\nabla^2+V\right\}\Psi(r)=E\Psi(r)$$

where E is the energy of the system and,

48] $$\nabla^2=\frac{\partial^2}{\partial x^2}+\frac{\partial^2}{\partial y^2}+\frac{\partial^2}{\partial z^2}$$

Equation 47 is often condensed to:

49] $$H\Psi = E\Psi$$

The Hamiltonian, *H*, operator consists of contributions for the kinetic (∇^2) and potential (*V*) energies of the particle.

3.2.1.2. Orbitals and Slater Determinants

The Schrödinger equation can be solved exactly for a hydrogen atom where the Hamiltonian operator is given by equation 59:

50] $$H = -\frac{\hbar^2}{2m_e}\nabla_e^2 - \frac{\hbar^2}{2m_N}\nabla_m^2 - \frac{Ze^2}{4\pi\varepsilon_0 r}$$

where m_e is the mass of the electron, m_N is the mass of the nucleus, ∇_e and ∇_N are the laplcian operators, see Equation 48, which act on the electron and nuclear coordinates respectively and ε_0 is the permittivity of free space. In Equation 50 the nucleus and electrons are moving in a spherical potential. In order to solve the Schrödinger equation the conditions are transformed to consider movement around the centre of mass where the equation has the form as in Equation 51 [132].

51] $$-\frac{\hbar^2}{2\mu}\nabla^2\psi - \frac{Ze^2}{4\pi\varepsilon_0 r}\psi = E\psi$$

where μ is the reduced mass of the nucleus and electron. Using polar coordinates allows wavefunction ψ to be separated into a radial and an angular part as in Equation 52 [132].

52] $$\psi(r,\theta,\phi) = R(r)Y(\theta,\phi)$$

Solutions to the Schrödinger equation concentrate on finding the form of the radial wavefunction as the angular wavefuntion can be cancelled out. It turns out that the radial wavefunctions can be characterised by three quantum numbers: n, l and m_l. n is known as the principle quantum number, it has any integer value and in one electron systems each integer uniquely defines the energy associated with the wavefunction. l is the angular momentum quantum number, it can have values from 0 to n-1 and it determines the number of orbitals with different angular momenta for a given value of n. m_l is the magnetic quantum number, it can have values from –l to +l and it specifies the which angular momentum component the wavefunction has got.

These one electron radial wavefunctions are commonly called orbitals and they are used as the basis for building more complex wavefunctions that contain more than one electron. An example is the helium atom and the Hamiltonian for this system is given in Equation 53.

53] $$H = -\frac{\hbar^2}{2m_e}\left(\nabla_1^2 + \nabla_2^2\right) - \frac{2e^2}{4\pi\varepsilon_0 r_1} - \frac{2e^2}{4\pi\varepsilon_0 r_1} + \frac{2e^2}{4\pi\varepsilon_0 r_{12}}$$

In Equation 53, it is the last term which prevents an analytical solution as it represents the potential between the two moving electrons. One way to approximate the solution is to separate out those parts of the equation which can be solved and consider the remaining parts as a perturbation, which in this case is the electron-electron interaction. The Hamiltonian of the unperturbed system is taken to be a sum of two one electron Hamiltonians which represent the orbitals described above as in Equation 54.

54] $$H^{(0)} = H_1 + H_2$$

where,

55] $$H_i = -\frac{\hbar^2}{2m_e}\nabla_i^2 - \frac{2e^2}{4\pi\varepsilon_o r_i}$$

When Hamiltonian operators are summed in this way, the resulting wavefunction turns out to be the product of the individual wavefunctions as in Equation 56.

56] $$\psi(r_1, r_2) = \psi_{n_1 l_1 m_{l_1}}(r_1)\psi_{n_2 l_2 m_{l_2}}(r_2)$$

Now the perturbation introduced by the electron-electron interactions must be considered. The first important perturbation is given by the Coulomb integral as in Equation 57:

57] $$J = \frac{e^2}{4\pi\varepsilon_0}\int\left|\psi_{n_1 l_1 m_{l_1}}(r_1)\right|^2\left(\frac{1}{r_{12}}\right)\left|\psi_{n_2 l_2 m_{l_2}}(r_2)\right|^2 d\tau_1 d\tau_2$$

The Coulomb integral, J, represents the perturbation to the energy of the system due to the Coulombic interation of the two electrons. Since the electrons have the same charge the Coulomb integral will be positive.

The second important perturbation arises from the consideration of excited states for the electron configuration of the helium atom such as $1s^1 2s^1$. The energy of the system must be the same whether electron 1 is in $1s^1$ and electron 2 is in $2s^1$ or vice versa which gives rise to the Exchange integral K:

58] $$K = \frac{e^2}{4\pi\varepsilon_0}\int\psi_{n_1 l_1 m_{l_1}}(r_1)\psi_{n_2 l_2 m_{l_2}}(r_2)\left(\frac{1}{r_{12}}\right)\psi_{n_1 l_1 m_{l_1}}(r_2)\psi_{n_2 l_2 m_{l_2}}(r_1)d\tau_1 d\tau_2$$

Unlike the Coulomb integral, the Exchange integral does not have a classical analogy and it considered to be a quantum correction term for the Coulomb intergral. A consequence of the need for the wavefunction to be antisymmetric (known as the Pauli principle), where the exchange of two electrons causes the wavefunction to change sign, is that the Exchange integral always makes a positive contribution to the energy. As the electrons come close together K causes the probability of finding the electrons both at that point to drop to zero, and this is known as the Fermi hole.

Note, electron spin is introduced via a fourth quantum number, s, which when combined with the orbitals form spinorbitals.

3.2.1.3. Born-Oppenheimer Approximation

An important assumption in electron structure calculations is the Born-Oppenheimer approximation whereby the potential from the nuclei is assumed to be fixed [134].

3.2.1.4. Fock Operator

The expectation value of an eigenvalue, such as the energy, is given by:

59] $$E = \frac{\int \Psi^* H \Psi d\tau}{\int \Psi^* \Psi d\tau}$$

where each side of Equation 49 has been multiplied by the complex conjugate of the wavefunction and integrated over all space dτ. Equation 59 can be written in a short hand form using the "bra-ket" notation:

60] $$E = \frac{\langle \Psi | H | \Psi \rangle}{\langle \Psi | \Psi \rangle}$$

The variation theory states that all approximate forms of a wavefunction will always give a higher expectation value for the energy that the exact wavefunction and so the lower the expectation value the more exact the form of the wavefunction. In the Hartree-Fock method the lowest possible expectation value is found via an iterative process, the Self Consistent Field (SCF) approach which will be discussed below [135].

The problem of solving the Schrödinger equation is reduced to considering the movement of N (the number of electrons) single electrons in the average field of all the

nuclei and other electrons. The overall wavefunction is built via a Slater determinant consisting of spinorbitals. To find the spinorbitals, single electron equations must be used of the form:

61] $$f_1\phi_a(1) = \varepsilon_a\phi_a(1),$$

where f_1 is the Fock operator, ϕ_a is the spinorbital and ε_a is the energy of the orbital. Note Fock operators, like Hamiltonian operators, are Hermitian and one consequence of this is that there are an infinite number of eigenfunctions (spinorbitals) and an infinite number of eigenvalues (energies) available. The N lowest spinorbitals will contain electrons and will be filled, whereas the remaining spinorbitals will be vacant. The form of the Fock operator is given in Equation 62.

62] $$f_1 = h_1 + \sum_u \{J_u(1) - K_u(1)\},$$

where h_1 is the core hamiltonian for electron 1, J is the Coulomb operator and K is the Exchange operator.

3.2.1.5. Self Consistent Field Approach

In order to be able to use the Fock operator for a spinorbital it is necessary to know the remaining N-1 spinorbitals. The self consistent field approach uses the variational theorem to find the lowest energy from a set of spinorbitals. A set of trial orbitals is chosen which are formed into a new set of orbitals via the Hartree-Fock equations and the process repeated until the orbitals do not change. In practice the SCF proceedure is implemented via the Roothaan-Hall equations as described below.

3.2.1.6. Roothan-Hall Equations

In the Roothaan-Hall approach spinorbitals, or more properly the spatial parts of spinorbitals, are built up from a set of basis functions and the problem is transformed into one involving the use of matrices [136, 137].

For a spatial function $\psi_a(1)$ we write:

63] $$f_1\psi_a(1) = \varepsilon_a\psi_a(1),$$

where the Fock operator is for a spatial function is:

64] $$f_1 = h_1 + \sum_u \{2J_u(1) - K_u(1)\}.$$

These spatial wavefunctions can be built from a linear combination of M basis functions as in Equation 65:

65] $$\psi_i = \sum_{j=1}^{M} c_{ji}\theta_j .$$

The basis functions are independent and the spatial wavefunctions are found by calculating the coefficients c_{ij}. By substituting Equation 65 into Equation 63 and multiplying each side by θ^* and integrating we get:

66] $$\sum_{j=1}^{M} c_{ja} \int \theta_i^*(1) f_1 \theta_j(1) dr_1 = \varepsilon_a \sum_{j=1}^{M} c_{ja} \int \theta_i^*(1) \theta_j(1) dr_1$$

Equation 66 can be simplied by the introduction of the overlap matrix S, where the elements are given as in Equation 67, and the Fock matrix where the elements are given as in Equation 68:

67] $$S_{ij} = \int \theta_i^*(1) \theta_j(1) dr_1$$

68] $$F_{ij} = \int \theta_i^*(1) f_1 \theta_j(1) dr_1$$

Then Equation 66 becomes:

69] $$\sum_{j=1}^{M} F_{ij} c_{ja} = \varepsilon_a \sum_{j=1}^{M} S_{ij} c_{ja}$$

Equation 69 is one of a set of simultaneous equations, one for each value of I, known as the Roothaan equations. The entire set of equations can be written in matrix format:

70] $$\mathbf{Fc = Sc}\varepsilon$$

where **c** is an M×M matrix of coefficients and **ε** is an M×M matrix of obital energies. The best possible set of coefficients is found using the self consistent field approach.

3.2.2. Density Functional Theory

In contrast to the Hartree-Fock method described above which is based on the concept of wavefunctions, DFT is based on the calculation of electron density. Although wavefunctions are used in the modern day implementation of DFT, it should be remembered that they are not a fundamental part of the theory as they are for Hartree-Fock and related methods.

3.2.2.1. Hohenberg-Kohn Theories

The essence of DFT is that there is a one to one relationship between the electron density of a system and its energy, in fact, if the electron density is known then all the properties of the system can be calculated. Furthermore, the variational theorem still applies to the energy expressed as a functional of the electron density. The above statements are known as the Hohenberg-Kohn Theorems [138].

A function is an expression which depends on a variable, whereas a functional is an expression which depends on a function. Since the electron density ρ is a function of position r, the energy E is a functional of the density:

71] $$E\left[\rho(r)\right]$$

3.2.2.2. Thomas-Dirac-Fermi Theory

The basic problem with DFT is that the form of the energy functional is unknown. Early attempts to find the form of the functional were made by Thomas and Fermi [139] and Thomas, Dirac and Fermi [140]. In both of these techniques the energy functional is broken down into a kinetic energy term ($T[\rho]$), a nuclear-electron attraction term ($E_{ne}[\rho]$) and an electron-electron repulstion term ($E_{ee}[\rho]$) with the nuclear-nuclear repulsion considered to be constant via the Born-Oppenheimer approximation. By analogy with Hartree-Fock theory the electron-electron repulsion term is broken down into a Coulomb ($J[\rho]$) and Exchange ($K[\rho]$) functional. The nuclear-electron attraction and Coulomb functionals are given by there classical counterparts as in Equations 72 and 73:

72] $$E_{ne}\left[\rho\right] = \sum_{a} \int \frac{Z_a \rho(r)}{|R_a - r|} dr$$

73] $$J[\rho]=\frac{1}{2}\int\int\frac{\rho(r)\rho(r')}{|r-r'|}dr$$

The factor of ½ in Equation 73 allows integration over all space for both variables.

In the Thomas-Fermi theory form of the kinetic energy functional was found by assuming the system is composed of a non-interacting uniform gas and is given in Equation 74:

74] $$T_{TF}=C_F\int\rho^{5/3}(r)dr$$

where

75] $$C_F=\frac{3}{10}\left(3\pi^2\right)^{2/3}$$

The Thomas-Fermi theory did not include exchange which was introduced in the Thomas-Fermi-Dirac Theory again for a non-interacting uniform electron gas. The form of the Exchange functional is given in Equation 76:

76] $$K_D[\rho]=-C_x\int\rho^{4/3}(r)dr,$$

where:

77] $$C_x=\frac{3}{4}\left(\frac{3}{\pi}\right)^{1/3}.$$

The assumption that a molecule can be represented by a uniform electron gas is clearly not very accurate and the errors in the calculated energies are of the order of 15-20%. However, the most serious draw back to these theories is that they do not predict bonding and molecules simply do not exist.

3.2.2.3. Kohn-Sham Method

Modern density functional theory is based on the work of Kohn and Sham [141]. The main problem with the early theories is that the kinetic energy is poorly represented and in the Kohn-Sham approach the kinetic energy functional is split into a part that can be solved exactly and a small correction term. The exact part of the kinetic energy is

calculated using a Slater determinant composed of orbitals ϕ_i which gives the exact kinetic energy for non-interacting electrons:

78] $$T_S = \sum_{i=1}^{N} \left\langle \phi_i \left| -\frac{1}{2}\nabla^2 \right| \phi_i \right\rangle$$

The difference in energy between the non-interacting and interacting systems is known as the exchange-correlation energy (E_{xc}). The overall DFT energy is given by:

79] $$E_{DFT}[\rho] = T_S[\rho] + E_{ne}[\rho] + J[\rho] + E_{xc}[\rho]$$

The major issue in density functional theory is to find suitable forms for the exchange-correlation term.

The problem of finding the best kinetic energy for the system is similar to that in HF theory where a set of orthogonal orbitals is found via a self consistent field approach to find the lowest energy for the system. A one electron operator (h_{KS}), similar to the Fock operator, is used to form a set of pseudo-eigenvalue equations known as the Kohn-Sham equations:

80] $$h_{KS}\phi_i = \varepsilon_i \phi_i$$

Note, if the exact exchange-correlation functional were known, the energy values found in Equation 80 would equal the orbital energies, but in practice this is not the case.

3.2.2.4. Local Density Approximation (LDA)

The simplest approach to finding exchange-correlation functionals is the use of the local density approximation where the local electron density is assumed to be a uniform electron gas. In other words the electron density is a slowly varying function.

The exchange and correlation functionals are separated out, in common with other techniques for finding these functionals. In the simplest version of LDA the exchange is given by the formula used in the Thomas-Fermi-Dirac theorem, see Equation 76. However, if the α and β spin densities are not equal the electron density of the α spinned electrons is separated from the electron density of the β spin electrons to

give the Local Spin Density Approximation (LSDA) where the exchange is given by Equation 81:

81] $$E_x^{LSDA}[\rho] = -2^{1/3} C_x \int \left[\rho_\alpha^{4/3} + \rho_\beta^{4/3} \right] dr$$

For closed shell systems, LSDA is identical to LDA.

The correlation energy for a uniform electron gas has been determined by Monte Carlo methods for a number of different densities. An interpolation technique is then used to make use of the correlation data such as those of Vosko, Wilk and Nusair (VWN) [142] and Perdew and Wang [143].

Despite the simplicity of the assumptions made in the LDSA method, the accuracy of the results are similar to the HF methods. The exchange energy is generally underestimated by ~10%, and the correlation energy is overestimated by around a factor of 2 leading to an overestimation of bond strength.

3.2.2.5. Generalised Gradient Approximation (GGA)

Improvements to the LSDA technique start to consider the system as a non-uniform electron gas by taking into account not only the local electron density, but the first derivative of electron density. Such methods are known as Generalised Gradient Approximations or GGA techniques. Many schemes have been proposed and each is known by the initials of their authors such as PW86 [144] and B88 [145] for the exchange energy, and LYP [146] for the correlation energy. Many of these methods attempt to modify the LSDA result; for example the PW86 exchange energy is given by Equation 82.

82] $$\varepsilon_x^{PW86} = \varepsilon_x^{LDA} \left(1 + ax^2 + bx^4 + cx^6 \right)^{1/15},$$

where

83] $$x = \frac{|\nabla \rho|}{\rho^{4/3}};$$

x is a dimensionless gradient variable and a, b and c are suitable constants. The LYP correlation function is the exception to the attempts to correct the LSDA solution.

3.2.2.6. Hybrid Functionals

Hybrid functionals contain the exact exchange energy from Hartree-Fock theory as introduced via the Adiabactic Connection Formula (ACF) [147]:

84] $$E_{xc} = \int_0^1 \left\langle \Psi_\lambda \left| V_{xc}(\lambda) \right| \Psi_\lambda \right\rangle d\lambda$$

In Equation 84, the exchange correlation energy is related to the factor λ which "turns on" the electron interaction where λ=0 represents a non-interacting system and λ=1 represents the real fully interacting system. $V_{xc}(\lambda)$ represents the potential needed to reproduce the real potential of the system as different values of λ, and Ψ are the corresponding wavefunctions. In the crudest case, where λ is a linear function, the integral can be taken as the average of the two end points:

85] $$E_{xc} \simeq \frac{1}{2}\left\langle \Psi_0 \left| V_{xc}(0) \right| \Psi_0 \right\rangle + \frac{1}{2}\left\langle \Psi_1 \left| V_{xc}(1) \right| \Psi_1 \right\rangle$$

The first term in Equation 85 is the exact exchange energy from HF theory. The second term in is unknown, but it can be approximated in a "Half and Half (H+H)" approach where it is taken as the sum of the exchange and correlation energies from LSDA [148]:

86] $$E_{xc}^{H+H} = \frac{1}{2}E_x^{exact} + \frac{1}{2}\left(E_x^{LSDA} + E_c^{LSDA}\right)$$

An improvement over the Half and Half method is to include gradient correction terms as found for GGA methods. A very popular form of the ACF formula is called B3 [149]:

87] $$E_{xc}^{B3} = (1-a)E_x^{LSDA} + aE_x^{exact} + b\Delta E_x^{B88} + E_c^{LSDA} + c\Delta E_c^{GGA}$$

a, b and c are parameters which have been fitted to experimental data and depend on the form chosen for the GGA correlation energy contribution, with typical values of a=0.2, b=0.7 and c=0.8.

3.3. Periodic Electronic Structure Methods

The application of electronic structure methods to condensed phases is considered in this section. In particular the application of density functional theory to these phases is described, although implementations using Hartree-Fock theory are available, see for example [150].

3.3.1. Bloch Theory

The basic issue in considering condensed phases is the number of electrons involved in the calculation, which for any realistic representation of the system will be infinite. For crystalline solid phases the problem is reduced to calculating the electronic structure for a unit cell of the system which is periodically repeated in three dimensions. Symmetry also plays an important role in these calculations as the higher the symmetry the fewer the number of calculations that need to be made.

One of the cornerstones in the application of electronic structure methods to the condensed phase is Bloch's theorem [109, 151, 152], where the form of the wavefunction in a regularly repeating lattice (i.e. periodic boundary conditions), is given by Equation 88:

88] $$\psi_k(r) = e^{ik.r} u_k(r)$$

In Equation 88 the wavefunction is the product of a periodic function $u_k(r)$ and a phase factor $e^{ik.r}$, where r is the position and k is the wave vector. The periodic function $u_k(r)$ has the following property:

89] $$u_k(r) = u_k(r + a_i)$$

where a_i is one of the lattice vectors of the crystal.

3.3.2. Basis Sets

The basis sets used to build up the wavefunctions used in either the Hartree-Fock or Kohn-Sham equations must obey Bloch's theorem for application to condensed phase systems. There are two choices for the mathematical form of such condensed phase basis sets: plane waves (PW) or atom based orbitals (similar to those used in

molecular based calculations). In this section the use of each of these types of basis set is considered.

3.3.2.1. Plane Waves

The most popular choice for building basis sets for condensed phases is the use of plane waves which are waves that propagate with a constant frequency and constant amplitude, and so they are perfectly periodic, obeying Bloch's theorem [139]. In a constant potential, plane waves are solutions of the Schrödinger equation. However, close to atomic centres the potential is far from constant and so a linear combination of plane waves is used to find solutions.

In general, any function in real space can be written as a function in reciprocal space via the Fourier transform:

90] $$u_k(r) = \int e^{ig\cdot r} u_k(g)\, dg$$

Since the function in real space is periodic, only values of g for which $e^{ig\cdot a_j} = 1$ are valid, where a_j are the three lattice vectors (j=1, 2, 3), which means that g must be a reciprocal lattice vector **G**. The general expression for the periodic wavefunction is given by Equation 91:

91] $$\varphi_k(r) = \frac{e^{ik\cdot r}}{\sqrt{\Omega}} \sum_{\mathbf{G}=0}^{\infty} C_k(\mathbf{G}) e^{i\mathbf{G}\cdot r}$$

As can be seen from Equation 91 to completely represent the periodic wavefunction an infinite summation is required over all possible values of **G**. However in practice, with increasing values of $|\mathbf{G}+k|$ the values of the Fourier coefficients, C_k become increasingly small and a suitable point to stop the summation must be decided. This point is decided by a kinetic energy cut off defined as in Equation 92:

92] $$\frac{\hbar^2}{2m}|k+\mathbf{G}|^2 < E_{cut}$$

The higher the cut off energy, the more plane waves that are included in the summation and the better the representation of the wavefunction. It is important during a calculation involving plane waves that the energy cut off is sufficiently high to ensure

that the properties of the system are well converged with respect to changes in the value of E_{cut}.

To reproduce the form of the wavefunction close to atomic nuclei would require a very large number of plane waves since the potential here rapidly changes and the shape of the orbitals is complex. In order to reduce the number of plane waves needed to describe the system the form of the wavefunctions close to the nuclei are ignored, so effectively ignoring the core electrons and concentrating on the valence electrons. The potentials of the atomic centres are modified in such a way as to form a potential which reproduces the properties of the valence electrons accurately, these new potentials are pseudopotentials [153].

3.3.2.2. Localised Gaussian Functions

The alternative to the use of plane waves is the use a linear combination of atom based functions such as Slater type orbitals (STOs) [154] or Gaussian type orbital (GTOs) [139, 155]. In the case of GTOs (χ), the unknown crystalline orbitals can be built using Equation 93

93] $$\varphi_k(r) = N\sum_{j=1}^{m} a_{ji}(k)\left(\sum_g \chi_{gj}(r)\exp(ik\cdot g)\right),$$

where φ_r are solutions to the one particle Kohn-Sham equations as in Equation 80.

The Kohn-Sham operator includes contributions from the kinetic, external potential, Coulomb and exchange-correlation operators as discussed above. In the case of the exchange-correlation contribution it is generally too computationally demanding the evaluate the integrals analytically. The numerical evaluation involves an expansion of an auxiliary basis set of contracted Gaussian type functions *G(r)*

94] $$E_{xc} = \sum_a^N c_a G_a(r).$$

During the SCF cycle the coefficients are adjusted to give the best fit to the analytic form of the exchange-correlation potential, which changes with the evolving charge density.

One of the main advantages of the use of localised basis sets is the removal of energy cut offs, as needed for plane waves, which leads to a better treatment of the Coulomb contribution as all the charge is correctly accounted for by summing to infinity using Ewald techniques.

Unlike in the use of plane wave basis sets, the use of pseudopotentials is not necessary when using localised basis sets for lighter atoms, however for heavier atoms the use of pseudopotentials becomes necessary to reduce computational demand.

3.4. Application of Computational Methods

The work in this thesis has made use of atomistic modelling and density functional theory.

Atomistic modelling has been used to study the structure and energetics, both in the bulk and at the surface, of the pure and nickel doped alkaline earth titanates. Surface calculations made use of the two region approach described in Section 3.1.8. Bulk defect calculations used the Mott Littleton method, see Section 3.1.5, whereas surface defect calculations were based on supercell simulations. In addition, the tetragonal to cubic phase change in strontium titanate was studied using atomistic modelling.

Density functional theory has been used to complement the atomistic modelling work by calculating the surface and bulk properties of the pure and nickel doped alkaline earth titanates. All defective systems were modelled using the supercell approach and the surfaces were modelling by slabs of material separated by a suitable vacuum gap. The most appropriate hybrid functional for use with strontium titanate was also considered.

4. Investigating the Use of Different Functionals to Model the Structure of Strontium Titanate

4.1. Introduction

The application of DFT to solid state materials is less mature than for molecular systems and the choice of appropriate functionals for condensed phases is more open to question, see for example Alfredsson [156]. In this chapter we discuss the work we have carried out to find the most appropriate hybrid functional to predict the structure and energetics of three possible phases of strontium titanate, $SrTiO_3$. In particular the work focused on the effect of adding different percentages of Hartree Fock (HF) exchange to the Becke DFT functional [149] into a hybrid exchange functional also containing the LYP correlation functional [142, 146]. According to Becke's original 3 parameter functional, B3LYP defined in Equation 95:

95] $$E_{xc} = (1-A)*\left(E_x^{LDA} + B*E_x^{BECKE}\right) + A*E_x^{HF} + (1-C)*_c^{VWN} + C*E_c^{LYP}$$

the parameter A controls the relative percentages of HF and DFT exchange, while B and C, control the weight of gradient corrected correlation and correlation respectively. Only the affect of varying the A parameter was considered here and the default values of unity for B and C were used. In the standard B3LYP functional A=0.2 (20%), B=0.9 and C=0.81. For comparison, simulations were also carried out using three exchange correlation functionals: LDA exchange [140] with VWN correlation [142]; PBE exchange and correlation [157]; and PWGGA exchange and correlation [144].

The basis sets used here, which are built from linear combinations of Gaussian type functions (GTFs), were all electron basis sets for oxygen [158] and titanium [159]. The strontium basis set used the small-core effective core pseudopotential (ECP) of Hay and Wadt [160, 161]. All of these basis sets are readily available from the CRYSTAL website [162]. The implementation of DFT in the CRYSTAL code requires the specification of a grid to evaluate the exchange-correlation potential numerically. In our work, the grid consisted of atom-centered contributions with 75 radial points covering a range of 4.0 ionic radii, and a very dense angular grid with 974 points. We employed a Monkhorst–Pack shrinking factor of 8 for reciprocal space sampling, truncation thresholds of 10^{-7}, 10^{-7}, 10^{-7}, 10^{-7} and 10^{-14} for the Coulomb and exchange series [163], and SCF convergence thresholds of 10^{-7} Hartree for both eigenvalues and total energies.

The three possible phases of $SrTiO_3$ considered were the room temperature cubic phase (space group $Pm\bar{3}m$) [10], the low temperature tetragonal phase where the TiO_6 octahedra have rotated around the z-axis (space group I4/mcm) [164], and a hypothetical ferroelectric phase based on the room temperature structure of $BaTiO_3$ (space group P4mm) [8] with the cell parameters reduced by 0.09 Å to give a=3.90 Å and c=3.93 Å to account for the smaller site of Sr^{2+} compared to Ba^{2+}. Below these phases are referred to as the cubic, tilted and ferroelectric phases respectively. The latter two represent the two stereotypical distortions exhibited by perovskites, which can be classified as rotation of the octahedra (tilted) and a displacement off-centre of the transition metal ion inside its octahedra (ferroelectric).

Table 10 Equilibrium lattice parameters for the three phases of strontium titanate calculated using a set of different DFT functionals.

	Cubic ($Pm\bar{3}m$)			**Tetragonal (Tilted)** (I4/mcm)			**Tetragonal (Ferroelectric)** (P4mm)		
Length /Å **Functional**	**a**	**c**	**c/a**	**a**	**c**	**c/a**	**a**	**c**	**c/a**
Hybrid (0% HF Exchange)	7.960	7.960	1.000	7.949	7.974	1.003	7.946	8.020	1.009
Hybrid (25% HF Exchange)	7.880	7.880	1.000	7.879	7.885	1.001	7.872	7.930	1.007
Hybrid (50% HF Exchange)	7.816	7.816	1.000	7.815	7.816	1.000	7.814	7.818	1.001
Hybrid (75% HF Exchange)	7.760	7.760	1.000	7.760	7.761	1.000	7.760	7.760	1.000
Hybrid (100% HF Exchange)	7.712	7.712	1.000	7.713	7.713	1.000	7.714	7.710	0.999
LDA	7.734	7.734	1.000	7.724	7.751	1.003	7.732	7.738	1.001
PBE	7.886	7.886	1.000	7.879	7.897	1.002	7.882	7.904	1.003
PWGGA	7.876	7.876	1.000	7.869	7.888	1.003	7.872	7.892	1.003
Experimental	7.806*	7.806*	1.000	7.788	7.796	1.001	-	-	-

* Room temperature

Table 11 Structural indicators of tetragonal distortion for the tilted phase (octahedral tilt) and ferroelectric phase (difference between the bond lengths of the long and short Ti-O bonds) for a set of difference DFT functionals.

	Tetragonal (Tilted) (I4/mcm)	**Tetragonal (Ferroelectric)** (P4mm)
Functional	Dihedral Tilt Angle (°)	(Ti-O long bond length) - (Ti-O short bond length) /Å
Hybrid (0% HF Exchange)	8.7	0.214
Hybrid (25% HF Exchange)	4.1	0.195
Hybrid (50% HF Exchange)	0.0	0.025
Hybrid (75% HF Exchange)	0.0	0.010
Hybrid (100% HF Exchange)	0.0	0.006
LDA	8.7	0.005
PBE	7.3	0.131
PWGGA	7.46	0.104
Experimental	4.1	-

4.2. Comparison of Structures

The relaxed structures for the cubic, tilted and ferroelectric phases of $SrTiO_3$ are compared in Table 10 and Table 11. Table 10 shows a simple comparison of the cell parameters and c/a ratio for the different functionals and phases. The trends are very clear: upon increasing the percentage of HF exchange, both the a and the c lattice parameters decrease by around 0.25 Å from 7.95 Å to 7.70 Å. The tetragonal distortion decreases, as shown by the c/a ratio approaching unity as the percentage of HF exchange increases. The tetragonal distortion is most pronounced for the ferroelectric phase at 0% HF exchange, although this distortion is also larger than the experimental value for the tilted phase with no HF exchange.

For the tilted structure, 25% HF exchange gives the best agreement with experiment for the tetragonal distortion, although the absolute values of the cell parameters are slightly overestimated, with the higher levels of HF exchange essentially predicting a cubic symmetry. By comparison, the LDA exchange predicts as expected an overcompressed structure with low values of the cell parameters, and the tetragonal distortion in the tilted structure is larger than experiment. The PBE and PWGGA functionals both predict the cell parameters to be larger than experiment for the cubic and tilted phases, and the tetragonal distortion is overestimated for the tilted material.

It should be noted that the length of the a and the c lattice parameters in Table 10 are not those of the unit cells. The smallest cell that can allow ready comparison between the three different structures can be thought of as a 2×2×2 supercell of the cubic perovskite unit cell, of formula $Sr_8Ti_8O_{24}$.

Table 11 shows how two more indicators of the tetragonal distortion for the tilted and ferroelectric phases vary with the exchange and correlation functionals used. For the tilted phase, the tilt angle between different octahedra looking down the z-axis of the crystal (see Figure 7), shows that the angle decreases with increasing HF exchange,dropping to zero above 50%. The tilt angle is overestimated with no HF exchange and agrees with experiment at 25% HF exchange. By comparison, all of the other LDA and GGA functionals predict the tilt angle to be larger than that measured experimentally. For the ferroelectric structure, the difference in the bond length between the long and the short Ti-O bonds, caused by the displacement of the Ti^{4+} cation, is considered. Once again, on increasing HF exchange, the difference in the

bond lengths reduces as the structure becomes less tetragonally distorted. Unlike for the tilted phase, the difference in the bond length of the LDA functional is small indicating a small tetragonal distortion. Its should be noted that this behaviour is in line with LDA studies of the stereotypical ferrroelectric material, $BaTiO_3$, for which LDA is unable to predict a stable distorted phase [165]. However, both the PBE and PWGGA functionals predict a difference of just over 0.1 Å for this structural.

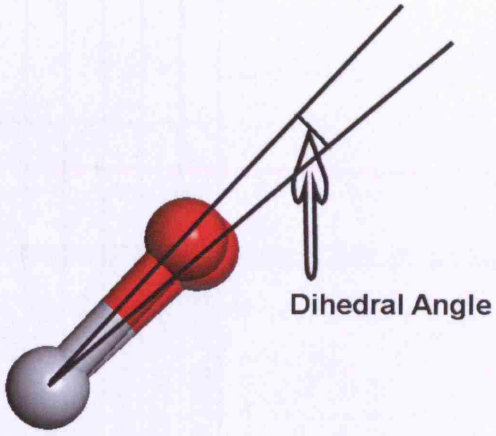

Figure 7 Image looking down the z-axis of the lattice Cartesian frame along a Ti-O-Ti bond showing the measured tilt angle of one octahedra relative to the next.

4.3. Comparison of Energies

The total energies for an $SrTiO_3$ unit of the three different phases using the different functionals are shown in Table 12. Figure 8 shows a plot of the energy difference between the tilted and ferroelectic structures (red), and the non-ferroelectric and cubic material (blue) at different levels of HF exchange.

As can be seen, the experimentally observed low temperature non-ferroelectric phase is predicted to have a slightly lower lattice energy than both the ferroelectric and cubic structures at all levels of HF exchange as well as for the LDA, PBE and PWGGA functionals. The energy differences generally decrease as the amount of HF exchange increases and the structures converge towards a cubic symmetry.

Table 12 Total energies calculated for three possible phases of $SrTiO_3$ using different DFT functionals.

	Total Energy (eV)		
	Cubic ($Pm\bar{3}m$)	**Tetragonal (Non ferroelectric)** (I4/mcm)	**Tetragonal (Ferroelectric)** (P4mm)
Hybrid (0% HF Exchange)	-30096.9340	-30096.9423	-30096.9371
Hybrid (25% HF Exchange)	-30094.4933	-30094.4934	-30094.4913
Hybrid (50% HF Exchange)	-30092.6025	-30092.6039	-30092.6007
Hybrid (75% HF Exchange)	-30091.1755	-30091.1761	-30091.1756
Hybrid (100% HF Exchange)	-30090.1788	-30090.1789	-30090.1781
LDA	-29999.8358	-29999.8397	-29999.8360
PBE	-30086.0944	-30086.0965	-30086.0945
PWGGA	-30098.3050	-30098.3068	-30098.3039

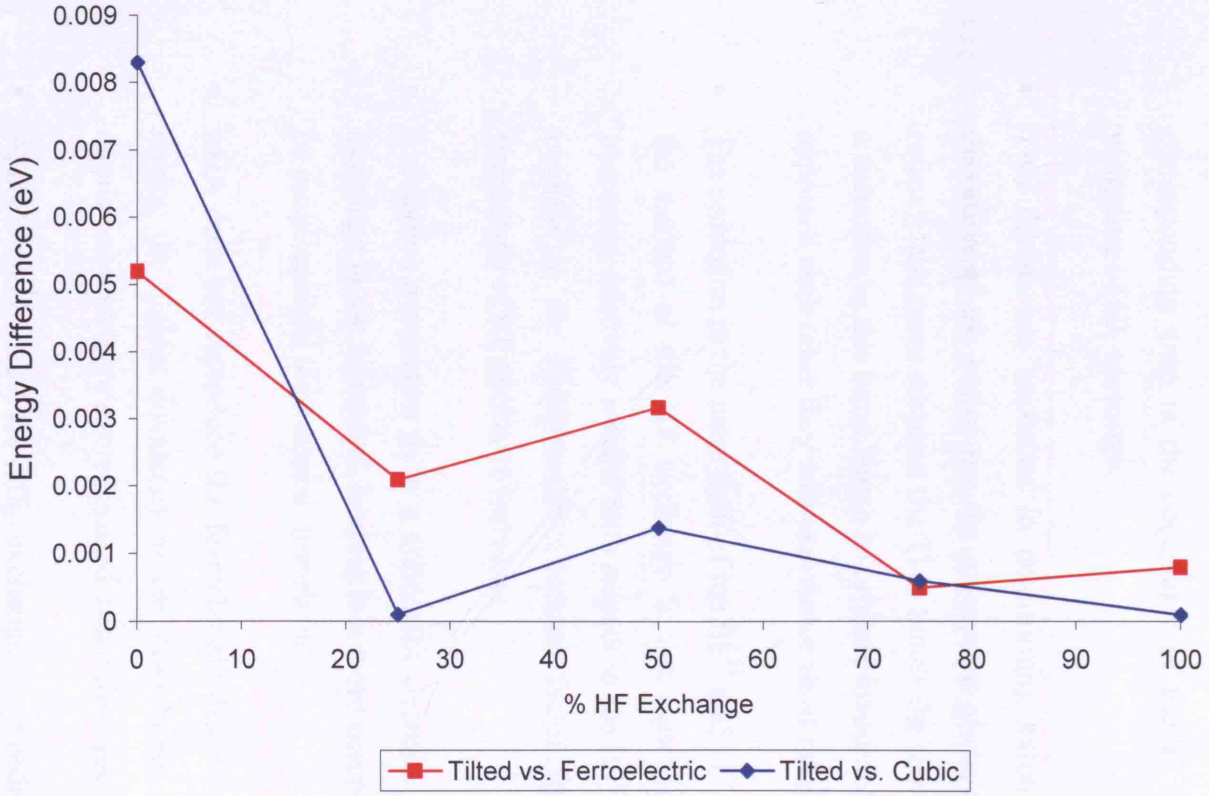

Figure 8 A plot showing the difference between total energies of the ferroelectric and cubic phases from the tilted phase of $SrTiO_3$ at different levels levels of Hartree-Fock exchange used in the DFT functional.

4.4. Discussion

In order to interpret these results, the findings of an extensive study into the effect of using different hybrid functionals to simulate different symmetries of $BaTiO_3$ by Cora [165] are considered. Some of Cora's conclusions were:

- The more HF exchange used in the functional the more ionic the Ti-O bond becomes, i.e. the O 2p orbitals become more occupied with a corresponding drop in the occupancy of the Ti 3d orbitals for higher weighting of HF exchange.

- Two factors are important in determining extent of the ferroelectric distortion of the lattice (i.e the movement along the z-axis of the Ti^{4+} cation): the more covalent the Ti-O bonds the more energy gained from a reduction in this bond length as orbitals favourably overlap; as the ions approach each other they will experience short range repulsions.

- The reduction in the ionic radii of the Ba^{2+} and Ti^{4+} cations on increasing the amount of the HF exchange is not matched by the Ti^{4+} cation becoming relatively smaller with respect to the Ba^{2+} cation, leading to an increase in the Goldschmidt tolerance factor for the system as the percentage of HF exchange increases.

- The lattice parameters show a systematic decrease on increasing the HF exchange in the functional, leading to a more compact system which will be more resistant to structural distortions.

- LDA does not reproduce the ferroelectric distortion in $BaTiO_3$, despite having the highest covalency of the Ti-O bond, since the short range repulsions which are overestimated, resist this type of distortion.

- Approximately 50-60% HF exchange is needed to reproduce the experimental polarisation of the $BaTiO_3$ system.

It can be seen that there is broad agreement between this work and Cora's study. In both cases there is a decrease in the lattice parameter predicted for the systems on increasing the amount of HF exchange, with LDA calculating a small lattice parameter and the GGA functionals predicting a larger value. The decrease in the lattice

parameter on increasing the amount of HF exchange can be assigned to the increasing ionic character of the system so reducing the effective size of the cations.

As the HF exchange increases there is a tendency for the systems to become more cubic which may be due to a change in the relative sizes of the Sr^{2+} and Ti^{4+} cations. The cubic to tilted tetragonal phase change observed experimentally at a temperature of 110 K and is caused by the softening of the phonon mode associated with librations of the Ti-O_6 octahedra. This implies that the Sr^{2+} ions are relatively small with respect to the Ti^{4+} ions to allow this distortion. Since the increasing amount of HF exchange will lead to an overestimate of the Sr^{2+}:Ti^{4+} ratio, higher HF exchange containing functionals will favour a more cubic symmetry.

The overestimation of the tetragonal distortion and octahedral tilt-angle for the tilted phase using LDA may be due to a combination of the small lattice parameter and the covalent character of the system allowing distortions of the system within a compact lattice. On the other hand the tetragonal distortion for the ferroelectric phase using LDA is small in agreement with the work by Cora.

The large ferroelectric distortions displayed by functionals with low HF exchange values may be ascribed to the energy gains obtained from shortening the Ti-O bonds increasing the orbital overlap of these covalent bonds. Clearly the energy gain will decrease as the bonds become more ionic with increasing HF exchange.

In terms of the reproduction of the tetragonal distortion (c/a ratio) and octahedral tilt angle of the low temperature phase of $SrTiO_3$, a functional containing 25% HF exchange is the most appropriate. In order to allow comparisons between simulations of the pure and doped alkaline earth titanates the functional containing 25% HF exchange was used throughout the following DFT calculations. It should be noted that the use of this functional is in contrast to the best predicted functional for the simulation of $BaTiO_3$ by Cora of ~60% HF exchange.

5. Bulk Structure and Energetics of Nickel Doped Alkaline Earth Titanates – Atomistic Modelling

In this chapter we present the results of the simulations of the bulk crystal properties of pure, and nickel doped, alkaline earth titanates using atomistic modelling.

5.1. Atomistic Modelling of Undoped Titanates

5.1.1. Calcium Titanate

The calcium titanate lattice has orthorhombic symmetry (space group PBNM) as discussed in Section 2.1.1. Relaxing the structure using atomistic modelling with the parameters given in Table 8 and Table 9 reproduces the experimental structure reliably as can be seen from the comparison given in Table 13. The only difference to note is the slight increase (1%) in length of the Ti-O bond.

Table 13 Comparison of the experimental [10] and relaxed structures of $CaTiO_3$.

Lattice Property	Experimental	Relaxed	% Change
a /Å	5.3789	5.3655	-0.2
b /Å	5.4361	5.4485	0.2
c /Å	7.6388	7.6688	0.4
Ti-O bond length /Å	1.96	1.98	1%
Energy per $CaTiO_3$ /eV	-150.54	-150.66	-

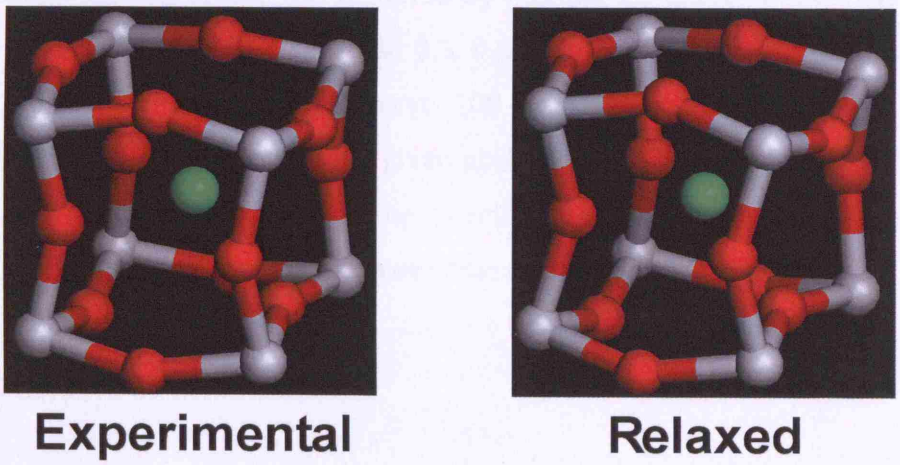

Figure 9 Comparison of the local environment surrounding the Ca^{2+} site in the experimental and relaxed structures of $CaTiO_3$ using atomistic modelling with the parameters listed in Table 8 and Table 9.

The local environment around the Ca^{2+} cations is exactly reproduced as can be seen in Figure 9, with all of the Ca-O bonds lengths remaining unchanged during energy minimisation.

Analysis of phonon dispersion curves for the relaxed structure confirmed that the structure is at an energy minimum on the potential energy surface, see below for a more detailed consideration of this process.

5.1.2. Strontium Titanate

As discussed in 2.1.1, at room temperature $SrTiO_3$ has cubic symmetry, space group $Pm\bar{3}m$, with a cell parameter of a=3.9034 Å. This structure is readily minimised using atomistic modelling with the parameters given in Table 8 and Table 9. A comparison of the experimental and relaxed structures is given in Table 14.

Table 14 A comparison of the experimental [10] and relaxed structures of the cubic phase of strontium titanate.

Lattice Parameter	Experimental	Relaxed	% Change
a /Å	3.9034	3.8967	-0.17
Volume ($Å^3$)	59.474	59.168	-0.51
Lattice Energy (eV per $SrTiO_3$ unit)	-149.26	-149.26	-

As can be seen, the simulation shows excellent agreement with the published experimental data. It was necessary to check that this structure is at a minimum on the potential energy surface, which was achieved by plotting six dispersion curves from k point 0,0,0 to k points: 0.5, 0.0, 0.0; 0.0, 0.5, 0.0; 0.0, 0.0, 0.5; 0.0, 0.5, 0.5; 0.5, 0.0, 0.5; 0.5, 0.5, 0.0. For each dispersion curve, 100 points were calculated along the line connecting the initial and final k-points given above. The results are plotted in Figure 10, and clearly show that for three of the directions one of the frequencies becomes imaginary, i.e. the relaxed structure is not at a true energy minimum.

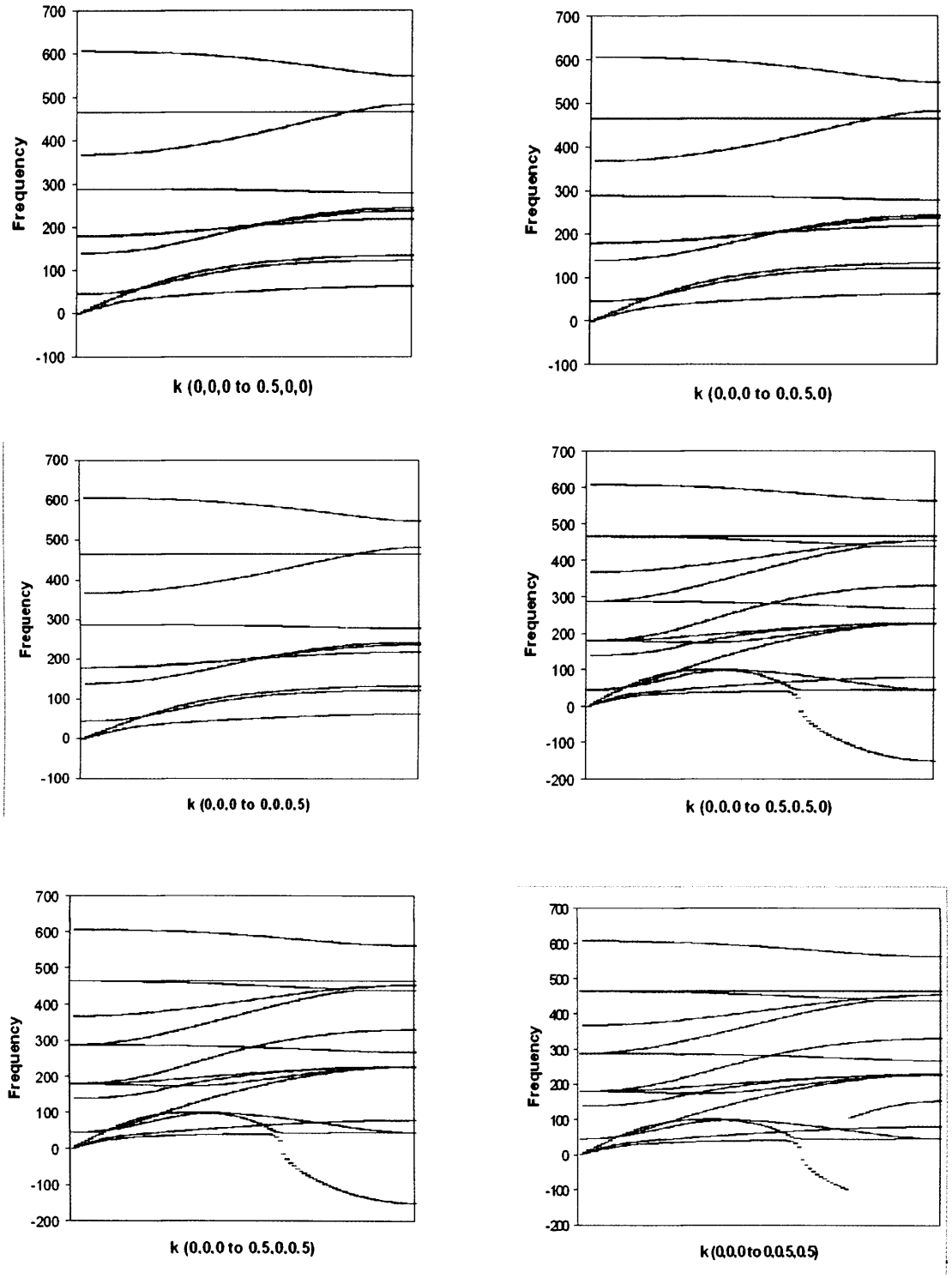

Figure 10 Dispersion curves for a cubic unit cell of strontium titanate following an energy minimisation calculation between six pairs of k-points.

Initial attempts at relaxing the structure to a true minimum by increasing the size of the simulation cell to a 2×2×2 supercell were unsuccessful. In order to relax the structure successfully, it was necessary to find the eigenvectors associated with the negative eigenvalues (which give the imaginary freqencies). Note, the negative eigenvectors show in which direction the atom needs to move to lower the energy of the system. It was found that the negative eigenvalues were all associated with the oxygen atoms. Furthermore, the associated eigenvectors indicated that the TiO_6 octahedra should rotate around the central Ti^{4+} ions as in Figure 11 to lower the energy of the system:

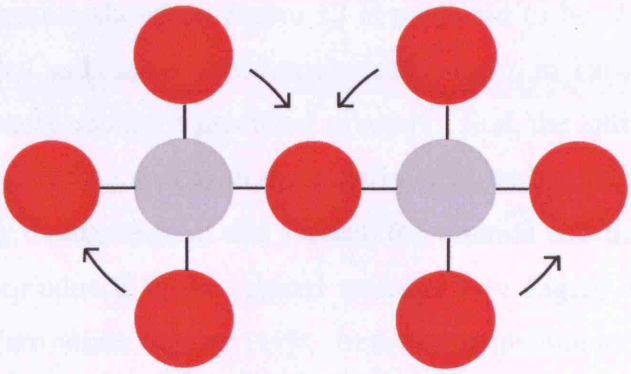

Figure 11 View of the four planar oxygen atoms surrounding the titanium atoms in two adjacent TiO_6 octahedra showing the rotations associated with reducing the energy of the system during atomistic relaxation of the cubic $SrTiO_3$ lattice.

Since adjacent octahedra do not rotate in the same direction, (see Figure 11), it was necessary to use a 2×2×2 supercell of the cubic unit cell combined with rotations around the x, y and z axes to eliminate all of the imaginary phonon frequencies.

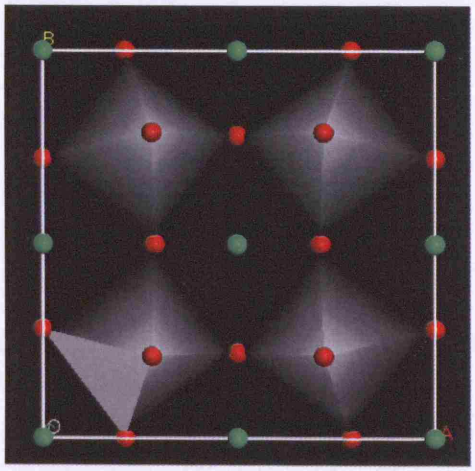

Figure 12 Relaxed structure of strontium titanate as predicted by atomistic modelling with parameters from Table 8 and Table 9.

Table 15 Comparison of the stable relaxed structure of strontium titanate with the experimental room temperature cubic structure and the low temperature tetragonal phase.

Lattice Property	Experimental* (Cubic)	Experimental (Tetragonal)	Relaxed	% Change c.f. cubic	% Change c.f. tet.
a /Å	7.8068	7.7881	7.7499	-0.7	-0.5
c /Å	7.8068	7.7960	7.7799	-0.3	-0.2
c/a	1	1.001	1.004	-	-
Volume /Å^3	475.79	472.86	467.27	-1.8	-1.2
Energy /eV per $SrTiO_3$ unit	-149.26	-	-149.38	-	-

* Cell lengths multiplied by 2 for comparison with relaxed structure

The conformation shown in Figure 12 is predicted to be stable. A comparison between the predicted and experimental structures is shown in Table 15. There are two important points to note about the predicted structure: first, the lattice is tetragonal with the cell parameters agreeing well with the experimental tetragonal values, although the distortion is slightly overestimated; and second, the internal coordinates of the oxygen atoms are poorly reproduced in the relaxed structure (see Figure 13 which shows the tetragonal phase of strontium titanate [11]). In the experimental tetragonal phase small rotations of the TiO_6 octahedra are observed around one axis only, whereas in the simulated structure large rotations around all three axes are found. Note, the difference in energy between the unrelaxed cubic and relaxed structure is very small, illustrating the flexible nature of the perovskite structure.

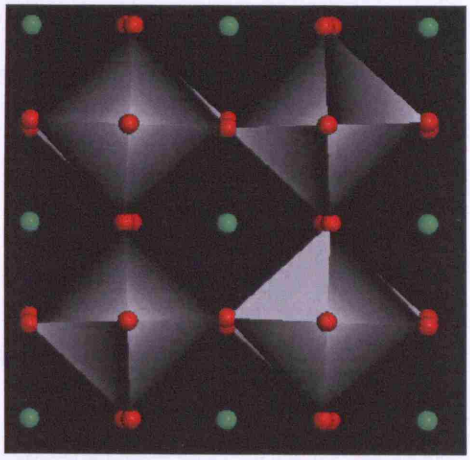

Figure 13 Low temperature experimental structure of strontium titanate highlighting the small rotations of the TiO_6 octahedra.

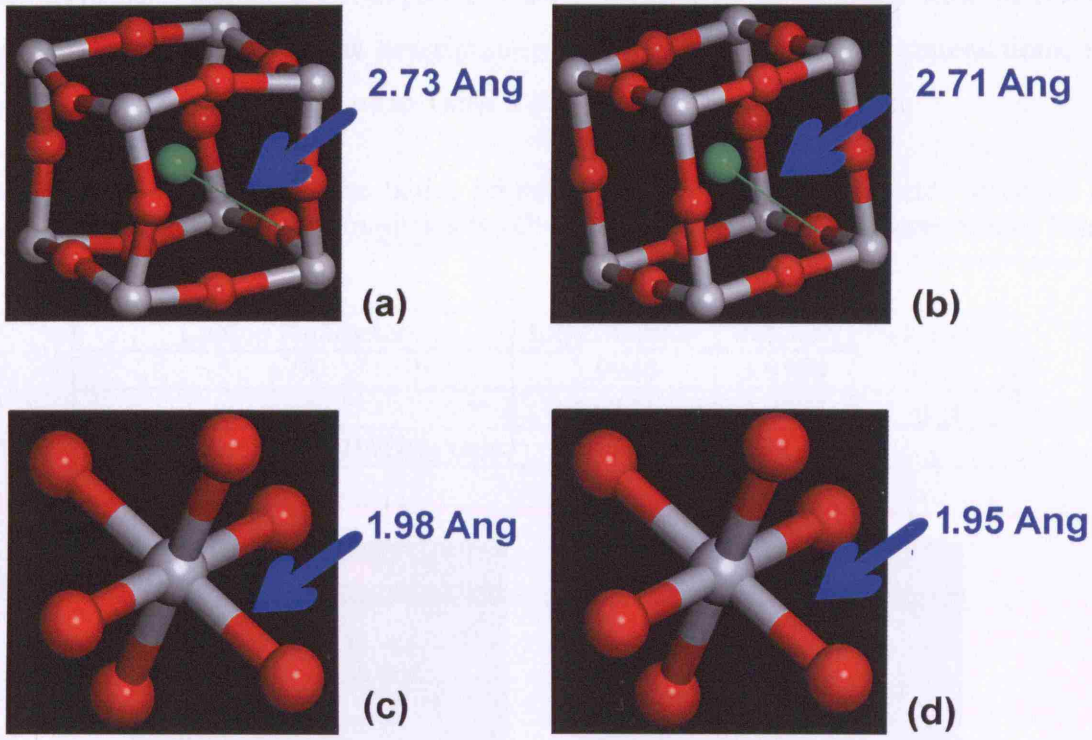

Figure 14 Comparison of the cationic sites of the perovskite structure where: (a) is the Sr^{2+} site of the modelled lattice; (b) is the Sr^{2+} site is the experimental tetragonal structure; (c) is the Ti^{4+} site of the modelled lattice; and (d) is the Ti^{4+} site of the experimental tetragonal lattice.

The local environment around the cation sites in the relaxed and experimental tetragonal structures are compared in Figure 14. The conformation around the Ti^{4+} site is essentially the same for the theoretical and experimental lattices with 6 oxygens arranged around the central cation is an octahedral coordination. For the Sr^{2+} site, the Sr-O distances are very similar, however there is a clear difference between the positioning of the oxygen atoms with respect to the Sr^{2+} cation.

5.1.3. Barium Titanate

At room temperature barium titanate has a tetragonal lattice (space group P4MM) where c/a = 1.01. The Ti^{4+} ions are displaced from the centre of the TiO_6 octahedral site to give one short Ti-O bond, one long Ti-O bond and 4 equal length Ti-O bonds around the equatorial region of the octahedra (see Figure 15). As can be seen from Figure 15 and Table 16, the energy minimised structure using atomistic modelling with the parameters given in Table 8 and Table 9, is cubic with no ferroelectric distortion. Although more recent parameter sets reproduce the ferroelectric distortion,

such as those of Sepliarsky et al [166], in order to maintain consistency with the rest of the work in this thesis in the description of the titanium and oxygen interactions, no modifications of the parameters in Table 8 and Table 9 were undertaken.

Table 16 Comparison of the lattice properties between the experimental structure of $BaTiO_3$ and its atomistically relaxed structure using the parameters in Table 8 and Table 9.

Lattice Parameter	Experimental	Relaxed	% Change
a /Å	3.9945	3.9594	-0.9
c /Å	4.0335	3.9593	-1.8
Latttice Energy per $BaTiO_3$ unit	-147.89	-148.05	-

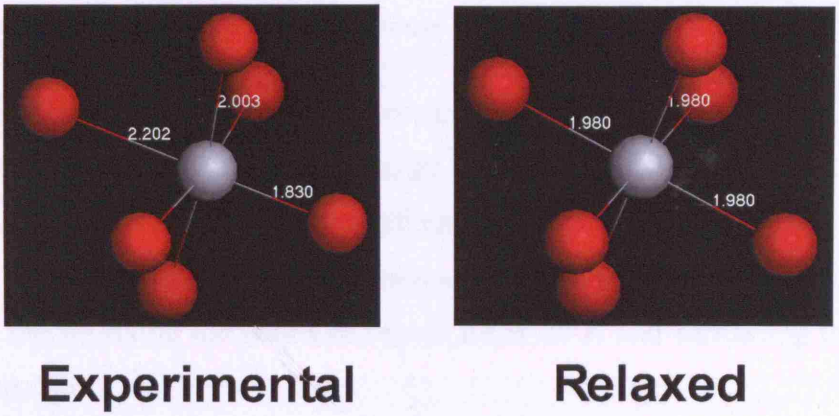

Figure 15 Comparison of the local conformation surrounding the Ti^{4+} site between the experimental and atomistically modelled (using the parameters given in Table 8 and Table 9) structures.

5.2. Atomistic Modelling of Isolated Divalent Nickel Defects in Alkaline Earth Titanates

In the next two sections, the substitution of divalent nickel into the alkaline earth titanate lattices is considered. The first section considers the subsitution of Ni^{2+} into the host to form isolated defects at both cationic sites.

When Ni^{2+} occupies the A site, the defect is charge neutral. However, when Ni^{2+} occupies the B site, the defect has a 2- charge and there is a need for charge compensation such an oxide ion vacancy or the reduction of two tetravalent titanium cations to Ti^{3+}. To maintain consistency with previous work [113], charge compensation is achieved via the formation of oxide ion vacancies. In this section the formation of the Ni^{2+} defect and the O^{2-} vacancy are considered separately, i.e. these defects are remote from each other. In Section 5.3, the effect of placing the oxygen

vacancy in the nearest neighbour and next nearest neighbour coordination shells around the Ni^{2+} defect is investigated.

Using the Kroger Vink notation, the dissolution of NiO into the alkaline earth titanates is as follows:

96] $$NiO + A_A^{\times} \rightarrow Ni_A^{\times} + AO,$$

97] $$NiO + Ti_{Ti}^{\times} + O_O^{\times} \rightarrow Ni_{Ti}^{/\!/} + V_O^{\bullet\bullet} + TiO_2,$$

where A=Ca, Sr, Ba.

5.2.1. Optimisation of Mott—Littleton Region Sizes

During calculations of defect lattices using the Mott Littleton approximation, it is necessary to ensure that the defect energy is converged with respect to the size of regions I and IIa. Nickel substituted strontium titanate was used to find the appropriate sizes of the regions to be used for all subsequent calculations. A series of calculations was carried out by fixing the radius of region IIa at 20 Å and increasing the radius of region I from 2 to 13 Å:

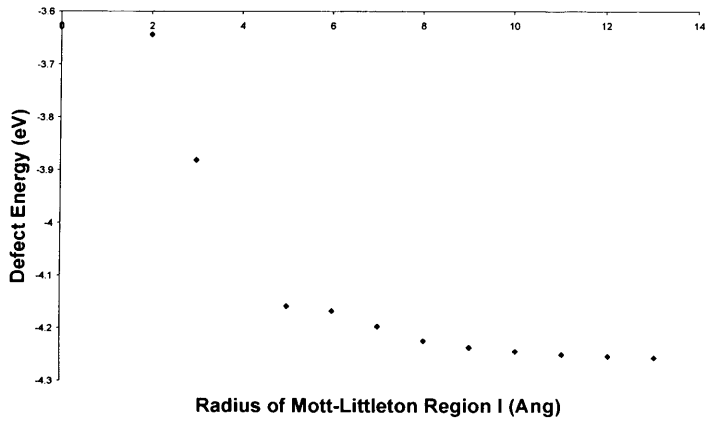

Figure 16 A plot of defect energy versus Mott-Littleton region I radius for substitution of a Ni^{2+} ion at the Sr^{2+} site.

The radius of region I was fixed at 13 Å and the radius of region II increased to 25 Å. Changing the size of region II had no effect on the calculated defect energy and so was fixed at 20 Å in all subsequent calculations. Figure 16 plots how the defect energy for substitution at the Sr^{2+} site varies with region I size from -3.64 to 4.26 eV between 2 to 13 Å. The plot shows that the defect energy is converged at a radius of 13

Å. These sizes for region I of 13 Å and region II of 20 Å radii were fixed for all subsequent calculations. The number of ions in region I was 1574 and in region II 4088.

5.2.2. $CaTiO_3$

Divalent nickel was substituted into the calcium titanate lattice at both the Ca^{2+} and Ti^{4+} sites. Table 17 and Figure 17 show a comparison between the pure and substituted lattices for the local conformation around the A site. There was no significant change in the local environment following relaxation around the defect. However, analysis of the distances to the atoms in the first (O^{2-}) and second (Ti^{4+}) coordination sphere reveals that:

- The four nearest oxygens, of the 12 fold coordination site, move around 0.15 Å closer to the nickel than they were to the calcium.
- The remaining 8 oxygens of the first coordination shell do not move significantly with respect to the A site cation.
- All of the titanium ions in the second coordination sphere move slightly closer to the A site cation follow substitution.

Table 17 Comparison of the conformation around the A site in $CaTiO_3$ between the pure and nickel substituted lattices.

Atom	Distance to Ca^{2+} (Unsubstituted Lattice) /Å	Distance to Ni^{2+} (Substituted Lattice) /Å	Change in Distance /Å
O	2.23	2.07	-0.16
O	2.24 (×2)	2.10 (×2)	-0.14
O	2.53	2.36	-0.17
O	2.69 (×2)	2.62 (×2)	-0.07
O	2.72 (×2)	2.74 (×2)	0.02
O	3.02	3.02	0.00
O	3.16	3.17	0.01
O	3.28 (×2)	3.33 (×2)	0.05
Ti	3.23 (×2)	3.20 (×2)	-0.03
Ti	3.27 (×2)	3.24 (×2)	-0.03
Ti	3.32 (×2)	3.28 (×2)	-0.04
Ti	3.42 (×2)	3.39 (×2)	-0.03

These observations can be readily explained in terms of the size mismatch between the Ca^{2+} (1.34 Å) and Ni^{2+} (0.69 Å) cations [104]. Clearly Ni^{2+} does not fill

the cavity normally occupied by the Ca^{2+} cation and will either move off centre from the A site position or attract nearest neighbour anions towards itself. In these calculations, the nickel has attracted the four nearest oxide ions most strongly reducing the A-O distance by around 7%. There has also been a general contraction of the lattice around the substitution site as evidenced by the Ni-Ti distances.

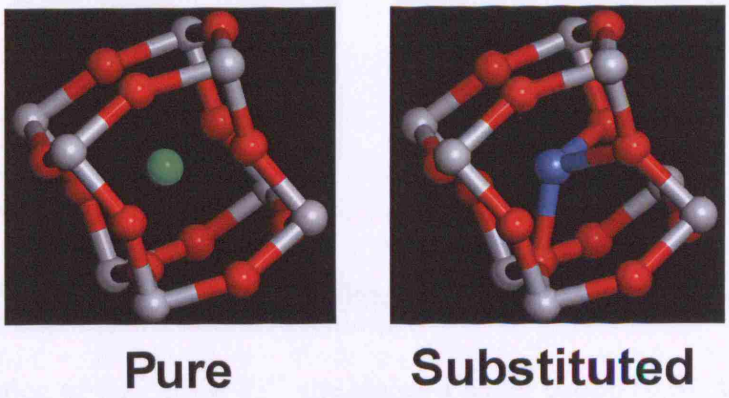

Figure 17 Comparison of the conformation around the A site in $CaTiO_3$ between the pure and nickel substituted lattices.

Substitution of Ni^{2+} at the Ti^{4+} site increases the distance of the oxide ions in the first coordination sphere, but decreases the distance to the calcium cations in the second coordination sphere:

Table 18 Comparison of the conformation around the B site in $CaTiO_3$ between the pure and nickel substituted lattices.

Atom	Distance to Ti^{4+} (Unsubstituted Lattice) /Å	Distance to Ni^{2+} (Substituted Lattice) /Å	Change in Distance /Å
O	1.97 (×2)	2.03 (×2)	0.06
O	1.98 (×2)	2.01 (×2)	0.03
O	1.98 (×2)	2.03 (×2)	0.05
Ca	3.23 (×2)	3.04 (×2)	-0.19
Ca	3.27 (×2)	3.16 (×2)	-0.11
Ca	3.32 (×2)	3.19 (×2)	-0.13
Ca	3.42 (×2)	3.25 (×2)	-0.17

As for the A site substitution there is little change in the overall conformation around the defect site:

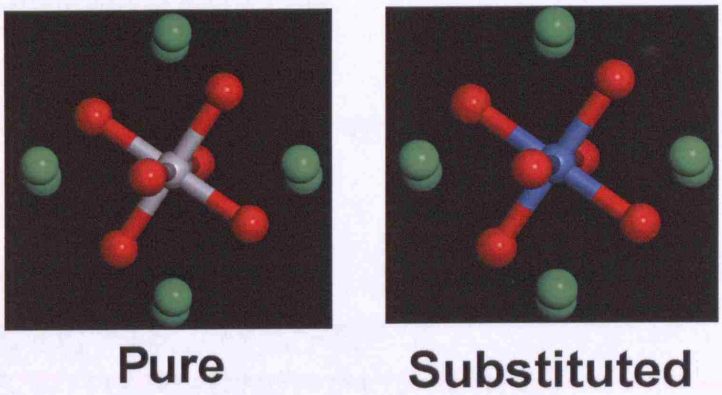

Figure 18 Comparison of the conformation around the B site in $CaTiO_3$ between the pure and nickel substituted lattices.

Substitution of Ni^{2+} at the Ti^{4+} site places a larger cation (0.69 Å) in the position of a smaller cation (0.61 Å), although the size mismatch is considerably smaller than between Ca^{2+} and Ni^{2+}. The slightly larger size of the dopant cation explains the small increase, of around 2%, in the length of the B-O bond distances. However, it may be expected that the Ni-Ca distances would also be slightly longer than the Ti-Ca distances. The decrease in the B-Ca distance observed is due to the effective negative charge of the defect attracting the Ca^{2+} cations.

Table 19 Calculated defect and lattice energies for the substitution of Ni^{2+} into $CaTiO_3$.

Description	Energy (eV)
Defect Energy: $Ni_{Ca}^{\times}$	-3.31
Defect Energy: $Ni_{Ti}^{//}$	54.15
Defect Energy: $V_O^{\bullet\bullet}$	19.05
Lattice Energy: CaO	-37.66
Lattice Energy: TiO_2	-112.34
Lattice Energy: NiO	-41.85

The Ni^{2+} solution energies for the processes described by Equations 96 and 97 can be calculated from the values given in Table 19:

1. Substitution at the "A" site.

$$E_S = E_L^{CaO} + E_{def}^{Ni/Ca} - E_L^{NiO}$$

$$E_S = (-37.66) + (-3.31) - (-41.85)$$

$$E_S = 0.88eV$$

2. Substitution at the "B" site.

$$E_S = E_L^{TiO_2} + E_{VAC}^{O} + E_{SUB}^{Ni/Ti} - E_L^{NiO}$$

$$E_S = (-112.34) + (19.05) + (54.15) - (-41.85)$$

$$E_S = 2.71eV$$

Despite the larger mismatch between the Ni^{2+} and Ca^{2+} ions, substitution of divalent into the $CaTiO_3$ lattice shows a clear preference for the A site suggesting that the charge mismatch between Ni^{2+} and Ti^{4+} for substitution at the B site may play a significant role in its instability.

5.2.3. $SrTiO_3$

The changes in the local structure resulting from the substitution of divalent nickel into the cationic sites of $SrTiO_3$ are illustrated in Figure 19 and Figure 20, with the distances to the first and second coordination sphere ions given in Table 20 and Table 21 for the Sr^{2+} and Ti^{4+} sites respectively. Since nickel doped strontium titanate is the most active of the three nickel doped alkaline earth titanates for the partial oxidation of methane [82, 83], the behaviour of this material is of particular interest. A direct comparison with both previous simulations [113] and experimental EXAFS analysis [83] is possible for this system.

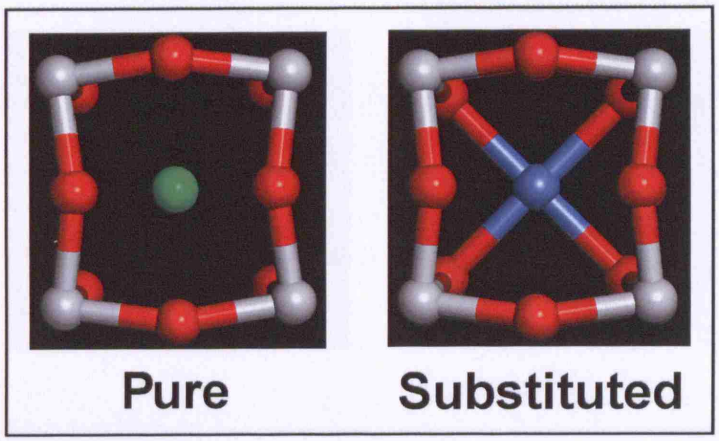

Figure 19 Comparison of the local conformation around the "A" site in pure and Ni^{2+} substituted $SrTiO_3$.

Figure 19 and Table 20 compare the local conformations around the A site between pure and nickel substituted $SrTiO_3$. Replacing the Sr^{2+} cation, of ionic radius 1.44 Å, with the much smaller Ni^{2+} cation, of ionic radius 0.69 Å, causes the 4 oxygens nearest to the A site to move by over 0.2 Å to form bonds with the dopant cation in a square planar arrangement. There is little perturbation of the remaining ions in the first and second coordination spheres. However, the effect of placing the smaller cation at the A site can be seen from the movement of the Ti^{4+} ions towards the A site.

Table 20 Comparison of the local conformation around the "A" site in pure and Ni^{2+} substituted $SrTiO_3$.

Atom	Distance to Sr^{2+} (Unsubstituted lattice) /Å	Distance to Ni^{2+} (Substituted lattice) /Å	Change /Å
O	2.37 (×4)	2.15 (×4)	-0.22
O	2.81 (×4)	2.82 (×4)	0.01
O	3.12 (×4)	3.13 (×4)	0.01
Ti	3.36 (×8)	3.30 (×8)	-0.06

At the B site, see Figure 20 and Table 21, the perturbation of the lattice around the defect is very small. The O atoms in the first coordination sphere move away from the "B" site by 0.05 Å as the Ni^{2+} ion is slight larger than the Ti^{4+} ion. The movement of ions is more marked in the second coordination sphere as two of the Sr^{2+} cations move towards the defect by nearly 0.4 Å, and the remaining four by just over 0.2 Å which is caused by the attraction of the cations to the negatively charged defect region.

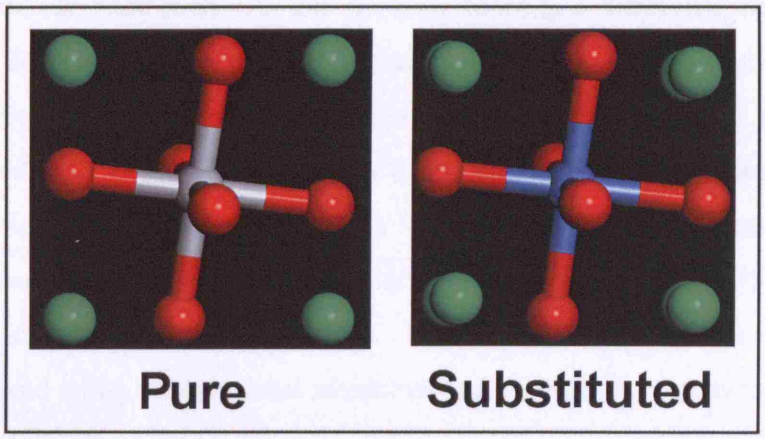

Figure 20 Comparison of the local conformation around the "B" site in pure and Ni^{2+} substituted $SrTiO_3$.

Table 21 Comparison of the local conformation around the "B" site in pure and Ni^{2+} substituted $SrTiO_3$.

Atom	Distance to Ti^{4+} (Unsubstituted lattice) /Å	Distance to Ni^{2+} (Substituted lattice) /Å	Change /Å
O	1.98 (×6)	2.03 (×6)	0.05
Sr	3.36 (×2)	2.98 (×4)	-0.38
Sr	3.36 (×6)	3.15 (×6)	-0.21

The lattice and defect energies calculated for the Ni^{2+} substituted $SrTiO_3$ lattice have been calculated as in Table 22:

Table 22 Comparison between this work and Akhtar et al for lattice and defect energies used in the calculation of solution energies for doping Ni^{2+} at the Sr^{2+} and Ti^{4+} sites in $SrTiO_3$.

System	Energy (eV)	
	This Work (Tetragonal Structure)	Akthar et al (Cubic Structure)
Lattice Energy NiO	-41.85	-41.58
Lattice Energy SrO	-36.33	-35.61
Lattice Energy TiO_2	-112.34	-111.10
Defect Energy Ni^{2+} in 'A' site	-4.26	-3.16
Defect Energy Ni^{2+} in 'B' site	54.62	55.01
Defect Energy O^{2-} vacancy	18.89	18.16

Table 22 also lists the results of simulations by Akthar et al [113] which can be directly compared to the calculations carried out for this thesis since the same atomistic

parameters were used for each. As can be seen, there is a difference between the two sets of results, for which two explanations can be suggested. Firstly, lattice energies for the oxides were based on experimental "unrelaxed" structures in the previous work, whereas relaxed structures have been used throughout this study to provide increased consistency. Secondly, defect calculations were based on a cubic structure, not the tetragonal phase, which seems to have a particularly pronounced effect on the defect energy for substitution into the Sr^{2+} A site. Note, the values obtained by Akhtar et al can be reproduced using experimental structures and a cubic perovskite lattice.

Using the figures from Table 22, the solution energies for substitution at the Sr^{2+} and Ti^{4+} sites are shown in Table 23:

Table 23 Comparison of solution energies for doping Ni^{2+} into strontium titanate between this work and Akhtar et al [113].

	Solution Energy (eV)	
Doping	This Work	Akhtar et al
Ni^{2+} in Sr^{2+} site	1.26	2.81
Ni^{2+} in Ti^{4+} site with O vacancy compensation	3.02	3.65

Once again the difference between the results is clear, which is assigned to the different structure modelled. Nevertheless, both sets of results clearly predict that Ni^{2+} has a lower energy at the Sr^{2+} site compared to the Ti^{4+} site with a solution energy difference of 1.76 eV in this work and 0.84 eV for Akhtar et al.

5.2.4. $BaTiO_3$

As for the other alkaline earth titanates the relaxation and energetics for the subsitution of Ni^{2+} at both cationic sites of $BaTiO_3$ were simulated using atomistic modelling. The effect of substitution at the A site is shown in Figure 21 and Table 24.

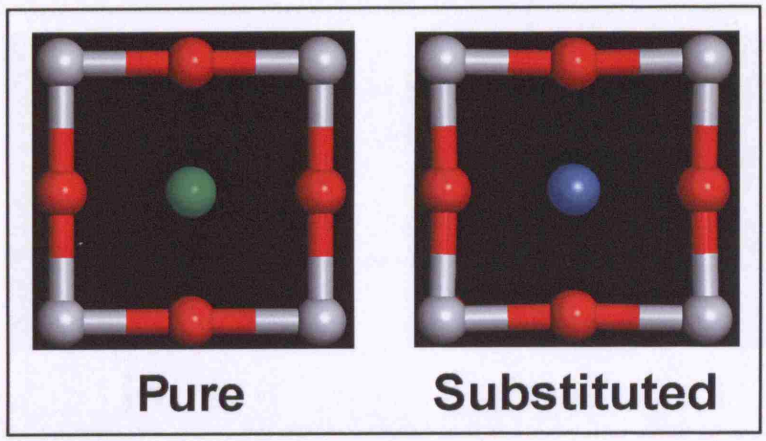

Figure 21 Comparison of local conformation around the "A" site of $BaTiO_3$ in the pure and Ni^{2+} substituted lattices.

The atomistically relaxed lattice of $BaTiO_3$ effectively has cubic symmetry and the relaxation around the nickel defect at both cation sites reflect the high symmetry of the system. At the A site, the difference in the ionic size of the Ba^{2+} (1.61 Å) and Ni^{2+} (0.69 Å) plays the dominant role in determining the behaviour of the calculated relaxation, as for the other alkaline earth titanates. All of the oxygen and titanium ions in the first and second coordination spheres increase their distance from the B site. However, in constrast to the other systems considered, none of the oxygens move close enough to the Ni^{2+} defect to form a "bond". Instead, 8 of the oxygens move to 2.68 Å from the nickel and the remaining 4 to 2.73 Å, with the overall conformation remaining highly symmetrical.

Table 24 Comparison of local conformation around the A site of $BaTiO_3$ in the pure and Ni^{2+} substituted lattices.

Atom	Distance to Ba^{2+} (Unsubsituted Lattice) /Å	Distance to Ni^{2+} (Substituted Lattice)	Change /Å
O	2.80 (×8)	2.68 (×8)	-0.12
O	2.80 (×4)	2.73 (×4)	-0.07
Ti	3.43 (×8)	3.37 (×8)	-0.06

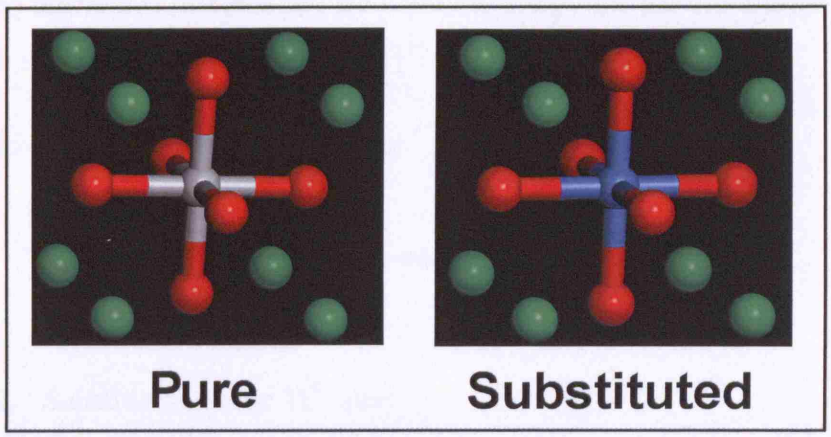

Figure 22 Comparison of local conformation around the "B" site of $BaTiO_3$ in the pure and Ni^{2+} substituted lattices.

The effect of substitution at the B site is shown in Figure 22 and Table 25. In line with the other alkaline earth titanates, substitution at the Ti^{4+} site leads to a very small perturbation of the system, with no change in the symmetry and a small increase in the B-O distance compared to the pure lattice. The B-Ca distances decrease due to the negative charge on the substitution site.

Table 25 Comparison of local conformation around the "B" site of $BaTiO_3$ in the pure and Ni^{2+} substituted lattices.

Atom	Distance to Ti^{4+} (Unsubsituted Lattice) /Å	Distance to Ni^{2+} (Substituted Lattice)	Change /Å
O	1.98 (×6)	2.05 (×6)	0.07
Ba	3.42 (×8)	3.28 (×8)	-0.14

Table 26 Calculated defect and lattice energies for the substitution of Ni^{2+} into $BaTiO_3$.

Description	Energy (eV)
Defect Energy: $Ni_{Ba}^{\times}$	-4.24
Defect Energy: $Ni_{Ti}^{//}$	55.24
Defect Energy: $V_O^{\bullet\bullet}$	18.70
Lattice Energy: BaO	-34.57
Lattice Energy: TiO_2	-112.34
Lattice Energy: NiO	-41.85

Using the values in Table 26, the solution energy for the dissolution of NiO into $BaTiO_3$ with substitution at the Ba^{2+} and Ti^{4+} sites are:

1. Substitution at the Ba^{2+} site:

$$E_s = E_L^{BaO} + E_{SUB}^{Ni^{2+}/Ba^{2+}} - E_L^{NiO}$$
$$E_S = (-34.57) + (-4.24) - (-41.85)$$
$$E_S = 3.04eV$$

2. Substitution at the Ti^{4+} site:

$$E_S = E_L^{TiO_2} + E_{VAC}^{O} + E_{SUB}^{Ni^{2+}/Ti^{4+}} - E_L^{NiO}$$
$$E_S = (-112.34) + 18.70 + 55.24 - (-41.85)$$
$$E_S = 3.45eV$$

Substitution at the A site is predicted to be energetically favourable compared to substitution at the B site.

5.3. Atomistic Modelling of Clustered Defect in Alkaline Earth Titanates

Since it is necessary to introduce oxygen vacancies when substituting Ni^{2+} at the Ti^{4+} sites, we considered clusters with the vacancy in the first and second coordination sphere of oxide anions around the dopant site. The cationic and anionic defects were introduced into the lattice simultaneously and the centre of the Mott Littleton regions was positioned at the mid point of the defect coordinates. The effect of clustering the defects in the three alkaline earth titanates is also considered in this section.

5.3.1. $CaTiO_3$

Figure 23 illustrates the structure of the complex in which the oxygen vacancy is in the first coordination shell, or nearest neighbour position. The most obvious effect is that the coordination number around the B site has dropped from 6 to 5. The nickel ion is displaced from the position of the Ti^{4+} ions in the perfect lattice by 0.17 Å, away from the oxygen vacancy.

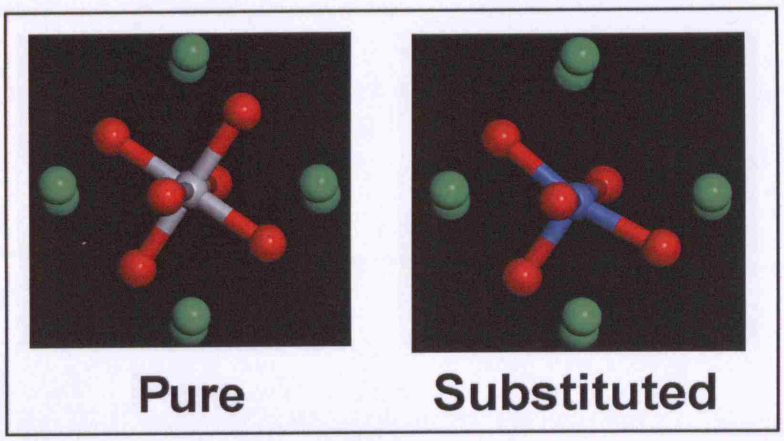

Figure 23 Comparison of the local conformation around the B site of pure and Ni^{2+} substituted with a nearest neighbour oxygen vacancy $CaTiO_3$ lattices.

The bond lengths of both Ti^{4+} and the substituted Ni^{2+} to the surrounding O and Ca atoms are given in Table 27:

Table 27 Comparison of the local conformation around the B site of perfect and Ni^{2+} substituted with a nearest neighbour oxygen vacancy $CaTiO_3$ lattices.

Atom	Distance to Ti^{4+} (Unsubstituted Lattice) /Å	Distance to Ni^{2+} (Substituted Lattice) /Å	Change in Distance /Å
O	1.97	1.90	-0.07
O	1.98 (×4)	2.00	0.02
Ca	3.23	3.28	0.05
Ca	3.23	3.04	-0.17
Ca	3.27	3.35	0.08
Ca	3.27	3.09	-0.18
Ca	3.32	3.17	-0.15
Ca	3.32	3.30	-0.02
Ca	3.42	3.24	-0.18
Ca	3.42	3.59	0.17

The movement of the Ni^{2+} towards the oxygen opposite to the vacancy is clear, with the remaining oxygens being only slightly further away from the B site of the undoped system. Some of the B-Ca distances have increased, whereas some have decreased, which is largely due to the displacement of the Ni^{2+} cation from the B site position. Unlike in the case of the isolated defect, there is no negative charge on the defect region attracting the Ca^{2+} cations.

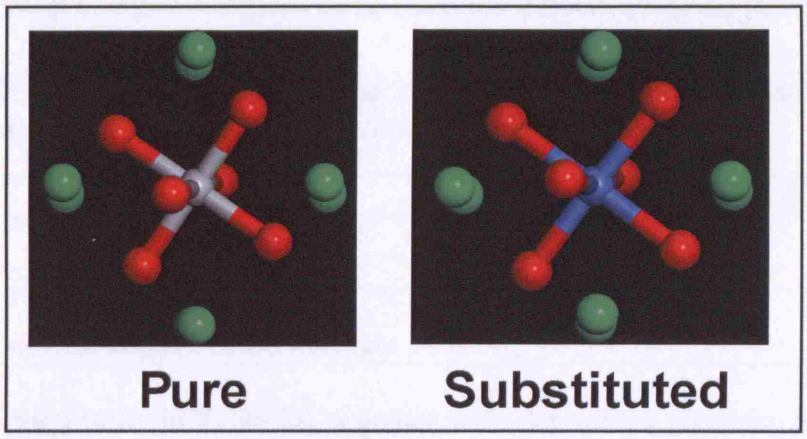

Figure 24 Comparison of the local conformation around the "B" site of pure and Ni^{2+} substituted with a next nearest neighbour oxygen vacancy $CaTiO_3$ lattices.

Placing the oxygen vacancy in the next nearest neighbour position maintains the 6 fold coordination around the B site. The relaxation around the defect shows the same trends as the isolated defect with the nickel staying on the B site, the B-O distances increasing and the B-Ca distances decreasing, see Table 28. However the size of the relaxation around the defect is much larger with the B-O distance increasing by up to 6.6%, c.f. 2.5% for the isolated defect, and the B-Ca distances decreasing by up to 8.1%, c.f. 4.8% for the isolated case. The lattice is likely to be more flexible with a vacancy present leading to the larger calculated relaxations.

Table 28 Comparison of the local conformation around the B site of perfect and Ni^{2+} substituted $CaTiO_3$ with a next nearest neighbour oxygen vacancy.

Atom	Distance to Ti^{4+} (Unsubstituted Lattice) /Å	Distance to Ni^{2+} (Substituted Lattice) /Å	Change in Distance /Å
O	1.98 (×3)	2.11 (×3)	0.13
O	1.98 (×2)	2.09 (×2)	0.11
O	1.98	2.07	0.09
Ca	3.23 (×2)	3.00 (×2)	-0.23
Ca	3.27 (×2)	3.15 (×2)	-0.12
Ca	3.32	3.05	-0.27
Ca	3.32	3.21	-0.11
Ca	3.42 (×2)	3.22 (×2)	-0.20

The defect energies found for these clustered defects are given in Table 29:

Table 29 Defect energies and binding energies with respect to isolated defects calculated for the clustered defects systems in $CaTiO_3$.

System	Energy /eV	Binding Energy /eV
Ni^{2+} substituted at the Ti^{4+} site nearest neighbour O^{2-} vacancy	72.94	-0.26
Ni^{2+} substituted at the Ti^{4+} site next nearest neighbour O^{2-} vacancy	73.58	0.38

From the results in Table 29, together with the values given in Table 19, it is possible to calculate solution energies for the systems with clustered defects:

1. Nearest Neighbour Vacancy:

$$E_S = E_L^{TiO_2} + E_{SUB/VAC}^{(Ni^{2+}Ti^{4+})/O^{2-}} - E_L^{NiO}$$
$$E_S = (-112.34) + 72.94 - (-41.85)$$
$$E_S = 2.45eV$$

2. Next Nearest Neighbour Vacancy:

$$E_S = E_L^{TiO_2} + E_{SUB/VAC}^{(Ni^{2+}Ti^{4+})/O^{2-}} - E_L^{NiO}$$
$$E_S = (-112.34) + 73.58 - (-41.85)$$
$$E_S = 3.09eV$$

Clustering of the defects reduces the energy cost of dissolving NiO into $CaTiO_3$ by 0.26 eV if the oxygen vacancy is placed in the first coordination sphere compared with isolated defects. However, if the vacancy is placed in the second oxygen coordination sphere the solution energy increases by 0.38 eV as compared to the isolated defects. The lowest solution energy predicted for substitution at the B site remains higher than the solution energy for the A site substitution.

5.3.2. $SrTiO_3$

Substitution of Ni^{2+} at the B site of $SrTiO_3$ with a nearest neighbour oxygen vacancy is illustrated in Figure 25 and the distances to the first coordination spheres of O^{2-} and Sr^{2+} ions are given in Table 30. The relaxation of the lattice around the defect site is similar to that shown for substitution into $CaTiO_3$, i.e.:

- The nickel ion is displaced by 0.13 Å from the position of the "B" site in the pure lattice.

- The Ni-O distances are shorter than the Ti-O distances, with the bond opposite the vacancy being 4.5% shorter.

- Some of the Ni-Sr are longer than the Ti-Sr distances and some of them are shorter due to the displacement of the Ni^{2+} cation.

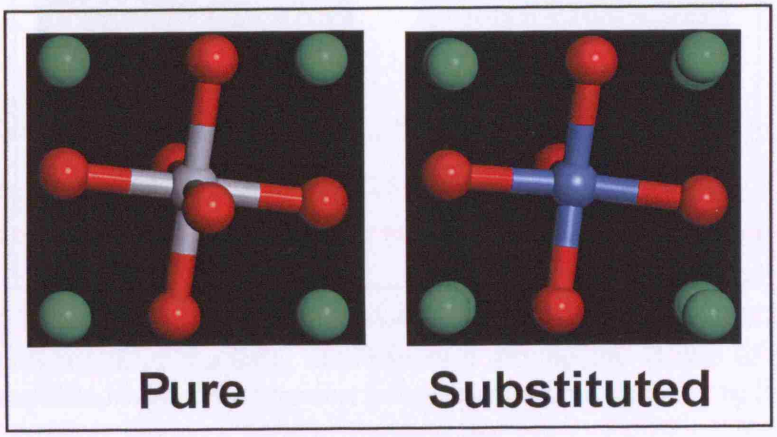

Figure 25 Comparison of the local conformation around the B site of pure and Ni^{2+} substituted with a nearest neighbour oxygen vacancy in $SrTiO_3$.

Table 30 Comparison of the local conformation around the "B" site of pure and Ni^{2+} substituted with a nearest neighbour oxygen vacancy in $SrTiO_3$.

Atom	Distance to Ti^{4+} (Unsubstituted lattice) /Å	Distance to Ni^{2+} (Substituted lattice) /Å	Difference /Å
O	1.98 (×4)	1.96 (×4)	-0.02
O	1.98	1.89	-0.09
Sr	3.36	3.13	-0.23
Sr	3.36	3.18	-0.18
Sr	3.36	3.20	-0.16
Sr	3.36	3.21	-0.15
Sr	3.36	3.29	-0.07
Sr	3.36	3.37	0.01
Sr	3.36	3.43	0.07
Sr	3.36	3.50	0.14

The effect of placing the vacancy in the second coordination sphere is shown Figure 26 and Table 31:

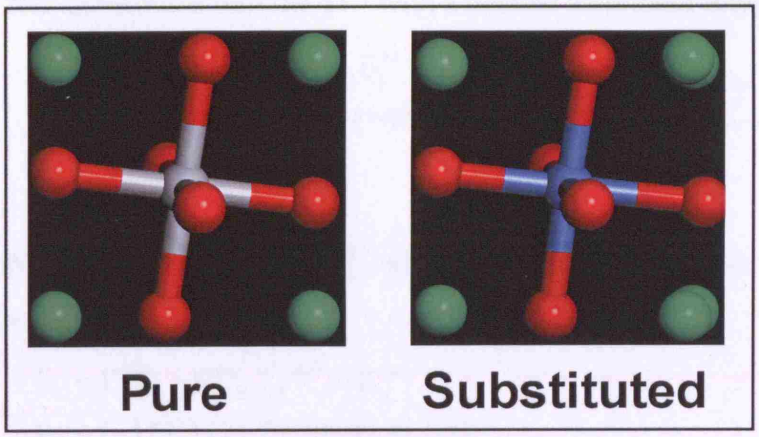

Figure 26 Comparison of the local conformation around the B site of pure and Ni^{2+} substituted with a next nearest neighbour oxygen vacancy in $SrTiO_3$.

Table 31 Comparison of the local conformation around the B site of pure and Ni^{2+} substituted with a next nearest neighbour oxygen vacancy in $SrTiO_3$.

Atom	Distance to Ti^{4+} (Unsubstituted lattice) /Å	Distance to Ni^{2+} (Substituted lattice) /Å	Difference /Å
O	1.98 (×4)	1.99 (×4)	0.01
O	1.98	2.02	0.04
O	1.98	2.06	0.08
Sr	3.36	2.97	-0.39
Sr	3.36 (×2)	3.25 (×2)	-0.11
Sr	3.36 (×5)	3.29 (×5)	-0.07

No displacement of the Ni^{2+} from the B site position in pure $SrTiO_3$ is predicted in this case, and the displacement of the ions in the O^{2-} and Sr^{2+} coordination spheres is very similar to that predicted for the isolated defects shown above.

The defect energy calculated for the substitution of Ni^{2+} at the Ti^{4+} site with oxygen vacancies in the first and second coordination spheres is given in Table 32:

Table 32 Defect and binding energies calculated for the clustered defects systems in $SrTiO_3$.

System	Energy /eV	Binding Energy /eV
Ni^{2+} substituted at the Ti^{4+} site nearest neighbour O^{2-} vacancy	72.61	-0.90
Ni^{2+} substituted at the Ti^{4+} site next nearest neighbour O^{2-} vacancy	73.20	-0.31

From the results in Table 32 and Table 19, the solution energies for the dissolution of NiO into $SrTiO_3$ with the formation of the clustered defects are:

1. Ni^{2+} substituted into the Ti^{4+} with a nearest neighbour oxygen vacancy:

$$E_S = E_L^{TiO_2} + E_{SUB/VAC}^{(Ni^{2+}Ti^{4+})/O^{2-}} - E_L^{NiO}$$
$$E_S = (-112.34) + 72.61 - (-41.85)$$
$$E_S = 2.12eV$$

2. Ni^{2+} substituted into the Ti^{4+} with a next nearest neighbour oxygen vacancy:

$$E_S = E_L^{TiO_2} + E_{SUB/VAC}^{(Ni^{2+}Ti^{4+})/O^{2-}} - E_L^{NiO}$$
$$E_S = (-112.34) + 73.20 - (-41.85)$$
$$E_S = 2.71eV$$

As for the $CaTiO_3$ system, the most favourable configuration is to place the oxygen vacancy in the nearest neighbour position. However, unlike the $CaTiO_3$ case locating the vacancy near to the Ni^{2+} dopant reduces the energy compared to the isolated defect situation for both the nearest neighbour (-0.9 eV) and the next nearest neighbour (-0.31 eV) situations.

5.3.3. $BaTiO_3$

Figure 27 and Table 33 illustrate the conformational changes around the substitution of Ni^{2+} into the Ti^{4+} site of $BaTiO_3$ with a nearest neighbour oxygen vacancy.

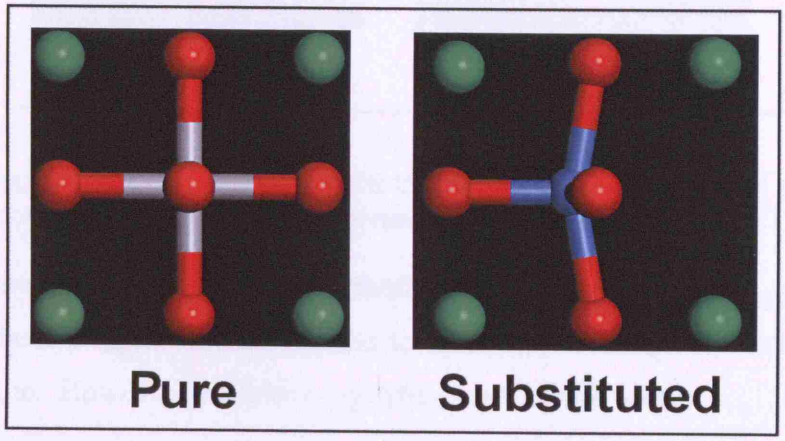

Figure 27 Comparison of the local conformation around the B site of pure and Ni^{2+} substituted with a nearest neighbour oxygen vacancy in $BaTiO_3$.

As can be seen, the lattice remains highly symmetrical around the defect cluster. The Ni^{2+} cation is displaced away from the vacancy by 0.24 Å from the B site position of the pure lattice. The oxygen opposite to the vacancy is pushed slightly away from the perfect lattice position giving a short Ni-O distance of around 1.90 Å. The remaining Ni-O distances are slightly longer than those for the pure lattice, primarily due to the displacement of the defect cation. Four of the Ni-Ba distances are longer than the Ti-Ba distances, and four are shorter, which again, is primarily due to the displacement of the Ni^{2+} cation.

Table 33 Comparison of the local conformation around the B site of pure and Ni^{2+} substituted with a nearest neighbour oxygen vacancy $BaTiO_3$ lattices.

Atom	Distance to Ti^{4+} (Unsubsituted Lattice) /Å	Distance to Ni^{2+} (Substituted Lattice)	Change /Å
O	1.98	1.90	-0.08
O	1.98 (×4)	2.01	0.03
Ba	3.42 (×4)	3.24 (×4)	-0.18
Ba	3.42 (×4)	3.52 (×4)	0.10

The effect of placing the vacancy in the next nearest neighbour shell is shown in Figure 28 and Table 34.

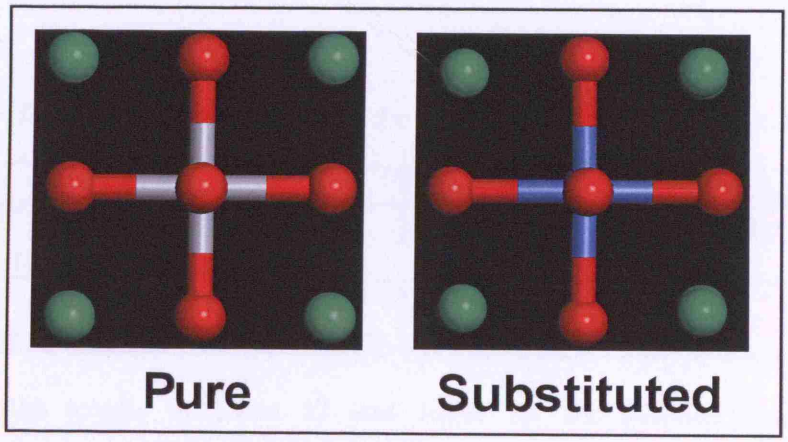

Figure 28 Comparison of the local conformation around the B site of pure and Ni^{2+} substituted with a next nearest neighbour oxygen vacancy $BaTiO_3$ lattices.

The changes in the local conformation with the oxygen vacancy in the next nearest neighbour oxygen shell are similar to those for the isolated substitution of Ni^{2+} into the Ti^{4+} site. However, the following differences can be noted:

- Not all of the oxygens in the first coordination sphere are equidistant from the Ni^{2+} dopant, with those nearer the vacancy being slightly closer than those further away.

- The Ni-O distances are around 3.5 % longer than for an isolated Ni^{2+} substitution site.

- There are three sets of Ni-Ba distances, with those nearest the vacancy shorter than those farthest from the vacancy, although the magnitude of the reduction is similar to the isolated defect (-0.14 Å).

Table 34 Comparison of the local conformation around the B site of pure and Ni^{2+} substituted with a next nearest neighbour oxygen vacancy $BaTiO_3$ lattices.

Atom	Distance to Ti^{4+} (Unsubsituted Lattice) /Å	Distance to Ni^{2+} (Substituted Lattice)	Change /Å
O	1.98 (×3)	2.11 (×3)	0.13
O	1.98 (×3)	2.13 (×3)	0.15
Ba	3.42 (×2)	3.24 (×2)	-0.18
Ba	3.42 (×2)	3.29 (×2)	-0.13
Ba	3.42 (×4)	3.33 (×4)	-0.09

The defect and binding energies calculated for the $BaTiO_3$ system are given in Table 35:

Table 35 Defect energies calculated for the clustered defects systems in $BaTiO_3$.

System	Energy /eV	Binding Energy /eV
Ni^{2+} substituted at the Ti^{4+} site nearest neighbour O^{2-} vacancy	73.01	-0.93
Ni^{2+} substituted at the Ti^{4+} site next nearest neighbour O^{2-} vacancy	73.34	-0.6

From the results in Table 32 and Table 19, the solution energies for the dissolution of NiO into $SrTiO_3$ with the formation of the clustered defects are:

1. Ni^{2+} substituted into the Ti^{4+} with a nearest neighbour oxygen vacancy:

$$E_S = E_L^{TiO_2} + E_{SUB/VAC}^{(Ni^{2+}Ti^{4+})/O^{2-}} - E_L^{NiO}$$
$$E_S = (-112.34) + 73.01 - (-41.85)$$
$$E_S = 2.52eV$$

2. Ni^{2+} substituted into the Ti^{4+} with a next nearest neighbour oxygen vacancy:

$$E_S = E_L^{TiO_2} + E_{SUB/VAC}^{(Ni^{2+}Ti^{4+})/O^{2-}} - E_L^{NiO}$$
$$E_S = (-112.34) + 73.34 - (-41.85)$$
$$E_S = 2.85eV$$

As for the $SrTiO_3$ system, both of the considered clustered defect lattices are predicted to have a lower solution energy than that for isolated defects with the nearest neighbour vacancy lowering the energy by -0.93 eV and the next nearest neighbour vacancy lowering the energy by -0.6 eV.

5.4. Atomistic Modelling of Ni(III) Doped Strontium Titanate

Potential parameters for Ni^{3+} are unavailable and so it was necessary to develop them for this project. The lack of parameters is due to the very limited number of compounds that contain nickel (III) and, in particular, the fact that this cation does not form stable binary compounds such as NiF_3 or Ni_2O_3.

Two independent sets of interatomic potential parameters for trivalent nickel were derived: first, the new parameters were based on the existing divalent nickel interatomic potentials; and second, the new parameters were formed by reference to the values for the other first row transition metal trivalent cations.

The starting point in deriving these parameters was to make use of those for Ni^{2+} and to scale the Buckingham A value according to the Huggins-Meyer relationship [106] which uses the difference in Shannon ionic radii [104], in this case, between divalent and trivalent nickel:

98] $$A_{Ni^{3+}} = A_{Ni^{2+}} \exp\left(\frac{r_{Shannon}^{Ni^{2+}} - r_{Shannon}^{Ni^{3+}}}{\rho}\right),$$

where it is assumed that the "hardness" (=0.2882 Å) of Ni^{2+} and Ni^{3+} are identical.

Table 36 Buckingham potential parameters for Ni^{2+} and Ni^{3+}. Ni^{2+} values were taken from Lewis and Catlow, [106], Ni^{3+} values were obtained by scaling using Equation 98.

Cation	Ionic Radii (Å) [104]	A (eV)	ρ (Å)
Ni^{2+}	0.690	1582.5	0.2882
Ni^{3+}	0.56	1008.0	0.2882

Using these parameters, the energy of replacing both of the lattice cations with Ni^{3+} (the defect energy) in strontium titanate was calculated using the Mott-Littleton method, see Section 3.1.5:

Table 37 Energy to substitute Ni^{3+} at the Sr^{2+} and Ti^{4+} sites of $SrTiO_3$.

System	Energy (eV)
Defect Energy for Ni^{3+} in Sr^{2+} site	-42.22
Defect Energy for Ni^{3+} in Ti^{4+} site	16.47

In order to compare the energy of introducing these defects into the lattice, the defect energy by itself is insufficient. The lattice from which the defect cation originates and the destination lattice of the displaced cation must also be considered. Throughout the work in this thesis it is assumed that the source of the defect ion and destination of the displaced cations are oxides. Chemical equations, using the Kroger Vink notation, can be set up to describe the dissolution of the dopant ions oxide and the evolution of the displaced ion oxide. The energy of the dissolution process is known as the solution energy.

To substitute Ni^{3+} into the lattice, two processes were considered. First, the direct substitution of Ni^{3+}, from Ni_2O_3, into the lattice with the evolution of either SrO or TiO_2, depending on the substitution site, or second, the substitution of Ni^{2+}, from NiO, followed by oxidation using atmospheric oxygen together with the evolution of the appropriate oxide. These processes are described by:

1. Dissolution of Ni_2O_3 into the host lattice

99] $$\frac{1}{2}Ni_2O_3+\frac{3}{2}Sr_{Sr}^{\times} \rightarrow Ni_{Sr}^{\bullet}+\frac{3}{2}SrO+\frac{1}{2}V_{Sr}^{//},$$

100] $$\frac{1}{2}Ni_2O_3+Sr_{Sr}^{\times}+\frac{1}{4}Ti_{Ti}^{\times}\rightarrow Ni_{Sr}^{\bullet}+\frac{3}{4}SrO+\frac{1}{4}SrTiO_3+\frac{1}{4}V_{Ti}^{////},$$

101] $$\frac{1}{2}Ni_2O_3+Ti_{Ti}^{\times}+\frac{1}{2}O_O^{\times}\rightarrow Ni_{Ti}^{/}+TiO_2+\frac{1}{2}V_O^{\bullet\bullet},$$

2. Dissolution of NiO into the host lattice, followed by oxidation

102] $$NiO+\frac{3}{2}Sr_{Sr}^{\times}+\frac{1}{4}O_{2(g)}\rightarrow Ni_{Sr}^{\bullet}+\frac{3}{2}SrO+\frac{1}{2}V_{Sr}^{//},$$

103] $$NiO+Sr_{Sr}^{\times}+\frac{1}{4}Ti_{Ti}^{\times}+\frac{1}{4}O_{2(g)}\rightarrow Ni_{Sr}^{\bullet}+\frac{3}{4}SrO+\frac{1}{4}SrTiO_3+\frac{1}{4}V_{Ti}^{////},$$

104] $$NiO+Ti_{Ti}^{\times}+\frac{1}{4}O_{2(g)}+\frac{1}{2}O_O^{\times}\rightarrow Ni_{Ti}^{/}+TiO_2+\frac{1}{2}V_O^{\bullet\bullet}$$

In addition to the energy of substituting nickel at the cation sites, several other energy values must be known for calculation of the energy of the above processes including: the lattice energy of the oxides; the energy to create lattice vacancies; the dissociation energy of O_2, the first and second electron affinities of oxygen; and the third ionisation energy of nickel:

Table 38 Energy values needed to calculate the solution energy of processes 99, 100, 101, 102, 103 and 104 in addition to the energy to substitute a cation into the $SrTiO_3$ lattice.

Description	Energy /eV
Lattice Energy of Ni_2O_3	-184.08
Lattice Energy of NiO	-41.85
Lattice Energy of SrO	-36.33
Lattice Energy of TiO_2	-112.34
Lattice Energy of $SrTiO_3$	-149.38
Energy to create Sr^{2+} vacancy	20.92
Energy of create Ti^{4+} vacancy	81.11
Energy of create O^{2-} vacancy	18.89
Dissociation of O_2	5.16
1st Electron Affinity of O	-1.46
2nd Electron Affinity of O	7.64
3rd Ionisation Energy of Ni	35.19

The lattice energies of the binary oxides given above were calculated by energy minimisation of the experimental structures using atomistic modelling with the parameters given in Table 8, Table 9 and Table 36. In the case of Ni_2O_3, the

experimental structure is not available and so the structure was relaxed starting from the α-hematite lattice [167]. The energy of the vacancies were calculated using the Mott Littleton method. The values for the dissociation of O_2, electron affinities and ionisation energy were obtained from the CRC Handbook of Chemistry and Physics [168].

Table 39 Solution energies for the dissolution of Ni^{3+} into the $SrTiO_3$ lattice.

Process	Description	Energy per defect /eV
99	Dissolution of Ni_2O_3 into $SrTiO_3$, with substitution at the Sr^{2+} site and creation of Sr^{2+} vacancies.	5.79
100	Dissolution of Ni_2O_3 into $SrTiO_3$, with substitution at the Sr^{2+} site and creation of Ti^{4+} vacancies.	5.51
101	Dissolution of Ni_2O_3 into $SrTiO_3$, with substitution at the Ti^{4+} site and creation of O^{2-} vacancies.	5.62
102	Dissolution of NiO into $SrTiO_3$, with oxidation and substitution at the Sr^{2+} site and creation of Sr^{2+} vacancies.	-4.84
103	Dissolution of NiO into $SrTiO_3$, with oxidation and substitution at the Sr^{2+} site and creation of Ti^{4+} vacancies.	-5.12
104	Dissolution of NiO into $SrTiO_3$, with oxidation and substitution at the Ti^{4+} site and creation of O^{2-} vacancies.	-5.01

Table 39 gives the calculated solution energies for the six possible mechanisms discussed above. Clearly the process of dissolving Ni_2O_3 into $SrTiO_3$ and dissolving NiO into $SrTiO_3$ followed oxidation of the nickel are quite different energetically. The non-oxidation route is highly endothermic, whereas the oxidation route is highly exothermic. Further consideration of the direct dissolution of Ni_2O_3 into the lattice can therefore be dismissed.

Although the oxidation process is a plausible mechanism, the highly exothermic values predicted for the solution energy implies that nickel would readily dissolve in strontium titanate. However, this is not the case experimentally [82, 83]. The validity of the Ni^{3+} parameters estimated by comparison with Ni^{2+} needed further investigation. Since Ni_2O_3 has not been prepared in a stable, stoichiometric form under ambient conditions, the calculated lattice parameters and energetics from the atomistic simulation could not be compared with any experimental data. To obtain data for

comparison we plotted the lattice parameters and internal lattice energies versus atomic radii for three known corundum structures: Al_2O_3; Cr_2O_3; and Fe_2O_3, see Figure 29 and Figure 30, and interpolated the values for Ni_2O_3 based on their respective atomic radii. The lattice energy data were taken from CRC Handbook of Chemistry and Physics [168], the cell parameters from the Inorganic Crystal Structure Data File web site [169], and the ionic radii from Shannon [104]. The values calculated by atomistic modelling are significantly different from those expected based on these plots as shown in Figure 29 and Figure 30. Furthermore, analysis of the Ni-O distance for Ni^{3+} doped into the Ti^{4+} site showed a length of only 1.76Å. These values are considerably shorter than other Ni (III)-O bonds such as found in $LaNiO_3$ of 1.93Å [170].

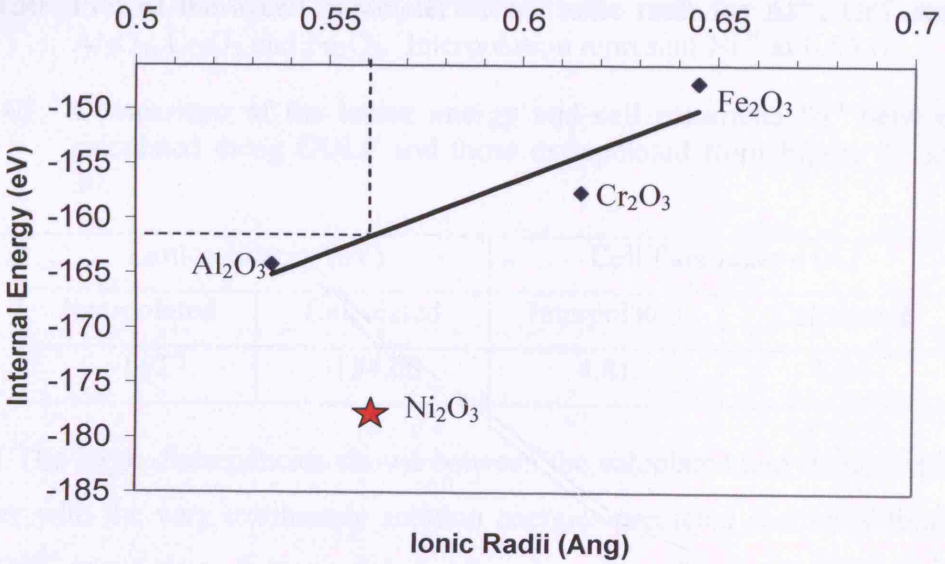

Figure 29 Plot of lattice energy versus ionic radii for Al^{3+}, Cr^{3+} and Fe^{3+} in the corundum structure. Extrapolations represent Ni^{3+} at 0.56 Å.

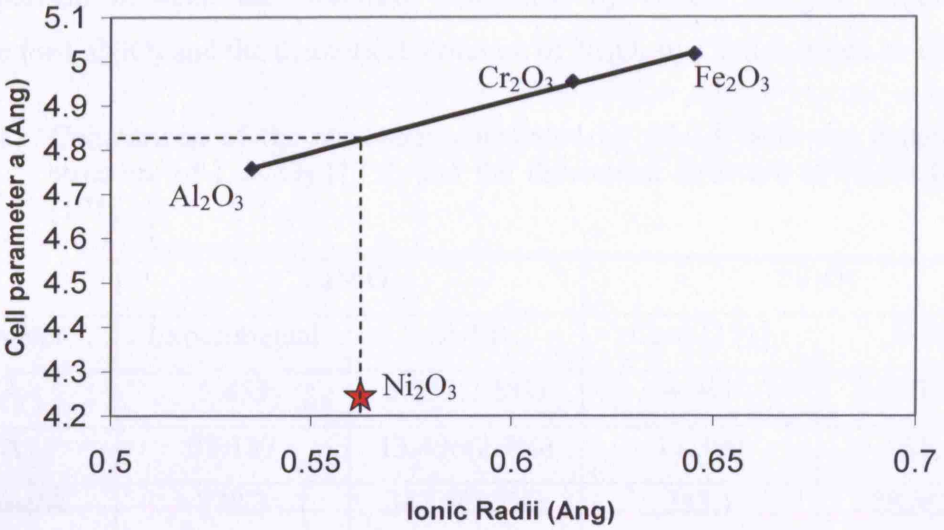

Figure 30 Plot of the a cell parameter versus ionic radii for Al^{3+}, Cr^{3+} and Fe^{3+} in Al_2O_3, Cr_2O_3 and Fe_2O_3. Interpolation represent Ni^{3+} at 0.56 Å.

Table 40 Comparison of the lattice energy and cell parameter "a" between values calculated using GULP and those extrapolated from Figure 29 and Figure 30.

Lattice Energy (eV)		Cell Parameter a (Å)	
Interpolated	Calculated	Interpolated	Calculated
-162	-184.08	4.81	4.24

The large discrepancies shown between the calculated and interpolated results, together with the very exothermic solution energies predicted cast considerable doubt on the Ni^{3+} parameters. It was concluded that the assumption that the "hardness" of the cations is the same for Ni^{2+} and Ni^{3+} may not be valid. An alternative assumption is that the hardness of Ni^{3+} is similar to that of other trivalent first row transition metal cations whose Buckingham ρ values are around 0.31 Å, see [106]. Furthermore, it was assumed that the structure predicted for Ni_2O_3 using the *ab initio* code CRYSTAL95 by Catti and Sandrone was reliable [171]. A new value for the A Buckingham parameter was found by assigning Ni^{3+} a ρ value of 0.31 Å and fitting to the Catti et al structure for Ni_2O_3. The new value for A was 1519.5 eV, Ni^{3+} was still considered to be a rigid ion.

This new parameter set was tested by modelling the structure of $LaNiO_3$. The oxygen parameters used were those given in Table 8 and Table 9, to remain consistent with the rest of this work. The lanthanum parameters were those derived for $LaCoO_3$ by Cherry et al [172], where A= 1545.21eV, r=0.3590Å, Y=-0.25e, and k=145 $eVÅ^{-2}$.

A comparison between the structures calculated by GULP and the experimental structure for $LaNiO_3$ and the theoretical structure of Ni_2O_3 by Catti is given in Table 41.

Table 41 Comparison of the structures calculated by GULP with the experimental structure of $LaNiO_3$ [173], and the theoretical structure of Ni_2O_3 by Catti [171].

	$LaNiO_3$		Ni_2O_3	
Parameter	Experimental	GULP	Catti [171]	GULP
a/Å	5.453	5.533(1.5%)	4.941	5.030(1.8%)
c/Å	13.137	13.496(2.7%)	13.390	13.182(-1.6%)
Volume/Å	338.3	347.5(2.7%)	283.1	288.8(2.0%)
Ni-O/Å	1.935	1.978(2.2%)	1.912	1.945(1.7%)

There is a better fit between the structures for Ni_2O_3 than for $LaNiO_3$, which is as expected as the parameters were fitted to the former structure. Except for the c cell parameter of Ni_2O_3, all other measures of the structure increased during the atomistic calculation which may suggest that the Buckingham A parameter is too large. However, the calculated structures for the two compounds containing Ni^{3+} are good enough to have a degree of confidence in this parameter set for trivalent nickel. Solution energies for doping of Ni^{3+} into strontium titanate were now calculated using this parameter set and assuming that nickel is oxidised by gaseous oxygen from Ni^{2+} to Ni^{3+} during the doping process. The results are given in Table 42.

Table 42 Solution energies calculated for oxidative doping Ni^{3+} into the strontium titanate lattice.

Dopant Site	Solution Energy (eV)
Ni^{3+} in a Sr^{2+} site with Sr^{2+} vacancy compensation	7.80
Ni^{3+} in a Sr^{2+} site with Ti^{4+} vacancy compensation	7.53
Ni^{3+} in a Ti^{4+} site with O^{2-} vacancy compensation	6.46

A comparison of Table 39 and Table 42 shows the sensitivity of the calculated solution energies to the parameter sets used. For the same reactions, the energies have changed from strongly exothermic to strongly endothermic. However, some confidence in the results in Table 42 is possible because the Ni^{3+} parameter set has been validated against the experimental structure of $LaNiO_3$ and nickel is known to have limited solubility in the $SrTiO_3$ lattice [82, 83]. Therefore, we predict that substitution of Ni^{3+}

into the $SrTiO_3$ lattice is extremely unfavourable and that the oxidation of any divalent nickel species within the lattice will not occur.

5.5. Summary of Atomistic Modelling of Nickel Substitution Alkaline Earth Titanates

In this chapter the atomistic modelling of pure and nickel doped alkaline earth titanates has been considered. In particular we have focussed on the local conformational changes around the defect region and the prediction of the energy required to dissolve NiO into the lattices.

The conformational changes around the defect regions can be largely explained in terms of the size mismatch between the Ca^{2+}, Sr^{2+}, Ba^{2+} and Ti^{4+} against that of Ni^{2+}. When substituting at the A site, the Ni^{2+} cation is considerably smaller than the alkaline earth cations and the lattice relaxes to reduce the distance to both the first O^{2-} and Ti^{4+} coordination shell. The relaxation for $CaTiO_3$ and $SrTiO_3$ in the first oxygen coordination sphere is particularly marked, with the nickel forming distorted quasi square planar structures.

When substituting Ni^{2+} at the B site, the Ti^{4+} cation is replaced by a slightly larger cation and there is an increase in the B-O distance. An additional factor to be considered for B site substitution is the need to introduce an oxygen vacancy to maintain charge neutrality. As expected, locating the oxygen vacancy in the first coordination sphere has the most significant effect on the structure of the surrounding lattice as the B site coordination is reduced from six to five. The removal of the oxygen in the first coordination sphere causes the Ni^{2+} cation to displace from the B site position of the pure lattice resulting in one of the Ni-O distance being much shorter than the other four.

Table 43 Summary of predicted solution energies for the dissolution of NiO into the alkaline earth titanates.

	Solution Energy /eV			
Perovskite	A site	B site isolated	B site nearest neighbour O^{2-} vacancy	B site next nearest neighbour O^{2-}vacancy
Calcium Titanate	0.88	2.71	2.45	3.09
Strontium Titanate	1.26	3.02	2.12	2.71
Barium Titanate	3.04	3.45	2.52	2.85

Table 43 summarises the predicted solution energies for the dissolution of divalent nickel into the alkaline earth perovskites. Some clear trends can be seen in the results:

- Substitution at the A site becomes less favourable as the size mismatch between the Ni^{2+} cation and the alkaline earth cation increases.
- As expected by simple electrostatic considerations, clustering of the defects for substitution at the B site decreases the energy cost for dissolution of NiO.
- Comparison with Table 42 shows that the substitution of Ni^{3+} into $SrTiO_3$ is considerably less favourable than for substitution of Ni^{2+}.
- Despite the much closer ionic size match between Ni^{2+} and Ti^{4+} compared to Ni^{2+} and the alkaline earth cations, substitution at the A site is favoured over the B site for $CaTiO_3$ and $SrTiO_3$. Charge mismatch must play a significant role for these systems.
- The lowest solution energy for the B site is for the $SrTiO_3$ lattice.

6. Bulk Structure and Energetics of Nickel Doped Alkaline Earth Titanates – Density Functional Theory Calculations

In this chapter, the modelling of the bulk defect properties of Ni^{2+} substituted alkaline earth titanates using density functional theory is considered. The density functional used throughout these studies is a hybrid functional of the form of Equation 95 and containing 25% Hartree Fock exchange (see Chapter 4 for details). The hybrid functional was found to reproduce the crystal properties of $SrTiO_3$ most reliably and to be able to compare results across all the systems the same density functional must be used.

The basis sets used for oxygen, titanium and strontium were given in Section 4.1. The basis sets used for Ca^{2+} and Ba^{2+} were small core effective core potential based values by Habas et al [161], whereas Ni^{2+} used an all electron basis set [174]. All the basis sets used are readily available from the CRYSTAL website [162]. The nickel cation was set to a high spin state with the electrons assigned α spin and the difference between the number of α spin and β spin electrons set to 2 throughout the calculations. The implementation of DFT in the CRYSTAL code requires the specification of a grid to evaluate the exchange-correlation potential numerically. In our work, the grid consisted of atom-centered contributions with 75 radial points covering a range of 4.0 ionic radii, and a very dense angular grid with 974 points. We employed a Monkhorst–Pack shrinking factor of 8 for reciprocal space sampling, truncation thresholds of 10^{-7}, 10^{-7}, 10^{-7}, 10^{-7} and 10^{-14} for the Coulomb and exchange series [175], and SCF convergence thresholds of 10^{-7} Hartree for both eigenvalues and total energies

6.1. Periodic DFT Modelling of Undoped Titanates

6.1.1. $CaTiO_3$

The relaxation of the $CaTiO_3$ structure using DFT is illustrated in Figure 31, with the changes in the unit cell parameters and atomic positions detailed in Table 44 and Table 45 respectively. As can be seen, the use of the hybrid functional containing 25% HF exchange reproduces the experimental structure accurately. The unit cell parameters increase by 1% or less and the displacement of the ions in the relaxed structure compared to the experimental structure are less than 0.1 Å.

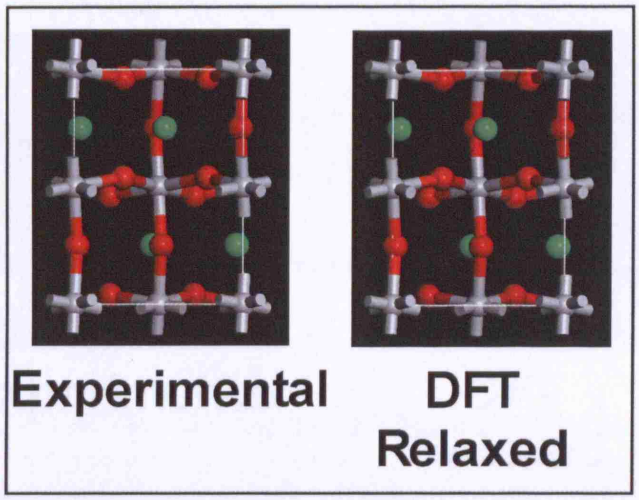

Figure 31 Comparison of the experimental and modelled using DFT structures for $CaTiO_3$.

Table 44 Comparison of the unit cell parameters of $CaTiO_3$ between the experiment and relaxed structure using DFT.

Unit Cell Length	Experimental /Å	Relaxed /Å	% Change
a_0	5.436	5.493	1.0
b_0	7.639	7.692	0.7
c_0	5.379	5.416	0.7

Table 45 Displacement of ions in $CaTiO_3$ during relaxation of the lattice using DFT.

Atom	Displacement /Å
O	0.02
O	0.02
Ca	0.09
Ti	0.00

6.1.2. $SrTiO_3$

The relaxation of the $SrTiO_3$ system is illustrated in Figure 32. The change in the lattice parameters and atomic positions are detailed in Table 46 and Table 47 respectively. The pure lattice of $SrTiO_3$ has been accurately modelled using DFT, although the changes in the unit cell parameters are slightly larger than those for the $CaTiO_3$ system. The internal coordinates of the lattice have been predicted to within 0.07 Å of experiment.

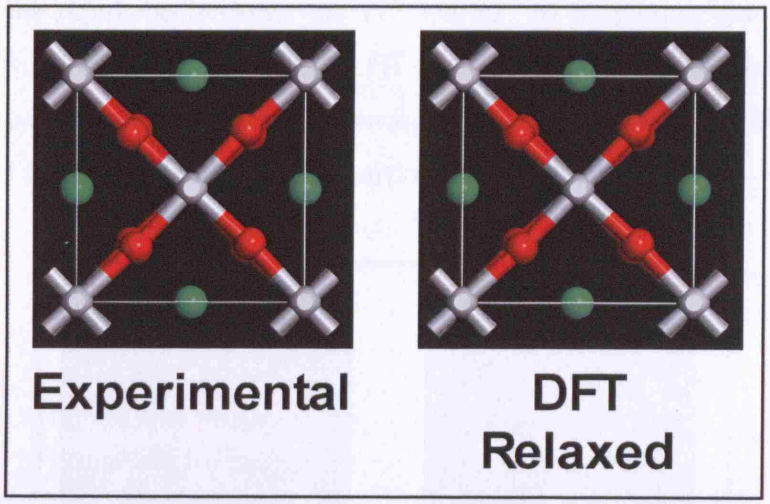

Figure 32 Comparison of the experimental and modelled using DFT structures for $SrTiO_3$.

Table 46 Comparison of the unit cell parameters of $SrTiO_3$ between the experiment and relaxed structure using DFT.

Unit Cell Length	Experimental /Å	Relaxed /Å	% Change
a_0	5.507	5.571	1.2
c_0	7.796	7.885	1.1

Table 47 Displacement of ions in $SrTiO_3$ during relaxation of the lattice using DFT.

Atom	Displacement /Å
O	0.02
O	0.02
Sr	0.07
Ti	0.00

6.1.3. $BaTiO_3$

The relaxation of the $BaTiO_3$ lattice is illustrated in Figure 33, with the changes in the unit cell parameters and internal coordinates detailed in Table 48 and Table 49 respectively. Of the three titanates considered, the $BaTiO_3$ structure is the most poorly reproduced using the hybrid functional containing 25% HF exchange. The tetragonal distortion of the lattice is overestimated, having a c/a ratio of 1.05 compared to the experimental value of 1.01. The displacement of the ions on energy minimisation is also relatively large with the O^{2-} and Ba^{2+} ions moving by 0.12 Å and 0.10 Å respectively. The short Ti-O bond length is 1.91 Å experimentally, whereas it is 1.81 Å in the simulated structure. These findings are consistent with the work by Cora [165] who concluded that the magnitude of the ferroelectric distortion was influenced by two opposing factors: the covalent nature of the Ti-O bond which drives the bond length to

decrease; and the repulsion between the Ti^{4+} and O^{2-} as they come into close contact. For a hybrid functional containing 20% HF exchange, Cora found that the covalent nature of the Ti-O was the dominant influence, as evidenced by the population of the Ti-3d orbitals, and therefore ferroelectric distortion was too large.

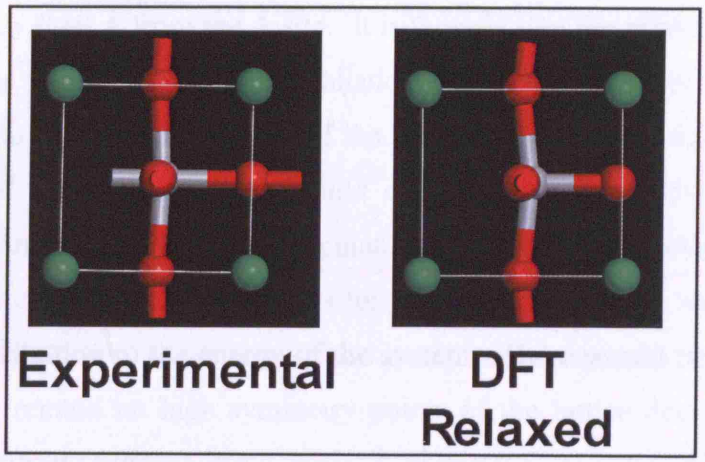

Figure 33 Comparison of the experimental and modelled using DFT structures for $BaTiO_3$.

Table 48 Comparison of the unit cell parameters of $BaTiO_3$ between the experiment and relaxed structure using DFT.

Unit Cell Length	Experimental /Å	Relaxed /Å	% Change
a_0	3.991	3.997	0.2
c_0	4.028	4.209	4.5

Table 49 Displacement of ions in $BaTiO_3$ during relaxation of the lattice using DFT.

Atom	Displacement /Å
O	0.12
O	0.12
Ba	0.10
Ti	0.01

6.2. *Periodic DFT Modelling of Ni(II) Doped Titanates*

6.2.1. $CaTiO_3$

The changes in the local conformation around the A site between pure and Ni^{2+} substituted $CaTiO_3$ as predicted by DFT are illustrated in Figure 34 and Table 50. As for the atomistic simulations (see Chapter 6) the relaxation of the lattice around the defect is dominated by the size mismatch between the Ca^{2+} (1.34 Å) and the Ni^{2+} (0.69 Å) cations. The Ni^{2+} cation is predicted to bond with three of the oxide ions of the

12 coordinate A site. There is in most cases close agreement between the lengths of these bonds predicted by atomistic and DFT simulations. However, there is a significant difference in the results of the atomistic and DFT modelling, in that, in the former, the Ni^{2+} cation remained in the centre of the A site and oxide ions relaxed towards the defect, whereas in the DFT case, the Ni^{2+} cation moved towards the O^{2-} ions being displaced by 0.49 Å from the A site. It is thought that the relaxation described by DFT calculations is more physically realistic than that of the interatomic potential simulations due to the likely resistance of the lattice to move four tightly bound oxide anions instead of one small weakly bound cation. A possible explanation for the behaviour of the interatomic potential calculations is that the parameters used are based on formal atomic charges, i.e. the model is fully ionic, which would further enhance the electrostatic contribution to the energy of the system. There would be a strong driving force for ions to remain on high symmetry points of the lattice due to the Madelung potential of the crystal [176].

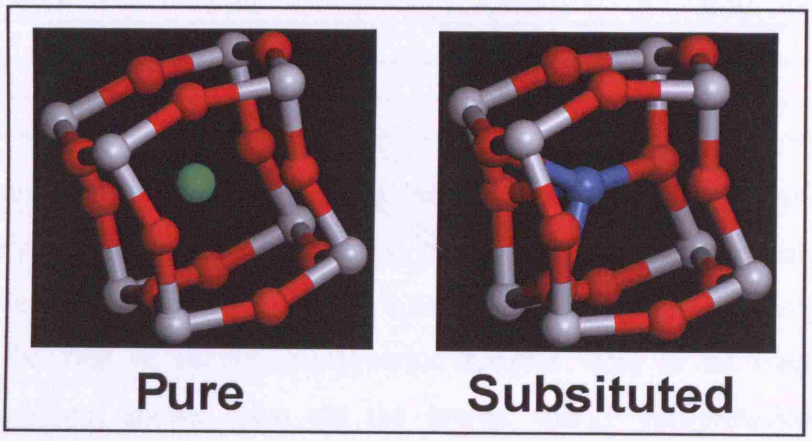

Figure 34 Comparison of the local conformation around the "A" site of pure and Ni^{2+} substituted $CaTiO_3$ using DFT.

Table 50 Comparison of the local conformation around the "A" site of pure and Ni^{2+} substituted $CaTiO_3$ using DFT.

Atom	Distance to Ca^{2+} (Pure Lattice) /Å	Distance to Ni^{2+} (Defect Lattice) /Å	Change /Å
O	2.30	2.06	-0.24
O	2.32	2.06	-0.26
O	2.76	2.10	-0.66
O	2.67	2.21	-0.46
O	2.75	2.46	-0.29
O	2.29	2.79	0.5
O	3.16	3.00	-0.16
O	2.76	3.12	0.36
O	2.75	3.15	0.40
O	2.88	3.24	0.36
O	3.10	3.33	0.23
O	3.16	3.63	0.47
Ti	3.35	2.78	-0.57
Ti	3.33	3.03	-0.30
Ti	3.31	3.20	-0.11
Ti	3.35	3.32	-0.03
Ti	3.36	3.37	0.01
Ti	3.33	3.51	0.18
Ti	3.31	3.66	0.35
Ti	3.36	3.85	0.49

The modelling of charged defect lattices cannot be carried out using DFT, therefore the simulation of the substitution of Ni^{2+} at the B site must include the O^{2-} vacancy needed for charge neutrality. We decided that only systems with the oxygen vacancy in the first or second coordination spheres were to be considered since atomistic modelling shows these are the lowest energy conformations and large supercells would be needed to model isolated defects.

Figure 35 illustrates the comparison between the pure and Ni^{2+} substituted, with a nearest neighbour oxygen vacancy, $CaTiO_3$ lattices and Table 51 details the changes in the distances to the B cation. The relaxation of the lattice agrees well with the atomistic modelling in that one short Ni-O bond is formed opposite to the vacancy and four longer Ni-bonds perpendicular to the vacancy.

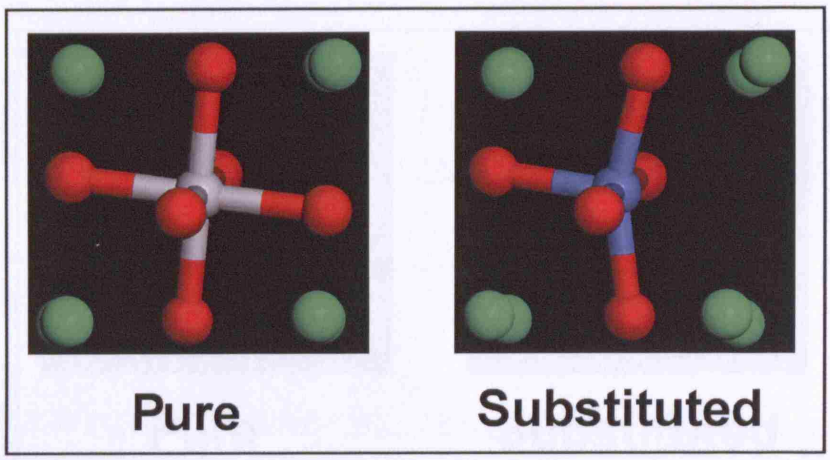

Figure 35 Comparison of the local conformation around the B site of pure and Ni^{2+} substituted, with a nearest neighbour oxygen vacancy, $CaTiO_3$ using DFT.

Table 51 Comparison of the local conformation around the B site of pure and Ni^{2+} substituted, with a nearest neighbour oxygen vacancy, $CaTiO_3$ using DFT.

Atom	Distance to Ti^{4+} (Pure Lattice) /Å	Distance to Ni^{2+} (Defect Lattice) /Å	Change /Å
O	1.97	1.96	-0.01
O	1.97	2.00	0.03
O	1.97 (×3)	2.04 (×3)	0.07
Ca	3.19	3.04	-0.15
Ca	3.36	3.14	-0.22
Ca	3.30	3.27	-0.03
Ca	3.30	3.35	0.05
Ca	3.19	3.38	0.19
Ca	3.52	3.48	-0.04
Ca	3.52	3.55	0.03
Ca	3.36	3.60	0.24

The relaxation of the doped structure with the oxygen vacancy in the next nearest neighbour position is shown in Figure 36 and the bond distances to the B site cation given in Table 52. The overall trend agrees with the atomistic modelling where a combination of the larger size of the Ni^{2+} (0.69 Å) cation with respect to the Ti^{4+} (0.61 Å) cation and the negative charge on the substitution site explains the differences predicted. Each of the Ni-O distances are longer than the respective Ti-O distances and each of the Ni-Ca distances are shorter than the Ti-Ca distances. The Ni^{2+} cation is not displaced from the perfect lattice B site position. The only difference to note in comparision with the atomistic simulations is that the average Ni-O is 2.06 Å in the DFT calculations and 2.10 Å in the atomistic simulations.

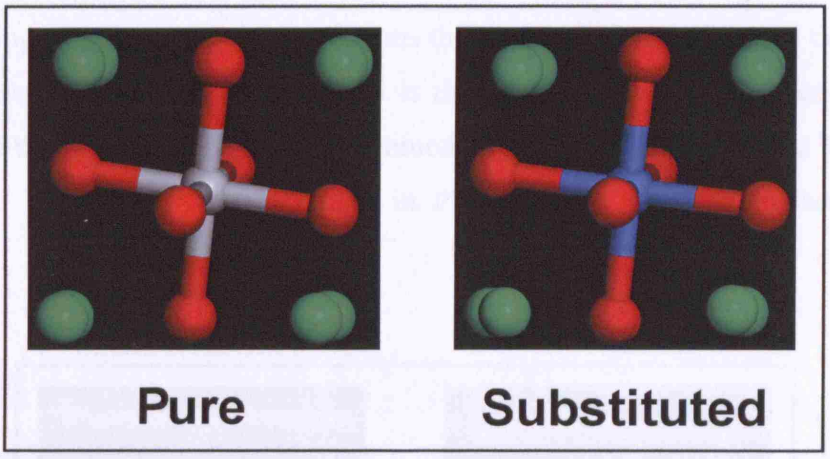

Figure 36 Comparison of the local conformation around the "B" site of pure and Ni^{2+} substituted, with a next nearest neighbour oxygen vacancy, $CaTiO_3$ using DFT.

Table 52 Comparison of the local conformation around the "B" site of pure and Ni^{2+} substituted, with a next nearest neighbour oxygen vacancy, $CaTiO_3$ using DFT.

Atom	Distance to Ti^{4+} (Pure Lattice) /Å	Distance to Ni^{2+} (Defect Lattice) /Å	Change /Å
O	1.97	2.03	0.06
O	1.97	2.05	0.08
O	1.97	2.06	0.09
O	1.97 (×3)	2.07 (×3)	0.10
Ca	3.19	3.02	-0.17
Ca	3.19	3.03	-0.14
Ca	3.30	3.05	-0.25
Ca	3.30	3.08	-0.22
Ca	3.36	3.23	-0.13
Ca	3.52	3.26	-0.26
Ca	3.36	3.29	-0.07
Ca	3.52	3.41	-0.11

6.2.2. $SrTiO_3$

The size mismatch between the A site cation, Sr^{2+} (1.44 Å), and the dopant cation, Ni^{2+} (0.69 Å), is greater for $SrTiO_3$ than for $CaTiO_3$ which is reflected in the more significant relaxation predicted when Ni^{2+} is substituted into $SrTiO_3$ at the A site. The dopant cation is displaced by 0.89 Å from the perfect lattice A site position and forms bonds with five of the twelve oxide ions surrounding the A site, with the shortest Ni-O distance being similar to the distances found for substitution at the B site of 2.01 Å, see Figure 37 and Table 53. As for the calcium titanate system, there is a

contrast in the behaviour of the lattice upon energy minimisation between atomistic and DFT modelling.. In the atomistic simulations the oxygens surrounding the defect cation move, whereas in the DFT calculations it is the dopant cation that moves. Since the movement of the oxide ions is more constrained, due to their bond with the Ti^{4+} cations, the predicted Ni-O distances are longer in the atomistic simulations than the DFT simulations.

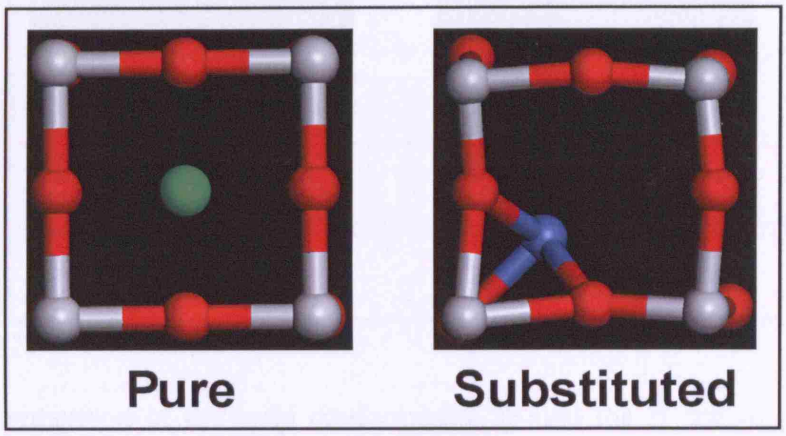

Figure 37 Comparison of the local conformation around the A site of pure and Ni^{2+} substituted $SrTiO_3$ using DFT.

Table 53 Comparison of the local conformation around the A site of pure and Ni^{2+} substituted $SrTiO_3$ using DFT.

Atom	Distance to Sr^{2+} (Pure Lattice) /Å	Distance to Ni^{2+} (Defect Lattice) /Å	Change /Å
O	2.84	2.01	-0.83
O	2.79 (×2)	2.10 (×2)	-0.69
O	2.74 (×2)	2.10 (×2)	-0.64
O	2.74	3.28	0.52
O	2.84	3.28	0.42
O	2.84	3.54	0.70
O	2.84	3.55	0.71
O	2.79 (×2)	3.56 (×2)	0.77
O	2.74	3.93	1.19
Ti	3.41 (×2)	2.76 (×2)	-0.55
Ti	3.41 (×2)	3.48 (×2)	0.07
Ti	3.41 (×2)	3.49 (×2)	0.08
Ti	3.41 (×2)	4.21 (×2)	0.80

There is good agreement in the behaviour predicted for the lattice relaxation around the B site, with a charge balancing nearest neighbour oxygen vacancy, between the $CaTiO_3$ and $SrTiO_3$ systems (see Figure 38 and Table 54) using DFT. The shorter

Ni-O bond is around 1.96 Å in both systems and the longer Ni-O distances around 2.00 Å. There is less good agreement between the atomistic and DFT results in that the short Ni-O distance is 1.89 Å in the atomistic prediction and the longer Ni-O distances are 1.96 Å in the atomistic case.

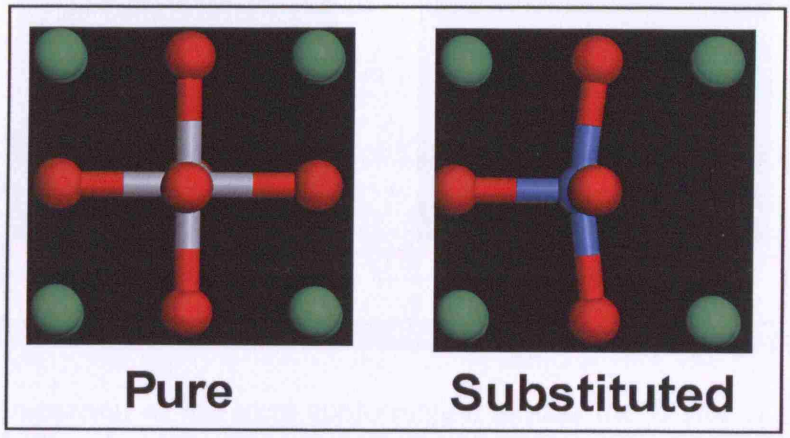

Figure 38 Comparison of the local conformation around the B site of pure and Ni^{2+} substituted, with a nearest neighbour oxygen vacancy, $SrTiO_3$ using DFT.

Table 54 Comparison of the local conformation around the B site of pure and Ni^{2+} substituted, with a nearest neighbour oxygen vacancy, $SrTiO_3$ using DFT.

Atom	Distance to Ti^{4+} (Pure Lattice) /Å	Distance to Ni^{2+} (Defect Lattice) /Å	Change /Å
O	1.97	1.95	-0.02
O	1.97 (×4)	2.03 (×4)	0.06
Sr	3.41 (×4)	3.32 (×4)	-0.09
Sr	3.41 (×4)	3.51 (×4)	0.10

The predicted conformation around the B site in the pure and Ni^{2+} substituted, with an oxygen vacancy in the next nearest neighbour position, $SrTiO_3$ lattices is shown in Figure 39 and the distances to the ions in the first and second coordination spheres given in Table 55. The effect of the vacancy in the second oxygen coordination sphere can be clearly seen as in that the 5 coordinate Ti^{4+} cations (not shown) are displaced away from the vacancy causing the oxygen atoms to move and break the octahedral symmetry around the defect B site. The Ni^{2+} cations are displaced by 0.19 Å from the B site position of the perfect lattice. The behaviour contrasts with the atomistic predictions in that the range of Ni-O distances in the atomistic calculations is 1.99-2.06 Å, whereas in the DFT work the range is 2.04-2.25 Å. The movement of the Ni^{2+} cation is negligible in the atomistic calculations and the NiO_6 octahedra are much

less distorted. There is a general contraction of the Sr^{2+} cations towards the defect cation due to the negative charge in this region.

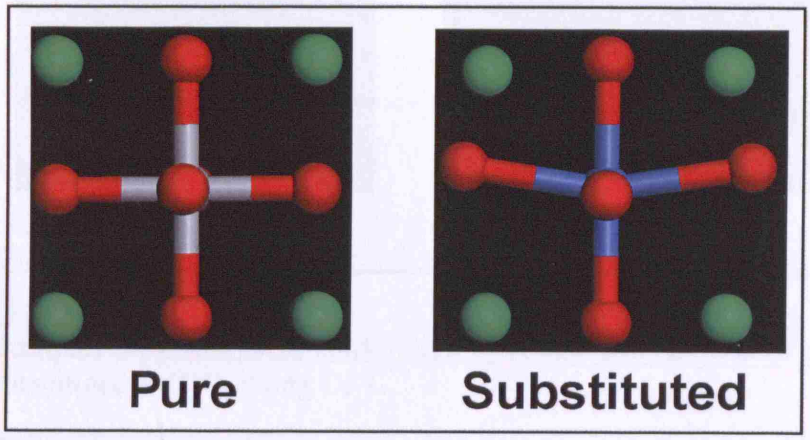

Figure 39 Comparison of the local conformation around the B site of pure and Ni^{2+} substituted, with a next nearest neighbour oxygen vacancy, $SrTiO_3$ using DFT.

Table 55 Comparison of the local conformation around the B site of pure and Ni^{2+} substituted, with a next nearest neighbour oxygen vacancy, $SrTiO_3$ using DFT.

Atom	Distance to Ti^{4+} (Pure Lattice) /Å	Distance to Ni^{2+} (Defect Lattice) /Å	Change /Å
O	1.97 (×3)	2.04 (×3)	0.07
O	1.97	2.11	0.14
O	1.97 (×2)	2.25 (×2)	0.28
Sr	3.41 (×4)	3.31 (×4)	-0.10
Sr	3.41 (×4)	3.42 (×4)	0.01

6.2.3. $BaTiO_3$

For substitution at the A site, see Figure 40 and Table 56, the trends shown in the $CaTiO_3$ and $SrTiO_3$ lattices are continued for the $BaTiO_3$ system since the size difference between the two cations (1.61 Å(Ba^{2+}) vs. 0.69 Å(Ni^{2+})) is still larger. The Ni^{2+} cation is calculated to move from the pure B site position by 1.26 Å, forming a bond with 4 of the 12 A site oxygens. The shortest of the Ni-O distances is predicted to be 1.93 Å, which is in sharp contrast to the atomistic modelling where very little relaxation around the doped A site was calculated. There is no significant displacement of the Ti^{4+} cations in the second coordination sphere.

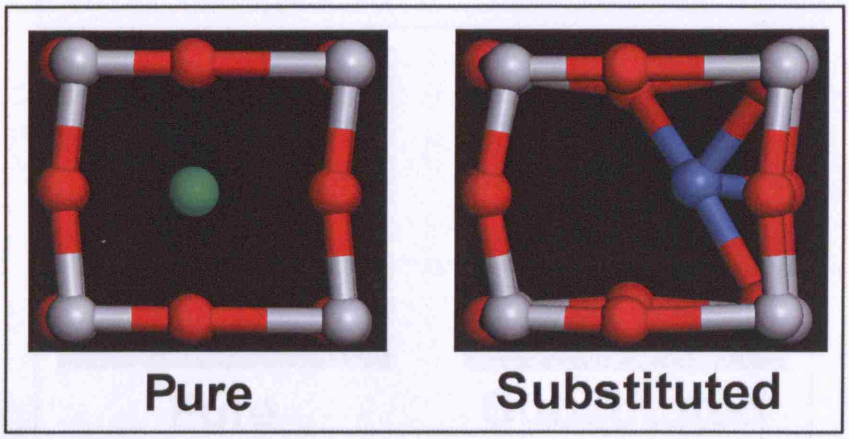

Figure 40 Comparison of the local conformation around the "A" site of pure and Ni^{2+} substituted $BaTiO_3$ using DFT.

Table 56 Comparison of the local conformation around the "A" site of pure and Ni^{2+} substituted $BaTiO_3$ using DFT.

Atom	Distance to Ba^{2+} (Pure Lattice) /Å	Distance to Ni^{2+} (Defect Lattice) /Å	Change /Å
O	2.83	1.93	-0.90
O	2.84	2.04	-0.80
O	2.83	2.18	-0.65
O	2.84	2.21	-0.63
O	2.83	2.57	-0.26
O	2.97	2.90	-0.07
O	2.97	3.28	0.31
O	2.97	3.47	0.50
O	2.83	3.54	0.71
O	2.84	3.73	0.89
O	2.84	3.85	1.01
O	2.97	4.08	1.11
Ti	3.70	2.82	-0.88
Ti	3.70	2.94	-0.76
Ti	3.70	3.40	-0.30
Ti	3.70	3.44	-0.26
Ti	3.37	3.59	0.22
Ti	3.37	3.77	0.40
Ti	3.37	4.18	0.81
Ti	3.37	4.26	0.89

The substitution of Ni^{2+} at the B site, with a nearest neighbour oxygen vacancy, in $BaTiO_3$ predicts the one short Ni-O distance and four longer Ni-O distances conformation, as for the other two titanates, see Figure 41 and Table 57. There is good agreement between the atomistic and DFT simulations in all of the Ni-O distances.

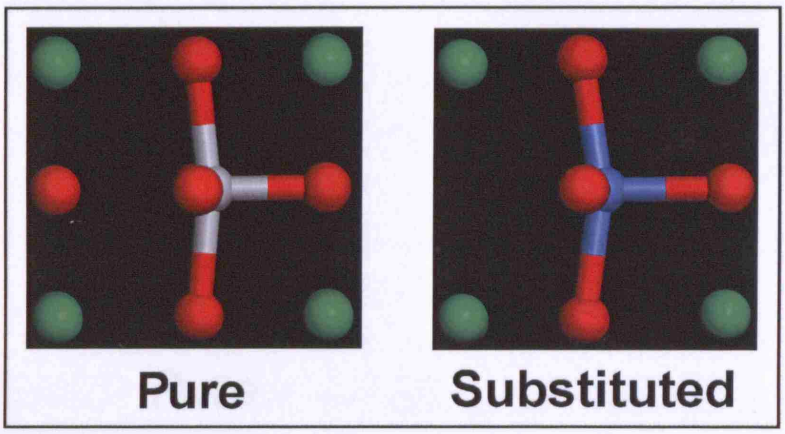

Figure 41 Comparison of the local conformation around the B site of pure and Ni^{2+} substituted, with a nearest neighbour oxygen vacancy, $BaTiO_3$ using DFT.

Table 57 Comparison of the local conformation around the B site of pure and Ni^{2+} substituted, with a nearest neighbour oxygen vacancy, $BaTiO_3$ using DFT.

Atom	Distance to Ba^{2+} (Pure Lattice) /Å	Distance to Ni^{2+} (Defect Lattice) /Å	Change /Å
O	1.81	1.98	0.17
O	2.01 (×4)	2.10 (×4)	0.09
Ba	3.37 (×4)	3.42 (×4)	0.05
Ba	3.70 (×4)	3.60 (×4)	-0.10

The relaxation of the doped lattice for B site substitution with a next nearest neighbour oxygen vacancy is shown in Figure 42 and the coordinating ion distances from the B site given in Table 58. The most noticeable effect of the substitution is the reduction of the ferroelectric distortion with the increase of the shortest B-O distance from 1.81 to 2.11 Å. The symmetry of the conformation around the B site is still less than that predicted using atomistic modelling, despite the large changes observed in the energy minimisation calculation.

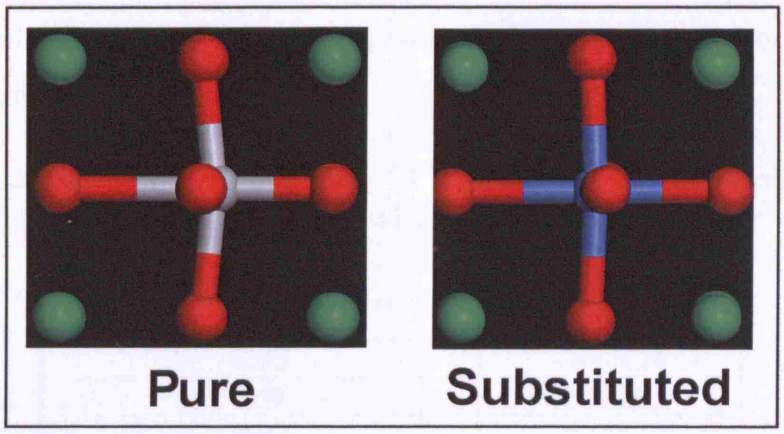

Figure 42 Comparison of the local conformation around the B site of pure and Ni^{2+} substituted, with a next nearest neighbour oxygen vacancy, in $BaTiO_3$, using DFT.

Table 58 Comparison of the local conformation around the B site of pure and Ni^{2+} substituted, with a next nearest neighbour oxygen vacancy, in $BaTiO_3$, using DFT.

Atom	Distance to Ba^{2+} (Pure Lattice) /Å	Distance to Ni^{2+} (Defect Lattice) /Å	Change /Å
O	1.81	2.11	0.30
O	2.01 (×2)	2.15 (×2)	0.14
O	2.01 (×2)	2.23 (×2)	0.22
O	2.40	2.30	-0.10
Ba	3.37 (×4)	3.54 (×4)	0.17
Ba	3.70 (×4)	3.43 (×4)	-0.27

6.2.4. Solution Energies

The total energies calculated using DFT for the binary, perfect tertiary and defect tertiary systems studied here are given in Table 59. These total energies can be used to calculate the solution energy for the dissolution of NiO into the perovskite hosts using Born Haber cycles based on the following equations:

a) Substitution at the "A" site:

105] $$NiO + A_8B_8O_{24} \rightarrow A_7NiB_8O_{24} + AO$$

Substitution at the "B" site:

106] $$NiO + A_8B_8O_{24} \rightarrow A_8B_7NiO_{23} + TiO_2$$

Units cells contain 40 atoms, or 39 for B site substitutions, were used for the defect calculations and so 1 in 40 atoms were Ni^{2+} cations, which corresponds to a substitution concentration of 2.5 atomic %.

Table 59 Total energies calculated using DFT for the calculation of solution energies for the dissolution of NiO into alkaline earth titanates.

System	Total Energy /eV
NiO	-43090.02
CaO	-3043.24
SrO	-2878.23
BaO	-2735.18
TiO_2	-27213.16
$Ca_8Ti_8O_{24}$	-242060.21
$Sr_8Ti_8O_{24}$	-240742.73
$Ba_8Ti_8O_{24}$	-239601.30
$Ca_7NiTi_8O_{24}$ (A site sub)	-282105.06
$Sr_7NiTi_8O_{24}$ (A site sub)	-280952.56
$Ba_7NiTi_8O_{24}$ (A site sub)	-279953.59
$Ca_8Ti_7NiO_{23}$ (B site sub) O^{2-} vac. nearest neighbour.	-257934.07
$Sr_8Ti_7NiO_{23}$ (B site sub) O^{2-} vac. nearest neighbour.	-256617.57
$Ba_8Ti_7NiO_{23}$ (B site sub) O^{2-} vac. nearest neighbour.	-255476.76
$Ca_8Ti_7NiO_{23}$ (B site sub) O^{2-} vac. next nearest neighbour.	-257933.50
$Sr_8Ti_7NiO_{23}$ (B site sub) O^{2-} vac. next nearest neighbour.	-256617.17
$Ba_8Ti_7NiO_{23}$ (B site sub) O^{2-} vac. next nearest neighbour.	-255476.42

The calculated solution energies are given in Table 60. Clear trends can be seen these results:

- Doping at the A site becomes more unfavourable as the size mismatch between the alkaline earth cation and the divalent nickel defect cation increases.

- Doping at the B site becomes more favourable as the unit cell lengths increase due to the larger size of the A site cation.

- Placing the oxygen vacancy in the nearest neighbour position gives a lower solution energy than placing the vacancy in the next nearest neighbour position.

- A site substitution is favoured for $CaTiO_3$, B site substitution is favoured for $BaTiO_3$, A and B site substitution equally favoured for $SrTiO_3$.

Many of these conclusions agree with the atomistic modelling predictions and there is reasonable agreement between the solution energies calculated by each technique. The only contrast with the atomistic results is that for substitution at the B site, with both a nearest and next nearest neighbour oxygen vacancy, the lowest solution energy is predicted for the $SrTiO_3$ system using atomistic modelling, and for the $BaTiO_3$ system using DFT.

Table 60 Solution energies for the dissolution of NiO into alkaline earth titanates.

System	Solution Energy /eV (DFT)	Solution Energy /eV (Atomistic)
Ni^{2+} at A site, $CaTiO_3$	1.93	0.88
Ni^{2+} at A site, $SrTiO_3$	1.96	1.26
Ni^{2+} at A site, $BaTiO_3$	2.55	3.04
Ni^{2+} at B site, $CaTiO_3$ O^{2-} vac. nearest neighbour.	3.00	2.45
Ni^{2+} at B site, $SrTiO_3$ O^{2-} vac. nearest neighbour.	2.02	2.12
Ni^{2+} at B site, $BaTiO_3$ O^{2-} vac. nearest neighbour.	1.40	2.52
Ni^{2+} at B site, $CaTiO_3$ O^{2-} vac. next nearest neighbour.	3.57	3.09
Ni^{2+} at B site, $SrTiO_3$ O^{2-} vac. next nearest neighbour.	2.42	2.71
Ni^{2+} at B site, $BaTiO_3$ O^{2-} vac. next nearest neighbour.	1.74	2.85

6.3. Summary

In this chapter the results of the DFT modelling of the bulk substitution of Ni^{2+} into the alkaline earth titanates was considered and compared with the results of the atomistic modelling of these systems.

The conformational changes around the defect sites were dominated by the size mismatch between the pure lattice and defect cations. At the A site, large displacements of the Ni^{2+} cation were predicted, to bring the defect into close contact with 4 or 5 of the 12 oxygens surrounding the A site. At the B site, relaxations around the defect were smaller than at the A site and the coordination number of the defect ion was determined by the position of the charge compensating oxygen ion vacancy. The most important

contrast in the behaviour of the atomistic and DFT calculations was that during relaxation of the lattice following A site substitution, it is the oxygen ions that move in the atomistic simulations, and the Ni^{2+} cation that moves in the DFT simulations which is thought to be due to the dominance of the electrostatics in the interatomic potential calculations.

The predicted solution energies clearly demonstrate that the larger the mismatch between the cation sizes of the lattice and dopant ion, the less favourable is the dissolution process. Although the size match between the Ti^{4+} cations and Ni^{2+} cations is much less than between the divalent nickel and the alkaline earth cations, substitution at the B site is not necessarily favoured over the A site which may be attributed to the charge mismatch between the cations. As the lattice expands, substitution at the B site becomes more favourable and there is a crossover between favoured A site and B site substitution between strontium and barium titanates. The energy cost of substituting Ni^{2+} at the A site and B site is predicted to be similar in $SrTiO_3$. Placing the oxygen vacancy next to the B substituted site is the most favoured conformation in all systems.

7. Study of the Surface Structure and Energetics of Nickel Doped Alkaline Earth Titanates using Atomistic Modelling

In this chapter the surface modelling, using atomistic simulations, of pure and divalent nickel substituted alkaline earth titanates is considered. For each of the perovskite lattices, two cuts parallel to the 001 bulk crystal plane were modelled. One of these cuts contained only A^{2+} and O^{2-} ions and are labelled OA layers, the other cut contained only Ti^{4+} and O^{2-} ions and was labelled OTiO. The modelling was carried out using the GULP code with the parameters given in Table 8 and Table 9.

The surfaces were modelled in two stages. First, surfaces were cleaved from the pure bulk lattice and relaxed, and secondly the defect lattice was formed from the relaxed surface. Initial investigations found that the energy was converged for a model containing four unit cells (each containing 40 atoms ($A_8Ti_8O_{24}$) "equivalent" to a 2×2×2 supercell of the cubic perovskite unit cell) in region 1 (160 atoms) and 5 unit cells in region 2 (200 atoms), giving 360 atoms in total in the simulation cell (see Section 3.1.8 for an explanation of "region 1" and "region 2").

7.1. Atomistic Modelling of the OSrO and OTiO Terminated (001) Surfaces of Undoped Titanates

7.1.1. $CaTiO_3$

The surface reconstructions of the OCa and OTiO cuts parallel to the 001 bulk crystal plane for pure CaTiO3 are illustrated in Figure 44 and Figure 45 respectively. The relaxation of both surfaces is small. The interlayer spacing shows that layers 1 and 2 move towards each other and consequently the spacing between layers 2 and 3 is slightly larger than the bulk value of 1.91 Å. There is some displacement of the ions in layer 1 of the OTiO terminated surface predicted, as the OTiO bond angles approach 180°.

The surface energy of the OCa terminated surface is 1.28 Jm^{-2}, and for the OTiO terminated surface is 1.50 Jm^{-2}, which implies that the former is slightly more stable than the latter.

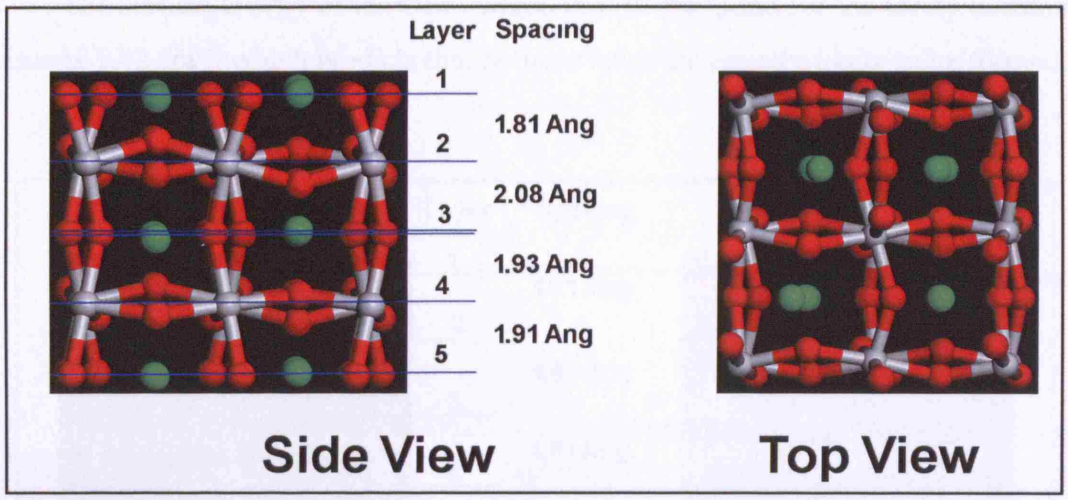

Figure 43 Relaxed conformation for the OCa terminated surface parallel to the 001 plane of the pure $CaTiO_3$ lattice.

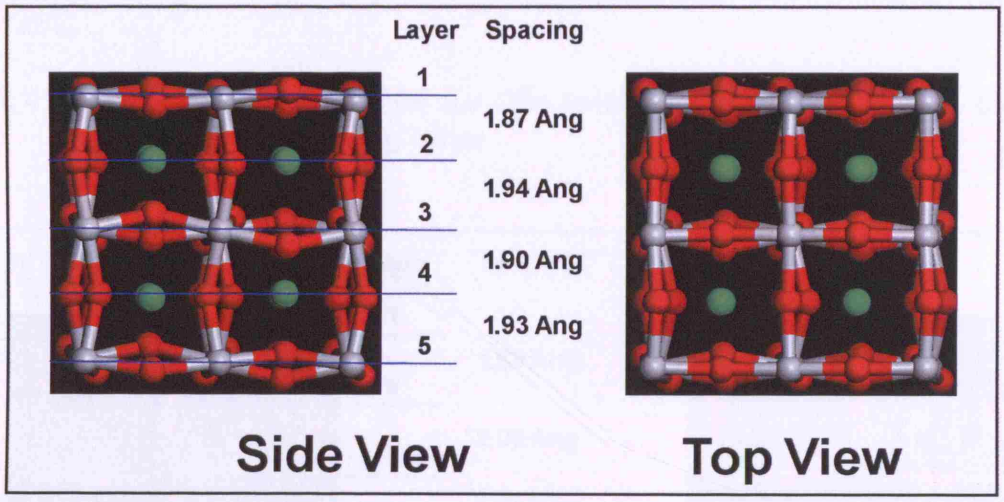

Figure 44 Relaxed conformation for the OTiO terminated surface parallel to the 001 plane of the pure $CaTiO_3$ lattice.

7.1.2. $SrTiO_3$

The surface constructions of the OSr and OTiO terminated surfaces for $SrTiO_3$ are illustrated in Figure 45 and Figure 46 respectively. As for the $CaTiO_3$ surfaces, layers 1 and 2 approach each other, causing an increase in the spacing between layers 2 and 3. For the OSr terminated surface, the four Sr ions of layer 1 are predicted to relax into the surface, being displaced by 0.42 Å, 0.40 Å, 0.30 Å, and 0.11 Å respectively. The relaxation of layer 1 of the OTiO terminated surface leads to an OTiO bond angle of 180°, as for the $CaTiO_3$ system.

The surface energy of the OSr surface is 1.49 Jm^{-2}, and for the OTiO terminated surface is 1.42 Jm^{-2}, which predicts that both surfaces are equally likely to be formed.

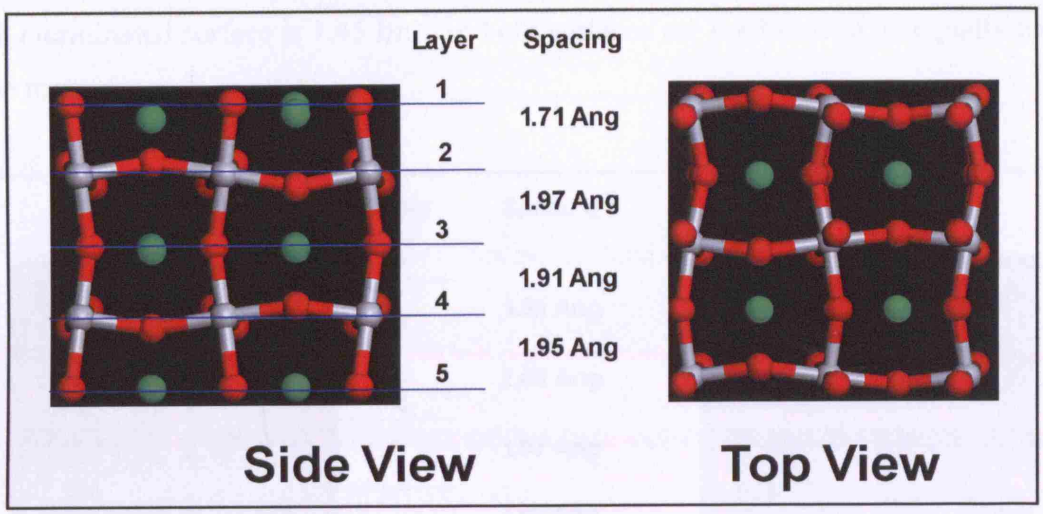

Figure 45 Relaxed conformation for the OSr terminated surface parallel to the 001 plane of the pure $SrTiO_3$ lattice.

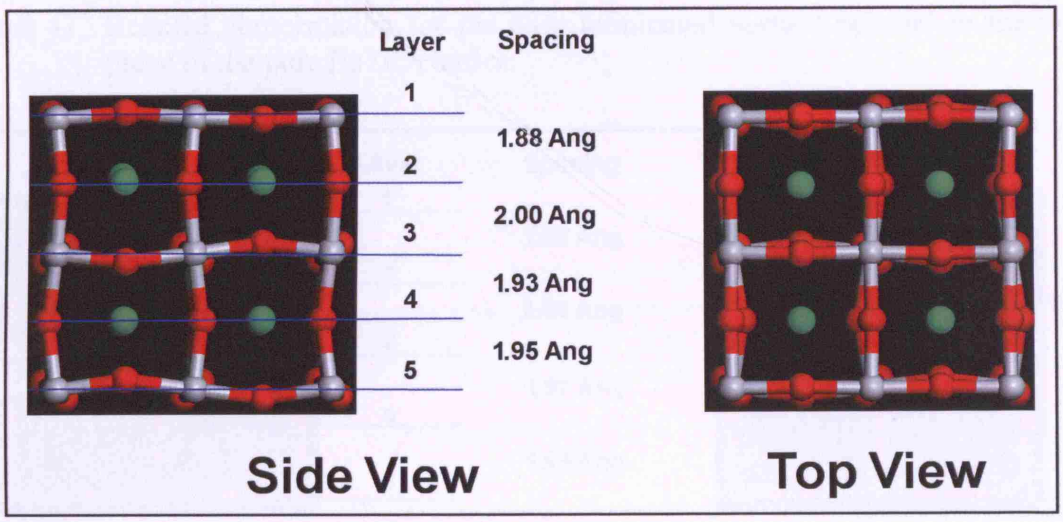

Figure 46 Relaxed conformation for the OTiO terminated surface parallel to the 001 plane of the pure $SrTiO_3$ lattice.

7.1.3. $BaTiO_3$

The relaxations of the OBa and OTiO terminated surfaces of $BaTiO_3$ are illustrated in Figure 47 and Figure 48 respectively. The interlayer spacings, as for the $CaTiO_3$ and $SrTiO_3$ systems, are smaller than the bulk between layers 1 and 2, larger than the bulk between layers 2 and 3 and approach the bulk value of 2.00 Å for

subsequent layers. The Ba^{2+} cations are displaced by 0.05 Å into the surface for the OBa terminated surface.

The surface energy for the OBa terminated surface is 1.48 Jm^{-2}, and for the OTiO terminated surface is 1.45 Jm^{-2}, so both surfaces are predicted to be equally likely to be formed.

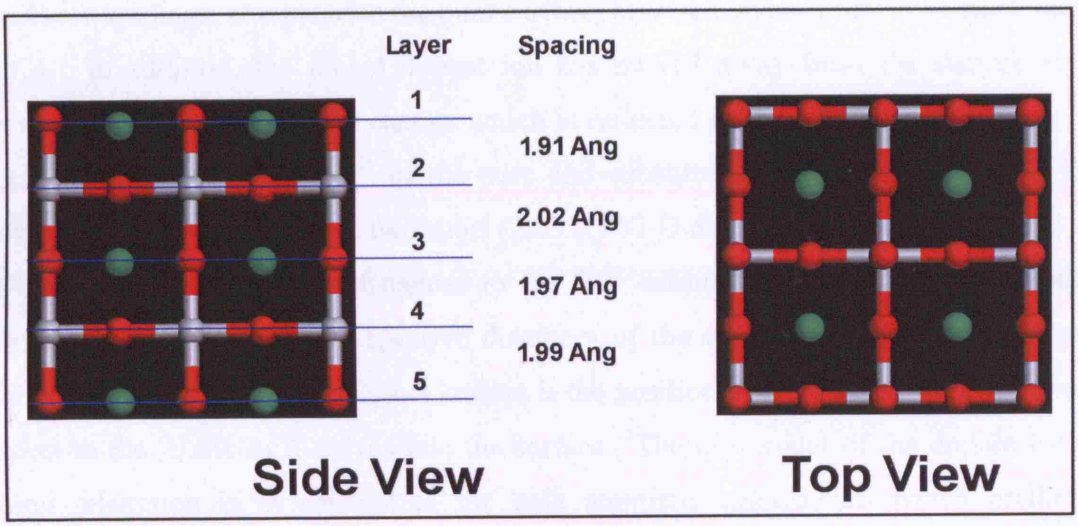

Figure 47 Relaxed conformation for the OBa terminated surface parallel to the 001 plane of the pure $BaTiO_3$ lattice.

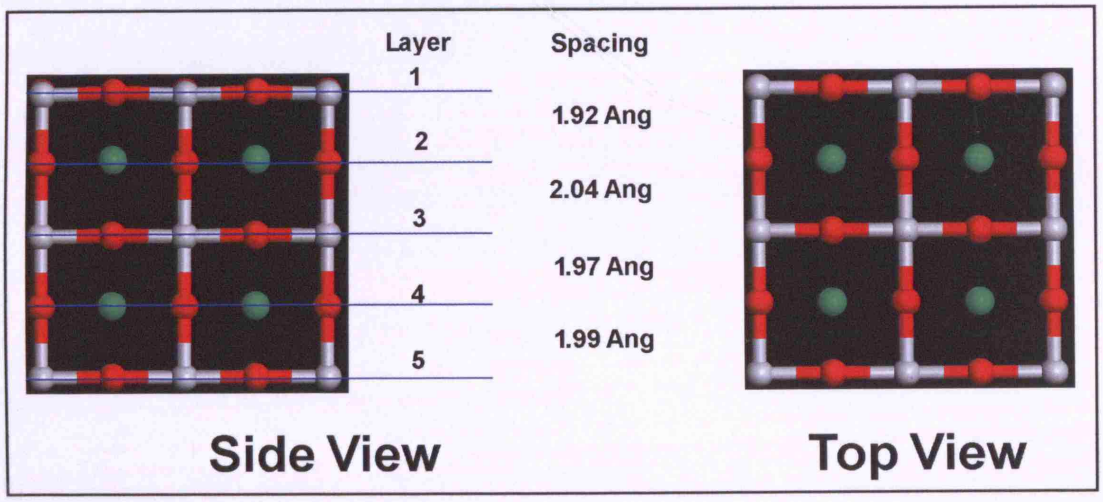

Figure 48 Relaxed conformation for the OTiO terminated surface parallel to the 001 plane of the pure $BaTiO_3$ lattice.

7.2. *Atomistic Modelling of the OSrO and OTiO Terminated (001) Surfaces of Ni(II) Doped Titanates*

7.2.1. $CaTiO_3$

Figure 49 and Table 61 compare the pure and Ni^{2+} A site substituted OCa terminated surfaces for the $CaTiO_3$ lattice. The relaxed defect surface shows reduced interlayer spacings, compared to the pure surface, between layers 1 and 2, 2 and 3, and 3 and 4. In addition, the nickel dopant ion has moved away from the surface layer towards the bulk by 0.48 Å, a change which is reflected in the differences between the distances to the Ca^{2+} and Ni^{2+} of the pure and substituted lattices respectively. The nickel ion is 4 coordinate with two short (2.03 Å) Ni-O distances and two long (2.23 Å) Ni-O distances. All of the distances to the Ti^{4+} cations of the second coordination sphere are shorter than the respective distances of the undoped surface. The largest change between the pure and defect lattices is the position of the defect Ni^{2+} cation with respect to the A site as it moves into the surface. The movement of the dopant cation during relaxation is in contrast to the bulk atomistic calculations which predicted movement of the O^{2-} ions. The relaxation of the Ni^{2+} cation into the surface is due to its small size compared with Ca^{2+}. There is very little change between the pure and defect lattices in the xy plane (i.e. parallel to the surface).

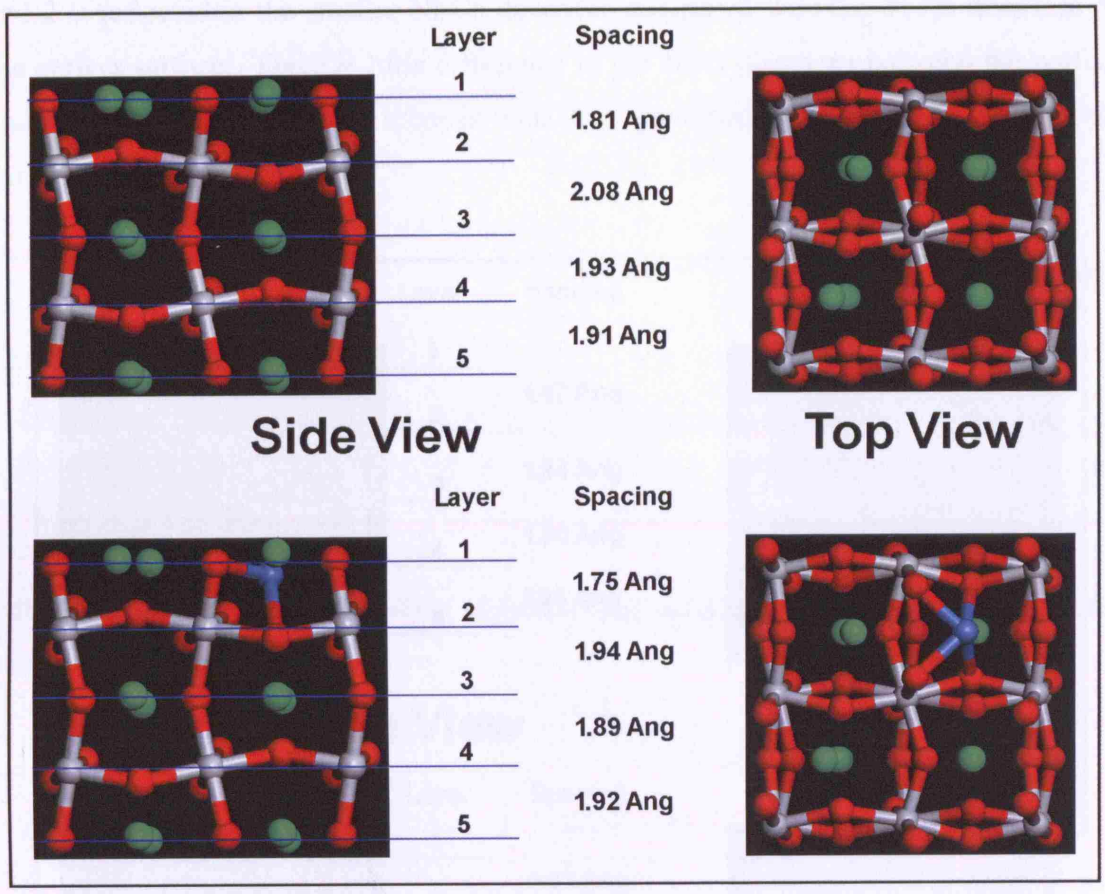

Figure 49 Comparison of the perfect (top) and Ni^{2+} A site substituted (bottom) OCa terminated surface for the $CaTiO_3$ lattice.

Table 61 Comparison of the perfect and Ni^{2+} A site substituted OCa terminated surface for the $CaTiO_3$ lattice.

Atom	Distance to Ca^{2+} (Pure Lattice) /Å	Distance to Ni^{2+} (Substituted Lattice) /Å	Change /Å
O	2.15 (×2)	2.03 (×2)	-0.12
O	2.68 (×2)	2.23 (×2)	-0.45
O	2.59	2.43	-0.16
O	3.21	2.84	-0.37
O	2.95 (×2)	3.07 (×2)	0.12
Ti	3.26 (×2)	2.98 (×2)	-0.28
Ti	3.29 (×2)	3.12 (×2)	-0.17

The comparison between the perfect and Ni^{2+} B site substituted (with a nearest neighbour oxygen vacancy) $CaTiO_3$ lattices is shown in Figure 50 and Table 62 for the OTiO terminated surfaces. The perturbation of the interlayer spacing is greater than that predicted for A site substitution, with the spacing between layers 3 and 4 being 0.18 Å larger than the bulk value of 1.93 Å, and between layers 4 and 5 being 0.22 Å less than the bulk interlayer spacing. The reduction of the interlayer spacing between layers 1

and 2 is reflected in the smaller Ni-Ca distances compared with the Ti-Ca distances of the perfect surface. There is little difference in the Ni-O distances between the perfect and defect surfaces, although there is relaxation predicted for the "NiO_4" units away from the oxygen vacancy.

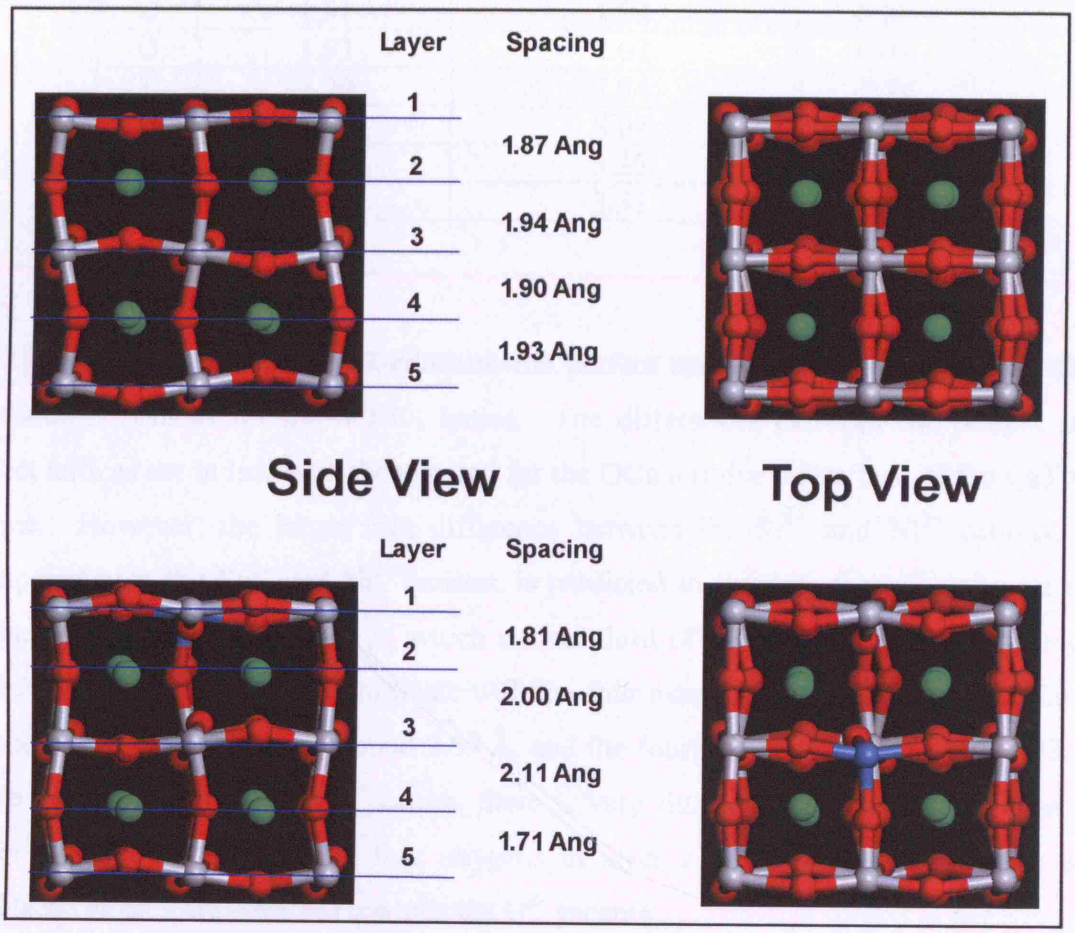

Figure 50 Comparison of the perfect (top) and Ni^{2+} B site substituted (bottom, with a nearest neighbour oxygen vacancy) OTiO terminated surface for the $CaTiO_3$ lattice.

Table 62 Comparison of the perfect and Ni^{2+} B site substituted (with a nearest neighbour oxygen vacancy) OTiO terminated surface for the $CaTiO_3$ lattice.

Atom	Distance to Ti^{4+} (Pure Lattice) /Å	Distance to Ni^{2+} (Substituted Lattice) /Å	Change /Å
O	1.95	1.91	-0.04
O	1.91	1.92	0.01
O	1.91	1.92	0.02
O	1.93	1.97	0.04
Ti	3.20	2.94	-0.24
Ti	3.29	3.04	-0.25
Ti	3.21	3.23	0.02
Ti	3.23	3.31	0.08

7.2.2. $SrTiO_3$

Figure 51 and Table 63 compare the perfect and Ni^{2+} A site substituted OSr terminated surfaces for the $SrTiO_3$ lattice. The differences between the perfect and defect lattices are in line with those noted for the OCa terminated surface of the $CaTiO_3$ lattice. However, the larger size difference between the Sr^{2+} and Ni^{2+} cations, as compared with the Ca^{2+} and Ni^{2+} cations, is predicted to increase the relaxation of the defect ion into surface to 0.69 A, which is over third of the distance between layers 1 and 2. The Ni^{2+} cation is 4 coordinate with the four nearest oxygens of layer 2. Three of these Ni-O distances are around 2.09 Å, and the fourth is slightly shorter at 2.03 Å. With the exception of the Ni^{2+} cation, there is very little displacement of the ions of layer 1 in the xy plane. The four oxygens in layer 2 nearest to the defect ion are displaced as they are attracted towards the O^{2-} vacancy.

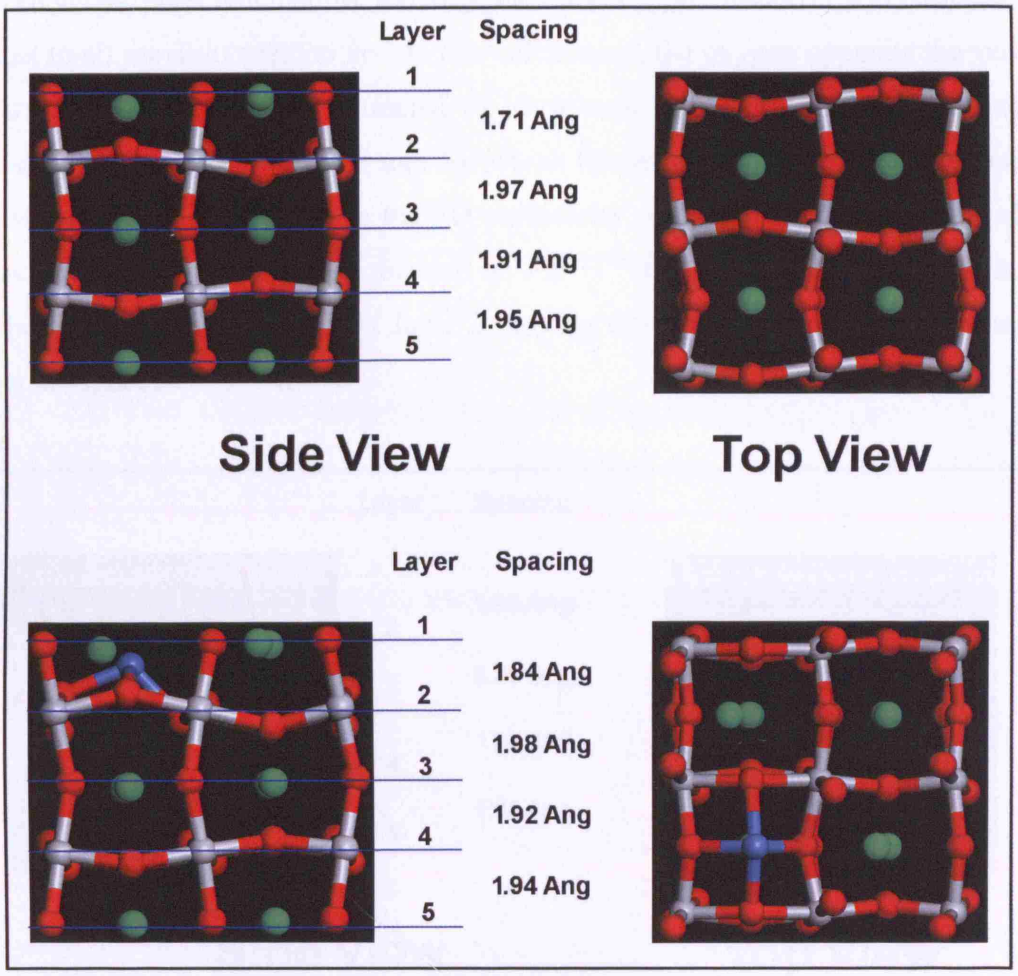

Figure 51 Comparison of the perfect (top) and Ni^{2+} A site substituted (bottom) OSr terminated surface for the $SrTiO_3$ lattice.

Table 63 Comparison of the perfect and Ni^{2+} A site substituted OSr terminated surface for the $SrTiO_3$ lattice.

Atom	Distance to Sr^{2+} (Pure Lattice) /Å	Distance to Ni2+ (Substituted Lattice) /Å	Change /Å
O	2.40	2.03	-0.37
O	2.40	2.08	-0.32
O	2.54 (×2)	2.09 (×2)	-0.45
O	2.77 (×2)	2.84 (×2)	0.07
O	2.77 (×2)	3.44 (×2)	0.67
Ti	3.15 (×2)	2.95 (×2)	-0.20
Ti	3.15 (×2)	3.11 (×2)	-0.04

The comparison between the perfect and Ni^{2+} B site substituted (with an oxygen vacancy nearest neighbour) OTiO terminated surfaces for the $SrTiO_3$ lattice are shown in Figure 52 and Table 64. The changes in the lattice between the perfect and doped surfaces are similar to those predicted for $CaTiO_3$. One difference that can be noted is that the Ni-O distance for the oxygen opposite the vacancy is longer, at 2.36 Å, than the

three oxygens perpendicular to the oxygen vacancy, at around 1.9 Å, which is in contrast to all previous predictions. In this calculation, the oxygen opposite the vacancy appears to be more strongly attracted to its nearest neighbour Ti^{4+} cation than the Ni^{2+}cation. In addition, the TiO_4 unit for which this oxygen is attached is predicted to tilt away from the Ni^{2+}. Due to the 2D periodicity of this simulation there is also a vacancy opposite the oxygen in question on the Ti^{4+} site. The tilting of the TiO_4 unit may be driven by the oxygens of layer 2 moving towards the site of the vacancy, as shown in Figure 52.

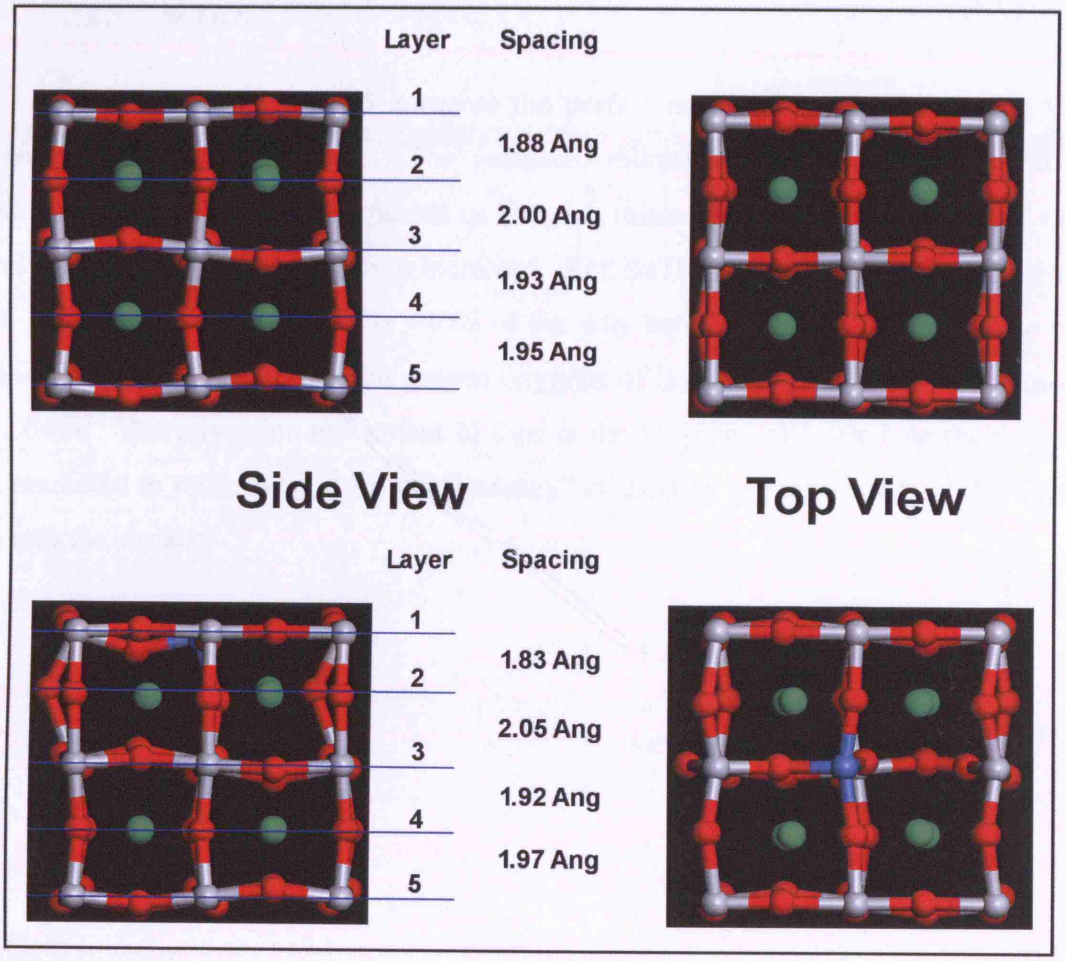

Figure 52 Comparison of the perfect (top) and Ni^{2+} B site substituted (bottom, with a nearest neighbour oxygen vacancy) OTiO terminated surface for the $SrTiO_3$ lattice.

Table 64 Comparison of the perfect and Ni^{2+} B site substituted (with a nearest neighbour oxygen vacancy) OTiO terminated surface for the $SrTiO_3$ lattice.

Atom	Distance to Ti^{4+} (Pure Lattice) /Å	Distance to Ni^{2+} (Substituted Lattice) /Å	Change /Å
O	1.90	1.95	0.05
O	1.95 (×2)	1.95 (×2)	0.00
O	1.94	2.36	0.42
Sr	3.24	2.96	-0.28
Sr	3.30	3.01	-0.29
Sr	3.20	3.18	-0.02
Sr	3.29	3.27	-0.02

7.2.3. $BaTiO_3$

Figure 53 and Table 65 compare the perfect and Ni^{2+} A site substituted OBa surfaces of the $BaTiO_3$ lattice. The predicted relaxation of the surface around the dopant continues the trends expected as the size mismatch between the alkaline earth divalent cation and the Ni^{2+} cation increases. For $BaTiO_3$, the defect cation relaxes by 0.76 Å into the surface, which is ~40% of the way between layers 1 and 2. The Ni^{2+} cation forms four bonds with the nearest oxygens of layer 2 with equal Ni-O distances of 2.04 Å. There is some movement of ions in the xy plane of layer 1 as the oxygens are predicted to relax away from the "vacancy" created by the movement of the dopant ion into the surface.

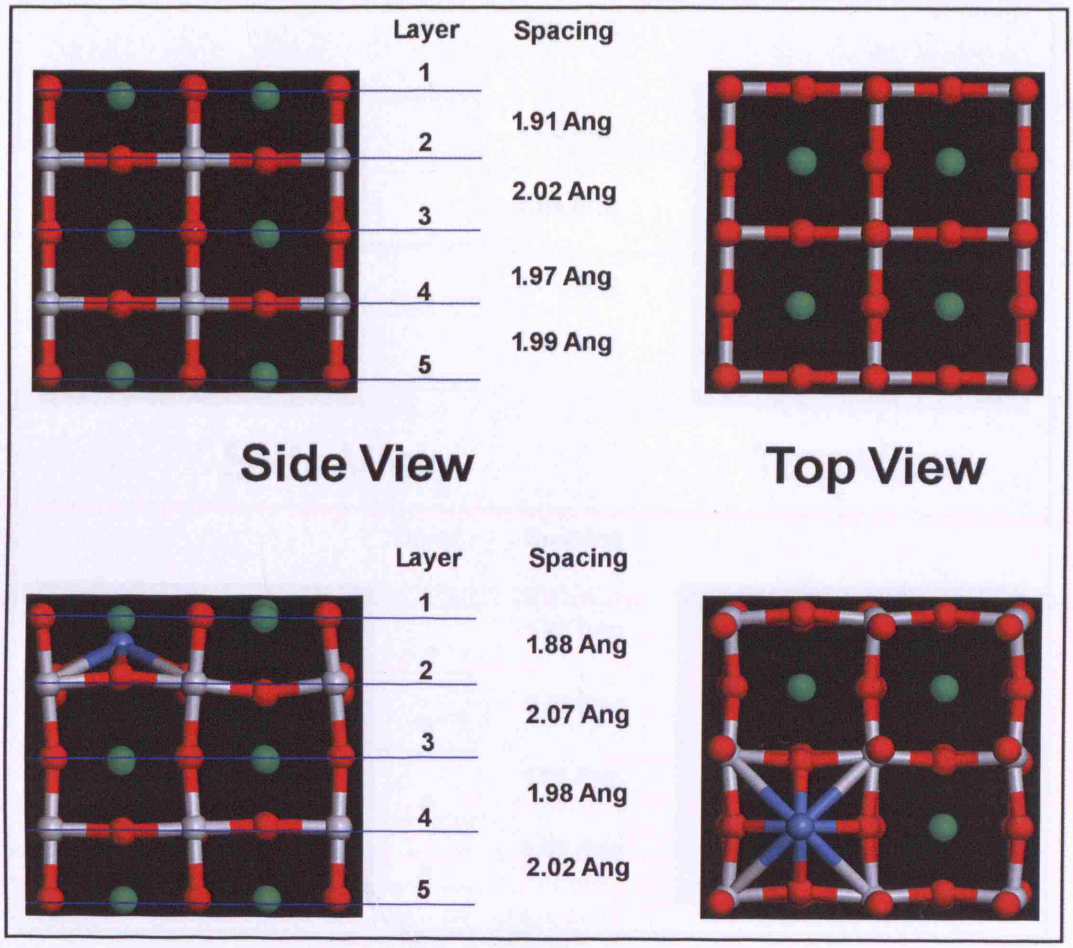

Figure 53 Comparison of the perfect (top) and Ni^{2+} A site substituted (bottom) OBa terminated surface for the $BaTiO_3$ lattice.

Table 65 Comparison of the perfect and Ni^{2+} A site substituted OBa terminated surface for the $BaTiO_3$ lattice.

Atom	Distance to Ba^{2+} (Pure Lattice) /Å	Distance to Ni^{2+} (Substituted Lattice) /Å	Change /Å
O	2.67 (×4)	2.04 (×4)	-0.63
O	2.81 (×4)	3.22 (×4)	0.41
Ti	3.32 (×4)	3.06 (×4)	-0.26

At the B site (see Figure 54 and Table 66) the relaxation of the surface around the defect is in line with that of the other alkaline earth titanate systems, with the movement of ions in layer 1 away from the oxygen vacancy site. Unlike $SrTiO_3$, the Ni-O distance for the oxygen opposite the vacancy is the shortest of the 4 Ni-O distances at a very small value of 1.83 Å. The oxygen in layer 2 nearest the vacancy site of layer 1 moves towards the vacancy.

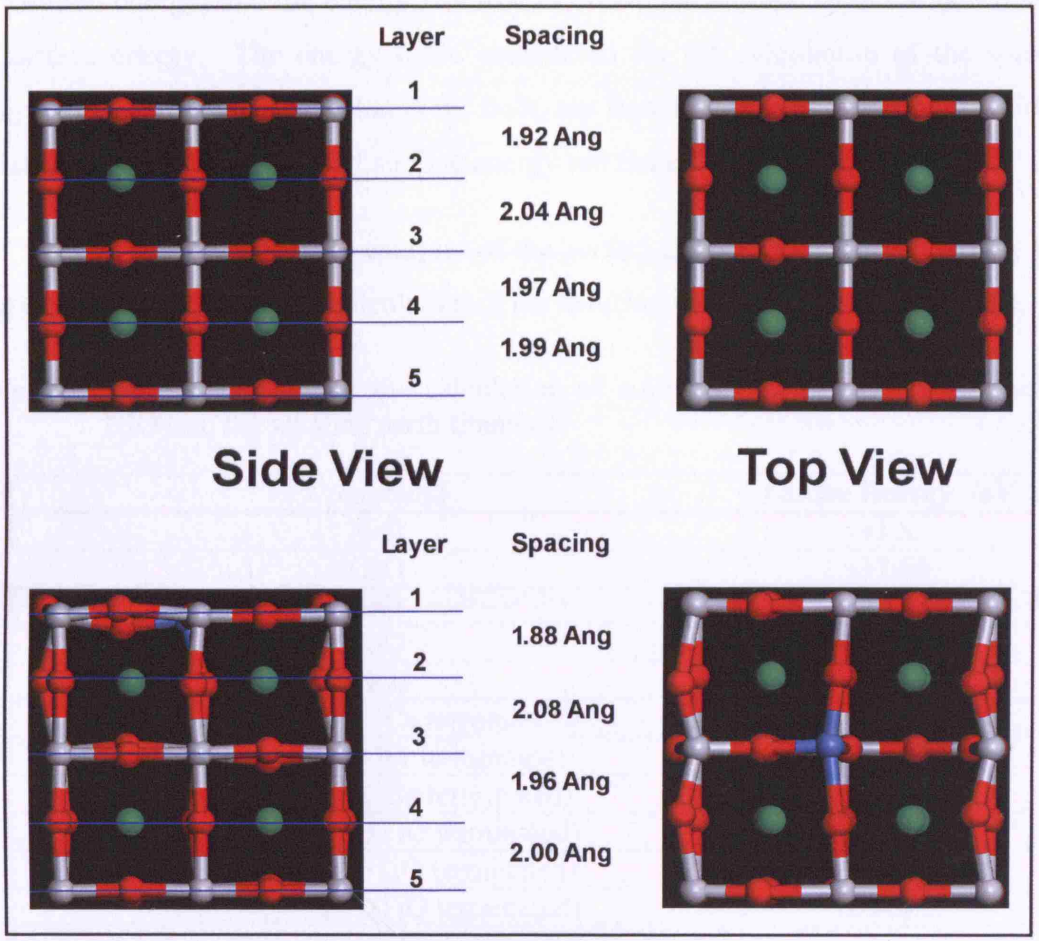

Figure 54 Comparison of the perfect (top) and Ni^{2+} B site substituted (bottom, with a nearest neighbour oxygen vacancy) OTiO terminated surface for the $BaTiO_3$ lattice.

Table 66 Comparison of the perfect (top) and Ni^{2+} B site substituted (bottom, with a nearest neighbour oxygen vacancy) OTiO terminated surface for the $BaTiO_3$ lattice.

Atom	Distance to Ti^{4+} (Pure Lattice) /Å	Distance to Ni^{2+} (Substituted Lattice) /Å	Change /Å
O	1.98	1.83	-0.15
O	1.92	1.96	0.04
O	1.98	1.97	-0.01
O	1.98	2.19	0.21
Ti	3.34	3.11	-0.23
Ti	3.34	3.15	-0.19
Ti	3.34	3.41	0.07
Ti	3.34	3.49	0.15

7.3. Solution and Defect Surface Energies

In this section the energetics of the perfect and doped surfaces are compared in two ways: the energy required to dissolve NiO into the lattice with surface substitution,

the solution energy; and the energy required to create the surface from the bulk lattice, the surface energy. The energy cycle considered for the calculation of the solution energy is exactly analogous to that in the bulk, see Equation 96 and Equation 97. For an explanation of the calculation of surface energy see Section 3.1.8.

Table 67 lists the lattice energies of the perfect and doped surfaces, and the bulk binary oxides, needed for the calculation of the solution energies given in Table 68.

Table 67 Lattice energies for the calculation of solution energies for dissolution of NiO into the alkaline earth titanates.

Compound	Lattice Energy /eV
NiO	-41.85
CaO	-37.66
SrO	-36.33
BaO	-34.57
TiO_2	-112.34
$Ca_{72}Ti_{72}O_{216}$ (OCa terminated)	-10834.20
$Sr_{72}Ti_{72}O_{216}$ (OSr terminated)	-10742.57
$Ba_{72}Ti_{72}O_{216}$ (OBa terminated)	-10646.89
$Ca_{72}Ti_{72}O_{216}$ (OTiO terminated)	-10833.39
$Sr_{72}Ti_{72}O_{216}$ (OTiO terminated)	-10742.85
$Ba_{72}Ti_{72}O_{216}$ (OTiO terminated)	-10646.93
$Ca_{71}NiTi_{72}O_{216}$ (OCa terminated) "A" site substituted	-10837.22
$Sr_{71}NiTi_{72}O_{216}$ (OSr terminated) "A" site substituted	-10747.83
$Ba_{71}NiTi_{72}O_{216}$ (OBa terminated) "A" site substituted	-10652.89
$Ca_{72}Ti_{71}NiO_{215}$ (OTiO terminated) "B" site substituted, nearest neighbour oxygen vacancy	-10761.40
$Sr_{72}Ti_{71}NiO_{215}$ (OTiO terminated) "B" site substituted, nearest neighbour oxygen vacancy	-10670.92
$Ba_{72}Ti_{71}NiO_{215}$ (OTiO terminated) "B" site substituted, nearest neighbour oxygen vacancy	-10575.07

Table 68 Solution energies of Ni^{2+} surface substituted alkaline earth titanates.

System	Energy /eV
Ni^{2+} substituted at the A site OCa terminated $CaTiO_3$	1.17
Ni^{2+} substituted at the A site OSr terminated $SrTiO_3$	0.26
Ni^{2+} substituted at the A site OBa terminated $BaTiO_3$	1.28
Ni^{2+} substituted at the B site with a nearest neighbour oxygen vacancy OTiO terminated $CaTiO_3$	1.50
Ni^{2+} substituted at the B site with a nearest neighbour oxygen vacancy OTiO terminated $SrTiO_3$	1.16
Ni^{2+} substituted at the B site with a nearest neighbour oxygen vacancy OTiO terminated $BaTiO_3$	1.37

The trends in the solution energies for the calcium and barium titanates can be readily understood in terms of the size mismatch between the perfect and defect lattice cations. At the A site, the size mismatch increases from Ca^{2+} to Ba^{2+} and so the solution energy increases from calcium to barium titanate. For B site substitution (with a nearest neighbour oxygen vacancy), the accommodation of the larger defect ion (i.e. Ni^{2+} vs. Ti^{4+}) is more favourable for the $BaTiO_3$ system than the $CaTiO_3$ system.

At both cationic sites, the substitution of Ni^{2+} into the $SrTiO_3$ surface is predicted to have a lower solution energy than for both of the other titanate systems which does not coincide with the trends described above. The lower solution energies predicted for $SrTiO_3$ surfaces may be an indication that the nickel ion is of an appropriate size to be incorporated into the surface more easily than for the calcium or barium titanate systems, which would be an important factor in the stability of nickel doped strontium titanate catalysts over that of the other host alkaline earth titanates.

Table 69 Segregation energies for nickel doped alkaline earth titanates.

System	Segregation Energy /eV
Ni^{2+} substituted at the A site OCa terminated $CaTiO_3$	0.29
Ni^{2+} substituted at the A site OSr terminated $SrTiO_3$	-1.00
Ni^{2+} substituted at the A site OBa terminated $BaTiO_3$	-1.76
Ni^{2+} substituted at the B site with a nearest neighbour oxygen vacancy OTiO terminated $CaTiO_3$	-0.95
Ni^{2+} substituted at the B site with a nearest neighbour oxygen vacancy OTiO terminated $SrTiO_3$	-0.96
Ni^{2+} substituted at the B site with a nearest neighbour oxygen vacancy OTiO terminated $BaTiO_3$	-1.15

Table 69 lists the segregation energy for the nickel doped alkaline earth titanates. The segregation energy is the difference between the solution energy at the surface and in the bulk ($E_{segregation} = E_{surface\ solution} - E_{bulk\ solution}$) where a negative value indicates a lower solution energy at the surface and, therefore, a driving force for the dopant cation to migrate to the surface. Unlike the solution energy values, clear trends can be noted for all of the titanate systems under investigation. Again at the A site there is an increasing driving force to segregate the dopant cations to the surface of the lattice as the size mismatch between the perfect lattice alkaline earth cation and the dopant cation increases. $CaTiO_3$, with substitution at the A site, is the only lattice for which segregation is not predicted. The segregation energies calculated for the B site are similar to each other and all predict a driving force for nickel to migrate to the surface which may be expect since the same cation has been replaced in each case. These findings, with the exception of the A site substituted $CaTiO_3$ lattice, are support by experimental results where migration of nickel to the surface has been positively identified [82].

The energies needed for the calculation of the surface energies of the defect systems are given in Table 70 which include bulk supercell lattice energies of defect systems, lattice energies of defect surfaces (region 1 in the models), region 1/2 (boundary) interaction energies and region 2 (subsurface block in the model) energies.

Table 70 Energies for the calculation of defect surface energies of Ni^{2+} substituted alkaline earth titanates.

System	Formula	Energy /eV
Ni^{2+} substituted at the A site of the bulk lattice	$Ca_{31}NiTi_{32}O_{96}$	-4824.46
	$Sr_{31}NiTi_{32}O_{96}$	-4784.71
	$Ba_{31}NiTi_{32}O_{96}$	-4742.01
Ni^{2+} substituted at the B site with an nearest neighbour oxygen vacancy of the bulk lattice	$Ca_{32}Ti_{31}NiO_{95}$	-4748.27
	$Sr_{32}Ti_{31}NiO_{95}$	-4708.20
	$Ba_{32}Ti_{31}NiO_{95}$	-4664.34
Ni^{2+} substituted at the A site of the OA terminated surface.	$Ca_{71}NiTi_{72}O_{216}$	-10837.22
	$Sr_{71}NiTi_{72}O_{216}$	-10747.83
	$Ba_{71}NiTi_{72}O_{216}$	-10652.89
Ni^{2+} substituted at the B site, with an oxygen vacancy nearest neighbour, of the OTiO terminated surface.	$Ca_{72}Ti_{71}NiO_{215}$	-10761.40
	$Sr_{72}Ti_{71}NiO_{215}$	-10670.92
	$Sr_{72}Ti_{71}NiO_{215}$	-10575.07
Energy of interaction between region 1 and region 2 for A site substitution	$Ca_{71}NiTi_{72}O_{216}$	-16.83
	$Sr_{71}NiTi_{72}O_{216}$	-15.33
	$Ba_{71}NiTi_{72}O_{216}$	-13.67
Energy of interaction between region 1 and region 2 for B site substitution	$Ca_{72}Ti_{71}NiO_{215}$	-16.82
	$Sr_{72}Ti_{71}NiO_{215}$	-15.27
	$Sr_{72}Ti_{71}NiO_{215}$	-13.73
Energy of region 2	$Ca_{40}Ti_{40}O_{120}$	-6009.45
	$Sr_{40}Ti_{40}O_{120}$	-5960.12
	$Ba_{40}Ti_{40}O_{120}$	-5908.27

The surface energies for the creation of perfect and defect surfaces from perfect and defect bulk lattices, respectively, are given in Table 71 for the nickel substituted alkaline earth titanates.

The surface energies for the calcium and barium titanate systems are consistent with the predictions from the solutions energies. In the case of $CaTiO_3$, the solution energy for substitution at the A site is lower in the bulk than at the surface, which reflected in the higher surface energy for the formation of an A site substituted surface. The B site substitution in $CaTiO_3$ is less favourable in the bulk, which leads to a lower surface energy. The situation is reversed in $BaTiO_3$, where the defect is more stable at the B site, and a lower surface energy has been calculated for A site substitution compared with B site substitution for this material.

The consistency between the predicted solution and surface energies for $SrTiO_3$ surfaces is less clear cut. The very low solution energy value predicted for substitution at the A site at the surface, is not reflected in a lower surface energy. However, when the perfect and doped surfaces are compared a trend is observed in the differences between the perfect and doped lattice surface energies. Specifically, there is a

correlation between how a lower solution energy for bulk doping and how favourable the formation of a defect surface is compared to the formation of a perfect surface. For example, for A site doping in $CaTiO_3$ the nickel is most easily accommodated in the bulk lattice and it is the only system which predicts a lower energy for perfect lattice surface formation than that for the defect lattice. For B site substitution in $SrTiO_3$, the solution energy at both the surface and in the bulk was predicted to be lower than the other alkaline earth titanate systems, and the resulting surface energy is slightly higher than the other lattices considered. Comparing the perfect and B site doped lattice surface energies reveals that the formation of the defect lattice is favoured over the prefect lattice surface in all cases. For the $CaTiO_3$ and $BaTiO_3$ lattices, the differences in solution energies are similar, whereas the difference is lower for $SrTiO_3$ which implies that the perturbation of the lattice caused by the introduction of the defect has less effect on the growth of a crystal face parallel to the 001 crystal plane than for the other titanate lattices.

Table 71 Surface energies of perfect and Ni^{2+} substituted surfaces.

System	Surface Energy /Jm^{-2} (Defect Surface)	Surface Energy /Jm^{-2} (Pure Surface)	Difference /Jm^{-2}
Ni^{2+} A site substituted OCa terminated surface $CaTiO_3$	1.39	1.28	0.09
Ni^{2+} A site substituted OSr terminated surface $SrTiO_3$	1.24	1.49	-0.25
Ni^{2+} A site substituted OBa terminated surface $BaTiO_3$	1.08	1.48	-0.40
Ni^{2+} B site substituted, with a nearest neighbour oxygen vacancy OTiO terminated surface $CaTiO_3$	1.29	1.50	-0.21
Ni^{2+} B site substituted, with a nearest neighbour oxygen vacancy OTiO terminated surface $SrTiO_3$	1.34	1.42	-0.08
Ni^{2+} B site substituted, with a nearest neighbour oxygen vacancy OTiO terminated surface $BaTiO_3$	1.13	1.45	-0.32

7.4. Summary of Surface Atomistic Modelling

In this chapter the surface conformations and energies of the pure and nickel substituted alkaline earth titanates modelled using atomistic techniques were considered. As for the bulk, the results were dominated by the size mismatch between the Ni^{2+} defect and the pure lattice cations. Very little relaxation of the surfaces for the pure lattices was predicted, with some alteration in the interlayer spacings noted. For A site substitution the defect ion was found to relax into the surface, with the magnitude of the displacement determined by the size of the cavity formed by the removal of the A site cation. For B site substitution, only the case of having the charge compensating oxygen vacancy as a nearest neighbour was considered. Some relaxation around the defect cluster was predicted, which was dominated by the movement of oxygens in the second outermost layer moving towards the vacancy site.

The predicted surface and solution energies predict that A site substitution is favoured over B site substitution for $CaTiO_3$, and vice versa for $BaTiO_3$. The situation for $SrTiO_3$ is less clear, with a very low solution energy predicted for surface A site substitution. The lower values of solution energy predicted for surface substitution compared with bulk substitution, expect for $CaTiO_3$ A site substitution, indicate that surface segregation is likely for most of the systems studied. Note, the calculated energies only provide information for the structure under equilibrium conditions, as will be seen in Chapter 10, kinetics factors play an important role in the synthesis of real catalytic materials.

8. Study of the Surface Structure and Energetics of Nickel Doped Alkaline Earth Titanates using Density Functional Theory

Analyses of the surface structure and energetics of perfect and nickel doped alkaline earth titanates were carried out using density functional theory. In contrast to the interatomic potential calculations described in Chapter 7, in DFT, surfaces are simulated by defining a symmetrical "slab" of the lattice where both the top and the bottom of the slab are surfaces exposed to vacuum. In this chapter, results of the DFT surface calculations are presented for the OA terminated surfaces, with substitution at the A site only, for the three titanates we are considering. Energy optimisations of the OTiO terminated surfaces were extremely slow to converge, which may be due to strong Ti-O interactions (and partial covalency of the Ti-O bonds) which exist on this surface in contrast to the purely ionic interactions of the OA surfaces, and reliable results were not obtained within the time available.

For each of the titanates, symmetrical slabs were formed by "removing" 7 layers (parallel to the 001 bulk crystal plane) for calcium and strontium titanates, and 11 layers for $BaTiO_3$. Parallel to the surface the simulation cell could be thought of as a 2×2 supercell (compared to the cubic perovskite structure) where each of the OA layers contained 8 atoms (A_4O_4) and the OTiO layers contained 12 atoms (Ti_4O_8). The use of 7 layers means that 3 complete TiO_6 octahedra are found from the top to the bottom of the slabs, and 11 layers gives 5 complete TiO_6 octahedra. It is important to note that these slabs are symmetrical with respect to the the layers present at the top and the bottom of the slab (both OA terminated) and consequently there is one more OA layer than OTiO layers which in turn means that slabs are not stoichiometric with respect to the bulk lattice. The "formulas" of the slabs are $Ca_{16}Ti_{12}O_{40}$, $Sr_{16}Ti_{12}O_{40}$ and, $Ba_{24}Ti_{20}O_{64}$. The calculation of surface energies cannot be carried out for the DFT results due to the non-stoichiometric nature of the slabs.

In surface calculations it is important that slabs contain a centre of inversion to ensure no dipole forms between the top and the bottom of the slab which would quickly cause the DFT calculation to fail. Slabs cut from the bulk of calcium and strontium titanates contained a centre of inversion. However, due to the ferroelectric distortion of barium titanate, no centre of inversion existed in the slabs cut from this lattice. A novel approach was therefore used to introduce a centre of inversion into the barium titanate

slabs whereby two "half" slabs were cut from the bulk crystal which were placed "back to back" to create a slab where the displacement of the titanium cations was in the +z direction in one half of the slab and in the –z direction in the other half of the slab.

The basis sets and computational details were as for the bulk calculations, and are given in Section 6.1.

8.1. Periodic DFT Modelling of the OA Terminated (001) Surface of Undoped Titanates

Figure 55 shows the predicted relaxation for the $CaTiO_3$ surface slab. As can be seen no significant displacement of the ions has occurred. Although the interlayer spacing shows a similar pattern to the interatomic potential results (with the distance between layers 1 and 2 being reduced compared to the bulk, and the distance between layers 2 and 3 being larger than the bulk), the magnitude of these changes are less marked for the DFT calculations. In the interatomic potential calculations the spacing between layers 1 and 2 was 1.81 Å (c.f. 1.91 Å for DFT), and the spacing between layers 2 and 3 was 2.08 Å (c.f. 1.97 Å for DFT). Note, no convergence tests were carried out with respect to the slab thickness due to time constraints.

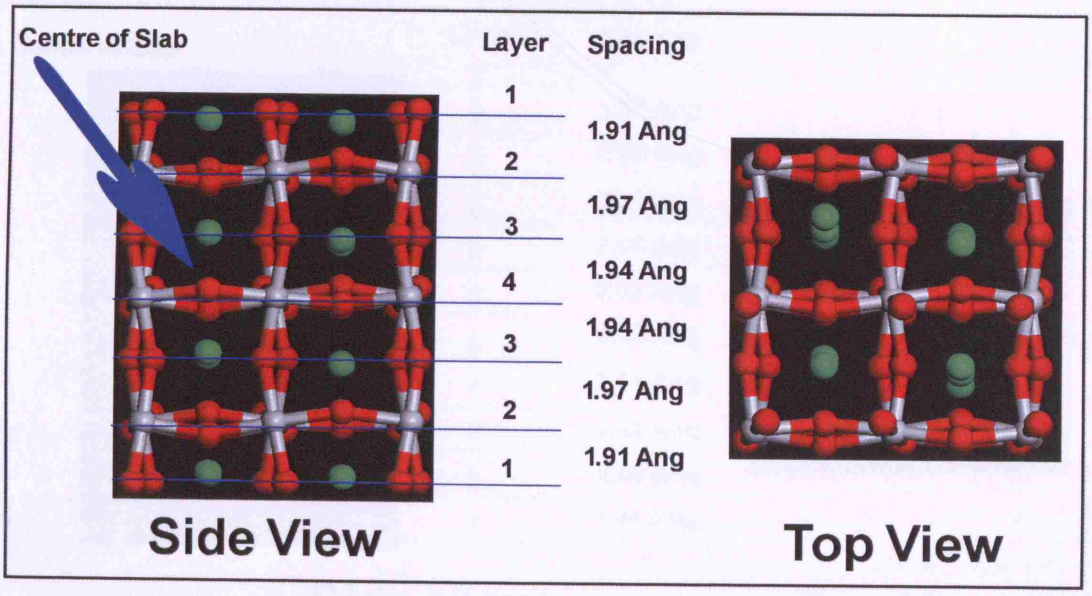

Figure 55 Conformation of the surface slab of the OCa terminated surface (parallel to the 001 bulk crystal plane) as predicted by DFT for $CaTiO_3$.

Figure 56 shows the relaxation for the $SrTiO_3$ slab to have similar features to those noted for $CaTiO_3$ i.e. no noticeable surface reconstruction and the interlayer

spacing between layers 1 and 2 showing a less marked movement than for the interatomic potential calculations (layer 1/2 spacing is 1.71 Å for interatomic potentials and 1.92 Å for DFT). However, the interlayer spacing between layers 2 and 3 is larger than that predicted by interatomic potentials (1.97 Å, c.f. 2.03 Å for DFT).

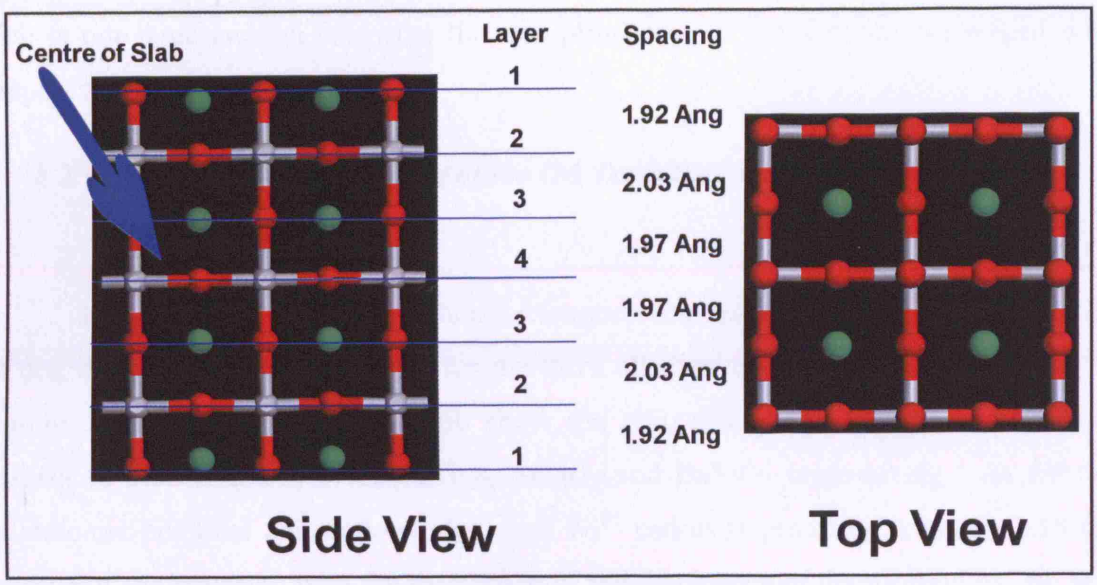

Figure 56 Conformation of the surface slab of the OSr terminated surface (parallel to the 001 bulk crystal plane) as predicted by DFT for $SrTiO_3$

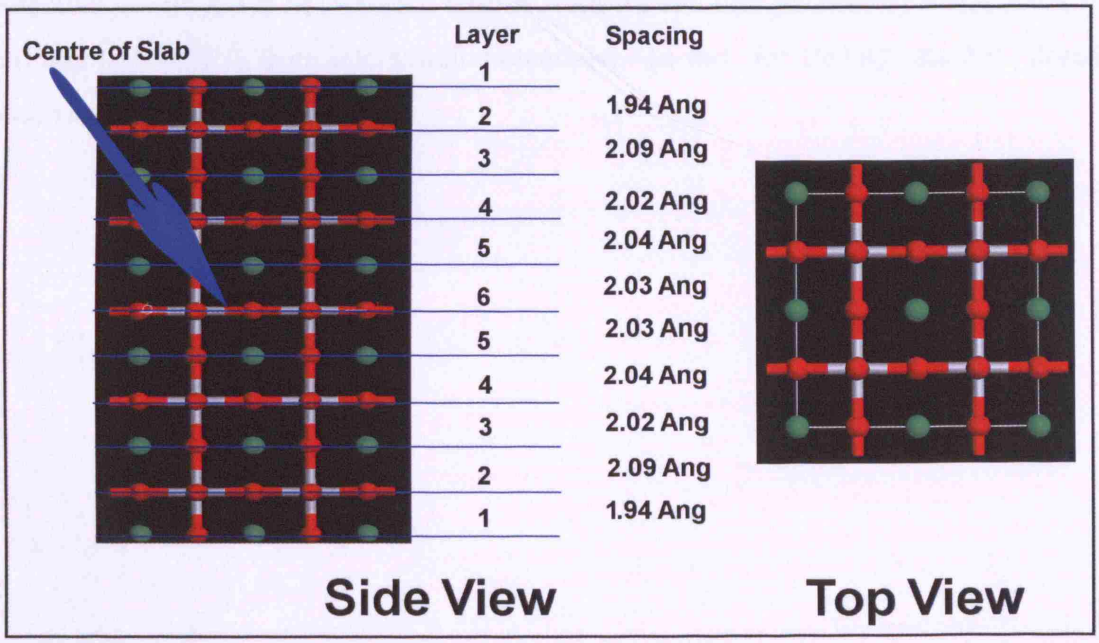

Figure 57 Conformation of the surface slab of the OBa terminated surface (parallel to the 001 bulk crystal plane) as predicted by DFT for $BaTiO_3$

Figure 57 shows the relaxation of the $BaTiO_3$ surface slab. As can be seen there are 5 layers either side of the centre of the slab in this slab. No displacement of the titanium cations from the centre of the B site positions can be seen, so no ferroelectric distortion is predict for this slab. The changes in the interlayer spacings are more in line with the interatomic potential calculations which may indicate that the thickness of the slab is not large enough to ensure that the properties of the slab are converged with respect to its thickness.

8.2. Periodic DFT Modelling of the OA Terminated (001) Surface of Ni(II) Doped Titanates

In this section the DFT predicted relaxation around a Ni^{2+} dopant cation placed at one of the four surface A sites, for the three alkaline earth titanates, is considered. Figure 58, Figure 59 and Figure 60 show the relaxation of the dopant cation with respect to the surface slab for $CaTiO_3$, $SrTiO_3$ and $BaTiO_3$ respectively. As for the interatomic potential calculations, the small Ni^{2+} cation is predicted to move into the surface of the material, with the magnitude of the displacement determined by the size mismatch between the perfect lattice A site cation and the Ni^{2+} dopant. The Ni^{2+} dopant is displaced into the surface by 0.55 Å for $CaTiO_3$ (c.f. 0.35 Å from interatomic potentials), 0.66 Å for $SrTiO_3$ (c.f. 0.60 Å from interatomic potentials) and 1.25 Å for BaTiO3 (c.f. 0.81 Å from interatomic potentials). In fact, for $BaTiO_3$ the Ni^{2+} dopant becomes part of layer 2.

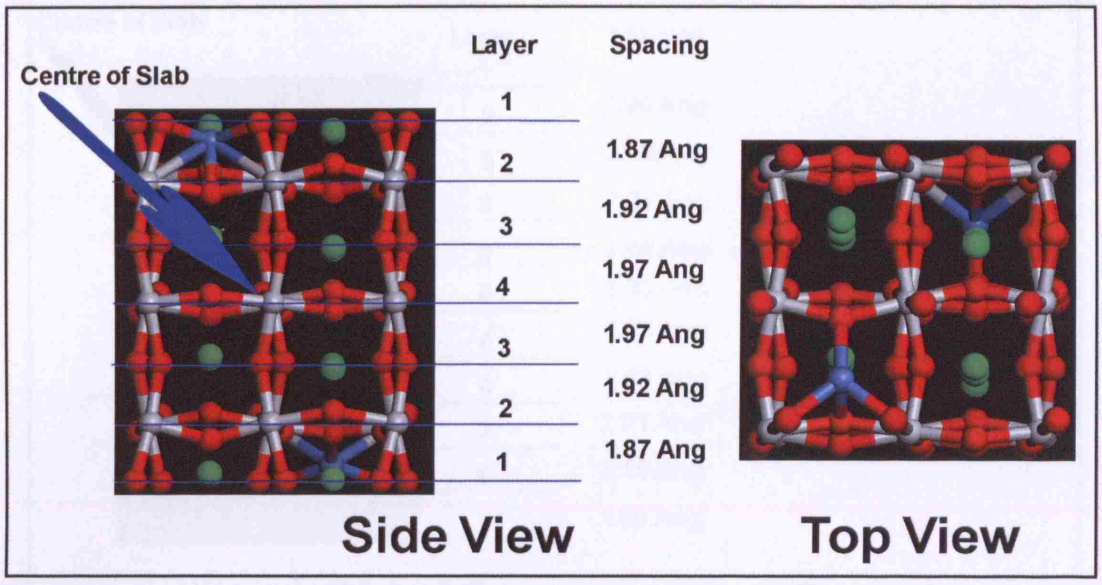

Figure 58 Conformation of the OCa terminated surface of $CaTiO_3$ following substitution of Ni^{2+} at a Ca^{2+} surface site as predicted by DFT.

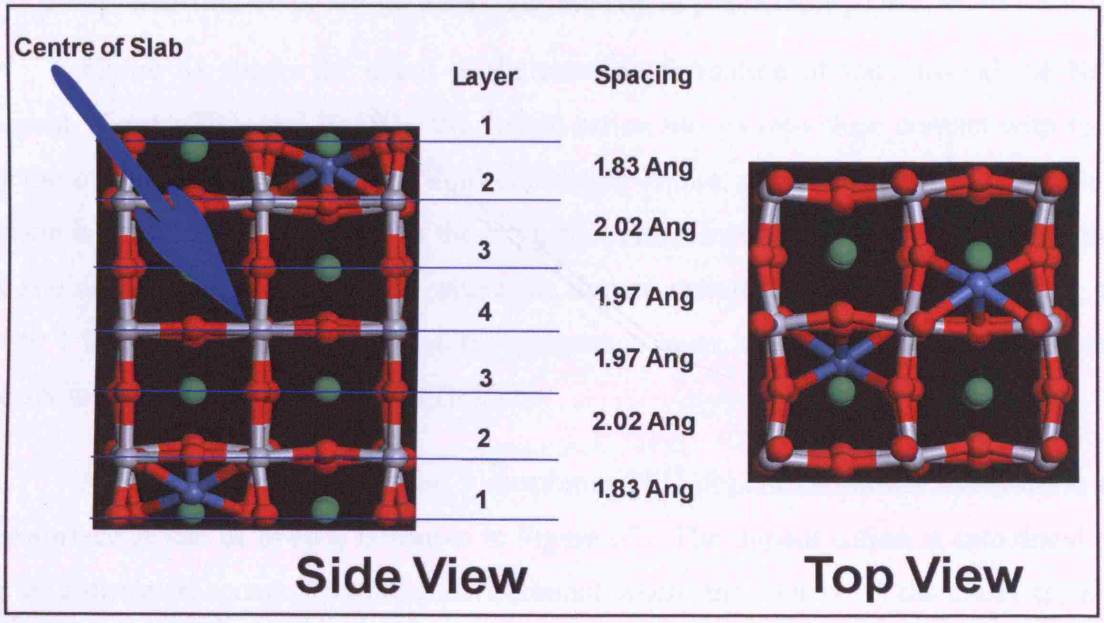

Figure 59 Conformation of the OSr terminated surface of $SrTiO_3$ following substitution of Ni^{2+} at a Sr^{2+} surface site as predicted by DFT

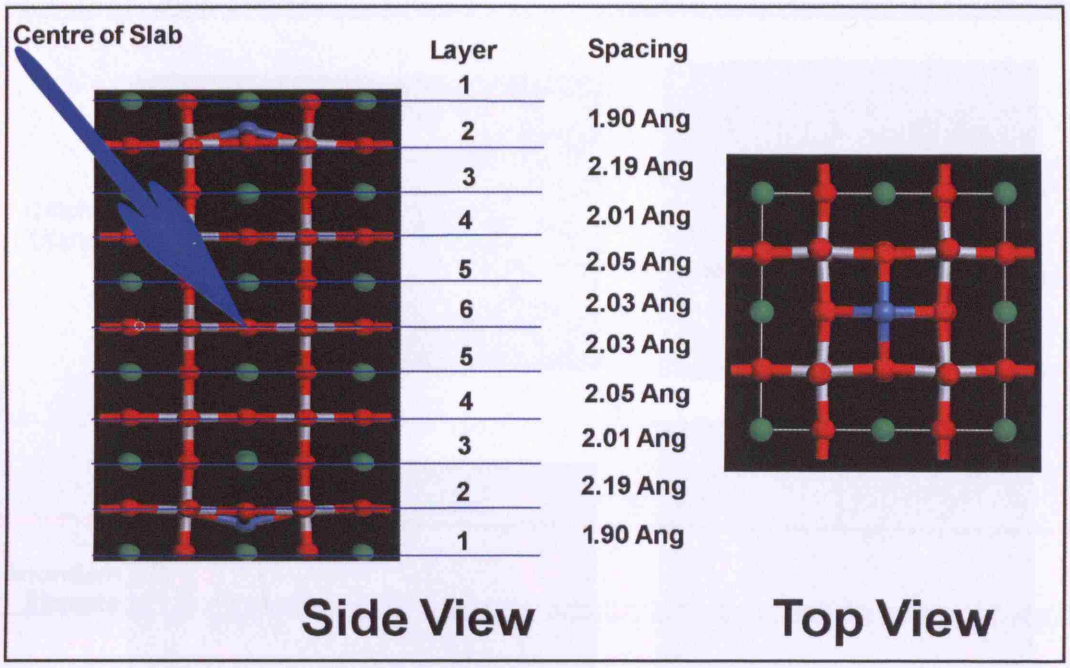

Figure 60 Conformation of the OBa terminated surface of $BaTiO_3$ following substitution of Ni^{2+} at a Ba^{2+} surface site as predicted by DFT.

Figure 61 shows the detail of the local conformation of ions around the Ni^{2+} dopant. For $CaTiO_3$ and $BaTiO_3$, the dopant cation moves into close contact with four of the oxygens making up the 12-fold coordinate A site, whereas for $SrTiO_3$ the Ni^{2+} cation is in close contact with 5 of the oxygens. The effect of increasing the size of the A site cavity can be seen clearly where the dopant cation is closer to the oxygens of layer 1 for $CaTiO_3$, equidistant from the oxygens in layer 1 and layer 2 for SrTiO3, and closer to the oxygens of layer 2 for $BaTiO_3$.

A more detailed view of the 5 coordinate Ni^{2+} dopant cation for substitution at the surface A site of $SrTiO_3$ is shown in Figure 62. The dopant cation is calculated to be in a distorted square pyramidal environment where the four Ni-O distances around the "base" of the pyramid are very close to the Ni-O distance of 2.09 Å in NiO [177]. The differences in the local conformation around the dopant cation in the three alkaline earth titanates may be a significant factor in determining how well anchored a nickel oxide cluster would be to the surface, as the conformation around the dopant for $SrTiO_3$, only, provides an accessible "seed" for the growth of such a cluster.

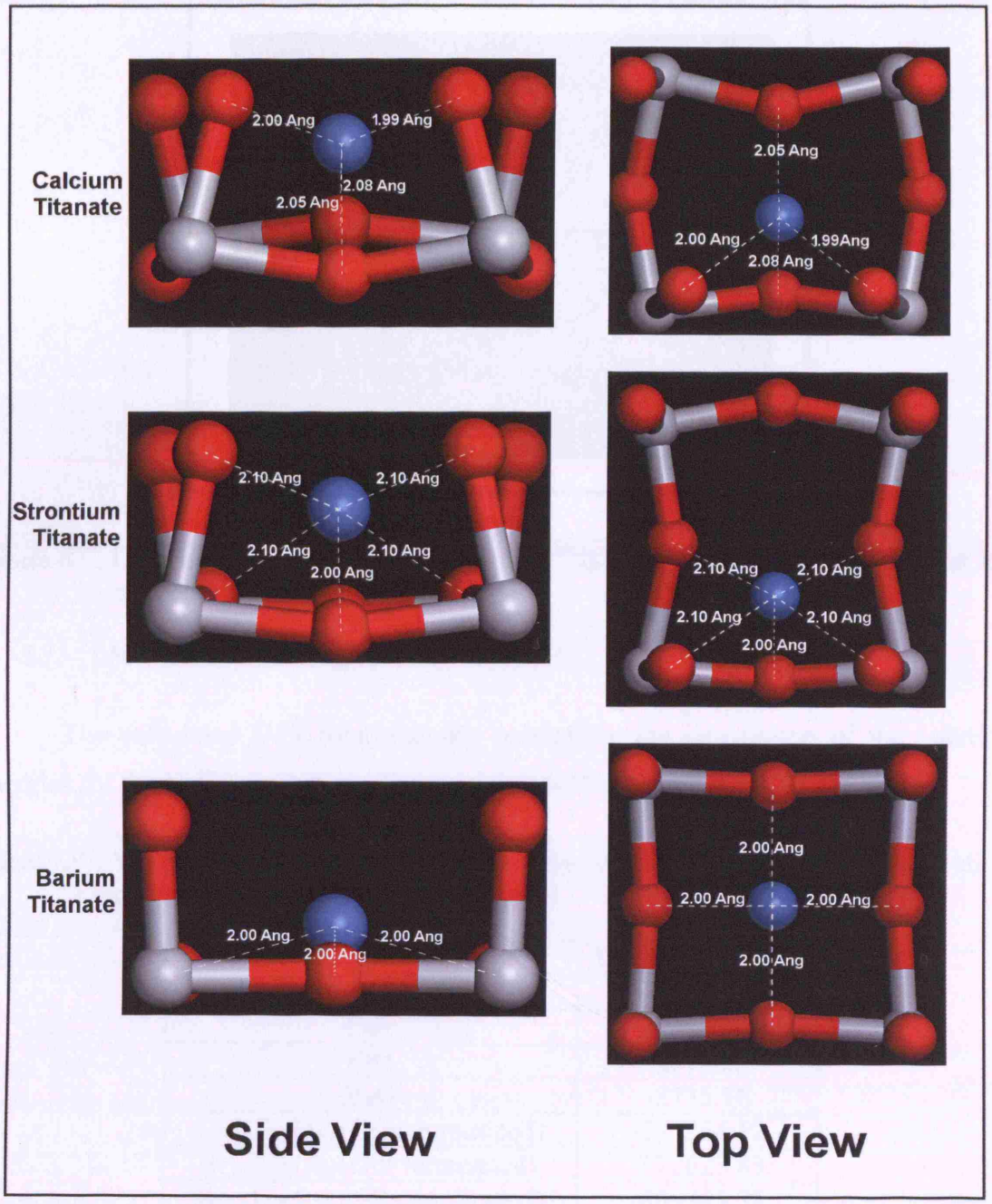

Figure 61 Local conformation around the Ni^{2+} dopant cation at the surface of the alkaline earth titanate structures as predicted by DFT.

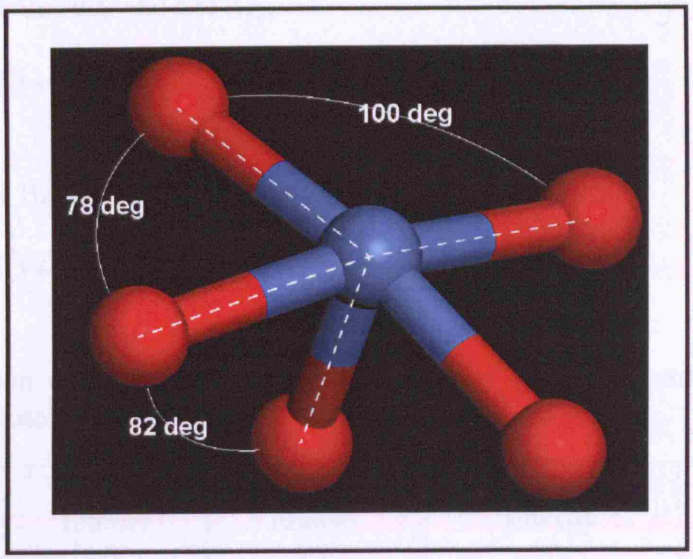

Figure 62 Detailed view of the 5 coordinate Ni^{2+} dopant cation for substitution at the surface A site of $SrTiO_3$.

8.3. Ni^{2+} Solution Energies

The calculated DFT total energies needed for the calculation of the solution energies for the Ni^{2+} substitutions discussed in this chapter are given in Table 72.

Table 72 Total energies needed for the calculation of solution energies for dissolution of NiO into the alkaline earth titanates.

Compound	Total Energy /eV
NiO	-43090.02
CaO	-3043.24
SrO	-2878.23
BaO	-2735.18
$Ca_{16}Ti_{12}O_{40}$ (OCa terminated)	-375254.12
$Sr_{16}Ti_{12}O_{40}$ (OSr terminated)	-372623.83
$Ba_{24}Ti_{20}O_{64}$ (OBa terminated)	-609945.78
$Ca_{14}Ni_2Ti_{12}O_{40}$ (OCa terminated) A site substituted	-455345.39
$Sr_{14}Ni_2Ti_{12}O_{40}$ (OSr terminated) "A" site substituted	-453043.10
$Ba_{22}Ni_2Ti_{20}O_{64}$ (OBa terminated) "A" site substituted	-690646.37

Using the total energy values in Table 72, the solution energies were calculated from energy cycles based on the following equations and are given in Table 73 along with the segregation energies ($E_{surface}$-E_{bulk}):

1. For $CaTiO_3$ and $SrTiO_3$:

$$NiO + \frac{1}{2}A_{16}Ti_{12}O_{40} \rightarrow \frac{1}{2}A_{14}Ni_2Ti_{12}O_{40} + AO$$

2. For $BaTiO_3$:

$$NiO + \frac{1}{2}Ba_{24}Ti_{20}O_{64} \rightarrow \frac{1}{2}Ba_{22}Ni_2Ti_{20}O_{64} + BaO$$

Table 73 Solution energies and surface energies for A site substitution at the OA terminated surface.

System	Solution Energy /eV (DFT)	Solution Energy /eV (Atomistic)	Segregation Energy /eV (DFT)	Segregation Energy /eV (Atomistic)
Ni^{2+} at A site $CaTiO_3$	0.97	1.17	-0.96	0.29
Ni^{2+} at A site $SrTiO_3$	2.00	0.26	0.04	-1.00
Ni^{2+} at A site $BaTiO_3$	4.55	1.28	2.00	-1.76

The solution energies, as calculated using DFT, show the expected trend that as the A site cavity becomes larger, with increasing alkaline earth cation size, the substitution at the surface A site becomes less favourable. There is reasonable agreement between the results predicted by DFT and interatomic potentials for $CaTiO_3$. However, DFT predicts the solution energy to be significantly higher for both $SrTiO_3$ and $BaTiO_3$ than for interatomic potentials. A possible explanation for these anomalies is that the 5-fold coordination predicted for the coordination of the dopant cation in the $SrTiO_3$ and $BaTiO_3$ lattices would be unfavourable, thus increasing the energy of the system. Clearly further calculations would be necessary to support this hypothesis. It should be noted that the bulk calculations, from both DFT and interatomic potentials, that B site doping is more favourable than A site doping in $BaTiO_3$ and the former would be expected to dominate in this system. Since there is a complete set of data from the interatomic potentials calculations, the discussion in Chapter 10 will concentrate on these data.

Comparing the calculated solution energies with the bulk results we find that there is a driving force for Ni^{2+} cations to migrate to the surface A site for $CaTiO_3$ since the segregation energy is -0.96 eV which is in contrast to the interatomic potential work. However, all of the solution energies are predicted to be endothermic and the system

would be expected to phase separate on heating. In the case of $SrTiO_3$, the segregation energy close to zero at 0.04 eV which may lead to a more controlled release of nickel from the bulk lattice during calcination of the catalyst material. For $BaTiO_3$, the segregation energy of 2.00 eV predicts a strong resistance to migration of nickel to the surface A sites which is in contrast to the interatomic potential result, but it reflects the instability of the system predicted using DFT. Unfortunately, results are not available from DFT for surface B site doping, which would be expected to be lower than for surface A site doping if the bulk trends are repeated at the surface, and may explain the release of nickel observed on heating nickel doped barium titanate [82].

8.4. Summary of Surface DFT Modelling

In this chapter the substitution of Ni^{2+} at the surface A site of the three alkaline earth titanates was considered. Analysis of the relaxed structures showed that the larger the cavity formed by the removal of the A site cation the further into the surface the small Ni^{2+} dopant cation moved. The solution energies calculated for the dissolution of NiO into the lattice showed that the larger the size mismatch between the Ni^{2+} dopant and the perfect lattice alkaline earth cation the larger the energy cost for the dissolution process. Comparison with bulk results showed that there is a strong driving force for the segregation to the surface of Ni^{2+} cations into the surface A sites for $CaTiO_3$, very little driving force for $SrTiO_3$ and a resistance to surface migration for $BaTiO_3$.

9. Investigating the Tetragonal to Cubic Solid State Phase Change in Strontium Titanate

The low temperature tetragonal phase of strontium titanate can be successfully modelled using atomistic modelling, see Chapter 5. Since $SrTiO_3$ is known to undergo a phase transition to cubic symmetry at 110 K [11], it was decided to investigate whether the phase change could be modelled using static interatomic potential calculations. Two sets of free energy calculations were carried out: over a range of 0-300 K at 10 K intervals; and over a range of 90-120 K at 1 K intervals. The data were analysed for evidence of the phase transition both structurally and thermodynamically. The results from these analyses are considered below.

Clearly the most obvious data to analyse when looking for a structural phase change are the atomic positions and cell parameters. Figure 63 shows plots of the percentage difference between the a and b, a and c, and b and c cell parameters versus simulation temperatures for free energy calculations on strontium titanate. There are two obvious outliers in these plots at 20 K and 230 K, which could possibly be due to a complex energy surface with the simulation finding a minimum that is inconsistent with the other calculated conformations. Despite these anomalies, the general trend in the results is clear where there is a decreasing difference between the a parameter and the b and c parameters between 10K and 110K, and a negligible difference at higher temperatures. Also there is a negligible difference between the b and c parameters across this temperature range. In other words, the system shows tetragonal symmetry up to 110 K and cubic at higher temperatures, as observed experimentally.

Having found evidence for a change in symmetry from the cell parameters, the tilting of the TiO_6 octahedra was analysed, to facilitate which Java code was written to analyse the atomic position data from the GULP output file. The data were analysed as follows:

1. Atomic positions are read in from the GULP output file.

2. The nearest neighbours to each Ti atom are found which, of course, are the six surrounding oxygens.

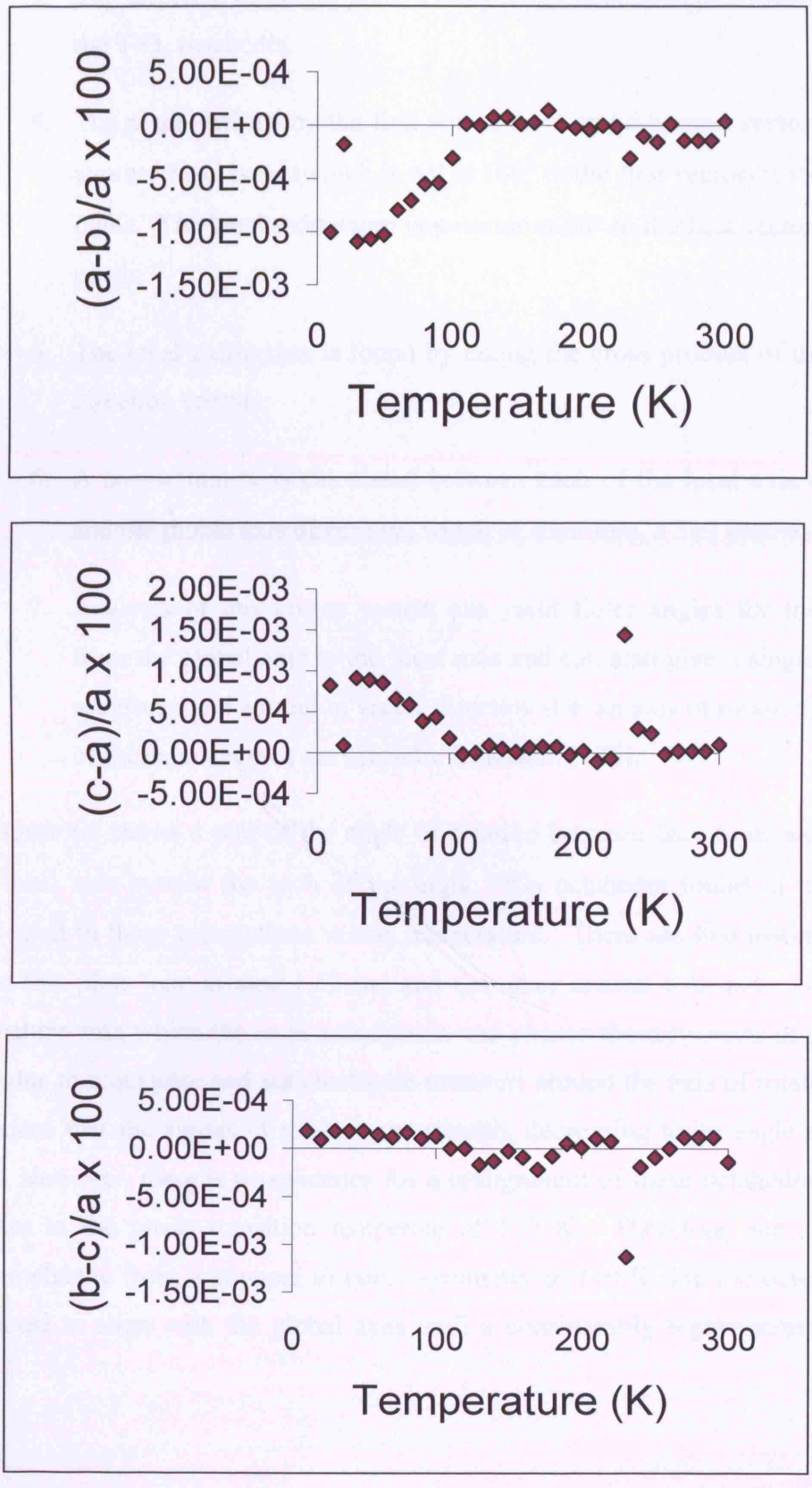

Figure 63 Plots of the percentage difference between the a and b, a and c, and b and c cell parameters versus temperature from free energy calculations on strontium titanate.

3. The direction of one of these Ti-O vectors is defined as a local x axis for the TiO_6 octahedra.

4. The plane defined by the first vector from and a second vector found by another Ti-O bond (which is not at 180° to the first vector) is the local xy plane. The local y direction is a vector at 90° to the first vector in the xy plane.

5. The local z direction is found by taking the cross product of the x and y direction vectors.

6. A cosine matrix is calculated between each of the local axis directions and the global axis directions, which is, therefore, a 3×3 matrix.

7. Analysis of this cosine matrix can yield Euler angles for the rotation from the global axis to the local axis and can also give a single angle of rotation about a rotation vector direction (i.e. an axis of rotation). Details of these procedures are given by Goldstein [178].

Figure 64 shows a plot of the angle of rotation between the global axis system and the local axis system for each of the eight TiO_6 octahedra found in the 2×2×2 supercell used in these calculations versus temperature. There are two distinct sets of angles on this plot: one around 1.63 rad and the other around 1.40 rad. Due to the random nature with which the local axis system was chosen these two sets of points are probably due to clockwise and anticlockwise rotations around the axis of rotation. This plot indicates that the angles of rotation are steadily decreasing to an angle of around 1.55 rad. However, there is no evidence for a realignment of these octahedra with the global axes at the phase transition temperate of 110 K. Therefore, the simulation indicates a change from tetragonal to cubic symmetry at 110 K, but the octahedra are not predicted to align with the global axes until a considerably higher temperature is reached.

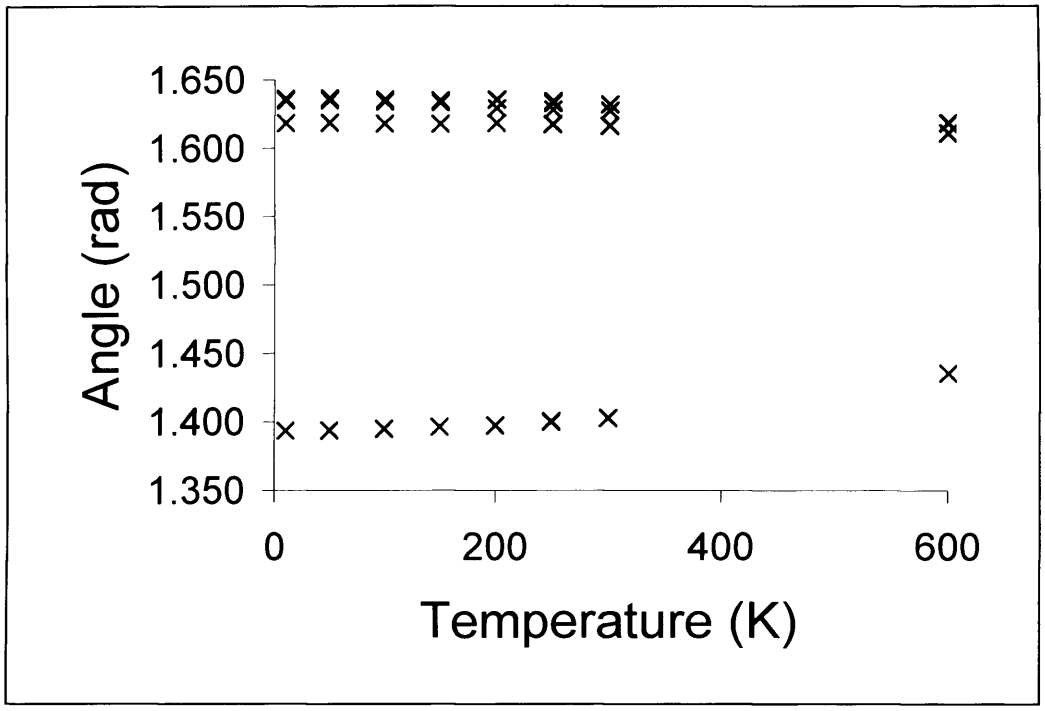

Figure 64 Plot of Angle of Rotation between the global axis and the local axis defined for each TiO_6 octahedra versus temperature from free energy calculations of strontium titanate.

Published experimental data on the structure of strontium titanate at room temperature consistently record that the TiO_6 octahedra are aligned with the global axes of the system, with each of the 12 oxygen nearest neighbours to Sr having the same Sr-O bond length. It was decided, therefore to examine the predicted free energy difference between energy minimised structure used so far and the experimental structure. The optimised structure has a free energy of -1194.63 eV at 300 K and the experimental structure has a free energy of -1193.92 eV, giving a difference of 0.71eV between these two structures. For each of these simulations there are 40 atoms in the unit cell (a 2×2×2 supercell has the formula $Sr_8Ti_8O_{24}$), therefore, the free energy difference between these structures is 0.018eV per atom, which can be compared to the value of k_BT at T=300K (where k_B is the Boltzmann constant) of 0.025 eV and it can be seen that the system would have enough energy to change from the tilted to the straight octahedral conformation. It must be remembered that the experimental structure is not a stable minimised structure using this parameter set in the simulation as shown by the presence of negative phonon frequencies. It may be suggested, therefore, that the observed experimental structure is in fact a saddle point and the measured structure is

time averaged over the librational conformation of the TiO_6 octahedra. This analysis is, of course, speculative at this stage.

In order to provide more evidence of a phase change around 110 K an analysis of the Helmholtz free energy F, provided in the GULP output files was undertaken. The Helmholtz free energy is related to the Gibbs free energy as shown in Equation 107:

107] $$G = F + PV$$

where G and F are the Gibbs and Helmholtz free energy respectively, P is the pressure and V is the volume. Since the external pressure in these simulations was zero, i.e. a vacuum, the Helmholtz and Gibbs free energies are identical in this case. For a first order phase transition a discontinuity in the first derivative of the free energy with respect to a thermodynamic parameter (such as temperature) would be expected as the temperature goes through the transition temperature, and for a second order phase change a discontinuity in the second derivative of the free energy would be expected.

Figure 65 shows plots of the free energy, the first derivative with respect to temperature and the second derivative with respect to temperature versus temperature across the range 10 K to 300K. A discontinuity in either the first or second derivative around 110 K would support the evidence provided by the cell parameter analysis for a phase change. Clearly there is no discontinuity in either the free energy or its first derivative plots, so the observed phase change does not appear to be first order, which is also the case for the second derivative of free energy. However deviations are observed at higher temperatures, above 220K. Since there is such a small distortion of the lattice at 110K, discontinuities in thermodynamic properties are likely to be small. Therefore, it was decided to analyse the suggested phase change temperature in more detail by taking free energy measurements over a small temperature range (90 K to 120 K) in steps of 1 K.

Figure 66 shows the results from these calculations. Once again there is no discontinuity in the free energy plot, which is consistent with the larger range results above. However, there is a feature on the first derivative plot at around 102 K which may indicate a first order phase change, although this discontinuity is not clear enough to provide firm evidence for the structural transition. A suggestion for future work to improve the resolution of plots would be to increase the size of the simulation cell.

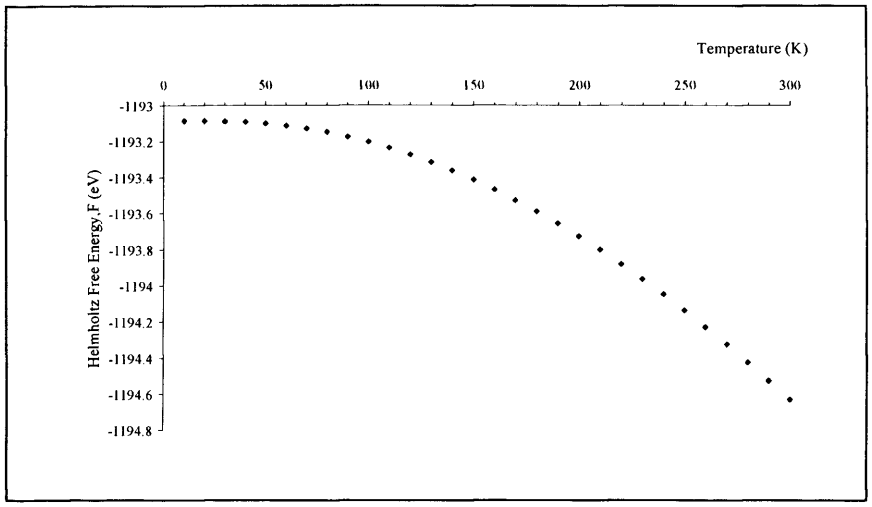

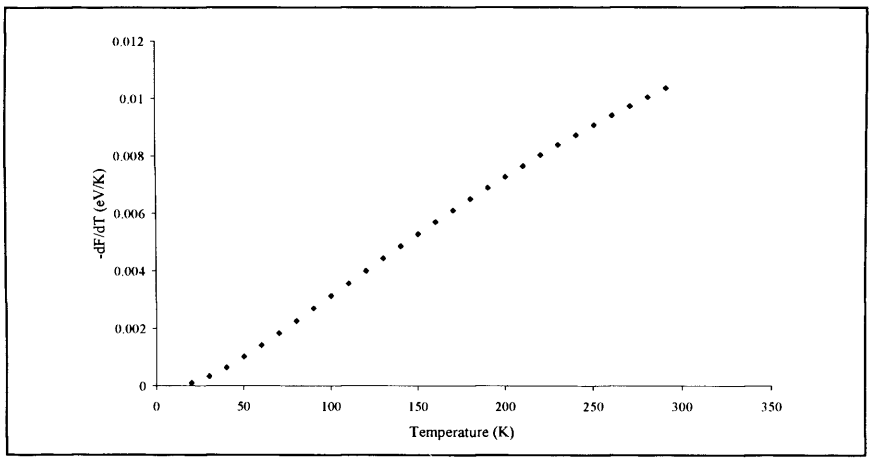

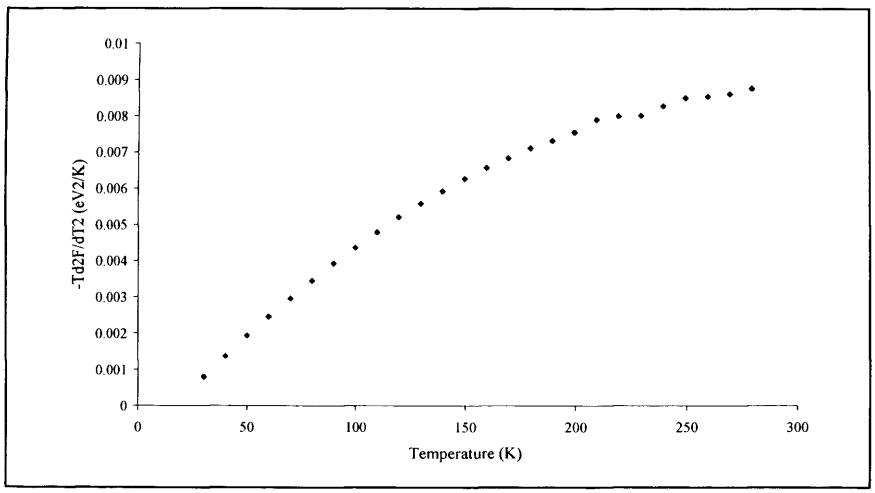

Figure 65 Plots of the Helmholtz free energy, F, -dF/dT and $-Td^2F/dT^2$ versus temperature for strontium titanate from 10 K to 300 K.

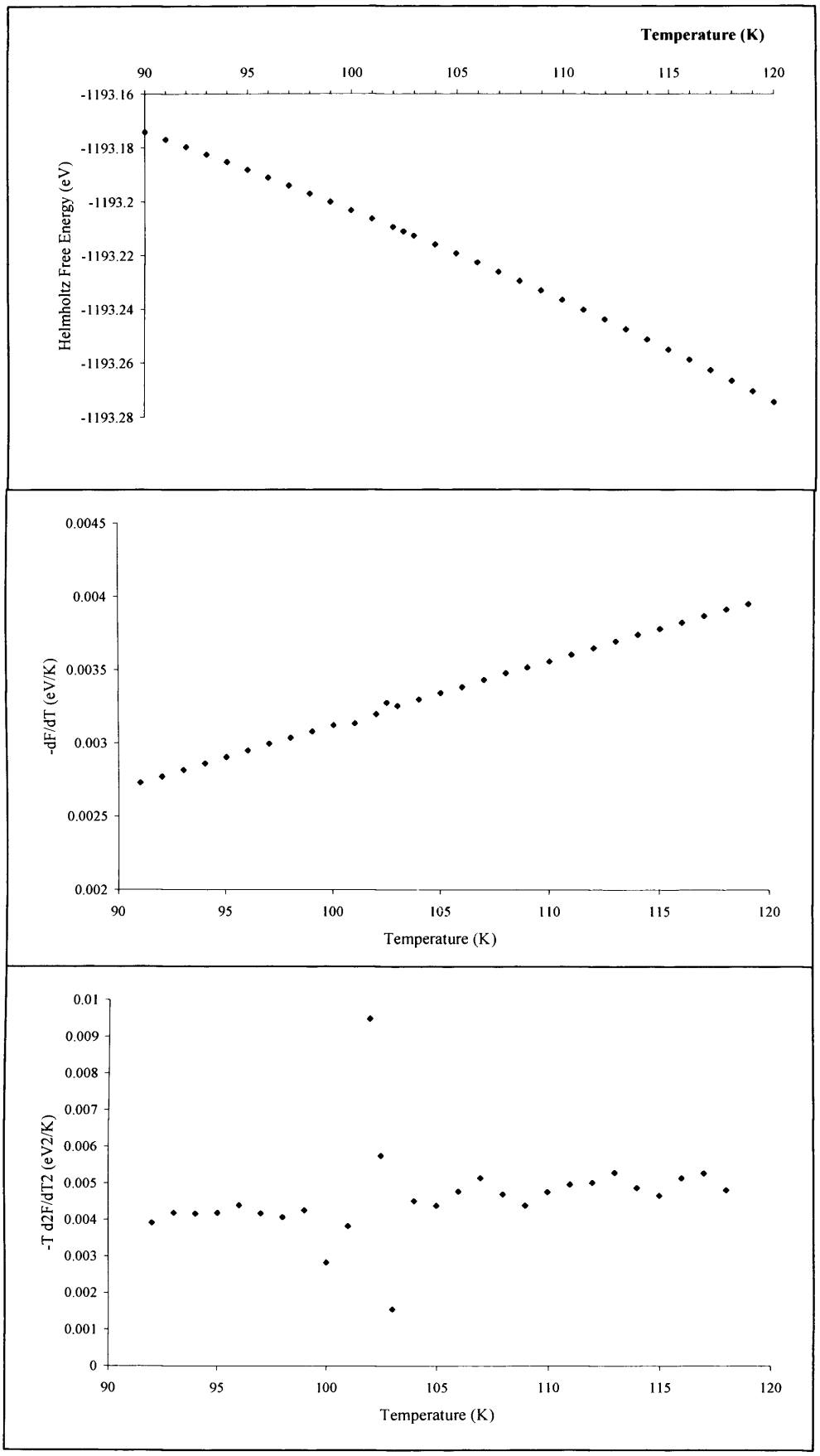

Figure 66 Plots of the Helmholtz free energy, F, -dF/dT and $-Td^2F/dT^2$ versus temperature for strontium titanate from 90 K to 120 K

There is clear evidence from the analysis of the lattice parameters that there is a change in symmetry from tetragonal to cubic around 102 K, and there is some suggestion from the free energy calculations for a first order phase change at this temperature. However, analysis of the TiO_6 octahedral tilt shows very poor agreement with experimental results. Although, due to the complex nature of the potential energy surface of perovsite structures, there will be many local energy minima, and the interatomic potential simulations will only find one of these minima. During an experimental study, a time averaged confirmation will be seen as the structure moves between the local minima during the analysis which may explain some of the disparity between the experimental and simulation results.

10.Discussion and Implications for Catalysis

The $Ni/SrTiO_3$ system is the most active of the nickel doped alkaline earth titanate materials investigated by Takehira et al [82] for the catalysis of the partial oxidation of methane. In this chapter, the predictions obtained from the computational modelling of perfect and nickel doped strontium titanate will be interpreted in the context of experimental results (from EXAFS analysis) to propose a model for the structure of this catalytic material. Once a model for the active system has been established, the likely differences, and similarities, for the $Ni/CaTiO_3$ and $Ni/BaTiO_3$ lattices, as predicted by computational modelling, can be considered. The main focus of this discussion will be to answer the question posed in the Introduction: "Why is nickel doped strontium titanate a material which forms small, well dispersed and stable particles of catalytically active nickel on its surface, whereas the other alkaline earth titanates do not?". Moreover, if this question can be answered, what are the wider implications for the production of catalysts based on the dispersion of metal particles on perovskite host lattices?

In outline, this chapter will present the experimental results obtained by Beale et al [83] for a nickel doped strontium titanate material followed by a proposal for the nature of the catalysts under investigation and, finally, the wider implications for the production of catalysts will be considered.

10.1. EXAFS Analysis of Nickel Doped Strontium Titanate (Prepared by Beale et al [83])

A nickel doped strontium titanate material was prepared using a hydrothermal synthesis technique whereby a mixture of solutions of nickel (II) nitrate tetrahydrate, strontium chloride hexahydrate, titanium tert-butoxide, ethylene glycol and potassium hydroxide (molar ratios 0.05:1:0.95:1:5, to achieve doping at the 5% level) were heated at a temperature of 150°C for 20 hours. The product was filtered, washed with HPLC grade water and dried. XRD powder patterns were recorded to confirm the synthesis of a crystalline material.

XAS measurements were carried out at station 7.1 of the Daresbury Synchrotron Radiation facility, which operates at 2 GeV with a typical current of 150 to 250 mA. The station was equipped with a Si(111) double crystal monochromator, and ion

chambers to measure incident and transmitted beam intensities for recording X-ray absorption spectra. Ni K-edge XAS data were recorded in the both transmission and fluorescence mode using a 9 element Canberra detector, in step scanning mode with an energy resolution of 1 eV per step over the XANES. Ti K-edge XAS data were recorded in transmission mode. 10 μm thick Ni and Ti foils were used to calibrate the monochromator positions. In order to record data on nickel strontium titanate samples after high temperature treatment self supporting discs (typically 40 mg of sample was pressed into a pellet) were mounted into a cell designed to allow *in situ* XAS measurements. The samples were heated at 5°C/minute from room temperature in either flowing air (for calcination) or a 5 % H_2/He mix up to 950°C and held at this temperature for 30 minutes. The cell was then cooled down to room temperature and sealed before beginning XAS measurements.

Table 74 Results of EXAFS analysis.

Sample	Shell	R(Å)	CN
Ni/$SrTiO_3$ (5%)	Ni-O	2.03	5.6 (6)
	Ni-Sr	3.35	8.0
	Ni-Ti	3.95	6.0
Calcined 850°C	Ni-O	2.02	4.5
	Ni-Sr	3.37	8.0
	Ni-Ti	3.98	6.0
	Ni-Ni	2.95	2.96
Reduced 900°C	Ni-O	2.01	3.4
	Ni-Sr	3.35	8.0
	Ni-Ti	3.98	6.0
	Ni-Ni	2.50	3.1
Reduced 950°C	Ni-O	2.01	2.4
	Ni-Sr	3.35	8.0
	Ni-Ti	3.97	6.0
	Ni-Ni	2.49	4.1

The local conformation (bond distances and coordination numbers) around the nickel dopant cation from the EXAFS analysis are listed in Table 74 for the nickel doped strontium titanate material at the different stages in its production.

10.2. Summary of Computational Modelling Energetic Data

For convenience, a summary of the solution and segregation energies ($E_{surface}$-E_{bulk}) is given in Table 75. Figure 67 plots the results and illustrates the general trends in the results whereby: A site doping becomes less favourable down the Group II titanates; B site doping (from simulations based on interatomic potentials) is equally favourable across all three titanates; and surface doping is more favourable than bulk doping. Figure 67 also illustrates the good agreement between the interatomic potential and DFT results, although the latter are generally slightly higher.

10.3. Model for Nickel Doped Strontium Titanate Catalyst Formation

10.3.1. Preparation

Analysis of nickel doped strontium titanate samples confirms that Ni will dissolve in this host lattice to a limited extent under low temperature, hydrothermal preparation conditions with an upper limit of approximately 5% atomic [83]. The potentially low solubility of Ni in bulk $SrTiO_3$ is also indicated by simulations based on interatomic potentials which gives a solution energy of 1.26 eV per Ni (as Ni^{2+}) which is endothermic. In addition, the results from EXAFS experiments strongly indicate that Ni substitutes at the octahedrally coordinated Ti^{4+} site under hydrothermal synthesis conditions. Such a substitution would require charge compensation by creation of oxygen vacancies for either Ni^{2+} or Ni^{3+} according to equations (97) or (104) respectively. In contrast to the experimental results, atomistic computational modelling data presented in Table 75 predict Ni substitution at the twelve fold coordinated Sr^{2+} site with no charge inbalance.

The apparent contradiction between experimental and computational results can be resolved by considering the kinetic effects operating under aqueous hydrothermal preparation conditions or indeed under any aqueous solution based methods compared to the theoretical predictions which represent a thermodynamic end point. In aqueous solution, Ni^{2+} well be present as a well defined octahedral, water coordinated species with a cation-oxygen bond distance of 2.07 Å (from neutron scattering experiments)

Table 75 Summary of the solution energies obtained for the dissolution of NiO into the alkaline earth titanates.

	Solution Energy /eV				
	BULK		SURFACE		
Substitution	Interatomic Potentials	DFT	Interatomic Potentials	DFT	Segregation Energy**** /eV
Ni^{2+} at the A site $CaTiO_3$	0.88	1.93	1.17	0.97	0.29
Ni^{2+} at the A site $SrTiO_3$	1.26	1.96	0.26	2.00	-1.00
Ni^{2+} at the A site $BaTiO_3$	3.04	2.55	1.28	4.55	-1.76
Ni^{2+} at the B site $CaTiO_3$*	2.45	3.00	1.50	-	-0.95
Ni^{2+} at the B site $SrTiO_3$*	2.12	2.02	1.16	-	-0.96
Ni^{2+} at the B site $BaTiO_3$*	2.52	1.40	1.37	-	-1.15
Ni^{3+} at the A site $SrTiO_3$**,§	7.80	-	-	-	
Ni^{3+} at the A site $SrTiO_3$***,§	7.53	-	-	-	
Ni^{3+} at the B site $SrTiO_3$*	6.46	-	-	-	

*All values quoted for B site substitution have a nearest neighbour oxygen vacancy. ** Sr^{2+} ion vacancy charge compensation. *** Ti^{4+} ion vacancy charge compensation. **** From interatomic potential results. § Doped with Ni^{2+} followed by oxidation with gaseous oxygen.

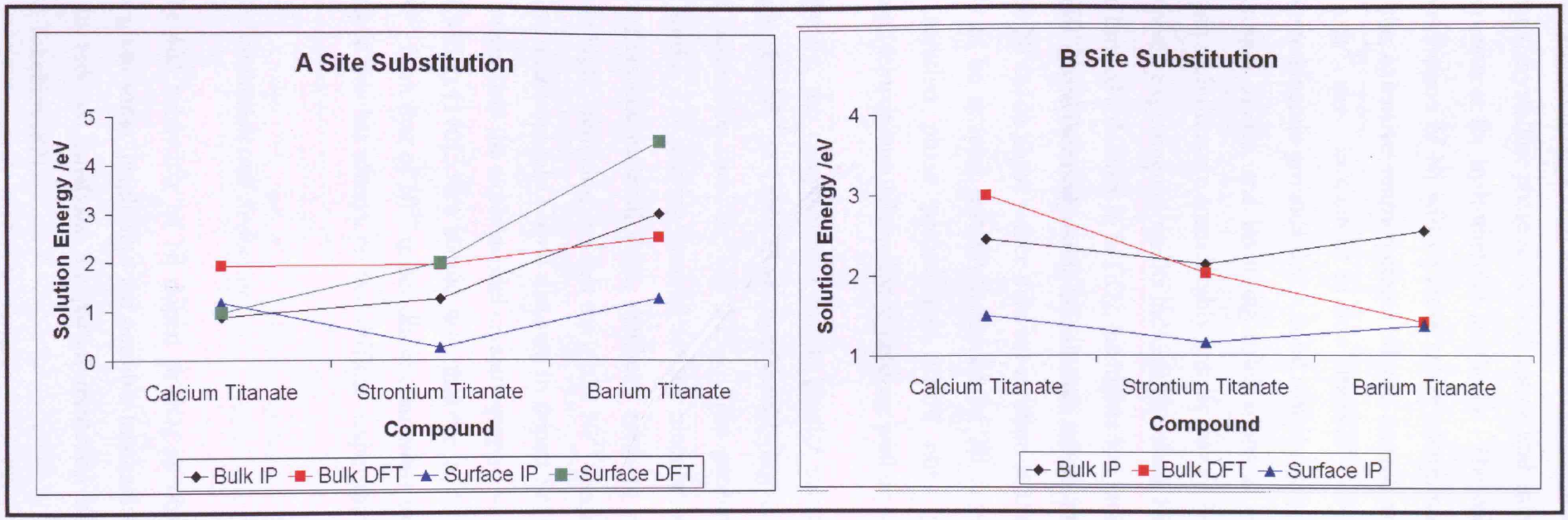

Figure 67 Illustration of the trends in the solution energies for the alkaline earth titanates for substitution of Ni^{2+} at the A site and B site (with a nearest neighbour oxygen vacancy).

[180]. During hydrothermal $SrTiO_3$ synthesis, this geometrical arrangement will persist in the precipitated crystalline phase since both cation and anion mobilities are negligible at typical temperatures for hydrothermal synthesis. The original solution phase with octahedral coordination of Ni will be more easily accommodated in a Ti^{4+} site rather than involve the extensive rearrangement of the coordination geometry required to substitute in a Sr^{2+} site. In contrast to this kinetically controlled process, we might predict on thermodynamic grounds that a solid state preparation, for example, starting from finely ground oxides, and involving calcinations at temperatures at 1000°C or higher, when ion mobilities are considerably greater, would lead to Ni substitution at the Sr^{2+} site. However, experimental results indicate that since Ni is predicted by modelling to have only a limited solubility in $SrTiO_3$, the higher ion mobilities at high temperature serve to achieve a true thermodynamic equilibrium where phase segregation occurs to give a separate Ni oxide phase rather than substitution at the Sr^{2+} site. The same end point is likely to be at least partially achieved for Ni doped materials produced by conventional solution phase preparations where non-crystalline precipitates are subjected to high temperature calcination to produce well crystalline material [82].

Specifically, the computational results predict substitution as Ni^{2+} since the solution energies for Ni^{3+} in Table 75 are considerably higher than for Ni^{2+} for either of the two host perovskite sites, Sr^{2+} or Ti^{4+}. This prediction is supported by the experimental work. The starting material for the preparation was a Ni^{2+} salt and the large amount of organic material in the synthesis medium means that the preparation conditions were highly reducing and that the initial Ni^{2+} species is unlikely to oxidise to form Ni^{3+}. The measured Ni-O bond distance in doped $SrTiO_3$ by EXAFS (2.03Å) is considerably longer than the experimental crystallographic value for the Ni^{3+}-O distance in LaNiO3 (1.935Å) [170]. We should note that the ability to distinguish the likely presence of Ni^{2+} from that of Ni^{3+} under dilute conditions by computational modelling is important since this has always proved difficult experimentally in the catalysis area [181].

10.3.2. Calcination and Reduction

The thermal behaviour of Ni doped $SrTiO_3$ as observed by *in situ* EXAFS measurements gives some insight into the possible mechanism for controlling Ni metal particle size in reduced catalysts for partial oxidation of methane as claimed by Hayakawa and Takehira [82].

Calcination in air at 850°C shows clear evidence from EXAFS data in Table 74 for segregation of a nickel oxide phase, probably NiO, due to the appearance of a feature which can be abscribed to a Ni-Ni distance of 2.95 Å as found for the NiO structure [177]. The NiO is thought to result from a transition from a metastable, Ni doped material prepared under kinetically controlled conditions (low temperature, hydrothermal synthesis) to a more thermodynamically stable phase segregated system.

There is strong evidence from the solution and segregation energies (Table 75) predicted by interatomic potentials, that any movement of nickel cations in the lattice would be driven from bulk B sites to surface A sites. Despite the limited mobility of cations likely at the calcination temperature (850°C) two factors can be considered to increase the feasibility of bulk B site to surface A site motion occurring:

- Computational modelling has shown that the lowest energy configuration for B site doping is to place the charge compensating oxygen vacancy in the nearest neighbour shell. Therefore, oxygen mobility, which occurs more readily than cation mobility, is likely to migrate oxygen vacancies towards defect B sites.

- Its has been shown by Kilo et al [182] using molecular dynamics, that A site and B site cationic migration is strongly coupled in perovskite lattices. Furthermore, a cluster of defects consisting of an A site vacancy, a B site defect and an oxygen vacancy is needed for B site to B site migration. The B site defect must migrate via A sites, whereas direct A to A site migration is possible.

We propose that nickel cations, which were placed at the B site during the low temperature hydrothermal synthesis, are able to migrate to the A site assuming that there is a nearest neighbour oxygen and A site vacancy. Once the nickel has migrated to the A site it will then move towards the surface. However, the segregation process is far from complete since Ni^{2+} can still be strongly observed according to the EXAFS results in Table 74. Its is likely that only nickel cations in the near surface region would like able to migrate to the surface a form the NiO particles observed. We note that there is no evidence from EXAFS that nickel occupies the A site following calcination. However, there is strong indication from both the interatomic potential (Table 63) and DFT (Figure 61) calculations that a Ni^{2+} cation occupying a surface A site in the $SrTiO_3$

lattice has a first oxygen coordination sphere which is very close that that of the NiO lattice. The significance of this is twofold: first, the nickel may act as a seed for the growth of a NiO cluster and second, the "seed" nickel is strongly anchored to the surface which would reduce the likelihood of sintering of the clusters. Assuming that the Ni^{2+} cations are able to migrate to the surface, it may be that the number of nickel cations occupying the A sites is small compared to those still occupying the B sites and those in the NiO clusters.

Finally, under reducing conditions in a 5% H_2/He mix at 900°C, reduced Ni metal is observed. Examination of the the results of the EXAFS modelling in Table 74 show that the process of segregation of Ni from the lattice is still not complete since oxidised lattice Ni can still be detected. At 950°C additional reduced metal is detected and less oxidized lattice Ni, but nonetheless some still remains.

10.4. Calcium and Barium Titanates

It was suggested by Takehira et al [82] that the enhanced activity of the Ni/$SrTiO_3$ system over the Ni/$CaTiO_3$ and Ni/$BaTiO_3$ systems was due to the stable, fine dispersion of nickel particles on the former material. The role of the metal particle dispersion was further shown by the lower activity of a sample of $SrTiO_3$ which had been prepared in a pure form and subsequently impregnated with a nickel solution. The nickel particles on the latter Ni/$SrTiO_3$ sample were much larger. It seems clear that, to form an active catalyst, there must be a controlled release of dopant onto the surface of the host and once the dopant has reached the surface any clusters that are formed must be well anchored to the surface to prevent sintering.

In the work of Takehira, the samples were prepared via a low temperature precipitation route from aqueous solution before being calcined at 850°C to form crystals as for the preparation of the Ni/$SrTiO_3$ material described above. Therefore, it is likely that all of the samples formed metastable lattices where the dopant nickel cations are substituted at the B site.

In the case of $CaTiO_3$, there is a strong driving force predicted by both interatomic potentials and DFT for the Ni^{2+} cations to migrate to the A site (Table 75). Further migration of the dopant to the surface is predicted by DFT, but not for interatomic potentials. Although it should be noted that the dissolution of NiO with

substitution at the A site for $CaTiO_3$ is predicted to be endothermic using interatomic potentials and the $Ni/CaTiO_3$ system would be expected to phase separate at thermodynamic equilibrium. Experimentally, there is clear evidence that nickel, probably NiO initially, does segregate from the perovskite phase as large (~20-30 nm in diameter) particles of nickel metal as are observed experimentally on the surface following reduction [82]. Unlike strontium titanate, the nickel dopant cation is not predicted to form a "seed" for the formation and anchoring of a nickel oxide cluster on the surface of the perovskite host (Figure 61) which may allow the growing NiO clusters to migrate along the surface and merge.

For $BaTiO_3$, the nickel dopant cations are predicted by the solution energies given in Table 75 not to migrate to the A site from the B site before migration to the surface. Although, as noted above B site to B site migration is expected to go via A sites. Once the cations have reached the surface, the solution energies would suggest a distribution across both cationic sites. Due to the very large size mismatch between the Ba^{2+} and Ni^{2+} cations, the dopant cations are located nearer to the first subsurface layer when doped at the A site (Figure 61). Although the location of the dopant cation may lead to it being well anchored to the surface, the depth away from the surface layer may also inhibit the formation of the NiO clusters. Consequently the observed nickel clusters (~20 nm in diameter) present on the nickel doped barium titanate surfaces would be seeded from nickel cations at the B site, which are predicted to sit at the surface of the perovskite lattice and not well anchored to the surface.

10.5. Implications for Catalysis

It is clear that, at 850°C, some Ni is expelled from the lattice, probably as NiO, which would be reduced to Ni metal in an H_2 atmosphere. This kind of metastable behaviour is well known from other oxide systems, for example, various transition metals doped in ZrO_2 [183].

It is postulated that the amount of Ni reduced is controlled by the level of NiO segregated from the doped lattice. The degree of segregation will be controlled by a temperature/time relationship and hence there is an increase in the level of surface Ni on going from 850 to 950°C. The doped material can be considered to operate as a slow release system where NiO segregates (the rate determining step) and is subsequently reduced within a very short time scale. Potentially this mechanism could lead to a high

dispersion of reduced metal crystallites depending on kinetic effects governed by the dispersion of Ni within the lattice and thermodynamic effects linked to the Ni solubility energy. We should note that the temperatures used in the experiments reported above are considerably higher than normally observed for reduction of bulk NiO (350°C) [184]. The rate of reduction would be faster than the rate at which NiO segregated from the lattice and could form clusters of substantial size.

Two key factors can be identified as particular significant for the development of other perovskite supported dispersed metal catalysts: the synthetic route and the relative size of the dopant and host cations. A low temperature, solution phase crystallisation synthesis allows the formation of metastable metal doped perovskite material with sufficiently high concentrations of the dopant cations to form the active phase on reduction. The unique feature identified from modelling for nickel doped strontium titanate was that Ni^{2+} was of such a size as to sit between the surface and first subsurface layer when substituted at the A site and provide a likely point for the nucleation of a NiO cluster.

11.Conclusions and Recommendations for Future Work

The use of computational molecular modelling to enhance our understanding of catalytic materials has been clearly demonstrated in this work. For the three nickel doped alkaline earth titanates we have been able to make predictions regarding both the formation of the metastable catalytic precursor materials and their transformation to active catalyst phases. We conclude that:

- The use of a low temperature, aqueous, synthetic route is essential for the formation of a metastable material which is likely to be surface enriched with dopant cations. Furthermore, on heating, the sample will release the dopant onto the surface in a controlled manner to form nickel oxide clusters at the surface.

- The presence of Ni^{3+} in the bulk of strontium titanate is predicted to be highly unfavourable.

- Nickel cations will migrate to the A site of a calcium titanate host followed by segregation of the perovskite and NiO phases at the surface. Since the NiO phases are not well anchored to the surface, they will grow into larger particles as they move across the surface. Due to the growth of large NiO particles at the surface the catalytic activity of $Ni/CaTiO_3$ materials will be restricted when the NiO phase is reduced.

- Nickel cations will migrate to the A site of a strontium titanate host followed by segregation of the perovskite and NiO phases at the surface, as for the calcium titanate host. However, in contrast to either the $CaTiO_3$ or $BaTiO_3$ host lattices, the position of the Ni^{2+} dopant in the surface A site forms a seed to nucleate a NiO cluster that would be well anchored to the surface. Consequently, the NiO clusters at the surface more remain as discrete small particles, leading to enhanced catalytic activity on reduction to Ni metal.

- Nickel cations are not readily accommodated at either perovskite cation sites in barium titanate. Nickel doped barium titanate would be expected to phase segregate on heating with the Ni^{2+} cations moving from B site to

A site to B site. At the surface NiO clusters would be difficult to nucleate when the Ni^{2+} is located at the surface A site and clusters formed from Ni^{2+} cations at the B site would be not well anchored to the surface. As for the $CaTiO_3$ host, the NiO clusters would be expected to merge forming larger particles at the surface restricting the catalytic activity of the reduced material.

- There is likely to be a strong correlation between the relative sizes of the cations and the probability of forming a dispersion of small, discrete, catalytically active particles on the host material. Computational modelling could readily predict other combinations of dopant/perovskite host that may form highly catalytically active materials.

Both computational and experimentally based studies can be suggested to extend the work in this thesis:

1. Computational:

To provide a complete set of data for both interatomic potential and DFT simulations, it would be useful to relax the surface with B site substitution using DFT. A study of the migration of Ni^{2+} cations through the lattice to understand how far through the lattice the cations are likely to move at the calcination and reduction temperatures would provide greater insight into the formation of the catalytically active phase. The NiO (and Ni metal) clusters formed at the surface could be modelled to gain an understanding of the reduction and, ultimately, catalytic pathways occurring in these materials. Other dopant/host material combinations could be investigated to provide leads for new catalytic materials.

2. Experimentally:

The synthesis of nickel doped strontium titanate using a high temperature solid state route would confirm if a single phase material could be formed under thermodynamic conditions, and if so which site the dopant cations occupied. In order to confirm the predictions made by computational modelling for the $Ni/CaTiO_3$ and $Ni/BaTiO_3$ systems, the hydrothermal synthesis of these materials and subsequent XAS analysis may be proposed.

12.Acknowledgements

I would like to express my thanks and appreciation to my supervisor Professor C. Richard A. Catlow and "unofficial" supervisor Professor Richard J. Oldman. Many others deserve a mention for their continued help and encouragement during these studies including Dr Scott Woodley, Dr Sam French, Dr Alexey Sokol, Dr Furio Cora, Dr Martin Fowles, Dr Dave Willock, Dr Phil Ingram and Dr David Birdsall. I would like to thank the Royal Institution of Great Britain, Johnson Matthey plc, the EPSRC and University College London for making this work possible.

References

1 Atake, I., Nishida, K., Li, D., Shishido, T., Oumi, Y., Sano, T., Takehira, K. *J. Mol. Catal. A*, 275, 130, (2007).

2 Tanaka, H., Uenishi, M., Taniguchi, M., Tan, I., Narita, K., Kimura, M., Kaneko, K., Nishihata, Y., Mizuki, J., *Catal. Today*, 117, 321, (2006).

3 Bedel, L., Roger, A.C., Estournes, C., Kiennemann, A., *Catal. Today*, 85, 207, (2003).

4 Takehira K., Shishido T., Kondo M., *J. Catal.*, **2002**, 207, 307

5 Wells A.F., "Structural Inorganic Chemistry", 5th Ed., 584, Oxford University Press (1984).

6 VGoldschmidt V.M., Skrifer Norske Videnskaps-Akad. Oslo, I. Mat.-Nat. Kl. 8, 1926.

7 Ali, R., Yashima, M., *J. Solid State Chem.*, 178, 2867, (2005).

8 Kwei, G.H.;Lawson, A.C.Jr.;Billinge, S.J.L.;Cheong, S.-W, *J. Phys. Chem.*, 97, 2368, (1993).

9 Hutton, J. and Nelmes, R.J, *J.Phys.C; Solid State Phys.*, 1713-1736, **14**, (1981).

10 Yamanaka, T.;Hirai, N.;Komatsu, Y., *American Mineralogist*, 1183-1189, **87**, (2002).

11 Jauch., W., Reehuis, M., *Acta Cryst. A*, 411-417, **A61**, (2005).

12 Cowley, R.A., *Phys. Rev.*, A981-A997, **134**, (1963).

13 Shirane, G., Yamada, Y., *Phys. Rev.*, 858-863, **177**, (1968).

14 Saifi, M.A., Cross, L.E., *Phys. Rev. B*, 677-684, **2**, (1970).

15 Stirling, W.G., *J. Phys. C: Solid State Phys.*, 2711-2730, **5**, (1972).

16 Jauch, W., Reehuis, M., *Acta Cryst. A*, 411-417, **A61**, (2005).

17 http://wok.mimas.ac.uk

18 Schaak, R.E., Mallouk, T.E., *Chem. Mater.*, 14, 1455, (2002).

19 Dion, M., Ganne, M., Tournoux, M., Revez, J., *J. Rev. Chim. Miner.*, 21, 92, (1984).

20 Ruddlesden, S.N., Popper, P., *Acta Crystallogr.*.11, 54, (1958).

21 Gopalakrishnan, J., Bhat, V., *Inorg. Chem.*, 26, 4301, (1987)

22 Aurrivillius, B., *Ark. Kemi*, 1, 499, (1949).

23 Bramwell, S.T., Gingras, M.J.P., *Science*, 294, 1495, (2001).

24 Colville, A.A., Geller, S., *Acta Cryst.*, B27, 2311, (1971).

25 Wu, Y., Yu, T., Dou, B., Wang, C., Xie, X., Yu, Z., Fan, S., Fan, Z., Wang, L., *J. Catal.*, 88-107, **120**, (1989).

26 Kroger, F.A., *Solid State Phys.*, 3, 307, (1956).

27 Glazer, A.M., *Acta Cryst.*, B28, 3384, (1972).

28 Goodenough, J.B., *Rep. Prog. Phys.*, 67, 1915, (2004).

29 Dove, M.T., "Structure and Dynamics: An atomic view of materials", Oxford University Press, (2003).

30 Cava, R.J., *J. Am. Ceram. Soc.*, 83, 5, (2000).

31 Moritomo, Y., Asamitsu, A., Kuwahara, H., Tokura, Y., *Nature*, 380, 141, (1996).

32 Rehrig, P.W., Park, S.E., Trolier,-McKinstry, S., Messing, G.L., Jones, B., Shrout, T.R., *J. Appl. Phys.*, 86, 1657, (1999).

33 Peña, M.A., Fierro, J.G.L., *Chem. Rev.*, 101, 1981, (2001).

34 Esaka, T., Sakaguchi, H., Kobayashi, S., *Sol. St. Ionics*, 166, 351, (2004).

35 Au, C., Chen, K.D., Dai, H.X., Liu, Y.W., Luo, J.Z., Ng, C.F., *J. Catal.*, 179, 300, (1998).

36 Cherry, M., Islam, M.S., Catlow, C.R.A., *J. Solid State Chem.*, 118, 125, (1995).

37 Bhalla, A.S., Guo, R., Roy, R., *Mat. Res. Innovat.*, 4, 3, (2000).

38 Ganguly, P., Rao, C.N.R., *J. Sol. State Chem.*, 24, 820, (1979).

39 Sleight, A.W., Gilson, J.L., Bierstedt, P.E., *Sol. State Commun,* 17, 27, (1975).

40 Bhalla, A.S., Roy, R., Cross, L.E., "Chemistry of Oxide Superconductors", Blackwell Scientific Publications, (1988).

41 Wu. M.K., Ashburn, J.R., Torng, C.J., Hor, P.H., Meng, R.L., Gao, L., Huang, Z.J., Wang, Y.Q., Chu, C.W., *Phys. Rev. Lett.*, 58, 908, (1987).

42 Prellier, W., Lecoeur, Ph., Mercey, B., *J. Phys.: Conden. Matter*, 13, R915, (2001).

43 Ventura, C.I., Gusmao, M.A., *Phys. Rev. B,* 65, 014422, (2002).

44 Ramakrishnan, T.V., *Phil. Trans. R. Soc. Lond. A*, 356, 41, (1998).

45 Wainer, E., Soloman, S., Titanium Alloy Manufacturing Co. Report 8-9

46 Wul, B.M., Goldman, I.M., *Doki Akad. Nauk SSSR*, 46, 154, (1945).

47 Miyake, S., Ueda, R., *J. Phys. Soc. Jpn.*, 1, 32, (1946).

48 Von Hippel, A., "Molecular Science and Molecular Engineering", MIT Press, (1959).

49 Kay, H.F., Vousden, P., *Phil Mag.*, 40, 1019, (1949).

50 Esaka, T., Sakaguchi, H., Kobayashi, S., *Solid State Ionics*, 166, 351, (2004).

51 Thangadurai, V., Weppner, W., *Ionics*, 12, 81, (2006).

52 Fergus, J.W., *Solid State Ionics*, 177, 1529, (2006).

53 Lashtabeg, A., Skinner, S.J., *J. Mater. Chem.*, 16, 3161, (2006).

54 Choudhary, T.V., Banerjee, S., Choudhary, V.R., *Appl. Catal. A*, 234, 1, (2002).

55 Tejuca, L.G., Fierro, J.L.G., Tascon, J.M.D., *Adv. Catal.*, 36, 237, (1989).

56 Ponce, S., Pena, M.A., Fierro, J.L.G., *Appl. Catal. B*, 24, 193, (2000).

57 Voorhoeve, R.J.H., "Advanced Materials in Catalysis", Academic Press, New York, (1977).

58 Sadykov, V.A., Isupova, L.A., Zolotarskii, I.A., Bobrova, L.N., Noskov, A.S., Parmon, V.N., Brushtein, E.A., Telyatnikova, T.V., Chernyshev, V.I., Lunin, V.V., *Appl. Catal. A*, 204, 59, (2000).

59 Wu, Y., Yu, T., Dou, B., Wang, C., Xie, X., Yu, Z., Fan, Sh., Fan, Zh., Wang, L., *J. Catal.*, 120, 88, (1989).

60 Tejuca, L.G., Fierro, J.L.G., Tascon, J.M.D., *Adv. Catal.*, 36, 237, (1989).

61 Tascon, J.M.D., Fierro, J.L.G., Tejuca, L.G., *Z. Phys. Chem.*, 124, 249, (1981).

62 Tabata, K., Hirano, Y., Suzuki, E., *Appl. Catal. A: Gen.*, 170, 245, (1998).

63 Falcon H., Martinez-Lope, M.J., Alonso, J.A., Fierro, J.L.G., *Appl. Catal. B: Environ.*, 26, 131, (2000).

64 Ward, T.R., Alemany, P., Hoffman, R., *J. Phys. Chem.*, 97, 7691, (1993).

65 Guilhaume, N., Primet, M., *J. Catal.*, 165, 197, (1997).

66 Watson, P.R., Somorjai, G.A., *J. Catal.*, 74, 282, (1982).

67 Abrahamson, H.B., Ginley, D.S., *J. Am. Chem. Soc.*, 98, 277, (1976).

68 Lehn, J.M., Sauvage, Ziessel, R., Hilaire, L., *Israel J. Chem.*, 22, 168, (1982).

69 Domen, K., Kudo, A., Onishi, T., Kosugi, N., Kuroda, K., *J. Phys. Chem.*, 90, 292, (1986).

70 Miyama, H., Fujii, N., Nagac, Y., *Chem. Phys. Lett.*, 74, 523, (1980).

71 Arakawa, T., Kurachi, H., Shiokawa, J., *J. Mater. Sci.*, 20, 1207, (1985).

72 Rostrup-Neilsen, J.R., Sehested, J., *Adv. Catal.*, 65-139, **47**, (2002).

73 Lui, .Q.S., Zhang, Q.C., Ma, W.P., He, R.X., Kou, L.J., Mou, Z.J., *Prog. in Chem.*, 17, 389, (2005).

74 York, A.P.E., Xiao, T., Green, M.L.H., *Topics in Catalysis*, 345-358, **22**, (2003).

75 Hu, Y.H., Ruckenstein, E., *Adv. Catal.*, 297-345, **48**, (2004).

76 Basile, F., Basini, L., Amore, M.D., Fornasari, G., Guarinoni, A., Matteuzzi, D., Del Piero, G., Trifiro, F., Vaccari, A., *J. Catal.*, 247-256, **173**, (1998).

77 Santos, A., Menéndez, M., Monzón, A., Santamaria, J., Miró, E.E., Lombardo, E.A., *J. Catal.*, 83-91, **158**, (1996).

78 Zhu, T., Flytzani-Stephanopoulos, M., *App. Catal. A: Gen.*, 403-417, **208**, (2001).

79 Urasaki, K., Sekine, Y., Kawabe, S., Kikuchi, E., Matsukata, M., *App. Catal. A:Gen.*, 23-29, **286**, (2005).

80 Hayakawa, T., Andersen, A.G., Shimizu, M., Suzuki, K., Takehira, K. *Cat. Lett.*, 307-317, **22**, (1993).

81 Hayakawa, T., Harihara, H., Andersen, A.G., Suzuki, K., Yasuda, H., Tsunoda, T., Hamakawa, S., York, A.P.E., Yoon, Y.S., Simizu, M., Takehira, K., *App. Catal. A: Gen.*, 391-410, (1997), **149**.

82 Takehira, K., Shishodo, T., Kondo, M, *J. Catal.*, 307-316, **207**, (2002).

83 Beale, A., Paul, M., Sankar, G., Oldman, R.J., Catlow, C.R.A., *in preparation for J. Phys. Chem C.*

84 Sadykov, V.A., Pavlova, S.N., Bunina, R.V., Alikina, G.M., Tikhov, S.F., Kuznetsova, T.G., Frolova, Yu.V., Lukashevich, A.I., Snegurenko, O.I., Sazonova, N.N., Kazantseva, E.V., Dyatlova, Yu.N., Usol'tsev, V.V., Zolotarskii, I.A., Bobrova, L.N., Kuz'min, V.A., Gogin, L.L., Vostrikov, Z.Yu., Potapova, Yu.V., Muzykantov, V.S., PAukshtis, E.B., Burgina, E.B., Rogov, V.A., Sobyanin, V.A., PArmon, V.N., *Kinetics Catal.*, 46, 243, (2005).

85 Nishihata, Y., Mizuki, J., Tanaka, H., Uenishi, M., Kimura, M., *J. Phys. Chem. Solids*, 274-282, **66**, (2005).

86 Cifà, F., Dinka, P., Viparelli, P., Lancione, S., Benedetti, G., Villa, P.L., Viviani, M., Nanni, P., *Appl. Catal. B: Env.*, 463-471, **46**, (2003).

87 Zacate, M.O., Grimes, R.W., Scrivener, K., *J. Mater. Sci.*, 35, 3727, (2000).

88 Mather, G.C., Islam, M.S., Figueiredo, F.M., *Adv Funct. Mater.*, 17, 905, (2007).

89 Buscaglia, M.T., Buscaglia, V., Viviani, M., Nanni, P., *J. Am. Chem. Soc.*, 84, 376, (2001).

90 Thomas, B.S., Marks, N.A., Begg, B.D., *Nucl. Instr. And Meth. in Phys. Res.* , 254, 211, (2007).

91 Astala, R., Bristowe, P.D., *Modelling Simul. Mater. Sci. Eng.*, 9, 415, (2001).

92 Evarestov, R.A., Piskunov, S., Kotomin, E.A., Borstel, G., *Phys. Rev. B*, 67, 064101, (2003).

93 Luo, W., Duan, W., Louie, S.G., Cohen, M.L., *Phys. Rev. B*, 70, 214109, (2004).

94 Evarestov, R.A., Kotomin, E.A., Zhukovskii, Yu. F., *Int. J. Quantum Chem.*, 106, 2173, (2006).

95 Piskunov, S., Heifets, E., Eglitis, R.I., Borstel, G., *Comp. Mater. Sci.*, 29, 165, (2004)..

96 Chen, S.P., *J. Mater. Res.*, 13, 1848, (1998).

97 Wang, Y.X., Arai, M., Sasaki, T., Wang, C.L., *Phys. Rev. B*, 73, 035411, (2006).

98 Heifets, E., Eglitis, R.I., Kotomin, E.A., Maier, J., Borstel, G., *Surf. Sci.*, 513, 211, (2002).

99 Heifets, E., Eglitis, R.I., Kotomin, E.A., Maier, J., Borstel, G., *Phys. Rev. B*, 64, 235417, (2001).

100 Padilla, J., Vanderbilt, D., *Surf. Sci.*, 418, 64, (1998).

101 Piskunov, S., Kotoman, E.A., Heifets, E., Maier, J., Eglitis, R.I., Borstel, G., *Surf. Sci.*, 575, 75, (2005).

102 Meyer, B., Padilla, J., Vanderbilt, D., *Faraday Discuss.*, 114, 395, (1999).

103 Padilla, J., Vanderbilt, D., *Phys. Rev. B*, 56, 1625, (1997).

104 Shannon, R.D., Prewitt, C.T., *Acta Crystallog.*, B25, 925, (1969).

105 Ewald, P.P.. *Ann. Phys.*, 64:253-287, (1921).

106 Lewis G.V., Catlow, C.R.A., *J. Phys. C*, 18, 1149, (1985).

107 Lennard-Jones, *J.E.*, *Proc. Phys. Soc.*, 43, 461, (1931).

108 Dick, B.G., Overhauser, A.W., *Phys. Rev.*, 112, 90, (1958).

109 Kittle C., "Introduction to Solid State Physics, 7th Ed", John Wiley & Sons, Inc., (1996).

110 Svedung, H., Krems, R., Marković, N., Nordholm, S., *Phys. Chem. Chem. Phys.*, 3, 2216, (2001).

111 Catlow, C.R.A, *Proc. R. Soc.*, 353, 533, (1977).

112 Lewis G.V., Catlow C.R.A., *J. Phys. Chem. Solids*, 47, 89, (1986).

113 Akhtar M.J., Akhtar Z.U.N., Jackson R.A., Catlow, C.R.A., *J. Am, Ceram. Soc.*, 78, 421, (1995).

114 Jensen, F., "Introduction to Computational Chemistry", John Wiley & Sons, (2002).

115 Press, W.H., Teukolsky, S.A., Vetterling, W.T, Flannery, B.P., "Numerical recipes in Fortran: The art of scientific computing", Cambridge University Press, (1986)

116 Press, W.H., Flannery, B.P., Teukolsky, S.A., Vetterling, W.T., "Numberical Recipes in C: The Art of Scientific Computing", Cambridge University Press, (1992).

117 Fletcher, R., Powell, M.J.D., *Comput. J.*, 6, 163-168, (1964).

118 Shanno, D.F., *Math. Comput.*, 24, 647-656, (1970).

119 Mott, N.F., Littleton, M.J., *Trans. Faraday Soc.*, 34, 485-499, (1938).

120 Widom, B., "Statistical Mechanics, A Concise Introduction for Chemists", Cambridge University Press, (2002).

121 Monkhorst, H.J., Pack, J.D., *Phys. Rev. B,* 13, 5188-5192, (1976).

122 Allen, M.P., Tildesley, D.J.. "Computer simulation of liquids", Oxford University Press, (1987).

123 Taylor, M.B., Barrera, G.D., Allan, N.L. Barron, T.H.K., *Phys. Rev. B*, 56, 14380, (1997).

124 Gale, J.D., *J. Phys. Chem. B*, 102, 5423-5431, (1998).

125 Kantorovich, L.N., *Phys. Rev. B*, 51:3520-3534, (1995).

126 Gibbs, J.W., "Collected Works", New York, Longman (1928).

127 Broadbelt, L.J., Snurr, R.Q., *Appl. Cat. A.- Gen.*, 200, 23, (2000).

128 Gay, D.H., Rohl, A.L., *J. Chem. Soc., Faraday Trans.*, 91, 925, (1995).

129 Tasker, P.W., *J. Phys. C*, 12, 4977, (1979).

130 Leach, A.R., "Molecular Modelling, Principles and Applications, 2nd Ed.", Pearson Education Ltd., (2001).

131 Jensen, F., "Introduction to Computational Chemistry", John Wiley and Sons, (2002).

132 Atkins, P.W., Friedman, R.S., "Molecular Quantum Mechanics", Oxford University Press, (1996)

133 Schrödinger, E., *Ann. d. Physik*, 79, 361, (1926).

134 Born, M., Oppenheimer, J.R., *Ann. d. Physik*, 84, 457, (1927).

135 Fock, V., *Z. Phys.*, 61, 126, (1930).

136 Roothaan, C.C.J., *Rev. Mod. Phys.*, 23, 69, (1951).

137 Hall, G.G., *Proc. R. Soc. (London)*, A205, 541, (1951).

138 Hohenburg, P., Kohn, W. *Phys. Rev.* 136, B864, (1964).

139 Block, F., *Z. Physik,* 57, 545, (1929).

140 Dirac, P.A.M., *Cambridge Phil. Soc.*, 26, 376, (1930).

141 Kohn, W., Sham, L.J., *Phys. Rev.* 140, A1133, (1965)

142 Vosko, S.J., Wilk, L., Nusair, M., *Can. J. Phys.*, 58, 1200, (1980).

143 Perdew, J.P., Wang, Y., *Phys. Rev. B*, 45, 13244, (1992).

144 Perdew, J.D., Wang, Y., *Phys. Rev. B*, 33, 8800, (1986).

145 Becke, A.D., *Phys. Rev. B*, 38, 3098, (1988).

146 Lee, C., Yang, W., Parr, R.G., *Phys, Rev, B*, 37, 785, (1988).

147 Harris, J., *Phys. Rev. A*, 29, 1648, (1984).

148 Becke, A.D., *J. Chem. Phys.*, 98, 1372, (1992).

149 Becke, A.D., *J. Chem. Phys.*, 98, 5648 (1993).

150 Pisani, C., Dovesi, R., *Int. J. Quantum Chem.*, 17, 501, (1980).

151 Kohanoff, J. "Electronic Structure Calculations for Solids and Molecules", Cambridge University Press, (2006).

152 Bloch, F., *Z. Phys.*, 52, 555, (1928).

153 Philips, J.C., Kleinman, L. *Phys. Rev.*, 136, 287, (1959).

154 Slater, J.C., *Phys. Rev.*, 42, 33, (1932).

155 Towler, M.D., Zupan, A., Causà, M., *Comp. Phys. Comm.*, 98, 181, (1996).

156 Alfredsson, M., Price, G.D., Catlow, C.R.A., Parker, S.C., Orlando, R., Brodholt, J.P., *Phys. Rev. B*, 70, 165111, (2004).

157 Perdew, J.P., Burke, K., Ernzerhof, M., *Phys. Rev. Lett.*, 77, 3865, (1996).

158 Valenzano, L., Torres, F.J., Doll, K., Pascale, F., Zicovich-Wilson, C.M., Dovesi, R., *Z. Phys. Chem.*, 220, 893, (2006)

159 Bredow, T., Heitjans, P., Wilkening, M., *Phys. Rev. B*, 70, 115111, (2004).

160 Wadt, W.R., Hay, P.J., *J. Phys. Chem.*, 82, 284, (1985).

161 Habas, M.-P., Dovesi, R., Lichanot, A., *J. Phys: Condes. Matter*, 10, 6897, (1998).

162 http://www.crystal.unito.it

163 Pisani, C., Dovesi, R., Roetti, C., "Lecture Notes in Chemistry", 48, , Springer-Verlag, Heidelberg (1998).

164 Jauch, W., Palmer, A., *Phys. Rev. B*, 60, 2961, (1999).

165 Cora, F., *Mol. Phys.*, 103, 2483, (2005).

166 Sepliarsky M, Asthagiri A, Phillpot S.R., Stachiotti M.G., Migoni R.L., *Curr. Opinion in Sol. St. and Mater. Sci.*, 9, 107, (2005).

167 Sawada, H., *Mater. Res. Bull.*, 31, 141, (1996).

168 Lide, D.R. (Ed.), "CRC Handbook of Chemistry and Physics, 2003-2004", 84th Edn., Boca Raton, Fla.

169 http://cds.dl.ac.uk/

170 Park, J-C, Kim, D-K, Byeon, S.H., Kim, D., *J. Synchotron Radiation*, 8, 704, (2001)

171 Catti, M, Sandrone G., *Faraday Discuss.*, 189-203, **106**, (1997).

172 Cherry, M., Islam, M.S., Catlow, C.R.A., *J. Sol. State Chem.*, **118**, 125-132 (1995).

173 Park, J.-C., Kim, D.-K., Byeon, S.-H., Kim, D., *J. Sync. Rad.*, **8**, 704-706, (2001).

174 Towler, M.D., Allan, N.L., Harrison, N.M., Saunders, V.R., Mackrodt, W.C., Apra, E., *Phys. Rev. B*, 50, 5041, (1994).

175 Pisani, C., Dovesi, R., Roetti, C., "Lecture Notes in Chemistry", 48, , Springer-Verlag, Heidelberg (1998).

176 Gale, J.D., "Handbook of Materials Modelling", Ed. Sidney Yip, Springer Netherlands, (2005).

177 Taguchi, H., *Sol. State Commun.*, 108, 635, (1998).

178 Goldstein, H., "Classical Mechanics", 2nd Ed., Addison-Wesley Publishing Company, Inc., (1980).

179 Neilson, G.W., Enderby, J.E., *Proc. Roy. Soc. London A*, 390, 353, (1983).

180 Carley, A.F., Jackson, S.D., O'Shea, J.N., Roberts, M.W., *Surf. Sci.*, 440, L868, (1999)

181 Kilo, M., Taylor, M.A., Argirusis, C., Borchardt, G., Jackson, R.A., Schulz, O., Martin, M., Weller, M., *Sol. St. Ionics*, 175, 823, (2004).

182 Kumar, P., Sun, Y., Idem, R.O., Energy & Fuels, 21, 3113, (2007).

183 Parravano, G., *J. Am. Chem. Soc.*, 74, 1194, (1952).